INTEGRATING ADVANCED 3D CELL CULTURE TECHNIQUES WITH RAPID-PROTOTYPING MICROFLUIDICS FOR TRANSLATIONAL APPLICATIONS

BY

SHINY AMALA PRIYA RAJAN

A Dissertation Submitted to the Graduate Faculty of

WAKE FOREST UNIVERSITY GRADUATE SCHOOL OF ARTS AND SCIENCES

In Partial Fulfillment of the Requirements

For the Degree of

DOCTOR OF PHILOSOPHY

Biomedical Engineering

December 2019

Winston-Salem, North Carolina

Approved By:

Dr. Adam R. Hall, Ph.D., Advisor

Dr. Aleksander Skardal, Ph.D., Co-Advisor

Dr. Konstantinos Votanopoulos, M.D., Ph.D., Chair

Dr. Jennifer Munson, Ph.D.

Dr. Scott Verbridge, Ph.D.

"..with God all things are possible." Matthew 19:26

To my mom and my sister, who has always supported my dreams,

To Julio, who helped those dreams come true, and

To everyone, who motivated this work.

TABLE OF CONTENTS

LIST OF FIGURES AND TABLES

APPENDIX: LIST OF FIGURES AND TABLES

LIST OF ABBREVIATIONS

2D	Two-dimensional
3D	Three-dimensional
5'-DFCR	5'-deoxy-S-fluorocytidine
5'-DFUR	5'-deoxy-S-fluorouridine
5-FU	5-fluorouracil
A549	Adenocarcinoma human alveolar basal epithelial cell
AFB	Adhesive film-based
ALI medium	Air-liquid interface medium
Alpha MEM	Minimum Essential Medium Eagle- Alpha Modification
ANOVA	Analysis of variance
ATP	Adenosine triphosphate
BDNF	Brain-derived neurotrophic factor
BEGM	Bronchial epithelial cell growth
B-Lap	B-Lapachone
BOC	Body-on-a-chip
cAMP	Cyclic adenosine monophosphate
CCM	Cardiomyocyte culture media
CE	Cardiac endothelium cells
Cis	Cisplatin
CM	Cardiomyocytes
CNC	Computer numerical control
COC/COP	Cyclo-olefin (co)polymer
CRC	Colorectal cancer cells
CRS	Cytoreductive surgery
CT	Computerized tomography
CTO	Cell line-based Tumor organoid
DAPI	4′,6-diamidino-2-phenylindole
DI water	Deionized water
DIC	Dicoumorol

DMEM	Dulbecco's Modified Eagle's Media
DMEM/F-12	Dulbecco's Modified Eagle Medium/Nutrient Mixture F-12
DMSO	Dimethylsulfoxide
DNA	Deoxyribonucleic acid
DST	Double-sided tape
ECFR-P	Phosphorylated epidermal growth factor receptor
ECM	Extracellular matrix
EDTA	Ethylenediaminetetraacetic acid
EGF	Epidermal growth factor
EGFR	Epidermal growth factor receptor
EGM	Endothelial cell growth media
ELISA	Enzyme-linked immunosorbent assay
EO	Ethylene Oxide sterilization
FBS	Fetal bovine serum
FDA	Federal Drug Administration
GAG	Glycosaminoglycan
GBM	Glioblastoma multiforme
GI	Gastro-Intestinal
HA	Human astrocytes cells
HA	Hyaluronic acid
HBMEC	Human brain microvascular endothelial cells
HBVP	Human brain vascular pericytes
HCM	Hepatocyte culture media
HCT116	Human colon carcinoma cells
HDRA	Histoculture drug response assay
HEMA	Hydroxyethyl methacrylate
HEPES	4-(2-hydroxyethyl)-1-piperazineethanesulfonic acid
HH	Human hepatocytes
HIPEC	Heated intraperitoneal chemotherapy
HLEc	Human liver-derived endothelial cells
HM	Human iPSC-derived microglia

HN	Human neural cells
HNSCC	Head and neck squamous cell carcinoma
HO	Human oligodendrocytes cells
HSc	Hepatic stellate cells
HUVEC	Human Umbilical Vein Endothelial Cells
ID	Internal diameter
IHC	Immunohistochemistry
IL	Interleukin
iPSCs	Induced pluripotent stem cells
IR	Irradiation
IRB	Institutional Review Boards
kDa	Kilo Dalton
KS test	Kolmogorov-Smirnov test
L/D	Live/Dead
METC	Mitochondrial electron transport chain
MMP	Matrix metalloproteinases
mRNA	Messenger RNA
MW	Molecular Weight
NAC	N-Acetyl-L-Cysteine
NADP+	Nicotinamide adenine dinucleotide phosphate
NADPH	Reduced nicotinamide adenine dinucleotide phosphate
NDRI	National Disease Research Interchange
NHBE	Normal Human Bronchial Epithelial cells
NHCF	Normal human cardiac fibroblast
NHLF	Normal Human Lung Fibroblast
NQO1	NAD(P)H quinone dehydrogenase 1
OD	Outer diameter
OFM	Organoid Formulation media
P/S	Penicillin-streptomycin
PARP1	Poly (ADP-ribose) polymerase
PBS	Phosphate Buffered Saline

PDGF-AA	Platelet-derived growth factor alpha type homodimer
PDGF-AB	Platelet-derived growth factor alpha type heterodimer
PDMS	Polydimethylsiloxane
PDO	Patient-derived organoids
PDX	Patient-derived xenografts
PEG	Polyethylene glycol
PEGDA	Polyethylene glycol diacrylate crosslinker
PEGSSDA	Disulfide-containing polyethylene glycol diacrylate
PH	Poly-hydroxyalkanoates
PI	Photo Initiator
PLA	Polycaprolactone
PLG	Polylactide-co-glycolide
PLL	Poly-L-lysine
PM	Personalised medicine
PMMA	Polymethylmethacrylate
PPE	Personal Protective Equipment
PTFE	Polytetrafluoroethylene
PVA	Polyvinyl alcohol
PVC	Polyvinyl chloride
RNA	Ribonucleic acid
ROCK	Rho Kinase
ROS	Receive oxygen species
RPMI	Roswell Park Memorial Institute Medium
rSCC-61	Radiation-resistant cellosaurus cells
SCC-61	Radiation-sensitive cellosaurus cell line
SDF-1α	Human stromal cell-derived factor 1-alpha (CXCL12)
SSC	Spermatogonial stem cells
TGF-β	Transforming growth factor beta
TME	Tumor microenvironment
THP-1	Monocyte cells
UV	Ultra Violet

ABSTRACT

3D cell culture recapitulates the physiological microenvironment more fully than 2D models by providing relevant physical and spatial interactions. These factors are known to affect cellular behavior by influencing signaling and gene expression pathways and are thus crucial to accurately represent *in vivo* systems. Microfluidics can further provide robust control, delivery, and analytical capabilities that would enable parallel testing of such 3D culture constructs in a miniaturized context. We have combined adhesive film-based rapid prototyping with a photopolymerizable hydrogel to produce 3D cell cultures *in situ* in the chambers of an active microfluidic device. We initially tested the biocompatibility, robustness, and stability of the platform for cell culture applications by integrating a series of healthy, tissue-like constructs (organoids) that included as many as 20 human primary cell types in total for an extended period. Having established a system that could maintain even sensitive primary cells with high viability, we then explored its capacity to support long-term drug studies, ultimately demonstrating multi-organ drug interactions. Next, we developed a tumor-on-a-chip model by incorporating non-passaged or low-passaged cells derived from patient tumor biopsies into the device architecture for personalized medicine applications. Then, we established a novel, multi-step photopatterning approach to producing devices for assaying cell invasion *in vitro*, performing validation experiments with both anti-proliferative and anti-migratory drugs. Finally, we integrated our projects by probing patient-derived tumor cells with the invasion assay to realize a drug screening platform with added functionality over conventional technologies. Ultimately, this dissertation advances our ability to develop sophisticated 3D tissue and disease models, provides an improved strategy for parallel drug testing, and

enables cellular dynamics to be studied *in vitro* with efficiency in a low-cost microfluidic

platform.

CHAPTER 1

Introduction

1.1 Why 3D cell culture?

For centuries, humans have been using animals for biomedical research[1]. Early Greek physicians and scientists have performed experiments on other vertebrate animals to advance their understanding of anatomy, physiology, and pathology. Later, animals were used to test and practice new surgical procedure before performing it on human subjects. During this age, there were no moral questions raised against the use of animals as the people viewed themselves as the superior image of God. They ranked themselves higher in the *scala naturae* – 'the chain of being' and ranked animals lower as they were viewed as a natural part of the world created to serve them[2]. However, in the modern world, the use of animals present ethical concerns as it is considered cruelty to make animals suffer to benefit humans.

Nevertheless, animal testing has become an integral part of drug discovery since the 20th century after multiple incidents of mass poisoning caused due to drugs not being studied for safety concerns before clinically testing. Thus the animal model has become the golden standard to test the drug for efficiency and safety and also improve understanding of disease mechanisms and advance treatment strategies on humans[3–5]. Despite their significant role in biomedical research advancement, physicians, even in the 17th century, become skeptical about the validity of the physiological experiments carried on these extremely altered state animals. They also doubted if these models can provide valuable and reliable information[6]. This idea of a poor association between animal models and

humans resonates even today. Clinical trials exist as most successful findings in a mouse or primate model may not necessarily translate to human subjects. About 90% of the clinical translation fails from animals to humans, highlighting the difficulties in interpretation from the preclinical model to actual patients[3]. Apart from these significant issues, there are additional challenges, including, high expense and infrastructure requirements for maintenance of animals, and limitations in analytical diagnostics of living systems.

In response to these challenges, and in balancing the need to protect human subjects with the need for experimentation, cell culture emerged as a critical technology in the early to the mid-20th century. The idea of *in vitro* maintenance of tissue or cells prompted when the 19th-century English physiologist, Sydney Ringer, first isolated an animal heart and sustained in a salt solution outside the body. Then, the pioneering work using explanted nerve fiber tissue[7] followed by extensive research to identify nutrient requirements for growth media[8] laid a foundation for this approach. However, only upon the report of the first human cell line[9], the full potential impact of cell culture in biomedical research became evident. In 1951, the cells from the cervical cancer of Henrietta Lacks were cultivated in the Tissue Culture Laboratory by Dr. Gey, who discovered that the cells were growing and reproducing on a plastic plate outside the body. These cells called "HeLa" cells revolutionized biomedical research by aiding in the development of vaccines and the study of cancer[10]. Since that time, a wide range of human cell lines and growth media have been produced and used to bolster fields like oncology, virology, and pharmaceutics. The cell culture experiments have helped to understand cell biology, mechanism of disease, mechanism of drug and safety, and development of tissue engineering[11].
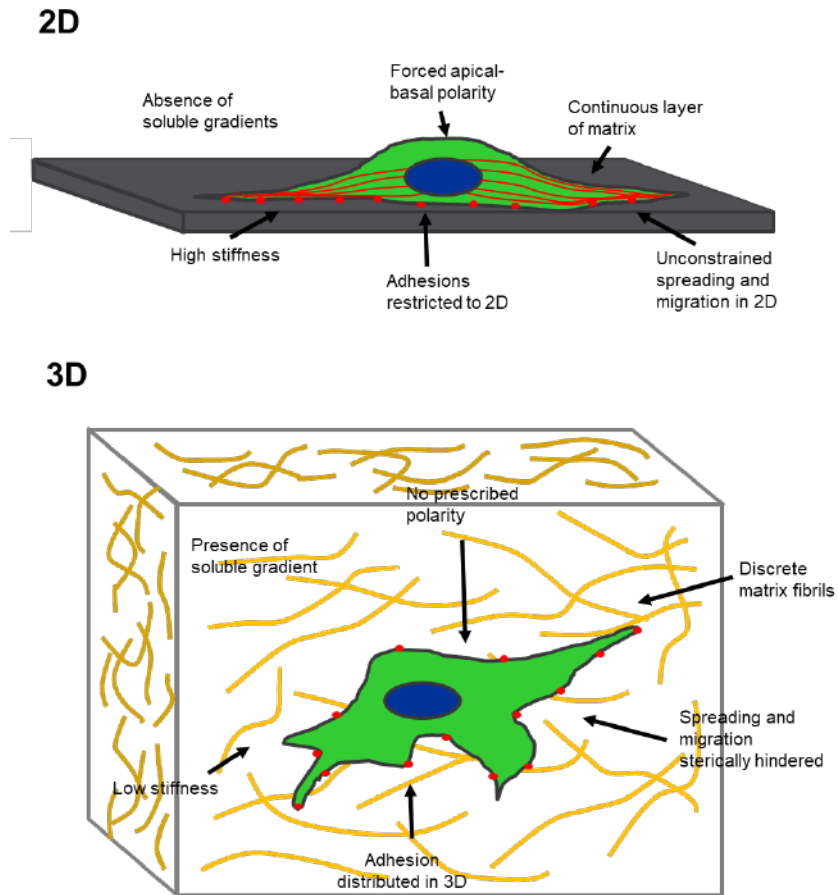
Figure 1.1 Adhesive, topographical, mechanical, and soluble cues in 2D and 3D. The cues encountered by a cell are strikingly different between an ECM-coated glass or plastic surface (2D) and a typical 3D ECM, such as collagen[12]. Adapted with permission from [12], Copyright© 2012, Company of Biologists Ltd.

Compared to animal testing, 2D cell cultures are relatively simplistic, low-cost, and easy to maintain. However, the disadvantage stems from the 2D nature itself that cannot faithfully mimic the native 3D structure of the tissue. As it cannot recapitulate the cell-cell and cell-extracellular matrix (ECM) environment of the tissue, the mechanism of cell proliferation, differentiation, gene and protein expression, drug metabolism, external and internal stimuli response among other cellular functions are not accurately captured[12–15]

(**Figure 1.1**). Also, when the cells are isolated from the tissue and transferred from a 3D state into 2D conditions, the cells naturally adapt their morphology to the surrounding and eventually lose their diverse phenotype[16,17]. These alterations affect their native functioning like cell signaling, secretion, and structural organization[18–20]. The cells also lose their polarity[21] while growing on a 2D surface due to the variation in their external environment interaction that leads to changes in response like apoptosis[22,23], spreading, migrating, and other microenvironmental cues[24]. The 2D culture involves growing a monolayer of cells on rigid materials such as polystyrene and glass. These simplified and unrealistic conditions cannot fully reflect the essential physiology of the actual tissue, such as limited source and a variable amount of oxygen, nutrients, metabolites, and signal molecules, as observed in the native architecture[15] (**Figure 1.2**). Besides, most of the 2D cultures are usually only one cell type of monocultures compared to the multi-cell native tissue.
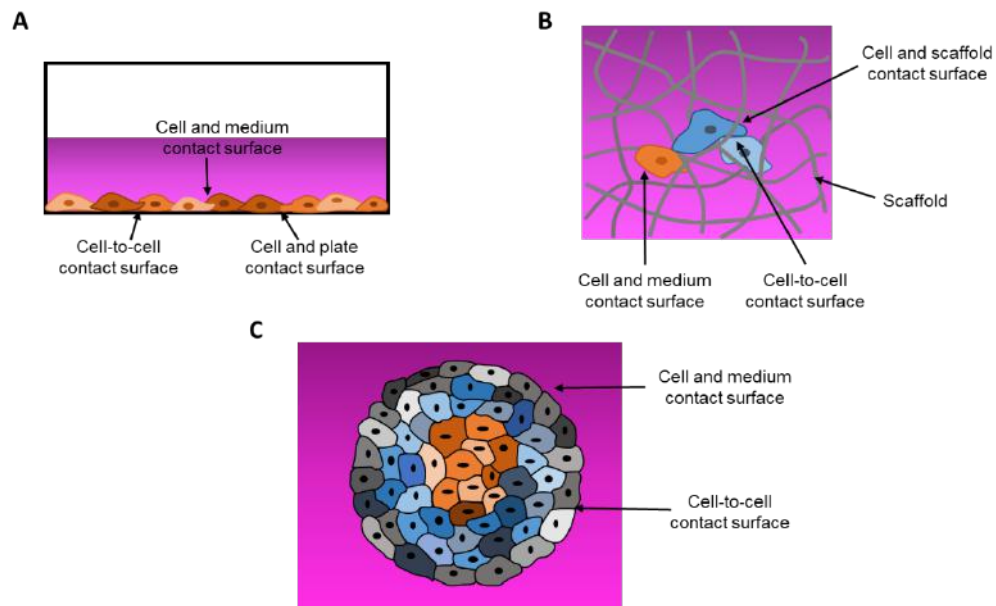
Figure 1.2. ***The contact surface of different cell culture methods.*** *A) 2D Cell culture with*

a monolayer of cells in maximum contact with the culture vessel, neighboring cells, and the culture medium. B) Cells attached to a 3D scaffold are in contact with the scaffolding, neighboring cells, and the culture medium. C) 3D spheroids that are in vivo like are in contact with neighboring cells and with the culture medium[11]. Adapted from an open-access image[11]

Though 2D cell culture has immensely advanced our knowledge in biomedical sciences, the inaccuracy of the model reflects on the 95% failure rate in drug development studies[25]. The unreliability of the existing model instigated the research of integrating a third dimension to the cell culture that becomes a more relevant and better alternative[26].

3D cell culture techniques overcome most of the limitations in 2D cell culture and animal models. The bioactivities performed by the cells in our body are the responses to highly complex stimuli in a 3D environment[27–29]. 3D cell culture approaches accurately model these stimuli responses and other *in vivo* interactions of tissues and organs that will help us understand better and study the underlying biochemical and biomechanical signals[30,31]. A well-designed 3D model would be able to mimic the intricate cell-cell and cell-matrix interaction and complex transport dynamics along with the spatial organization of the cells. These features promote viability, proliferation, migration into surrounding tissue, angiogenesis stimulation, matrix production, stem cell differentiation, cell polarization, response to stimuli, drug metabolism, gene expression and protein synthesis, and cell-cell communication[32] that mimics relevant *in vivo* physiology. Another significant advantage is the stability and robustness of the culture. A 3D cell culture can be maintained for the long term, up to 4 weeks, whereas 2D culture can be maintained only until the plate gets confluent. This stability makes the 3D culture more appropriate for long term studies and

assays. Unlike 2D cell culture, which is made mostly of a homogenous cell population, 3D culture can use multiple cell types to replicate the tissue. This heterogeneity helps to express significantly relevant *in vivo like* genetic and metabolic profiles [33]. These advantages show that 3D culture is not merely about adding another dimensionality but providing an appropriate micro physiological system that facilitates *in vivo* like responses to stimuli.

1.2 Types of 3D cell culture techniques

In recent years, there has been an exponential growth in developing new techniques to create optimal 3D models. These techniques are broadly divided into (i) scaffold-free culture techniques and (ii) scaffold-based culture techniques. For generating scaffold-free 3D culture, the cells suspended in growth media either aggregate naturally by developing their own ECM or anchors cells together through direct cell-cell interaction. The complex tissue-like structures generated are made with a wide range of cell types that tend to adhere and aggregate from a single or multi-cell type. These are the most commonly used 3D cell culture technique to model tumor growth and proliferation. They can mimic the protein and gene expression profiles, and the necrotic core formed as a result of oxygen and nutrient gradient[34,35]. The scaffold-based 3D cell culture is fabricated by seeding cells on an acellular 3D matrix that solidifies or by encapsulating cells in a polymerizable gel matrix. Most commonly used scaffold are either (i) biologically derived, like commercially available BD Matrigel^{TM} (BD Sciences), Cultrex® (BME; Trevigen), components like collagen, gelatin, elastin, silk fibroin, chitosan, chitin, fibrin, fibrinogen, and hyaluronic acid or (ii) synthetic-based biomaterial matrix, like Polyethylene glycol (PEG), polyvinyl

alcohol (PVA), poly lactide-co-glycolide (PLG), and polycaprolactone (PLA)[36–39]. A combination of both natural and synthetic material can also be used to make matrices. These composites mimic ECM through mechanical and physical properties like porosity, permeability, stability, stiffness, and microarchitecture. This matrix act as an active biological environment to enhance biophysical and biochemical cell interaction, promote proliferation, differentiation, and stimuli response. The type of matrix or scaffold to be used depends on the type of cell used and the goal and nature of the experiment.

1.2.1 Scaffold-free culture techniques

There are three commonly used methods to develop scaffold-free spheroids. They are (i) hanging drop methods, (ii) non-adherent surface methods, and (iii) suspension culture. Each of these methods has its advantage and disadvantage[40], and selecting the right platform based on the experimental design criteria is critical.

1.2.1.1 Hanging droplet method

Bacterial studies that require a confined and controlled environment initially used this method. In this technique, we can generate spheroids by placing drops of cell suspension on the underside of the cell culture dish lid or hanging droplet plates[41– 43], as shown in **Figure 1.3.a.** The lid is then placed back onto the culture dish with sterile liquid to prevent evaporation due to dehydration of the droplets. The cell density is adjusted, based on the required size of the spheroid. Due to gravity, the cells start to aggregate at the bottom of the droplet, eventually forming a spheroid[44,45]. This technique does not require any additional supplementary materials as the cells naturally attach without relying on matrices or scaffold.

This method is a simple yet consistent technique that produces uniform-sized spheroids in high throughput fashion while maintaining *in vivo* relevance[41]. This technique can preserve the native cell-cell and cell-ECM interaction and can be maintained for the long-term to employ complex experiments[42,43]. Despite the advantages, the spheroids generated are size- and volume-limited as any liquid volume over 50μL does not attach to the lid as the liquid surface tension overcomes gravity. Another drawback is the difficulty in changing spent media without disturbing or aspirating the spheroid.

1.2.1.2 Non-Adherent surface method/Ultra-Low Attachment Plates

Sutherland et al. pioneered the technique of spheroid production, where they used the *in vitro* tumor model to study the effect of radiation[46,47]. In this method, the cell suspension is added to ultra-low attachment plates that are pre-coated with an inert substrate (agar or poly-2-hydroxyethyl methacrylate (poly-HEMA)) to generate spheroids. The coating will prevent the cells from attaching to the bottom surface of the place and force them to aggregate into spheroids, as seen in **Figure 1.3.b.**[44,48]. Round and conical bottomed 96-well plates that were pre-coated with 0.5% poly-HEMA were implemented to improve the method and efficiency further to produce well-formed 3D spheroids[49]. An alternative is coating the plates with a thin layer of 1.5% agarose that prevents cell adhesion to the surface resulting in spheroid formation[34,50]. There was a wide range of cells used in this technique to generate spheroids. The cells that did not aggregate were boosted by adding 2.5% of the liquid reconstituted basement membrane to the suspension. This method is also compatible with high-throughput and is relatively cheap and reproducible. As the coating is stable and non-toxic, the spheroids can be in long-term culture before retrieving for experiment/assay. The time required to pre-coat the plates to avoid the expense of

purchasing pre-coated plates and the heterogeneous sizes and composition of the resulting spheroids make this technique unattractive.

A. Hanging droplet methods

Dispense cell suspension on petri dish lid → Flip the lid 180° to form hanging drop → Cell aggregates to form single spheroid

B. Non-Adherent surface method

Adherent culture → Seeding in ultra-low attachment plate → Cell aggregates to form single spheroid

C. Suspension culture

Spinner Flask

Seeding → Spheroid

Bioreactor

Seeding → Spheroid

D. Scaffold-based model

Spheroid ← Seeding mixed with hydrogel ← Plate coated with Hydrogel → Seeding mixed with hydrogel → Spheroid

E. Magnetic levitation

Magnet

Magnetize cells overnight → Seeding in ultra-low attachment plate-Magnet on the top

Figure 1.3 Common 3D cell culture techniques[51]. *Adapted from an open-access image[51].*

11

1.2.1.3 Suspension or agitation-based culture

In this technique, cells aggregate by keeping the cell suspension inside the container at constant agitation (stirring or rotation) or by increasing the viscosity of the media by adding carboxymethyl cellulose[52,53]. By continuous agitation, the suspended cells do not attach to the surface but adhere to themselves, creating a cell-cell anchorage and interaction. This technique is loosely categorized as (i) spinner flask bioreactors[53,54] and (ii) rotational culture systems[55].

    a. *Spinner Flask bioreactors:*

This bioreactor includes a container with the cell suspension and a stirring element to continuously stir medium, ensuring cells to be suspended (**Figure 1.3.c, left)**. This method offers a relatively straightforward procedure for spheroids generation and scalability based on the size of the bioreactor[53]. The design of the spinner/bioreactor facilitates easy medium change and assistance in the transportation of nutrients, oxygen, and waste removal[54]. However, the shear stress applied to the cells due to the constant stirring can adversely affect cellular physiology[53]. Compared to the other two techniques, this requires a large volume of media (100-300mL) inside the bioreactor container[56]. However, the primary drawback is the broad range of spheroid sizes produced that require manual selection of similar-sized organoids as are necessary for any optimized experiment. To overcome this dissimilarity, uniform-sized spheroids initially formed in a low-adherent plate are transferred later into the spinner flask to provide a controlled environment of nutrients and oxygen for long-term growth[57,58].

    b. *Rotational culture system:*

This system functions similar to the spinner bioreactor, except the whole culture container,

rotates instead of the spinner element (**Figure 1.3.c, right).** This rotating vessel was initially designed for NASA to mimic microgravity and culture cells and tissue during spaceflight[59]. The constant motion of the vessel prevents the cells from adhering to the walls. The rotation speed is adjusted during the aggregation to maintain the cell suspension in lower rotation per minute (rpm) and increase the speed once cells aggregate to maintain the heavier 3D structure in suspension. This method has decreased shear force as both the content, and the vessel rotates [55]. It is a simple method that is compatible with large scale production of the spheroids and can be cultured for long-term[60]. Similar to the spinner flask, the bioreactor produces a range of spheroid sizes that cannot be controlled and requires a manual selection step to separate the spheroids based on size[53].

1.2.2 Scaffold-based culture technique

Cell-ECM interaction is import to the various cell function, cellular organization, and therapy response. Therefore, developing a 3D model that recapitulates not only cell-cell communication but also cell-ECM interaction becomes optimal. In the scaffold-based culture, the scaffold itself represents the ECM architecture. There are various naturally derived hydrogels, synthetic polymer, and a combination of natural and synthetic polymers used in developing the scaffold[56]. In this technique, cells can either be embedded within the matrix or seeded on top of a solidified matrix (**Figure 1.3.d).** Below are some of the commonly used scaffolds for 3D cell culture.

1.2.2.1 Biopolymer scaffolds

There has been quite a lot of advancement in developing customizable 3D tissue-engineering scaffolds that encapsulate cells and mimic the cell-ECM interaction. As ECM

plays a vital role in cell functioning, the natural polymers present in native ECM serve as a target material to be used to develop scaffold. These materials with controlled properties can faithfully recapitulate native architecture. There are three classes of these natural polymers, namely polysaccharides (Alginate[61,62], chitosan[63,64], heparin[65], hyaluronic acid[66], and other glycosaniboglycans[67–69]), proteins (collagen, elastin, fibrinogen[70,71], fibronectin[72], silk[73]) and polyhydroxyalkanoates (PHA)[74,75]. The most commonly used natural polymers are hyaluronic acid, gelatin, collagen, and chondroitin sulfate. As each of these biopolymers has specific properties, they are characterized for specific tissue model. Biopolymers are widely used in the tissue regeneration of cartilages[76,77], bones[78], skin[79], and arteries[80,81]. However, the main disadvantage of these biomaterials stems from its inability to have control over mechanical properties like matrix elasticity, and macroporosity and biochemical property of the scaffold that influence cell bioactivities[76,82].

1.2.2.2 Prefabricated scaffolds

Matrix scaffolds can also be prefabricated before cell seeding, providing a high level of customization in biochemical composition, matrix elasticity, and micro-architectures, compared to biopolymers. These scaffolds are conventionally fabricated using salt leaching[83–85], gas forming[86], phase separation[87,88] and freeze-drying/ lyophilizing[89,90]. Nevertheless, these techniques do not provide precise control over the microarchitecture. Hence rapid prototyping techniques that use a computer-aided design like 3D printing[91], stereo-lithography[92,93], selective laser sintering[94,95], and electrospinning[96] are employed to produce a consistent matrix that enables control in both macro and micro level architecture[97,98]. In conventional methods, the use of toxic solvent, extreme pressure, and

non-physiological salt concentration become too harsh to maintain cell viability[99]. Diffusing cells into the scaffold yields better viability[99–101], which often results in undesirably poor scaffold cellularization due to low penetration. Recently, there have been scaffolds fabricated using silk fibroin with pre-vascularized hollow channels that aided in tube formation within the matrix[102]. On the other hand, though rapid prototyping techniques, we can overcome most of the harsh environment, but the limited amount of biomaterials available for this technique discourages this scaffolding method[103].

1.2.2.3 Building blocks-based scaffold formation

Building blocks-based scaffold formation provides precise control over the ECM mechanical properties to overcomes the issue of poor scaffold cellularization[104–106]. Here, the designer base units are built and crosslinked under controlled conditions to obtain desired porosity. The resulting microribbon-based scaffolds enable cell proliferation, natural ECM production, nutrient diffusion, and cell engraftment[107]. Due to its precision in architecture, it has been widely used in bone regeneration scaffolds. The implanted building block-based scaffolds seeded with adipose-derived stromal cells was demonstrated to accelerated bone regeneration in a mouse[104].

1.2.2.4 Hydrogels

The natural polymer materials like collagen, hyaluronic acid, fibrin, alginate, and chitosan are not often the ideal choice for developing an optimized and standardized matrix that can be customized to fit the tissue type. The vagueness and complexity of the biopolymers scaffold make it hard to understand and determine accurately which signals are influencing cellular function[108]. Also, manipulation to alter material properties are not easily achieved,

15

and they have an inherent batch to batch variability. On the other hand, the hydrogels are hydrophilic network formed of synthetic materials like poly(ethylene glycol)[109], poly(vinyl alcohol)[110], and poly(2-hydroxy ethyl methacrylate)[111] that encapsulates a wide range of cell types[89,112,113]. In contrast to biopolymers, hydrogels are a water-swollen network that can easily manipulate the biochemical and mechanical properties like pore size and stiffness of the scaffold and also is highly reproducible. The porosity of the hydrogel allows diffusion of oxygen, nutrients, and removal of waste from the cellular construct. PEG hydrogels are commonly used due to their ability to maintain high cell viability. They also facilitate ECM deposition and cellular bioactivities as they degrade and provide internal space[114]. Though these scaffolds offer a simplistic approach to model soft-tissue like environment, integrating other relevant components into the scaffold would better mimic the ECM complexity.

Although hydrogel seems to be advantageous over other polymers, they suffer from matrix degradation over time that alters the biochemical and physical element. They also lack the endogenous factors that facilitate and promote cell behavior and only act as a template to permit cell function[108].

In this dissertation, we use hyaluronic acid (HA) and gelatin-based hydrogel extensively to fabricate 3D cell culture models. HA, a non-sulfated glycosaminoglycan (GAG) and gelatin, a hydrolyzed collagen, are the major components of the extracellular matrix (ECM). It plays a vital role in various biological processes, especially in cancer progression. HA, unlike other synthetic polymers, are biologically active. It also naturally has an abundant negative charge that absorbs large volumes of water and forms a loose hydrated network that controls the transport of plasma protein, proteases, and water,

making it an ideal choice for hydrogel[115]. They help in maintaining the viscoelasticity of tissue and activate the signaling pathway that directs cell functions like cell adhesion, cytoskeletal rearrangement, cell migration, cell proliferation, and differentiation[116,117]. In the tumor microenvironment (TME), they are highly expressed and direct the metastasis of tumor cells. As native HA is susceptible to degradation and has inferior mechanical properties, they are usually chemically modified to establish covalent crosslinking that improves stability and mechanical properties.

The hydrolyzed collagen is a heterogeneous mixture of proteins that is found substantially throughout the body. It influences cellular behavior like migration and differentiation, as metalloproteinase (MMP) degrades it during the process. HA and gelatin enable native tissue-like ECM and promotes cell adhesion. Our *in situ* photopatterning method utilizes commercially available hyaluronic and gelatin-based hydrogel, HyStem (ESI-BIO, Alameda, CA)[118,119], which is a biocompatible and animal component-free system. The hydrogel is composed of thiol-modified hyaluronan, thiol-modified heparin, thiol-modified denatured collagen, and thiol-reactive crosslinker, polyethylene glycol diacrylate (PEGDA)[120]. The hydrogel is mostly prepared by using the thiolated HA in conjugation with collagen as HA alone does not have cell attachment sites, and also it helps to reduce the gel stiffness by diluting HA concentration. Due to their flexibility, we can add other ECM components like laminin, fibronectin, matricellular proteins, attachment peptides, and macromers based on the desired tissue composition or decellularized ECM itself [121,122]. Also, the immobilized heparin facilitates the addition of other growth factors like Stromal cell-derived factor 1 (SDF-1α) and provides controlled, slow-release of the cytokine into the medium while mimicking the heparin sulfate proteoglycans present in the

ECM. They have general attachment proteins for a wide range of cells, and their mechanical stabilities and stiffness profiles are similar to that of native ECM[123]. The critical advantage is the ability to modify and manipulate the concentration and mixing ratio of the components to customize the gel to our desired morphology, gelation time, or stiffness. This flexibility provides a consistent and controlled material to produce synthetic ECM (sECM). In natural form, these materials take up to 30 minutes to polymerize. Hence the conventional photoinitiator can be added to the hydrogel solution to induce near-instantaneous polymerization initiated by UV irradiation[124]. It is also optimal for cell delivery applications[125].

1.3 Interfacing 3D cell culture with microfluidic systems

Current 3D cell culture has taken us a step closer to physiologically relevant tissue models, but they still pose certain limitations. The self-assembling organoids are challenging to replicate precisely and often vary in shape and size. This inconsistency may affect comparative drug studies to certain extents. Also, the system only allows for discrete-time point medium change instead of being continuous, highlighting the absence of fluid flow. Apart from medium change, fluid flow is essential to mimic mechanical cues like fluid shear stress and cell interaction of circulating tumor cells or immune cells[126]. These models do not entirely capture the multicellular complexity or in vivo growth factors/signaling gradients [127].

Integrating microfluidics with 3D cell culture overcomes most of these limitations. Microfluidics is the science of manipulating fluids in relatively small dimensional channels

(i.e., in microliter quantities). These micrometer-sized channels provide a dynamic fluid flow that can be precisely controlled and tuned by their miniaturization, integration, and automation. Microfluidics facilitates controlled mechanical cues like shear stress, interstitial flow, and vessel-like perfusion, as well as chemical cues like spatiotemporal gradients of signal/concentrations and diffusion of nutrients[128]. This precise control over gradient and flow helps to better model cellular morphology[129] and biological phenomena like angiogenesis, migration, and invasion. The perfusion flow allows having a steady stream of nutrient supply through media, removal of waste metabolites, and oxygen supply[130,131]. The variation in gradient patterns can be altered by just altering the flow rates and channel geometry[131]. Microfluidics also has the unique capability to induce stretch and tension in cells that is not capable of static cell culture.[129]. Apart from the controlled flow, they have the central advantage of spatial control over the size and shape of the organoid constructs itself. This control enables spatial patterning of the scaffold and ECM[132], separation of culture, organized co-culturing, and cell attachment support without the need for a membrane.

Microfluidic 3D cell culture plays a dominant role in (i) cancer study and (ii) drug development. This platform facilitates the development of highly characterized cancer models since it can incorporate even the mechanical factors that influence cancer progression, modification, angiogenesis[133], and migration[134,135]. These physiological behaviors are essential features of the model, as they affect the efficacy of drug response. This platform has also enabled multiplexed high-throughput screening of drugs in both cancer and organ 3D models (organs-on-a-chip). Organs-on-a chip is 3D tissues or organ models developed using microfluidic platforms with continuous perfusion. These models

simulate the critical physiological functions of the organ or tissue as minimal level functional units, not to miniaturize the entire organ per se. The standardization and automation of the platform have led to high reproducibility, massively parallel processing, cost-effectiveness, easy handling, and convenient-high throughput fabrication. Even with scaling, the consumption of reagents/drugs for quantitative and qualitative analysis is still very minimal (microliter-level)[136].

The fabrication and design of the microfluidic device depend on the 3D models and their functionality. The microfluidic platform can be designed and engineered to accommodate a wide range of 3D cell culture techniques. Some of the 3D models developed within the realm of microfluidics are spheroids[137], gel-free 3D constructs[138], hydrogel scaffold-based models[110], cell patterning, 3D printed structures[139] and whole tissue perfusion[140] (**Figure 1.4**). The types of microfluidic platforms commonly used for cell culture applications are glass-, paper-, and PDMS- based. The glass-based microfluidics system is fabricated by wet etching using photoresist to form channels on a microscopic glass slide. This technique uses inexpensive substrates and can form intricately designed channels. The material exhibits chemical stability, solvent compatibility, biocompatibility, and optical transparency. However, the overall process requires complex and expensive machining. The rigidness of the material and inability to produce gas exchange makes it a less favorable option for most 3D cell culture applications. Paper microfluidics, on the other hand, is an emerging technology built on chromatographic or filter papers fabricated using photolithography. The chemical and physical properties of the paper are modified to make it more suitable for this application[141]; however, this scaffold has mostly been used as a supporting scaffold than as a standalone platform[142].
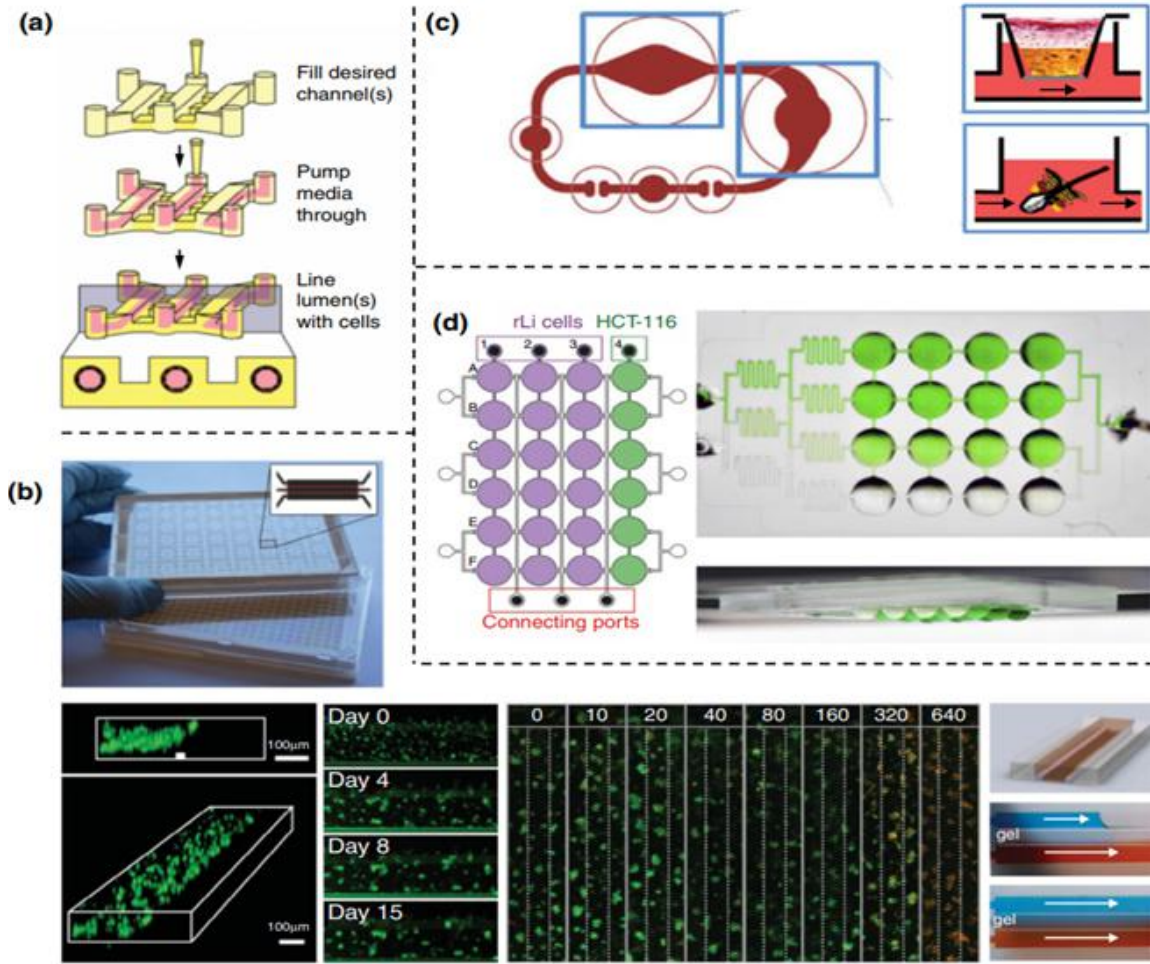
Figure 1.4. Microfluidic techniques for 3D cell culture. *(a) Cell patterning inside a hydrogel*[143]. *(b) Selectively patterned ECM gel in 96 microfluidic culture chambers with an integrated microtiter plate below*[144]. *(c) Spheroids created using the hanging droplet method in a microfluidic* device[137]. *(d) A whole tissue perfusion system in microfluidic channels*[140]. *Reproduced from an open-access image*[127]

1.3.1 Current microphysiological systems

The most commonly used material for fabricating microfluidic devices for cell culture applications is PDMS. This fabrication technique involves soft lithography, where a master

patterned surface is created on a silicon wafer using photolithography. SU-8 is the most commonly used negative photoresist. PDMS is then added to the master mold and cured to polymerize, forming a featured substrate that is attached to a glass substrate or another PDMS membrane with or without features (**Figure 1.5**). The tubings are inserted through the punched holes to facilitate fluid delivery. These devices have the advantage of being biocompatible, flexible, and optical transparent; moreover, they are gas permeable. The biocompatibility enables culturing cells without requiring any surface modification. The high flexibility of PDMS allows the precise control of fluid flow through the fabricated microtissue models. Also, this material can be used for fabricating porous flexible membrane as described in the lung-on-the-chip developed by Huh et al. Here, human alveolar epithelial cells were cultured on one side and pulmonary microvascular endothelial cells on the other, and was exposed to mechanical stretching forces to emulate breathing[145]. Due to their flexibility, such membranes are also used as built-in microvalves or as pumps as part of the platform[31]. Their optically transparent property facilitates imaging and real-time microfluorimetric measurements[146], while their gas permeability allows constant oxygen supply to the cells in the microchannels. The cost of fabrication is lower than those of previously described techniques. PDMS-based devices are flexible in stiffness and microfabrication design, rendering them desirable for most 3D cell cultures.
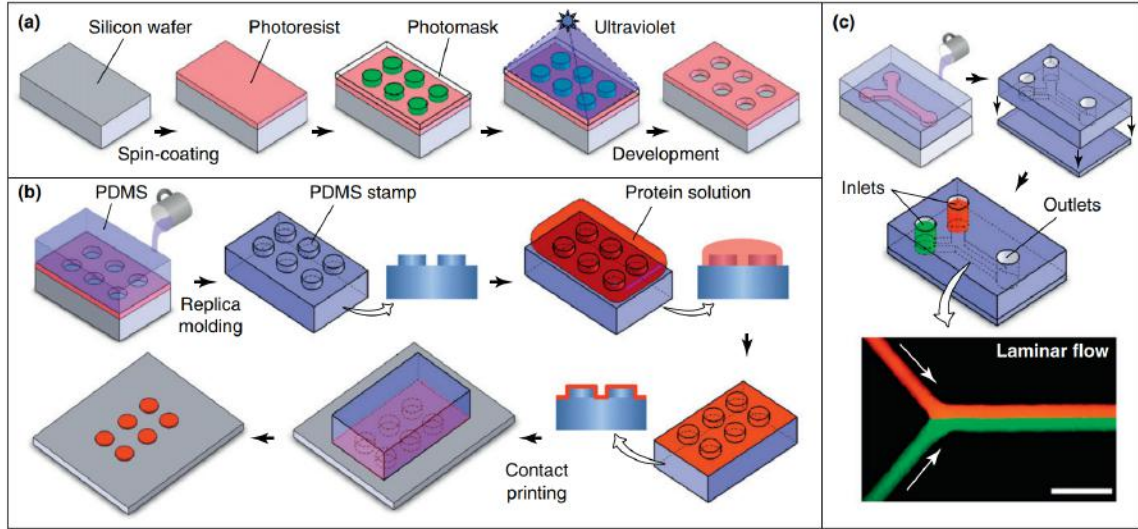
Figure 1.5*. **Fabrication of PDMS based microfluidic device.** (a) A photomask is developed using a photolithography technique. A silicon wafer is spin-coated with a uniform film of the desired thickness of the channel dimension requirement of a photoresist. A photomask is aligned on top of the photoresist, which is exposed to high-intensity UV light through the photomask. The UV exposed pattern becomes soluble in a developer solution and dissolves away during the development phase. This leaves the desired micropattern etched into the photoresist. (b) The PDMS mold is fabricated via the soft lithography technique. PDMS is previously poured onto the developed photoresist pattern. This replica-molding technique produces a PDMS substrate that replicates the micropattern of the original master. For microcontact printing, the protein solution is inked onto the PDMS stamp and dried. This generates a surface pattern that accurately replicates the original master micropattern. (c) Microfluidic devices are then created by bonding the PDMS substrate onto a PDMS slab, glass, or polystyrene slide using typical plasma bonding. Inlet and outlets are created by merely punching through the membrane[31]. Reproduced with permission from [31], Copyrights © 2011, Elsevier.*

1.3.2. Adhesive-film based microfluidics

Although PDMS membranes have been the choice of material for microfluidic cell culture applications, they also have disadvantages that can impact drug studies specifically. They are incompatible with hydrophobic compounds as they nonspecifically adsorb into the walls' or swell when exposed to strong solvents[147]. These undesirable outcomes make it incompatible for rigorously testing some potential therapeutic agents. PDMS is reported to adsorb plasma proteins rapidly and dynamically, thus varying their composition as protein competes to be adsorbed by the surface (known as the "Vorman effect")[148,149]. This phenomenon affects the protein level and alters cellular behavior, which causes significant setbacks during studies. There can also be some degree of evaporation in the system, causing changes in medium concentration during long-term experiments leading to osmosis in a gradient study or skew the data in concentration-based studies. Especially in devices with microchannel, small changes in concentration can magnify these effects. Due to their material properties during high temperatures/pressures, they may not withhold stress as efficiently or may even become distorted by collapsing or swelling. Recently, researchers have shown concerns about un-crosslinked oligomers from PDMS leaching out and binding to cell membranes[150]. The fabrication process itself requires cleanroom facilities and sophisticated equipment like aligners for developing multi-layer devices. This technique, however, is also not optimal for mass production and scaling at low cost[145] for clinical translation. Understanding the increasing awareness of potential artifacts and biases associated with PDMS-based microfluidic devices, it has become essential to consider other materials or fabrication techniques that will overcome these shortcomings.

One such rapid prototyping fabrication approach is a tape or AFB microfluidic device. AFB microfluidic is an emerging technique developed by Cooksey et al. [151], wherein the device is fabricated by layering patterned adhesive films. The layer of double-sided tape is patterned using a razor plotter or laser etching and sandwiched between solid substrates (e.g., glass, polystyrene slides, or polymethylmethacrylate (PMMA)) or non-adhesive elastomeric films[151]. The solid substrates have drilled, or laser cut ports to facilitate fluid delivery through inlet and outlet tubing attached to the ports, as seen in **Figure 1.6.a**. The dimensions of the channel thickness depend on the thickness of the adhesive film, and lateral dimensions are limited to razor plotter resolution (typically 200 microns). This simple yet powerful fabrication technique enables the creation of complex structures with multiple layers by directed folding along with featured perforation patterns integrated with the overall chip design itself. One such possibility of sophisticated features is a gradient mixer, as demonstrated in **Figure 1.6.b**. This mixer does automated delivery of drugs in series of dilutions, which can then be functionally adapted to screen minimally effective dose concentrations. To engineer built-in actuators or pumps, a layer of flexible polymeric films like PDMS or polyvinyl chloride is sandwiched between the strata (**Figure 1.6.c**). This fabrication technique not only has the advantages of PDMS such as biocompatibility, optically transparent, high flexibility in designing, low cost, and quick fabrication, but it also overcomes some of the latter's shortcomings. On the fabrication front, these devices can be scaled up and mass-produced in a manner that makes them attractive for commercialization in order to conduct drug studies or disease modeling. These devices do not need sophisticated equipment or a cleanroom setting that largely reduces the fabrication cost. This method eliminates several of the microfabrication steps like photolithography,

soft lithography, chemical etching, and bonding. For engineering a multilayered feature, unlike PDMS, there is no need for aligners. Instead, the monolithic film featuring perforations promotes directed folding, enabling self-alignment of the overall structure, as shown in **Figure 1.6.d**. The thickness of the channel is controlled by that of the adhesive film itself and is altered simply by layering.
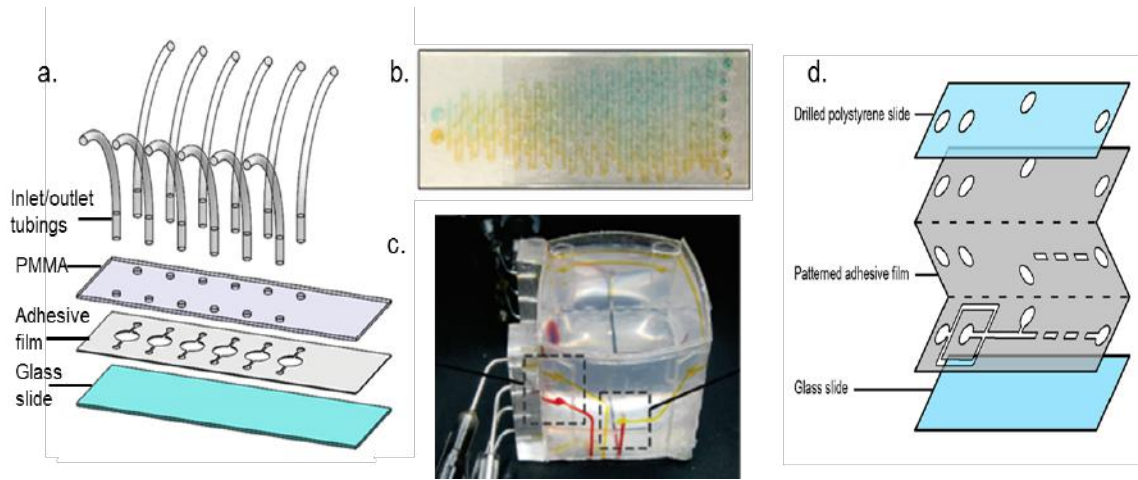
Figure 1.6. Adhesive film based Microfluidic chip (a) fabrication schematic of AFB microfluidic device. The patterned adhesive film sandwiched between a glass substrate and a PMMA slide with laser-cut ports for connecting the inlet and outlet tubings for fluid delivery through the system. (b) Complex, multilayered AFB gradient mixer showing the gradient in concentration of two different colored dyes. (c) a 3D AFB microfluidic cube with fluidic and pneumatic channels[151]. (d) Complex multilayering technique of AFB with directed folding by engineering perforations in the design.

PDMS devices made by soft lithography are still limited to the design features developed in the molds. To produce even minor changes in its design requires a new mold, which can be time-consuming and shows a lack of design flexibility. Whereas in tape fluidics, features are added or redesigned by merely altering the computer-aided design. When considering

material stability, the adhesive membrane withstands various dynamic physical conditions like mechanical force, ultraviolet resistance, heat, and electrical discharge. These characteristics vary depending on the specifications of commercially available adhesive films used. These devices have shown to integrate functional units like vibrating elements, high-temperature bioreactors, and interdigitated electrode arrays without the need for cleanroom processing[152]. Though much biological work has not been explored in this platform, biocompatibility has been confirmed in a few studies[152,153]. The main disadvantage with tape microfluidics as compared to conventional PDMS is feature resolution, which is typically hundreds of micrometers laterally and limited by tape thickness vertically. Depending on the application, this aspect may be a trivial feature. By moving towards customized adhesive films rather than commercially available sizes, we can mitigate some of these issues. Besides, these devices also typically still rely on external infrastructure for hydraulic actuation (much like PDMS microfluidics). However, this approach provides us with a straightforward and cost-effective technique that alleviates most of the shortcomings of PDMS.

1.4 Micro-engineered models

Most of our current understanding of the biological process and disease progression is based on 2D models or animal studies. However, We have extensively discussed previously in the "*why 3D cell culture?*" section, the importance of 3D models over 2D or animal model to better understand tissue functioning, organ pathophysiology, disease mechanisms, cell-matrix interaction, and drug interactions. These 3D models bridge the

gap between 2D and animal models by capturing most of the mechanical, physical, chemical, and biological complexity of native tissue.

With the growing knowledge about the importance of microenvironment cues, like mechanical properties, transport phenomenon, and reaction kinetics[154] that influence disease progression and drug resistance, it has become critical to incorporate these features into the model. Recently, researchers have been developing strategies by integrating biology, tissue engineering, and microfabrication to enhance the biologically-inspired 3D culture models. These models have the potential to mitigate the discrepancy between the responses and functioning of *in vitro* and *in vivo* models. To achieve this complexity, Tissue engineering technologies like biomaterial, scaffold fabrication techniques, 3D bioprinting, and bioreactor designing is combined with microfabrication techniques that can control and precisely model the required mechanical and topographical properties[155-158]. Previously, we briefed the capabilities of these platforms in the "*integration of microfluidics with 3D cell culture application*" section. As mentioned, these models can be easily interfaced with analytical instrumentation to probe into the cellular and biomolecular dynamics[154, 159, 160].

These micro-engineered technologies are a powerful tool that has been extensively adapted to fabricate microphysiological organ models and disease states, especially cancer. The organ system is generally composed of multiple tissue types that are organized in a specific architecture to be functional. Similarly, the disease models require various mechanical and chemical cues to faithfully emulate the disease mechanism and progression, which can only be modeled with the micro-engineered technologies.

1.4.1 3D Organ model

Microfluidic technologies can enable precise control of fluid delivery that produces organ-relevant dynamic mechanical signals and spatiotemporal chemical gradients that are an essential part of the microenvironment that induces cells to express appropriate phenotype[161, 162]. These *in vivo*-like microengineered models, called 'Organ-on-a-chip,' are used to study organ-specific physiology or further modify to develop specialized disease models. This platform does not necessarily represent the complete organ system but mimics some of the essential aspects of the functional unit microarchitecture found in the organ. Organ-on-a-chip can potentially replace the current preclinical models for toxicology and pharmaceutical applications and help reduce cost and improve efficiency in the drug development pipeline.

The liver is an import organ that is responsible for plasma bile production, glycogen storage, detoxification, and drug metabolism. This organ is commonly modeled in a static system as self-assembled 3D spheroids/ organoids or cell embedded hydrogel scaffold of primarily hepatocyte cells[163-167] and used for testing drug metabolism and possible hepatotoxicity. However, as spheroids models do not provide structural control, and the scaffold-based model does not provide the mechanical cues, liver-on-a-chip becomes attractive. They provide physiological shear stress, oxygen gradient, and automated delivery of nutrients and waste removal. Liver organoids usually incorporate coculture of hepatocyte cells with nonparenchymal liver cells like Kupffer cell, hepatic stellate cells, and liver sinusoidal endothelial cells (LSEC) to improve their cellular and metabolic functions[168]. Though there are multiple models of microengineered liver, the most progressive liver microarchitecture model was coculturing the hepatocyte with Kupffer cell

in a bioreactor with LSEC supported on arrays of scaffolds. The system was continuously perfused by pneumatic micropumps and continuously adjusted for oxygen concentration. The resulting model was able to capture the complex liver sinusoid behavior in a simple and scalable format[169].

The heart has a primary function of pumping blood throughout the body, microphysiological systems studying it mainly model the contraction/relaxation phases during beating. These organoids are primarily made of cardiomyocytes (CM) though advanced models include vascular smooth muscle cells and vascular endothelial cells. While the static 2D CM culture on Matrigel is effective to spontaneously beat[170], the functional readout of contractile stress cannot be measured effectively. Also, cardiac organoids require controlled cyclic strain to dramatically improve the maturation level and contractile performance[171, 172]. Consequently, Marsano et al. developed a heart-on-a-chip that was able to mimic the mechanical and biochemical stimuli similar to native tissue. Later, the Varghese lab developed a 3D cardiac microtissue with micropatterning of methacrylate gelatin hydrogel in a microfluidic platform that has real-time contractile stress readout[173]. These models were not only cost-effective and straightforward but allowed dynamic functional readout and output analysis, which would be critical during disease modeling and drug testing.

Lung has a complex architecture comprising of the airway and vascular trees. The functional unit of the lung that is commonly modeled is the air-liquid interface of the alveoli and blood vessel. Their physiological environment includes breathing motion-induced mechanical strain, blood and interstitial flow-induced shear stress, and surface tension[174]. These mechanical cues, along with the air-liquid interface, have been micro-

engineered in several microfluidic platforms. These microphysiological models are modeled with or without a porous membrane. The first model has cell cultured on microwells, and mechanical strain is induced using flat pillars[175], pneumatic[176-178], or hydrodynamic actuators[179]. The later model comprises of a thin porous membrane to facilitate transport across cultures layers to mimic the *in-vivo* barriers. In the established air-liquid interface model, the cells on either side of the membrane communicate via paracrine and endocrine signaling and provide nutrients to the apical side though the membrane. The flexible membrane allows the introduction of mechanical strain through unidirectional stretching by vacuum[180] or by inflating and deflating the actuation membrane through pressure variations[181].

Other microphysiological systems have been used to model skin[182], vascular system[183, 184], brain[185-188], kidney[189, 190], gut[191, 192], bone[193] and eye[194]. These micro-engineered organs provide powerful alternatives to existing 3D models by recreating complex cell behavior in a dynamic physiologically context. The complexity of these systems is enhanced by interconnecting multiple organs through the microfluidic circulatory system to establish an integrated functional unit called "body-on-a-chip." These systems achieve complete physiological biomimicry by linking the complex micro-engineered organs to study systemic drug interaction, interstitial absorption, and hepatic metabolism. This system considers appropriate physiological liquid-to-cell ratios, physiologically relevant pharmacokinetics and pharmacodynamics, hydrodynamic shear stress, and differential velocity patterns between organs. In chapter 2, we have developed a body-on-a-chip system that integrated six functional organs and validated using the liver metabolizing drug. The importance and existing platform are described in detail in that chapter.

1.4.2 3D Disease model

Existing organ-on-a-chip models can be adapted to induce organ-specific disease states in a highly controlled environment. The intricate representation of native tissue allows us to model the key feature of disease accurately and helps to understand better the biological mechanism involved in disease progression. Modeling diseased tissue is critical for drug testing as healthy tissue responds differently to drugs or their metabolites.

Huh et al. developed a lung-on-a-chip system with a bilayer culture of lung alveolar epithelial cells and microvascular endothelial cells on a porous membrane captured organ-level physiology[195]. To mimic complex disease progression, the micro-engineered system was challenged with IL-2 (Interleukin-2), which physiologically causes microvascular inflammation and injury, eventually resulting in pulmonary edema as fluid starts accumulating in the alveoli chamber. The results from the micro-engineered disease model were comparable to that of the animal model. As the system allows precise control of variables in the system, the authors were able to make insightful deductions regarding the onset and progression of pulmonary edema that could not be realized in animals. This system can be further modified to form small airway-on-a-chip by introducing human airway epithelial cells in the air chamber[196]. These microsystems can model airway inflammatory disease like asthma and chronic obstructive pulmonary disease (COPD) by treating healthy tissue with IL-13 or lipopolysaccharide endotoxin (LPS), respectively. Their results were consistent with the preclinical model proving feasibility for replacing the existing drug testing model.

Another disease model studied through micro-engineered systems is fibrosis formed after cardiac infarction wherein dead cardiac cells are replaced by fibrous scar tissue formed by

activated cardiac fibroblasts. The biomimetic cardiac fibrosis model was engineered using cardiac fibroblast that was patterned on a hydrogel substrate with varying rigidity mimicking the mechanical heterogeneity of myocardium post-infarction[197]. This model captured the mechanism of fibrosis post-infarction and demonstrated its potential for testing the efficacy of anti-fibrosis drug candidates.

One of the most studied micro-engineered 3D models is cancer because of the complexity and heterogeneity of the disease itself. Cell-cell and cell-matrix interactions play a critical role in the disease and drug response. Most of the current *in vitro* models fail to mimic this microenvironment interaction accurately. Microengineered models can recapitulate many aspects of the tumor microenvironment, including biomaterials that resemble physiological ECM from the perspective of composition and mechanical properties, non-malignant cells like stromal cells and immune cells, and interstitial flow and chemical gradients through the use of microfluidic networks[198].

Micro-engineered cancer models have been used primarily for *(i)* understanding the biology of cancer, including tumor initiation, progression, and invasion, *(ii)* studying the role of the tumor microenvironment, *(iii)* developing therapeutic strategies and drug development, and *(iv)* personalized medicine. There are highly specialized 3D cancer models developed to study specific interaction or progression state of the disease. These models help to understand the relation of TME with the tumor so that it can be exploited for therapeutic targets. Some of the critical components of TME studied in this dissertation are briefly introduced below.

1.4.2.1 3D tumor model – Tumor microenvironment

Many studies have emphasized the significant role of the interactions between the cancer cell and neighboring cells and tissues[199]. Surrounding cells, extracellular matrix, and myriad soluble factors collectively form the tumor microenvironment (**Figure 1.7)**. During cancer progression, the tumor cells set off a cascade of changes that dramatically alters the TME. These changes cause physical changes in the environment to which cancer cells are sensitive and lead to tumor growth, metastasis, and drug resistance. Each cell present in the ECM plays a role in the progression of the disease. The fibroblasts or cancer-associated fibroblasts[200] maintain matrix surrounding, create the tumor stroma by secreting ECM molecules (collagen and fibronectin), and also produce factors like matrix metalloproteases, chemokines, and growth factors that ultimately induce invasion[201, 202]. Immune cells such as macrophages, lymphocytes, and neutrophils secrete factors that support tumor progression by preventing the tumor cells from being reecognized[203]. TME is a dynamic environment that changes and adapts to facilitate tumor growth and invasion.
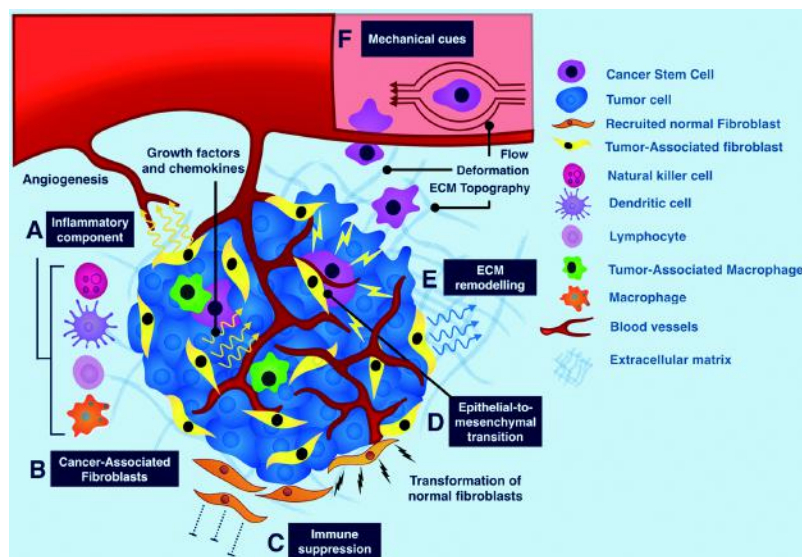
Figure.1.7 The influence of the tumor microenvironment in cancer progression.
Reproduced with permission from [199], Copyrights © 2016, Royal Society of Chemistry

Extracellular Matrix (ECM) components

The non-cellular component of the TME is the ECM, along with other physical and chemical parameters. ECM is a dynamic element remodeled by both cancer and stromal cells and is composed of water, protein, and polysaccharides. This alteration causes irregular deposition of fibronectin, collagen, elastin, laminin and hyaluronan, leading to the stiffer matrix[204]. ECM, in general, is responsible for cell-cell communication, cell adhesion and proliferation, but in cancer, they regulate migration, angiogenesis, and cancer metastasis[205]. In addition to being a scaffold, ECM components have several growth factor binding sites for controlled release to target cells.

Stiffness

Only recently have researchers begun to unravel the critical role of the mechanical properties of the ECM. The mechanics of the microenvironment are controlled by the matrix composition, the spatial orientation of the ECM, and post-translational modifications such as glycosylation and cross-linking. The mechanical environment is governed by forces generated by both the cells themselves (cell contraction) and the surrounding ECM. In general, cancer ECM is stiffer than healthy tissue, affecting cellular behavior by promoting β-integrin clustering and inducing actin cytoskeletal reorganization and Rho/ROCK-generated cell contractility[206]. Matrix stiffness also increases the number of focal adhesions (FAs) and traction force generated between FAs and the ECM. As FAs function as mechanosensors, they can direct the cells to migrate towards regions of higher stiffness[207] and induce malignant phenotypes[208]. The vinculin–talin–actin complex-mediated PI3K signaling in stiffer ECM also promotes cancer cell malignancy [209].

Interstitial flow

Interstitial flow refers to the fluid flow in the tissue stroma. In cancer, interstitial fluid is poorly drained due to the irregularities in the vasculature and lack of lymphatic vessels [210, 211]. This leads to a dramatically elevated fluid pressure, increased flow rates through the tissue, and extending of the elastic ECM[212]. The elevated pressure and flow rate are known to stimulate cell proliferation and affect cell behavior. Interstitial flows can also apply shear stress directly to the cells, impacting integrin coupling. Using a pressure regulation model, Heldin et al. showed that integrins regulate tension applied to ECM in fibroblasts under interstitial flow, enabling them to modify tension on the collagen fiber network and leading to stiffer ECM[213]. Additionally, interstitial flow creates cytokine gradients and upregulates the MMP-1 activity of stromal cells to induce directed cell migration[214]. Elevated levels of interstitial flow increase CCL21 expression, downregulate VE-cadherin and PECAM-1, and upregulate cell adhesion molecules. All of these changes facilitate cell migration and subsequent invasion[215]. The clinical implication of increased interstitial fluid pressure are known to include decreased efficacy of radiation and chemotherapeutic therapy[216].

1.5 Conclusion

Microfluidic platforms enable sophisticated and extensive experiments in a miniaturized system. They have additional ability to support cellular growth and proliferation in a 3D controlled environment and potential for direct assessment of outcomes. The technology facilitates a high level of automation with minimal infrastructure and reagent requirements. Here, we have discussed the need for 3D cell culture in modeling disease and drug development. The different methods of 3D culture have their advantages and disadvantages

and should be carefully selected based on the design and functional criteria of the study. By coupling 3D cell culture with microfluidics, the *in vivo* relevance of the system can be drastically improved.

In this dissertation, we integrate a microfluidic platform with multiple 3D cell culture techniques to demonstrate a sophisticated system built with low cost and rapid prototyping techniques. The central innovation here is to develop an innovative biofabrication strategy to improve both the complexity of 3D cell culture and the adaptability of tissue modeling in the microfluidics platform. We achieve this by first using AFB microfluidics, which have not been investigated extensively for 3D cell culture applications. A photopatterning technique is adapted to fabricate patient-specific tumor models and expanded to study the migration of cancer cells under drug influence. The innovation of this study lies in both the microfluidic platform and the predictive 3D models it enables to address challenges in drug development.

In Chapter 2, we first implement an *in situ* photopatterning technique developed in our lab to biofabricate multiple organ-specific 3D tissues in a AFB microfluidic platform. These organ models are developed with both immobilized spheroids and cells suspensions in hydrogel within the same device. Single organs-on-a-chip can provide excellent value in terms of pharmaceutical testing and necessary organ-level studies. However, integrating multiple organs, especially with primary human cells, allows accurate prediction of drug pharmacokinetics and drug toxicity in organs. This specific aim will allow us to expand different 3D cell culture methods and explore the complexity of the system by integrating multiple organs. As a result, our work is the first to our knowledge to achieve a humanized multi-integrated organ-on-a-chip platform with six different tissues made of primary

human cells on an AFB system. We thus demonstrate an innovative and novel microfluidic platform that has not been used for cell culture application prior but has excellent potential to develop highly sophisticated models with simple fabrication methods.

In Chapter 3, the platform and photopatterning technique are modified to study disease models like cancer. In traditional cancer therapies, the treatment plan is based on the statistical likelihood of success in a population of patients with similar tumors or genetic profiles (i.e., precision medicine). The effectiveness of a drug is highly patient-dependent, thus bringing out the need to develop technologies that can easily access the drug efficacy in the patient but *in vitro*. We can achieve this in our study by bio-fabricating multiple hydrogel-based 3D constructs from patient-derived tumor cells in parallel. This innovative platform produces patient-specific cancer models that closely mimic the physiological *in vivo* condition and drug response. This model enables the parallel production of cancer organoids and drug testing to aid in treatment planning. The system enables modeling the response of not only chemotherapeutic drugs but also immunotherapy and radiation. There has not been a study done on a microfluidic platform that adapts to all three types of cancer treatment modalities.

In Chapter 4, the established tumor model is probed to demonstrate the ability to monitor and analyze *in situ* cell migration through a multidomain 3D construct. Metastasis is an essential hallmark of cancer. Cancer cell motility plays a central role in metastasis and tumor invasion, but it can be challenging to study accurately *in vitro*. Here, our novel approach for step-wise fabrication of adjoining hydrogel regions with and without cancer cells with defined borders enable migration quantification. Previous methods could not

isolate invasive cells through sECM to enable extensive quantification or further studies on migrating cells without damaging the construct.

Then in Chapter 5, we demonstrate our ability to study the migration dynamics of patient-specific constructs and analyze the phenotype of the invaded cells. Our innovative step-wise multi-domain 3D construct fabrication and integrated isolation of migrated cells provide a new tool to better understand drug effects on metastatic tumor. In our study, we obtain high-resolution images using cutting edge confocal microscopy and quantify migration utilizing highly sophisticated segmentation tool.

Overall, this project integrates various capabilities that include innovative microfluidic platforms, novel *in situ* 3D cell culture technique, and sophisticated image/data processing methods to achieve a unique system that can be expanded in complexity and applications.

References

[1]   Hajar, R. Animal testing and medicine. *Heart Views* **12**, 42 (2011).

[2]   Franco, N. H. Animal Experiments in Biomedical Research: A Historical Perspective. *Anim. Open Access J. MDPI* **3**, 238–273 (2013).

[3]   Hackam, D. G. & Redelmeier, D. A. Translation of research evidence from animals to humans. *JAMA* **296**, 1731–1732 (2006).

[4]   Perel, P. *et al.* Comparison of treatment effects between animal experiments and clinical trials: systematic review. *BMJ* **334**, 197 (2007).

[5]   Hackam, D. G. Translating animal research into clinical benefit. *BMJ* **334**, 163–164 (2007).

[6]   van der Worp, H. B. *et al.* Can animal models of disease reliably inform human studies? *PLoS Med.* **7**, e1000245 (2010).

[7]   Harrison, R. G., Greenman, M. J., Mall, F. P. & Jackson, C. M. Observations of the living developing nerve fiber. *Anat. Rec.* **1**, 116–128 (1907).

[8]   Eagle, H. Nutrition needs of mammalian cells in tissue culture. *Science* **122**, 501–514 (1955).

[9]   Gey, G. O. Some aspects of the constitution and behavior of normal and malignant cells maintained in continuous culture. *Harvey Lect.* **50**, 154–229 (1954).

[10]   Sharrer T. He-La" Herself. Celebrating the woman who gave the world its first immortalized cell line. *The Scientist* 20:22 (2006).

[11]   Kapałczyńska, M. *et al.* 2D and 3D cell cultures - a comparison of different types of cancer cell cultures. *Arch. Med. Sci. AMS* **14**, 910–919 (2018).

[12]   Baker, B. M. & Chen, C. S. Deconstructing the third dimension: how 3D culture microenvironments alter cellular cues. *J. Cell Sci.* **125**, 3015–3024 (2012).

[13]   Hickman, J. A. *et al.* Three-dimensional models of cancer for pharmacology and cancer cell biology: capturing tumor complexity in vitro/ex vivo. *Biotechnol. J.* **9**, 1115–1128 (2014).

[14]   Bissell, M. J., Rizki, A. & Mian, I. S. Tissue architecture: the ultimate regulator of breast epithelial function. *Curr. Opin. Cell Biol.* **15**, 753–762 (2003).

[15]   Pampaloni, F., Reynaud, E. G. & Stelzer, E. H. K. The third dimension bridges the gap between cell culture and live tissue. *Nat. Rev. Mol. Cell Biol.* **8**, 839–845 (2007).

[16]   Bissell, M. J., Rizki, A. & Mian, I. S. Tissue architecture: the ultimate regulator of breast epithelial function. *Curr. Opin. Cell Biol.* **15**, 753–762 (2003).

[17] Petersen, O. W., Rønnov-Jessen, L., Howlett, A. R. & Bissell, M. J. Interaction with basement membrane serves to rapidly distinguish growth and differentiation pattern of normal and malignant human breast epithelial cells. *Proc. Natl. Acad. Sci. U. S. A.* **89**, 9064–9068 (1992).

[18] Debnath, J. & Brugge, J. S. Modelling glandular epithelial cancers in three-dimensional cultures. *Nat. Rev. Cancer* **5**, 675–688 (2005).

[19] Nelson, C. M. & Bissell, M. J. Of extracellular matrix, scaffolds, and signaling: tissue architecture regulates development, homeostasis, and cancer. *Annu. Rev. Cell Dev. Biol.* **22**, 287–309 (2006).

[20] Kilian, K. A., Bugarija, B., Lahn, B. T. & Mrksich, M. Geometric cues for directing the differentiation of mesenchymal stem cells. *Proc. Natl. Acad. Sci. U. S. A.* **107**, 4872–4877 (2010).

[21] Mseka, T., Bamburg, J. R. & Cramer, L. P. ADF/cofilin family proteins control formation of oriented actin-filament bundles in the cell body to trigger fibroblast polarization. *J. Cell Sci.* **120**, 4332–4344 (2007).

[22] Weaver, V. M. *et al.* beta4 integrin-dependent formation of polarized three-dimensional architecture confers resistance to apoptosis in normal and malignant mammary epithelium. *Cancer Cell* **2**, 205–216 (2002).

[23] Meyers, J., Craig, J. & Odde, D. J. Potential for control of signaling pathways via cell size and shape. *Curr. Biol. CB* **16**, 1685–1693 (2006).

[24] Ihalainen, T. O. *et al.* Differential basal-to-apical accessibility of lamin A/C epitopes in the nuclear lamina regulated by changes in cytoskeletal tension. *Nat. Mater.* **14**, 1252–1261 (2015).

[25] Hutchinson, L. & Kirk, R. High drug attrition rates--where are we going wrong? *Nat. Rev. Clin. Oncol.* **8**, 189–190 (2011).

[26] Saleh, F. A. & Genever, P. G. Turning round: multipotent stromal cells, a three-dimensional revolution? *Cytotherapy* **13**, 903–912 (2011).

[27] Burdick, J. A. & Vunjak-Novakovic, G. Engineered microenvironments for controlled stem cell differentiation. *Tissue Eng. Part A* **15**, 205–219 (2009).

[28] Scadden, D. T. The stem-cell niche as an entity of action. *Nature* **441**, 1075–1079 (2006).

[29] Underhill, G. H. & Bhatia, S. N. High-throughput analysis of signals regulating stem cell fate and function. *Curr. Opin. Chem. Biol.* **11**, 357–366 (2007).

[30] Gu, L. & Mooney, D. J. Biomaterials and emerging anticancer therapeutics: engineering the microenvironment. *Nat. Rev. Cancer* **16**, 56–66 (2016).

[31] Huh, D., Hamilton, G. A. & Ingber, D. E. From 3D cell culture to organs-on-chips. *Trends Cell Biol.* **21**, 745–754 (2011).

[32] Antoni, D., Burckel, H., Josset, E. & Noel, G. Three-dimensional cell culture: a breakthrough in vivo. *Int. J. Mol. Sci.* **16**, 5517–5527 (2015).

[33] Smith, S. J. *et al.* Recapitulation of tumor heterogeneity and molecular signatures in a 3D brain cancer model with decreased sensitivity to histone deacetylase inhibition. *PloS One* **7**, e52335 (2012).

[34] Friedrich, J., Seidel, C., Ebner, R. & Kunz-Schughart, L. A. Spheroid-based drug screen: considerations and practical approach. *Nat. Protoc.* **4**, 309–324 (2009).

[35] LaBarbera, D. V., Reid, B. G. & Yoo, B. H. The multicellular tumor spheroid model for high-throughput cancer drug discovery. *Expert Opin. Drug Discov.* **7**, 819–830 (2012).

[36] Breslin, S. & O'Driscoll, L. Three-dimensional cell culture: the missing link in drug discovery. *Drug Discov. Today* **18**, 240–249 (2013).

[37] Gurski, L. A., Petrelli, N. J., Jia, X. & Farach-Carson, M. C. 3D Matrices for Anti-Cancer Drug Testing and Development. *Oncol. Issues* **25**, 20–25 (2010).

[38] Tibbitt, M. W. & Anseth, K. S. Hydrogels as extracellular matrix mimics for 3D cell culture. *Biotechnol. Bioeng.* **103**, 655–663 (2009).

[39] Rimann, M. & Graf-Hausner, U. Synthetic 3D multicellular systems for drug development. *Curr. Opin. Biotechnol.* **23**, 803–809 (2012).

[40] Katt, M. E., Placone, A. L., Wong, A. D., Xu, Z. S. & Searson, P. C. In Vitro Tumor Models: Advantages, Disadvantages, Variables, and Selecting the Right Platform. *Front. Bioeng. Biotechnol.* **4**, 12 (2016).

[41] Tung, Y.-C. *et al.* High-throughput 3D spheroid culture and drug testing using a 384 hanging drop array. *The Analyst* **136**, 473–478 (2011).

[42] Hsiao, A. Y. *et al.* Micro-ring structures stabilize microdroplets to enable long term spheroid culture in 384 hanging drop array plates. *Biomed. Microdevices* **14**, 313–323 (2012).

[43] Hsiao, A. Y. *et al.* 384 hanging drop arrays give excellent Z-factors and allow versatile formation of co-culture spheroids. *Biotechnol. Bioeng.* **109**, 1293–1304 (2012).

[44] Kelm, J. M. *et al.* Design of Artificial Myocardial Microtissues. *Tissue Eng.* **10**, 201–214 (2004).

[45] Jørgensen, A. *et al.* Hanging drop cultures of human testis and testis cancer samples: a model used to investigate activin treatment effects in a preserved niche. *Br. J. Cancer* **110**, 2604–2614 (2014).

[46]   Sutherland, R. M., McCredie, J. A. & Inch, W. R. Growth of multicell spheroids in tissue culture as a model of nodular carcinomas. *J. Natl. Cancer Inst.* **46**, 113–120 (1971).

[47]   Sutherland, R. M., Inch, W. R., McCredie, J. A. & Kruuv, J. A multi-component radiation survival curve using an in vitro tumour model. *Int. J. Radiat. Biol. Relat. Stud. Phys. Chem. Med.* **18**, 491–495 (1970).

[48]   Yuhas, J. M., Li, A. P., Martinez, A. O. & Ladman, A. J. A simplified method for production and growth of multicellular tumor spheroids. *Cancer Res.* **37**, 3639–3643 (1977).

[49]   Ivascu, A. & Kubbies, M. Rapid generation of single-tumor spheroids for high-throughput cell function and toxicity analysis. *J. Biomol. Screen.* **11**, 922–932 (2006).

[50]   Li, Q. *et al.* 3D models of epithelial-mesenchymal transition in breast cancer metastasis: high-throughput screening assay development, validation, and pilot screen. *J. Biomol. Screen.* **16**, 141–154 (2011).

[51]   Hoarau-Véchot, J., Rafii, A., Touboul, C. & Pasquier, J. Halfway between 2D and Animal Models: Are 3D Cultures the Ideal Tool to Study Cancer-Microenvironment Interactions? *Int. J. Mol. Sci.* **19**, (2018).

[52]   Yamada, K. M. & Cukierman, E. Modeling tissue morphogenesis and cancer in 3D. *Cell* **130**, 601–610 (2007).

[53]   Lin, R.-Z., Lin, R.-Z. & Chang, H.-Y. Recent advances in three-dimensional multicellular spheroid culture for biomedical research. *Biotechnol. J.* **3**, 1172–1184 (2008).

[54]   Kim, J. B. Three-dimensional tissue culture models in cancer biology. *Semin. Cancer Biol.* **15**, 365–377 (2005).

[55]   Goodwin, T. J., Prewett, T. L., Wolf, D. A. & Spaulding, G. F. Reduced shear stress: a major component in the ability of mammalian tissues to form three-dimensional assemblies in simulated microgravity. *J. Cell. Biochem.* **51**, 301–311 (1993).

[56]   Caliari, S. R. & Burdick, J. A. A practical guide to hydrogels for cell culture. *Nat. Methods* **13**, 405–414 (2016).

[57]   Rodday, B., Hirschhaeuser, F., Walenta, S. & Mueller-Klieser, W. Semiautomatic growth analysis of multicellular tumor spheroids. *J. Biomol. Screen.* **16**, 1119–1124 (2011).

[58]   Hirschhaeuser, F., Leidig, T., Rodday, B., Lindemann, C. & Mueller-Klieser, W. Test system for trifunctional antibodies in 3D MCTS culture. *J. Biomol. Screen.* **14**, 980–990 (2009).

[59] Schwarz, R. P., Goodwin, T. J. & Wolf, D. A. Cell culture for three-dimensional modeling in rotating-wall vessels: an application of simulated microgravity. *J. Tissue Cult. Methods Tissue Cult. Assoc. Man. Cell Tissue Organ Cult. Proced.* **14**, 51–57 (1992).

[60] Barrila, J. *et al.* Organotypic 3D cell culture models: using the rotating wall vessel to study host-pathogen interactions. *Nat. Rev. Microbiol.* **8**, 791–801 (2010).

[61] Chueh, B. *et al.* Patterning alginate hydrogels using light-directed release of caged calcium in a microfluidic device. *Biomed. Microdevices* **12**, 145–151 (2010).

[62] Khalil, S. & Sun, W. Bioprinting Endothelial Cells With Alginate for 3D Tissue Constructs. *J. Biomech. Eng.* **131**, 111002 (2009).

[63] Ji, C., Khademhosseini, A. & Dehghani, F. Enhancing cell penetration and proliferation in chitosan hydrogels for tissue engineering applications. *Biomaterials* **32**, 9719–9729 (2011).

[64] Muzzarelli, R. A. A. *et al.* Stimulatory effect on bone formation exerted by a modified chitosan. *Biomaterials* **15**, 1075–1081 (1994).

[65] Matsuda, T. & Magoshi, T. Preparation of vinylated polysaccharides and photofabrication of tubular scaffolds as potential use in tissue engineering. *Biomacromolecules* **3**, 942–950 (2002).

[66] Burdick, J. A., Chung, C., Jia, X., Randolph, M. A. & Langer, R. Controlled Degradation and Mechanical Behavior of Photopolymerized Hyaluronic Acid Networks. *Biomacromolecules* **6**, 386–391 (2005).

[67] Pieper, J. S. *et al.* Loading of collagen-heparan sulfate matrices with bFGF promotes angiogenesis and tissue generation in rats. *J. Biomed. Mater. Res.* **62**, 185–194 (2002).

[68] Pieper, J. S. *et al.* Attachment of glycosaminoglycans to collagenous matrices modulates the tissue response in rats. *Biomaterials* **21**, 1689–1699 (2000).

[69] Pieper, J. S., Hafmans, T., Veerkamp, J. H. & van Kuppevelt, T. H. Development of tailor-made collagen-glycosaminoglycan matrices: EDC/NHS crosslinking, and ultrastructural aspects. *Biomaterials* **21**, 581–593 (2000).

[70] Passaretti, D. *et al.* Cultured chondrocytes produce injectable tissue-engineered cartilage in hydrogel polymer. *Tissue Eng.* **7**, 805–815 (2001).

[71] Ye, Q. *et al.* Fibrin gel as a three dimensional matrix in cardiovascular tissue engineering. *Eur. J. Cardio-Thorac. Surg. Off. J. Eur. Assoc. Cardio-Thorac. Surg.* **17**, 587–591 (2000).

[72] Underwood, S. *et al.* Wet extrusion of fibronectin-fibrinogen cables for application in tissue engineering. *Biotechnol. Bioeng.* **73**, 295–305 (2001).

[73]   Sofia, S., McCarthy, M. B., Gronowicz, G. & Kaplan, D. L. Functionalized silk-based biomaterials for bone formation. *J. Biomed. Mater. Res.* **54**, 139–148 (2001).

[74]   Sodian, R. *et al.* Fabrication of a trileaflet heart valve scaffold from a polyhydroxyalkanoate biopolyester for use in tissue engineering. *Tissue Eng.* **6**, 183–188 (2000).

[75]   Stock, U. A. *et al.* Patch augmentation of the pulmonary artery with bioabsorbable polymers and autologous cell seeding. *J. Thorac. Cardiovasc. Surg.* **120**, 1158–1167; discussion 1168 (2000).

[76]   Han, L.-H., Lai, J. H., Yu, S. & Yang, F. Dynamic tissue engineering scaffolds with stimuli-responsive macroporosity formation. *Biomaterials* **34**, 4251–4258 (2013).

[77]   Hollister, S. J. Porous scaffold design for tissue engineering. *Nat. Mater.* **4**, 518–524 (2005).

[78]   Zanetti, A. S., Sabliov, C., Gimble, J. M. & Hayes, D. J. Human adipose-derived stem cells and three-dimensional scaffold constructs: A review of the biomaterials and models currently used for bone regeneration. *J. Biomed. Mater. Res. B Appl. Biomater.* **101B**, 187–199 (2013).

[79]   Sun, B. K., Siprashvili, Z. & Khavari, P. A. Advances in skin grafting and treatment of cutaneous wounds. *Science* **346**, 941–945 (2014).

[80]   Pashneh-Tala, S., MacNeil, S. & Claeyssens, F. The Tissue-Engineered Vascular Graft—Past, Present, and Future. *Tissue Eng. Part B Rev.* **22**, 68–100 (2016).

[81]   Huang, A. H. & Niklason, L. E. Engineering of arteries in vitro. *Cell. Mol. Life Sci.* **71**, 2103–2118 (2014).

[82]   Wang, T., Lai, J. H., Han, L.-H., Tong, X. & Yang, F. Chondrogenic Differentiation of Adipose-Derived Stromal Cells in Combinatorial Hydrogels Containing Cartilage Matrix Proteins with Decoupled Mechanical Stiffness. *Tissue Eng. Part A* **20**, 2131–2139 (2014).

[83]   Chen, V. J. & Ma, P. X. Nano-fibrous poly(l-lactic acid) scaffolds with interconnected spherical macropores. *Biomaterials* **25**, 2065–2073 (2004).

[84]   Hong, Y. *et al.* Tailoring the degradation kinetics of poly(ester carbonate urethane)urea thermoplastic elastomers for tissue engineering scaffolds. *Biomaterials* **31**, 4249–4258 (2010).

[85]   Mondrinos, M. *et al.* Porogen-based solid freeform fabrication of polycaprolactone–calcium phosphate scaffolds for tissue engineering. *Biomaterials* **27**, 4399–4408 (2006).

[86]   Salerno, A., Guarnieri, D., Iannone, M., Zeppetelli, S. & Netti, P. A. Effect of Micro- and Macroporosity of Bone Tissue Three-Dimensional-Poly(ε-

Caprolactone) Scaffold on Human Mesenchymal Stem Cells Invasion, Proliferation, and Differentiation *In Vitro*. *Tissue Eng. Part A* **16**, 2661–2673 (2010).

[87]   Nam, Y. S. & Park, T. G. Porous biodegradable polymeric scaffolds prepared by thermally induced phase separation. *J. Biomed. Mater. Res.* **47**, 8–17 (1999).

[88]   Schugens, C., Maquet, V., Grandfils, C., Jerome, R. & Teyssie, P. Polylactide macroporous biodegradable implants for cell transplantation. II. Preparation of polylactide foams by liquid-liquid phase separation. *J. Biomed. Mater. Res.* **30**, 449–461 (1996).

[89]   Choi, S.-W., Yeh, Y.-C., Zhang, Y., Sung, H.-W. & Xia, Y. Uniform Beads with Controllable Pore Sizes for Biomedical Applications. *Small* **6**, 1492–1498 (2010).

[90]   Xiao, J. *et al.* Construction of the recellularized corneal stroma using porous acellular corneal scaffold. *Biomaterials* **32**, 6962–6971 (2011).

[91]   Fierz, F. C. *et al.* The morphology of anisotropic 3D-printed hydroxyapatite scaffolds. *Biomaterials* **29**, 3799–3806 (2008).

[92]   Fozdar, D. Y., Soman, P., Lee, J. W., Han, L.-H. & Chen, S. Three-Dimensional Polymer Constructs Exhibiting a Tunable Negative Poisson's Ratio. *Adv. Funct. Mater.* **21**, 2712–2720 (2011).

[93]   Gauvin, R. *et al.* Microfabrication of complex porous tissue engineering scaffolds using 3D projection stereolithography. *Biomaterials* **33**, 3824–3834 (2012).

[94]   Williams, J. M. *et al.* Bone tissue engineering using polycaprolactone scaffolds fabricated via selective laser sintering. *Biomaterials* **26**, 4817–4827 (2005).

[95]   Hutmacher, D. W., Sittinger, M. & Risbud, M. V. Scaffold-based tissue engineering: rationale for computer-aided design and solid free-form fabrication systems. *Trends Biotechnol.* **22**, 354–362 (2004).

[96]   Lim, S. H. & Mao, H.-Q. Electrospun scaffolds for stem cell engineering. *Adv. Drug Deliv. Rev.* **61**, 1084–1096 (2009).

[97]   Leong, K. F., Chua, C. K., Sudarmadji, N. & Yeong, W. Y. Engineering functionally graded tissue engineering scaffolds. *J. Mech. Behav. Biomed. Mater.* **1**, 140–152 (2008).

[98]   Leong, K. F., Cheah, C. M. & Chua, C. K. Solid freeform fabrication of three-dimensional scaffolds for engineering replacement tissues and organs. *Biomaterials* **24**, 2363–2378 (2003).

[99]   Yin, N., Stilwell, M. D., Santos, T. M. A., Wang, H. & Weibel, D. B. Agarose particle-templated porous bacterial cellulose and its application in cartilage growth in vitro. *Acta Biomater.* **12**, 129–138 (2015).

[100] Yang, B. *et al. In vitro* cartilage tissue engineering using cancellous bone matrix gelatin as a biodegradable scaffold. *Biomed. Mater.* **5**, 045003 (2010).

[101] Wang, Y. *et al.* The synergistic effects of 3-D porous silk fibroin matrix scaffold properties and hydrodynamic environment in cartilage tissue regeneration. *Biomaterials* **31**, 4672–4681 (2010).

[102] Zhang, W. *et al.* Vascularization of hollow channel-modified porous silk scaffolds with endothelial cells for tissue regeneration. *Biomaterials* **56**, 68–77 (2015).

[103] Yang, S., Leong, K.-F., Du, Z. & Chua, C.-K. The design of scaffolds for use in tissue engineering. Part II. Rapid prototyping techniques. *Tissue Eng.* **8**, 1–11 (2002).

[104] Han, L.-H. *et al.* Winner of the Young Investigator Award of the Society for Biomaterials at the 10th World Biomaterials Congress, May 17-22, 2016, Montreal QC, Canada: Microribbon-based hydrogels accelerate stem cell-based bone regeneration in a mouse critical-size cranial: Microribbon-Based Hydrogels Accelerate Stem Cell-Based Bone Regeneration. *J. Biomed. Mater. Res. A* **104**, 1321–1331 (2016).

[105] Han, L.-H., Yu, S., Wang, T., Behn, A. W. & Yang, F. Microribbon-Like Elastomers for Fabricating Macroporous and Highly Flexible Scaffolds that Support Cell Proliferation in 3D. *Adv. Funct. Mater.* **23**, 346–358 (2013).

[106] Han, L.-H., Tong, X. & Yang, F. Photo-crosslinkable PEG-Based Microribbons for Forming 3D Macroporous Scaffolds with Decoupled Niche Properties. *Adv. Mater.* **26**, 1757–1762 (2014).

[107] Griffin, D. R., Weaver, W. M., Scumpia, P. O., Di Carlo, D. & Segura, T. Accelerated wound healing by injectable microporous gel scaffolds assembled from annealed building blocks. *Nat. Mater.* **14**, 737–744 (2015).

[108] Cushing, M. C. & Anseth, K. S. MATERIALS SCIENCE: Hydrogel Cell Cultures. *Science* **316**, 1133–1134 (2007).

[109] Sawhney, A. S., Pathak, C. P. & Hubbell, J. A. Bioerodible hydrogels based on photopolymerized poly(ethylene glycol)-co-poly(.alpha.-hydroxy acid) diacrylate macromers. *Macromolecules* **26**, 581–587 (1993).

[110] Martens, P. & Anseth, K. S. Characterization of hydrogels formed from acrylate modified poly(vinyl alcohol) macromers. *Polymer* **41**, 7715–7722 (2000).

[111] Chirila, T. V. *et al.* Poly(2-hydroxyethyl methacrylate) sponges as implant materials: in vivo and in vitro evaluation of cellular invasion. *Biomaterials* **14**, 26–38 (1993).

[112] Nii, M. *et al.* The effects of interactive mechanical and biochemical niche signaling on osteogenic differentiation of adipose-derived stem cells using combinatorial hydrogels. *Acta Biomater.* **9**, 5475–5483 (2013).

[113] Slaughter, B. V., Khurshid, S. S., Fisher, O. Z., Khademhosseini, A. & Peppas, N. A. Hydrogels in Regenerative Medicine. *Adv. Mater.* **21**, 3307–3329 (2009).

[114] Bryant, S. J. & Anseth, K. S. Hydrogel properties influence ECM production by chondrocytes photoencapsulated in poly(ethylene glycol) hydrogels. *J. Biomed. Mater. Res.* **59**, 63–72 (2002).

[115] Laurent, T. C. & Fraser, J. R. Hyaluronan. *FASEB J. Off. Publ. Fed. Am. Soc. Exp. Biol.* **6**, 2397–2404 (1992).

[116] Turley, E. A., Noble, P. W. & Bourguignon, L. Y. W. Signaling properties of hyaluronan receptors. *J. Biol. Chem.* **277**, 4589–4592 (2002).

[117] Knudson, C. B. & Knudson, W. Hyaluronan-binding proteins in development, tissue homeostasis, and disease. *FASEB J. Off. Publ. Fed. Am. Soc. Exp. Biol.* **7**, 1233–1241 (1993).

[118] Prestwich, G. D. & Kuo, J.-W. Chemically-modified HA for therapy and regenerative medicine. *Curr. Pharm. Biotechnol.* **9**, 242–245 (2008).

[119] Prestwich, G., Skardal, A. & Zhang, J. Modified macromolecules and methods of making and using thereof. *Eur. Pat. EP2399940 A2* (2012).

[120] Shu, X. Z., Liu, Y., Palumbo, F. & Prestwich, G. D. Disulfide-crosslinked hyaluronan-gelatin hydrogel films: a covalent mimic of the extracellular matrix for in vitro cell growth. *Biomaterials* **24**, 3825–3834 (2003).

[121] Skardal, A. *et al.* Tissue specific synthetic ECM hydrogels for 3-D in vitro maintenance of hepatocyte function. *Biomaterials* **33**, 4565–4575 (2012).

[122] Deegan, D. B., Zimmerman, C., Skardal, A., Atala, A. & Shupe, T. D. Stiffness of hyaluronic acid gels containing liver extracellular matrix supports human hepatocyte function and alters cell morphology. *J. Mech. Behav. Biomed. Mater.* **55**, 87–103 (2015).

[123] Vanderhooft, J. L., Alcoutlabi, M., Magda, J. J. & Prestwich, G. D. Rheological properties of cross-linked hyaluronan-gelatin hydrogels for tissue engineering. *Macromol. Biosci.* **9**, 20–28 (2009).

[124] Skardal, A. *et al.* A tunable hydrogel system for long-term release of cell-secreted cytokines and bioprinted *in situ* wound cell delivery: Tunable Hydrogel for Cytokine Release and Cell Delivery. *J. Biomed. Mater. Res. B Appl. Biomater.* **105**, 1986–2000 (2017).

[125]   Murphy, S. V., Skardal, A. & Atala, A. Evaluation of hydrogels for bio-printing applications. *J. Biomed. Mater. Res. A* **101**, 272–284 (2013).

[126]   Bhatia, S. N. & Ingber, D. E. Microfluidic organs-on-chips. *Nat. Biotechnol.* **32**, 760–772 (2014).

[127]   van Duinen, V., Trietsch, S. J., Joore, J., Vulto, P. & Hankemeier, T. Microfluidic 3D cell culture: from tools to tissue models. *Curr. Opin. Biotechnol.* **35**, 118–126 (2015).

[128]   Benya, P. D. & Shaffer, J. D. Dedifferentiated chondrocytes reexpress the differentiated collagen phenotype when cultured in agarose gels. *Cell* **30**, 215–224 (1982).

[129]   Polacheck, W. J., German, A. E., Mammoto, A., Ingber, D. E. & Kamm, R. D. Mechanotransduction of fluid stresses governs 3D cell migration. *Proc. Natl. Acad. Sci. U. S. A.* **111**, 2447–2452 (2014).

[130]   Altmann, B. *et al.* Differences in morphogenesis of 3D cultured primary human osteoblasts under static and microfluidic growth conditions. *Biomaterials* **35**, 3208–3219 (2014).

[131]   Baker, B. M., Trappmann, B., Stapleton, S. C., Toro, E. & Chen, C. S. Microfluidics embedded within extracellular matrix to define vascular architectures and pattern diffusive gradients. *Lab. Chip* **13**, 3246–3252 (2013).

[132]   Skardal, A., Devarasetty, M., Soker, S. & Hall, A. R. In situ patterned micro 3D liver constructs for parallel toxicology testing in a fluidic device. *Biofabrication* **7**, 031001 (2015).

[133]   Verbridge, S. S. *et al.* Physicochemical regulation of endothelial sprouting in a 3D microfluidic angiogenesis model. *J. Biomed. Mater. Res. A* **101**, 2948–2956 (2013).

[134]   Hockemeyer, K. *et al.* Engineered three-dimensional microfluidic device for interrogating cell-cell interactions in the tumor microenvironment. *Biomicrofluidics* **8**, 044105 (2014).

[135]   Haessler, U., Teo, J. C. M., Foretay, D., Renaud, P. & Swartz, M. A. Migration dynamics of breast cancer cells in a tunable 3D interstitial flow chamber. *Integr. Biol. Quant. Biosci. Nano Macro* **4**, 401–409 (2012).

[136]   Toh, Y.-C. *et al.* A novel 3D mammalian cell perfusion-culture system in microfluidic channels. *Lab. Chip* **7**, 302–309 (2007).

[137]   Frey, O., Misun, P. M., Fluri, D. A., Hengstler, J. G. & Hierlemann, A. Reconfigurable microfluidic hanging drop network for multi-tissue interaction and analysis. *Nat. Commun.* **5**, 4250 (2014).

[138] Ong, S.-M. *et al.* A gel-free 3D microfluidic cell culture system. *Biomaterials* **29**, 3237–3244 (2008).

[139] Murphy, S. V. & Atala, A. 3D bioprinting of tissues and organs. *Nat. Biotechnol.* **32**, 773 (2014).

[140] Ataç, B. *et al.* Skin and hair on-a-chip: in vitro skin models versus ex vivo tissue maintenance with dynamic perfusion. *Lab. Chip* **13**, 3555–3561 (2013).

[141] Ng, K. *et al.* Paper-based cell culture platform and its emerging biomedical applications. *Mater. Today* **20**, 32–44 (2017).

[142] Bhattacharya, M. *et al.* Nanofibrillar cellulose hydrogel promotes three-dimensional liver cell culture. *J. Control. Release Off. J. Control. Release Soc.* **164**, 291–298 (2012).

[143] Bischel, L. L., Young, E. W. K., Mader, B. R. & Beebe, D. J. Tubeless microfluidic angiogenesis assay with three-dimensional endothelial-lined microvessels. *Biomaterials* **34**, 1471–1477 (2013).

[144] Trietsch, S. J., Israëls, G. D., Joore, J., Hankemeier, T. & Vulto, P. Microfluidic titer plate for stratified 3D cell culture. *Lab. Chip* **13**, 3548–3554 (2013).

[145] Huh, D. *et al.* Reconstituting organ-level lung functions on a chip. *Science* **328**, 1662–1668 (2010).

[146] D'Amico Oblak, T., Root, P. & Spence, D. M. Fluorescence monitoring of ATP-stimulated, endothelium-derived nitric oxide production in channels of a poly(dimethylsiloxane)-based microfluidic device. *Anal. Chem.* **78**, 3193–3197 (2006).

[147] Lee, W. S., Jambovane, S., Kim, D. & Hong, J. W. Predictive model on micro droplet generation through mechanical cutting. *Microfluid. Nanofluidics* **7**, 431–438 (2009).

[148] Vroman, L. Effect of Adsorbed Proteins on the Wettability of Hydrophilic and Hydrophobic Solids. *Nature* **196**, 476–477 (1962).

[149] Anderson, J. M. *et al.* Protein adsorption and macrophage activation on polydimethylsiloxane and silicone rubber. *J. Biomater. Sci. Polym. Ed.* **7**, 159–169 (1995).

[150] Regehr, K. J. *et al.* Biological implications of polydimethylsiloxane-based microfluidic cell culture. *Lab. Chip* **9**, 2132–2139 (2009).

[151] Cooksey, G. A. & Atencia, J. Pneumatic valves in folded 2D and 3D fluidic devices made from plastic films and tapes. *Lab. Chip* **14**, 1665–1668 (2014).

[152] Nath, P. *et al.* Rapid prototyping of robust and versatile microfluidic components using adhesive transfer tapes. *Lab. Chip* **10**, 2286–2291 (2010).

[153] Yuen, P. K. & Goral, V. N. Low-cost rapid prototyping of flexible microfluidic devices using a desktop digital craft cutter. *Lab. Chip* **10**, 384–387 (2010).

[154] P. DelNero, Y.H. Song, and C. Fischbach, *Microengineered tumor models: insights & opportunities from a physical sciences-oncology perspective.* Biomedical Microdevices, 2013. **15**(4): p. 583-593.

[155] G.M. Walker, H.C. Zeringue, and D.J. Beebe, *Microenvironment design considerations for cellular scale studies.* Lab on a Chip, 2004. **4**(2).

[156] E. Burdett, F.K. Kasper, A.G. Mikos, and J.A. Ludwig, *Engineering Tumors: A Tissue Engineering Perspective in Cancer Biology.* Tissue Engineering Part B: Reviews, 2010. **16**(3): p. 351-359.

[157] L.G. Griffith and M.A. Swartz, *Capturing complex 3D tissue physiology in vitro.* Nature Reviews Molecular Cell Biology, 2006. **7**(3): p. 211-224.

[158] A. Khademhosseini, R. Langer, J. Borenstein, and J.P. Vacanti, *Microscale technologies for tissue engineering and biology.* Proceedings of the National Academy of Sciences, 2006. **103**(8): p. 2480-2487.

[159] J.R. Enders, J.P. Wikswo, K.T. Seale, A. Kole, J.A. McLean, C.C. Marasco, S. Sevugarajan, and B. Nguyen, *Towards monitoring real-time cellular response using an integrated microfluidics-matrix assisted laser desorption ionisation/nanoelectrospray ionisation-ion mobility-mass spectrometry platform.* IET Systems Biology, 2010. **4**(6): p. 416-427.

[160] A.L. Paguirigan, J.P. Puccinelli, X. Su, and D.J. Beebe, *Expanding the Available Assays: Adapting and Validating In-Cell Westerns in Microfluidic Devices for Cell-Based Assays.* ASSAY and Drug Development Technologies, 2010. **8**(5): p. 591-601.

[161] J. El-Ali, P.K. Sorger, and K.F. Jensen, *Cells on chips.* Nature, 2006. **442**(7101): p. 403-411.

[162] G.M. Whitesides, *The origins and the future of microfluidics.* Nature, 2006. **442**(7101): p. 368-373.

[163] T. Ohkura, K. Ohta, T. Nagao, K. Kusumoto, A. Koeda, T. Ueda, T. Jomura, T. Ikeya, E. Ozeki, K. Wada, K. Naitoh, Y. Inoue, N. Takahashi, H. Iwai, H. Arakawa, and T. Ogihara, *Evaluation of human hepatocytes cultured by three-dimensional spheroid systems for drug metabolism.* Drug Metab Pharmacokinet, 2014. **29**(5): p. 373-8.

[164] A.A. Chen, S.R. Khetani, S. Lee, S.N. Bhatia, and K.J. Van Vliet, *Modulation of hepatocyte phenotype in vitro via chemomechanical tuning of polyelectrolyte multilayers.* Biomaterials, 2009. **30**(6): p. 1113-20.

[165] A. Sivaraman, J.K. Leach, S. Townsend, T. Iida, B.J. Hogan, D.B. Stolz, R. Fry, L.D. Samson, S.R. Tannenbaum, and L.G. Griffith, *A microscale in vitro physiological model of the liver: predictive screens for drug metabolism and enzyme induction.* Curr Drug Metab, 2005. **6**(6): p. 569-91.

[166] V. Liu Tsang, A.A. Chen, L.M. Cho, K.D. Jadin, R.L. Sah, S. DeLong, J.L. West, and S.N. Bhatia, *Fabrication of 3D hepatic tissues by additive photopatterning of cellular hydrogels.* FASEB J, 2007. **21**(3): p. 790-801.

[167] M.P. Lutolf and J.A. Hubbell, *Synthetic biomaterials as instructive extracellular microenvironments for morphogenesis in tissue engineering.* Nat Biotechnol, 2005. **23**(1): p. 47-55.

[168] T.T. Chang and M. Hughes-Fulford, *Monolayer and spheroid culture of human liver hepatocellular carcinoma cell line cells demonstrate distinct global gene expression patterns and functional phenotypes.* Tissue Eng Part A, 2009. **15**(3): p. 559-67.

[169] K. Domansky, W. Inman, J. Serdy, A. Dash, M.H. Lim, and L.G. Griffith, *Perfused multiwell plate for 3D liver tissue engineering.* Lab Chip, 2010. **10**(1): p. 51-8.

[170] B.I. Goldman and J. Wurzel, *Effects of subcultivation and culture medium on differentiation of human fetal cardiac myocytes.* In Vitro Cell Dev Biol, 1992. **28A**(2): p. 109-19.

[171] W.H. Zimmermann, K. Schneiderbanger, P. Schubert, M. Didie, F. Munzel, J.F. Heubach, S. Kostin, W.L. Neuhuber, and T. Eschenhagen, *Tissue engineering of a differentiated cardiac muscle construct.* Circ Res, 2002. **90**(2): p. 223-30.

[172] H. Parsa, K. Ronaldson, and G. Vunjak-Novakovic, *Bioengineering methods for myocardial regeneration.* Adv Drug Deliv Rev, 2016. **96**: p. 195-202.

[173] A. Aung, I.S. Bhullar, J. Theprungsirikul, S.K. Davey, H.L. Lim, Y.J. Chiu, X. Ma, S. Dewan, Y.H. Lo, A. McCulloch, and S. Varghese, *3D cardiac mutissues within a microfluidic device with real-time contractile stress readout.* Lab Chip, 2016. **16**(1): p. 153-62.

[174] S. Chatterjee, K. Fujiwara, N.G. Perez, M. Ushio-Fukai, and A.B. Fisher, *Mechanosignaling in the vasculature: emerging concepts in sensing, transduction and physiological responses.* Am J Physiol Heart Circ Physiol, 2015. **308**(12): p. H1451-62.

[175] C. Moraes, J.H. Chen, Y. Sun, and C.A. Simmons, *Microfabricated arrays for high-throughput screening of cellular response to cyclic substrate deformation.* Lab Chip, 2010. **10**(2): p. 227-34.

[176] F. Michielin, E. Serena, P. Pavan, and N. Elvassore, *Microfluidic-assisted cyclic mechanical stimulation affects cellular membrane integrity in a human muscular dystrophy in vitro model.* RSC Advances, 2015. **5**(119): p. 98429-98439.

[177] X. Gao, X. Zhang, H. Tong, B. Lin, and J. Qin, *A simple elastic membrane-based microfluidic chip for the proliferation and differentiation of mesenchymal stem cells under tensile stress.* Electrophoresis, 2011. **32**(23): p. 3431-6.

[178] C.S. Simmons, J.Y. Sim, P. Baechtold, A. Gonzalez, C. Chung, N. Borghi, and B.L. Pruitt, *Integrated strain array for cellular mechanobiology studies.* J Micromech Microeng, 2011. **21**(5): p. 54016-54025.

[179] N.J. Douville, P. Zamankhan, Y.C. Tung, R. Li, B.L. Vaughan, C.F. Tai, J. White, P.J. Christensen, J.B. Grotberg, and S. Takayama, *Combination of fluid and solid mechanical stresses contribute to cell death and detachment in a microfluidic alveolar model.* Lab Chip, 2011. **11**(4): p. 609-19.

[180] D. Huh, B.D. Matthews, A. Mammoto, M. Montoya-Zavala, H.Y. Hsin, and D.E. Ingber, *Reconstituting organ-level lung functions on a chip.* Science, 2010. **328**(5986): p. 1662-8.

[181] A.O. Stucki, J.D. Stucki, S.R. Hall, M. Felder, Y. Mermoud, R.A. Schmid, T. Geiser, and O.T. Guenat, *A lung-on-a-chip array with an integrated bio-inspired respiration mechanism.* Lab Chip, 2015. **15**(5): p. 1302-10.

[182] O.T. Guenat and F. Berthiaume, *Incorporating mechanical strain in organs-on-a-chip: Lung and skin.* Biomicrofluidics, 2018. **12**(4): p. 042207.

[183] C.M. Hovell, Y.J. Sei, and Y. Kim, *Microengineered vascular systems for drug development.* J Lab Autom, 2015. **20**(3): p. 251-8.

[184] Y. Zheng, J. Chen, M. Craven, N.W. Choi, S. Totorica, A. Diaz-Santana, P. Kermani, B. Hempstead, C. Fischbach-Teschl, J.A. Lopez, and A.D. Stroock, *In vitro microvessels for the study of angiogenesis and thrombosis.* Proc Natl Acad Sci U S A, 2012. **109**(24): p. 9342-7.

[185] J.A. Brown, V. Pensabene, D.A. Markov, V. Allwardt, M.D. Neely, M. Shi, C.M. Britt, O.S. Hoilett, Q. Yang, B.M. Brewer, P.C. Samson, L.J. McCawley, J.M. May, D.J. Webb, D. Li, A.B. Bowman, R.S. Reiserer, and J.P. Wikswo, *Recreating blood-brain barrier physiology and structure on chip: A novel neurovascular microfluidic bioreactor.* Biomicrofluidics, 2015. **9**(5): p. 054124.

[186] A.K. Achyuta, A.J. Conway, R.B. Crouse, E.C. Bannister, R.N. Lee, C.P. Katnik, A.A. Behensky, J. Cuevas, and S.S. Sundaram, *A modular approach to create a neurovascular unit-on-a-chip.* Lab Chip, 2013. **13**(4): p. 542-53.

[187]   D. Kilinc, J.M. Peyrin, V. Soubeyre, S. Magnifico, L. Saias, J.L. Viovy, and B. Brugg, *Wallerian-like degeneration of central neurons after synchronized and geometrically registered mass axotomy in a three-compartmental microfluidic chip.* Neurotox Res, 2011. **19**(1): p. 149-61.

[188]   J.M. Peyrin, B. Deleglise, L. Saias, M. Vignes, P. Gougis, S. Magnifico, S. Betuing, M. Pietri, J. Caboche, P. Vanhoutte, J.L. Viovy, and B. Brugg, *Axon diodes for the reconstruction of oriented neuronal networks in microfluidic chambers.* Lab Chip, 2011. **11**(21): p. 3663-73.

[189]   K.J. Jang, H.S. Cho, D.H. Kang, W.G. Bae, T.H. Kwon, and K.Y. Suh, *Fluid-shear-stress-induced translocation of aquaporin-2 and reorganization of actin cytoskeleton in renal tubular epithelial cells.* Integr Biol (Camb), 2011. **3**(2): p. 134-41.

[190]   K.J. Jang and K.Y. Suh, *A multi-layer microfluidic device for efficient culture and analysis of renal tubular cells.* Lab Chip, 2010. **10**(1): p. 36-42.

[191]   Y. Imura, Y. Asano, K. Sato, and E. Yoshimura, *A microfluidic system to evaluate intestinal absorption.* Anal Sci, 2009. **25**(12): p. 1403-7.

[192]   H. Kimura, T. Yamamoto, H. Sakai, Y. Sakai, and T. Fujii, *An integrated microfluidic system for long-term perfusion culture and on-line monitoring of intestinal tissue models.* Lab Chip, 2008. **8**(5): p. 741-6.

[193]   J. Park, H. Koito, J. Li, and A. Han, *Microfluidic compartmentalized co-culture platform for CNS axon myelination research.* Biomed Microdevices, 2009. **11**(6): p. 1145-53.

[194]   C.M. Puleo, W. McIntosh Ambrose, T. Takezawa, J. Elisseeff, and T.H. Wang, *Integration and application of vitrified collagen in multilayered microfluidic devices for corneal microtissue culture.* Lab Chip, 2009. **9**(22): p. 3221-7.

[195]   D. Huh, D.C. Leslie, B.D. Matthews, J.P. Fraser, S. Jurek, G.A. Hamilton, K.S. Thorneloe, M.A. McAlexander, and D.E. Ingber, *A human disease model of drug toxicity-induced pulmonary edema in a lung-on-a-chip microdevice.* Sci Transl Med, 2012. **4**(159): p. 159ra147.

[196]   K.H. Benam, R. Villenave, C. Lucchesi, A. Varone, C. Hubeau, H.H. Lee, S.E. Alves, M. Salmon, T.C. Ferrante, J.C. Weaver, A. Bahinski, G.A. Hamilton, and D.E. Ingber, *Small airway-on-a-chip enables analysis of human lung inflammation and drug responses in vitro.* Nat Methods, 2016. **13**(2): p. 151-7.

[197]   H. Zhao, X. Li, S. Zhao, Y. Zeng, L. Zhao, H. Ding, W. Sun, and Y. Du, *Microengineered in vitro model of cardiac fibrosis through modulating myofibroblast mechanotransduction.* Biofabrication, 2014. **6**(4): p. 045009.

[198] M.E. Katt, A.L. Placone, A.D. Wong, Z.S. Xu, and P.C. Searson, *In Vitro Tumor Models: Advantages, Disadvantages, Variables, and Selecting the Right Platform.* Front Bioeng Biotechnol, 2016. **4**: p. 12.

[199] T.D. Tlsty and L.M. Coussens, *Tumor stroma and regulation of cancer development.* Annu Rev Pathol, 2006. **1**: p. 119-50.

[200] R. Kalluri and M. Zeisberg, *Fibroblasts in cancer.* Nat Rev Cancer, 2006. **6**(5): p. 392-401.

[201] A. Orimo, P.B. Gupta, D.C. Sgroi, F. Arenzana-Seisdedos, T. Delaunay, R. Naeem, V.J. Carey, A.L. Richardson, and R.A. Weinberg, *Stromal fibroblasts present in invasive human breast carcinomas promote tumor growth and angiogenesis through elevated SDF-1/CXCL12 secretion.* Cell, 2005. **121**(3): p. 335-48.

[202] C.F. Singer, N. Kronsteiner, E. Marton, M. Kubista, K.J. Cullen, K. Hirtenlehner, M. Seifert, and E. Kubista, *MMP-2 and MMP-9 expression in breast cancer-derived human fibroblasts is differentially regulated by stromal-epithelial interactions.* Breast Cancer Res Treat, 2002. **72**(1): p. 69-77.

[203] J.A. Joyce and J.W. Pollard, *Microenvironmental regulation of metastasis.* Nat Rev Cancer, 2009. **9**(4): p. 239-52.

[204] P. Lu, V.M. Weaver, and Z. Werb, *The extracellular matrix: a dynamic niche in cancer progression.* J Cell Biol, 2012. **196**(4): p. 395-406.

[205] C. Frantz, K.M. Stewart, and V.M. Weaver, *The extracellular matrix at a glance.* J Cell Sci, 2010. **123**(Pt 24): p. 4195-200.

[206] A.J. Steward and D.J. Kelly, *Mechanical regulation of mesenchymal stem cell differentiation.* J Anat, 2015. **227**(6): p. 717-31.

[207] S.V. Plotnikov, A.M. Pasapera, B. Sabass, and C.M. Waterman, *Force fluctuations within focal adhesions mediate ECM-rigidity sensing to guide directed cell migration.* Cell, 2012. **151**(7): p. 1513-27.

[208] F. Kai, H. Laklai, and V.M. Weaver, *Force Matters: Biomechanical Regulation of Cell Invasion and Migration in Disease.* Trends Cell Biol, 2016. **26**(7): p. 486-497.

[209] M.G. Rubashkin, L. Cassereau, R. Bainer, C.C. DuFort, Y. Yui, G. Ou, M.J. Paszek, M.W. Davidson, Y.Y. Chen, and V.M. Weaver, *Force engages vinculin and promotes tumor progression by enhancing PI3K activation of phosphatidylinositol (3,4,5)-triphosphate.* Cancer Res, 2014. **74**(17): p. 4597-611.

[210] T.P. Padera, A. Kadambi, E. di Tomaso, C.M. Carreira, E.B. Brown, Y. Boucher, N.C. Choi, D. Mathisen, J. Wain, E.J. Mark, L.L. Munn, and R.K. Jain, *Lymphatic metastasis in the absence of functional intratumor lymphatics.* Science, 2002. **296**(5574): p. 1883-6.

[211] A.J. Leu, D.A. Berk, A. Lymboussaki, K. Alitalo, and R.K. Jain, *Absence of functional lymphatics within a murine sarcoma: a molecular and functional evaluation.* Cancer Res, 2000. **60**(16): p. 4324-7.

[212] Y. Boucher, L.T. Baxter, and R.K. Jain, *Interstitial pressure gradients in tissue-isolated and subcutaneous tumors: implications for therapy.* Cancer Res, 1990. **50**(15): p. 4478-84.

[213] A. Oldberg, S. Kalamajski, A.V. Salnikov, L. Stuhr, M. Morgelin, R.K. Reed, N.E. Heldin, and K. Rubin, Collagen-binding proteoglycan fibromodulin can determine stroma matrix structure and fluid balance in experimental carcinoma. Proceedings of the National Academy of Sciences, 2007. 104(35): p. 13966-13971

[214] Z.D. Shi, X.Y. Ji, H. Qazi, and J.M. Tarbell, *Interstitial flow promotes vascular fibroblast, myofibroblast, and smooth muscle cell motility in 3-D collagen I via upregulation of MMP-1.* Am J Physiol Heart Circ Physiol, 2009. **297**(4): p. H1225-34.

[215] D.O. Miteva, J.M. Rutkowski, J.B. Dixon, W. Kilarski, J.D. Shields, and M.A. Swartz, *Transmural flow modulates cell and fluid transport functions of lymphatic endothelium.* Circ Res, 2010. **106**(5): p. 920-31.

[216] H.D. Roh, Y. Boucher, S. Kalnicki, R. Buchsbaum, W.D. Bloomer, and R.K. Jain, *Interstitial hypertension in carcinoma of uterine cervix in patients: possible correlation with tumor oxygenation and radiation response.* Cancer Res, 1991. **51**(24): p. 6695-8.

CHAPTER 2

Development of an integrated multi-tissue adhesive film-based organ-on-a-chip

platform for assessing drug efficiency and toxicity

In recent years, it has been proven that 3D cell cultures are better predictive models for most biological testing than 2D or animal models. So it becomes critical to innovate novel biofabrication techniques to develop a 3D cell culture system. This led to the integration of 3D cell culture with a dynamic microfluidics platform that provides various advantages over the traditional static culture. Currently, most of the cell culture-based microfluidic systems are poly(dimethylsiloxane) (PDMS)-based. This is mainly because of its material properties like being biocompatible, optically clear and low-cost. But there are a few shortcomings in these microfluidic systems when running a long-term experiment, including evaporation through the material and adsorption of molecules through the walls of the channels. Also, the platform requires a cleanroom for the fabrication of the master mold, which can be expensive and time-consuming. Above all the platform suffers from time and resource-consuming processes during fabrication and thus lacks scalability. Nowadays, scientists and commercial microfluidic manufacturers are moving towards cost-effective thermoplastics based microfluidic platform which proves to be more robust and overcome most of the shortcomings of the PDMS-based system. These plastic microfluidic devices can be mass-produced but require sophisticated machinery and process like injection molding, computer numerical control (CNC) machine etc. Hence, it is critical to developing a low-cost, robust and easy fabrication technique to build in-house microfluidic devices that do not require sophisticated fabrication-assist devices.

Here, the primary goal of this chapter was to develop a rapid prototyping microfluidic platform based on an adhesive film that can be utilized for various 3D cell culture applications. To accomplish this, the biocompatibility, robustness, and stability of the system for cell culture applications were challenged by integrating a series of healthy organ tissue that included up to 20 primary cells for an extended period. Having established a highly viable fluidic platform that supports even the sensitive primary cells, we explored the capability of conducting long term drug studies. The results of these experiments are discussed extensively in the chapter. It was shown that the relatively inert surface of the platform allowed for thriving 3D cell culture and on-chip drug testing. Also, the optical transparency of the system enabled high-resolution optical microscopy observations directly on the chip. In conclusion, we were able to develop a simple yet robust microfluidic chip that supports highly sophisticated 3D cell culture modules.

Note:

The contents of this chapter have been submitted as two different peer-reviewed articles.

Peer-reviewed Publication:

'Probing prodrug metabolism and reciprocal toxicity with an integrated and humanized multi-tissue organ-on-a-chip platform' **S. Rajan,** *J Aleman, M. Wan, N. P. Zarandi, G Nzou, S. Murphy, C. Bishop, H. Sadri-Ardekan[1], T. Shupe, A. Atala, A.R. Hall, A Skardal. Acta Biomaterialia 2020. (In press)*

'Drug compound screening in single and integrated multi-organoid body-on-a-chip Systems,' *A. Skardal, J. Aleman, S. Forsythe,* **S. Rajan**, *S. Murphy, M. Devarasetty, N. P.*

Zarandi, G. Nzou, R. Wicks, H. Sadri-Ardekani, C Bishop, S Soker, A.R. Hall, T Shupe, and A. Atala. Biofabrication 2020. (In press)

Abstract

Current drug development techniques are expensive and inefficient, partially due to the use of preclinical models that do not accurately recapitulate *in vivo* drug efficacy and cytotoxicity. To address this challenge, we report on an integrated, *in vitro* multi-organoid system that enables parallel assessment of drug efficiency and toxicity on multiple 3D tissue organoids. Built-in a low-cost, adhesive film-based microfluidic device, these miniaturized structures require less than 200 µL fluid volume and are amenable to both matrix-based 3D cell culture and spheroid aggregate integration. Here, we demonstrate this technology first with a three-organoid device consisting of liver, cardiac, and lung constructs. We show that these multiple tissue types can be kept in joint circulation with high viability for 21 days and validate the platform by investigating liver metabolism of the prodrug capecitabine into 5-fluorouracil (5-FU) and observing downstream toxicity in lung and cardiac organoids. Then we expand the integrated system to accommodate six humanized constructs, including liver, cardiac, lung, endothelium, brain, and testes organoids. Following a 14-day incubation in common media, we demonstrate multi-tissue interactions by metabolizing the alkylating prodrug ifosfamide in the liver organoid to produce chloroacetaldehyde and induce downstream neurotoxicity. Our results establish an expandable, multi-organoid body-on-a-chip system that can be fabricated easily and used for the accurate characterization of drug interactions *in vitro*.

2.1 Introduction

A key challenge for the pharmaceutical industry is the lack of predictive models for drug discovery and toxicity testing. From the compound/drug development stage, only about 10% of drugs achieve FDA approval in clinical trials and are subsequently effective in humans.[1, 2] Most failures occur in slowly invested-in phase III trials and could be mitigated with superior drug testing models.[3] The current drug development process is heavily reliant on inefficient 2D cell cultures and expensive and time-consuming animal models. However, these preclinical models mostly fail to either recapitulate human physiology or the structural and functional complexity of tissues and organs. For example, static 2D *in vitro* models are often composed of single-cell types, which is not representative of functional multicellular tissue. On the other hand, while animal models represent a complete and integrated system, differences in drug metabolism and cellular response to chemical signals relative to humans[4] make their predictive accuracy debatable. 3D cell culture models are known to mimic the mechanical, chemical, and physiological properties of *in vivo* tissue better than simple 2D models and can contain heterogeneous human cells to provide relevant assessments.[5, 6] Though some 3D models such as organoids can faithfully represent some aspects of *in vivo* tissues, their isolated and often static nature coupled with the typical use of a single drug dose does not reproduce complex multi-organ intercommunication through metabolite and chemical exchange or *in vivo* pharmacokinetics of drug delivery. Consequently, there is a critical need to develop dynamic systems with physiologically relevant tissue models and controlled spatiotemporal media conditions to better model drug and organ interactions.

Integrating 3D cell culture constructs with microfluidics provides the capability to control dynamic factors of the microenvironment with spatial precision and supports the introduction of mechanical and chemical cues missing in static 3D models. These minimalist microfluidic constructs represent fundamental organ-level structural, functional, and mechanical properties and are collectively referred to as organ-on-a-chip systems. As functional *in vitro* units of organs that display highly accurate biological response analogous to *in vivo* systems*,* organ-on-a-chip technologies have been an emerging interest for a decade.[7-12] Such systems have targeted well-known drug challenges to further support platform efficacy for drug discovery processes [10, 12-17], especially in the preclinical phase. However, single-organoid platforms lack the complex and interactive nature of the human body and consequently fall short of replicating systemic drug interactions. To partially capture *in vivo* intricacy, multiple microphysiological systems can be integrated and maintained under a common media to promote interactions between organs and study drug effects[18-21]. These body-on-a-chip (BOC) devices represent physiologically-based pharmacokinetic models that can simulate recirculation in a closed system. Furthermore, they can be designed not only to reproduce relative organ sizes[22] and liquid-to-organ volume ratios[17, 23] faithfully but can also generate realistic concentration dynamics for each tissue compartment and emulate temporal dose changes[24] in a more consistent and controlled manner than can be achieved in alternative platforms.

There have been various approaches to realize BOC systems are integrating multiple organs[19, 20, 25-29]. A primary concern in these efforts is the development of a complete common media that can support the multiple cell types incorporated in different

organoids.[23, 30] Compared to cell line-based BOCs that can often employ simple media formulations,[31, 32] BOC systems with primary cells or induced pluripotent stem cells (iPSCs) can present additional challenges due to their individualized media needs. This weighs the need for integration of multiple organs against maintaining high viability and functionality of the organoids. A second obstacle arises from the materials used for microfluidic device fabrication. Traditionally, microfluidic chips are fabricated using polydimethylsiloxane (PDMS), which is biocompatible, optically clear, and allows passive gas exchange. However, because of its hydrophobic nature, PDMS can adsorb hydrophobic compounds, including many proteins and drugs[33], and can also allow for evaporation of liquid over long-term experiments. Consequently, it is critical to consider materials that will not alter the pharmacokinetic profiles of tested drugs or the concentrations of secreted macromolecules over long-term studies. A third challenge is the production of a closed-circuit, unidirectional fluid flow between organoids that allows physiologically relevant volume ratios to be maintained. In addition to these central considerations, the system should also enable direct imaging and on-demand media access for analysis.

Here, we demonstrate a multi-tissue system containing organoids constructed entirely with human cells. We employ a straightforward and low-cost technique to build our microfluidic devices with biocompatible thermoplastic polymers[33] and then biofabricate functional spheroids or 3D cell-laden hydrogel constructs in them. The resulting system mimics basic circulatory and physiological aspects of the complex human body in a miniaturized format (30 µL per organoid chamber) using 3 or 6 discrete tissues collectively composed of up to 20 different cell types, including primary and iPS-derived cells. We maintain these integrated constructs under a common circulating media for extended experimentation and

challenge them by conducting drug studies in which prodrugs with no intrinsic reactivity are metabolized by a functional liver organoid to produce reactive metabolites that influence adjoining organoids. While still, simple distillation of complex human physiology, the system described herein offers an easy-to-fabricate multi-tissue platform to begin to explore complex drug and toxin interactions between tissue types *in vitro*.

2.2 Experimental Methods

2.2.1 Fabrication of adhesive film-based multi-tissue chips:

The adhesive film-based *(*AFB) microfluidic chip was fabricated with a low-cost technique that uses rapid-prototyping of patterned adhesive films.[16] The channels in these chips were formed with a computer-controlled razor plotter (CE6000-40, Graphtec, Irvine, CA) in a double-sided adhesive film (140 μm thickness, part number 3M9495MPF, Strouse, Westminster, MD) employing engineered perforations between each layer to aide self-alignment (**Figure 2.1.a**). Channels consisting of multiple adhesive film layers were essential to accommodate the varying sizes of functional spheroids, ranging from 150μM to 500μM in diameter. Hence, each microfluidic chip consisted of 4 layers of adhesive film for the 3- and 6-organoid systems to produce a channel height of 560μM. The 3- and 6-organoid systems had similar fabrication approaches, except for a slightly modified channel design: the 3-organoid design featured 3 discrete chambers (3 mm in diameter) connected in series by external tubing (**Figure 2.1.b, top**) whereas the 6-organoid design was optimized to form 5 internally-connected chambers (4 mm in diameter) as well as one additional 4 mm chamber connected to the rest of the system via external tubing (**Figure 2.1.b, bottom**). This design was tailored to accommodate the optional integration of one

organoid (liver) that could be removed from the circulation for comparative studies. The multi-layered patterned films were securely adhered to a glass microscope slide (VWR, Radnor, PA) to facilitate direct imaging.
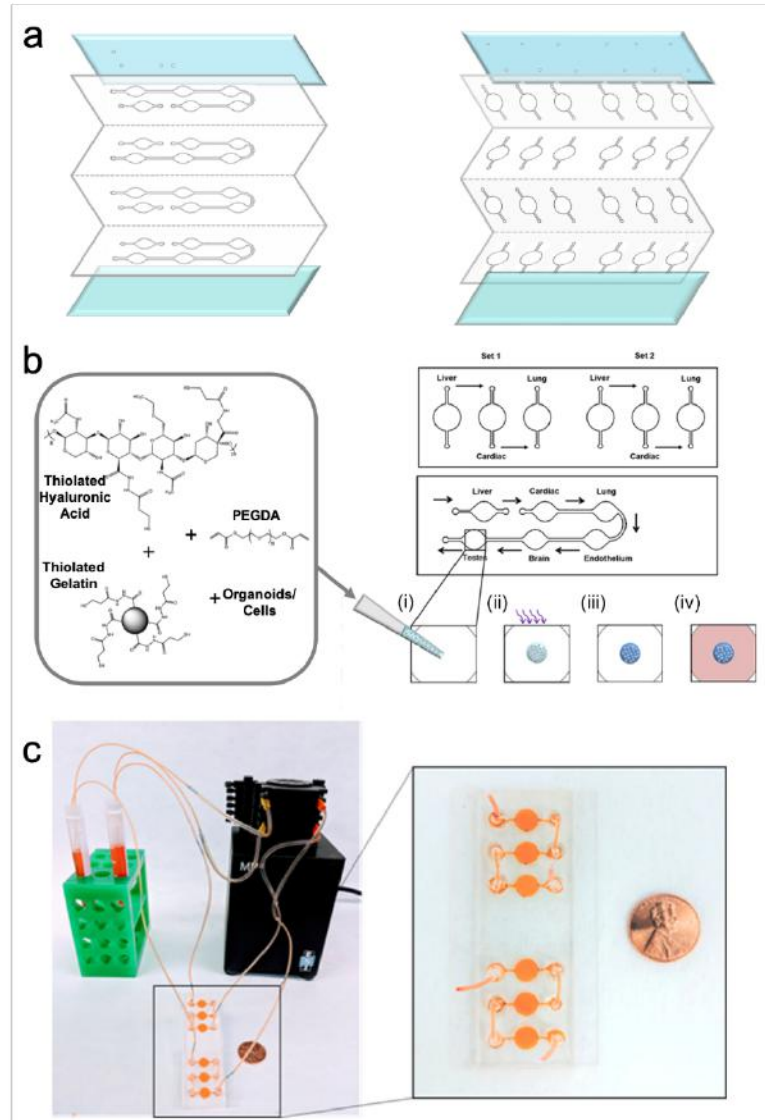
Figure 2. 1. In situ photopatterning of multiple organ-specific tissues. *(a) Schematics of microfluidic device layers for the AFB 3-organoid (left) and 6-organoid (right) platform. (b) In situ organoid patterning technique using a hydrogel comprised of thiolated hyaluronic acid, thiolated gelatin, PEGDA, and a photoinitiator: in a microfluidic*

chamber (i) the hydrogel mixture containing HA hydrogel, photoinitiator, and organ-specific spheroid/cells are pipetted as a drop (light blue) and then illuminated with UV light directly (ii). The exposed precursor is crosslinked into a hydrogel (dark blue), encapsulating spheroids, or cells within the region (iii). Finally, common media formulation (red) is added to the chamber for incubation (iv). (c) The total measurement set-up, featuring a low-volume, closed-loop fluidic circuit for each organoid system facilitated by a computer-controlled peristaltic pump.

All organoids were then biofabricated in the designated chambers (see *In situ patterning of organoids*) and the top side was firmly sealed using a PMMA (1/8" thickness, McMaster-Carr, Elmhurst, IL) lid cut to the slide dimensions and furnished with ports using a laser etcher (Full Spectrum Laser H-series, Las Vegas, NV). The ports were fitted with polytetrafluoroethylene (PTFE) tubing (0.022"ID x 0.042"ID, Cole Parmer, Vernon Hills, IL) and secured using a UV-cure polyester resin (Solarez, Vista, CA).

2.2.2 Cell sources, culture, and organoid formation:

Note that the nomenclature used to define spheroids, organoids, and 3D tissue constructs varies between research groups as well as between fields of biomedical research. Here, spheroids refer to cellular constructs formed without an extrinsic hydrogel scaffold via approaches like the hanging drop method, in which cells self-assemble and form native cell-cell and/or cell-ECM junctions internally. Organoids refer to any cellular construct having specific organ-like function, and thus include both spheroids and scaffold-supported mixtures of individual cells consisting of multiple cell types designed to emulate

organ complexity. The term 3D tissue construct refers to a fabricated 3D hydrogel scaffold structure containing individual cells or cells in spheroid form.

Liver constructs –Primary human hepatocytes (HH, Bioreclamation VT, Westbury, NY) were thawed in human cryopreserved hepatocyte thawing media (Lonza, Morristown, NJ) as per manufacturer instructions and transferred to hepatocyte culture media (HCM; Lonza) in 50 mL conical tube. This cell suspension was centrifuged, and the resulting pellet collected for immediate use. Both hepatic stellate cells (HSc, Bioreclamation VT) and Kupffer cells (Sekisui XenoTech, Kansas City, KS) were obtained frozen, thawed in 37°C water bath, and used immediately. Human liver-derived endothelial cells (HLEc, Lonza) were expanded with minimal passaging and cultured in endothelial cell growth media (EGM™; Lonza) with 10% fetal bovine serum (FBS) (Atlanta Biologicals, Flowery Branch, GA) and other supplements provided by the manufacturer and then cryopreserved until use. Except for HH, all cell types were thawed and centrifuged to form a cell pellet that was used directly in experiments. Compositions of 75% HH, 10% HSc, 10% Kupffer cells, and 5% HLEc were prepared and then aggregated in a Corning® Costar® 96-well ultra-low adherent culture plates (Sigma Aldrich, St. Louis, MO, USA). Each well had approximately 2,000 cells in the above-mentioned ratio per 100 μL of HCM (Lonza) with 20% FBS and 1000X dilute Gentamicin. They were then incubated and observed for the formation of spheroids that were subsequently integrated into organoids (see *In situ patterning of organoids*).

Important considerations in our study and in other in vitro studies employing primary human hepatocytes are the limitations intrinsic to such cells, such as batch-to-batch variation and functional depreciation. Indeed, in our experience working with hepatocytes,

we have found cell sourcing to be challenging, with new lots and different donors yielding variable functional results. Consequently, many studies incorporating the cell type can require frequent recharacterization, ultimately leading to lost productivity difficulty in planning. In the long term, it may be that iPSC-derived hepatocytes will be a superior and less limited cell source. But to date, these cells suffer from significant functional limitations of their own.

Cardiac constructs – Commercially sourced iPSC-derived cardiomyocytes (CM, Cor.4U® Ncardia, Leiden, The Netherlands) were cultured on a Matrigel-coated (17 µL/mL of media; Corning) six-well plate in Pluricyte® complete cardiomyocyte culture media (CCM; Ncardia) with 10% FBS and 1% penicillin-streptomycin (P/S). After a 24 hr incubation, the complete media was renewed, and the cells were incubated until they began beating spontaneously (up to 48 hrs). To facilitate the efficient harvesting of CM cells, the plate was first washed with PBS and 0.5M EDTA. Then the cells were detached from the plate with trypsin (0.25%; Difco Laboratories, Detroit, MI) under mild agitation and used immediately. Both normal human cardiac fibroblast (NHCF) and cardiac endothelium cells (CE) were sourced commercially (ScienCell) and used as purchased after thawing to room temperature. A cell mixture was prepared to consist of 75% CM, 20% NHCF, and 5% CE and loaded into wells of a 96-well non-adherent round bottom plate (Sigma Aldrich) and incubated to aggregate in 100 µL of cardiomyocyte maintenance media (Stem Cell Theranostics, Redwood City, CA). Each well contained approximately 2,500 cells. The well plates were observed regularly until spheroids fully developed and produced a beating-like contractile movement. These were used directly in organoid formation (see *In situ patterning of organoids*).

Lung constructs – Alveolar epithelial cells (A549, Lonza) were expanded in a cell culture-treated flask (T-175, Thermofisher) and cultured in high glucose Dulbecco's Modified Eagle's media (DMEM; Thermofisher, Waltham, MA), 10% fetal bovine serum (FBS, Atlanta Biologicals), and 1% P/S. In the 3-organoid system and first 6-organoid system, the lung construct was biofabricated as a suspension of these cells in polymerized hydrogel scaffold (see *In situ patterning of organoids*).

Normal Human Lung Fibroblast (NHLF, Lonza) were cultured and expanded in Alpha MEM (Stemcell Technologies, Cambridge, MA), 10% FBS (Atlanta Biologicals) and 1% (P/S). The cells were harvested using 0.05% trypsin (Difco) prior to use. Primary Normal Human Bronchial Epithelial cells (NHBE, Lonza) were expanded in a culture flask coated with Type I Bovine Collagen (0.04 mg/ml, Sigma Aldrich) in Bronchial Epithelial Cell Growth media (Lonza) with supplements provided by the manufacturer and 5 µM Y-27632 (ROCK inhibitor). Irradiated primary lung fibroblast was used as feeder cells. NHBE and NHLF were mixed at a ratio of 4:1 and added to an ultra-low attachment U-bottom plate (Sigma-Aldrich) for aggregation in Organoid Formulation media (OFM) that consisted of complete DMEM with 20% FBS and rat tail collagen I (10 ng/µL; Corning). The plate was incubated at 37°C and monitored daily for spheroid formation. Resulting spheroids were used in the 6-organoid system (see *In situ patterning of organoids*).

Blood vessel constructs – Human Umbilical Vein Endothelial Cells (HUVEC; Lonza) were expanded and maintained in EGM (Lonza) with 10% FBS and other supplements provided by the manufacturer prior to use. Only cells under passage five were used for experiments. The blood vessel construct was biofabricated as a suspension of these cells in polymerized hydrogel scaffold (see *In situ patterning of organoids*).

Testis constructs – Testis spheroids consisted of human primary testicular cells, including spermatogonial stem cells (SSC), Leydig cells, Sertoli cells, and peritubular cells. These cells were sourced from the cryopreserved fragments of adult testicular tissues (whole organ) of brain-dead patients that were procured through the National Disease Research Interchange (NDRI). Briefly, human testicular cells were isolated and cultured from frozen tissue according to a previously established method[34-36] using the primary Sertoli, Leydig, and peritubular cells as the somatic feeder layer. Testicular cells were seeded and expanded up to 5-6 passages in a cell culture treated 75 cm^2 flask (Thermo Scientific) using enriched Stempro-34 media.[36] The spheroids were made by suspending the trypsin-treated cells in testicular spheroid formation media that was made from enriched StemPro-34, 30% FBS, and 1 μg/mL solubilized human testis ECM. The cells were seeded to aggregate into 96-well format ultra-low attachment round-bottom plates (Corning 7007) at a density of 10,000 cells/100 μL volume. Plates were then spun at 150×g for 30 seconds to initiate and facilitate the aggregation process. After 48 hours incubation, the compact spheroids were transferred into 96-well format ultra-low attachment U-bottom plates (Sigma-Aldrich, St. Louis, MO, USA)[37] and subsequently integrated (see *In situ patterning of organoids*).

Brain constructs – Brain spheroids were prepared as previously reported,[38] consisting of six commercially-sourced human primary and iPSC-derived cell types: 30% primary human brain microvascular endothelial cells (HBMEC), 15% human brain vascular pericytes (HBVP), 15% human astrocytes (HA), 5% human microglial (HM), 15% human oligodendrocytes (HO), and 20% human neural (HN) cells. HBMEC (Cell Systems, Kirkland, WA) were cultured and expanded in the attachment factor-coated plate and incubated in complete classic media (Cell Systems, Kirkland, WA) that was supplemented

with CultureBoost™ and attachment factor (Cell Systems). HBVP and HA cells (ScienCell Research Laboratories, Carlsbad, CA) were cultured and expanded in plates coated with Poly-L-Lysine (15 µg/ml; ScienCell Research Laboratories). HBVP cells were cultured in pericyte media (ScienCell Research Laboratories) with 2% FBS, 1% pericyte growth supplement (ScienCell Research Laboratories, Carlsbad, CA), and 1% penicillin-streptomycin. HA cells were cultured in astrocyte media (ScienCell Research Laboratories) containing 2% FBS, 1% astrocyte growth supplement (ScienCell Research Laboratories), and 1% penicillin-streptomycin. Human iPSC-derived microglia (HM; Tempo Bioscience Inc., San Francisco, CA) and HO progenitor cells (Tempo Bioscience Inc., San Francisco, CA) were expanded in plates coated with Matrigel (0.2 mg/ml; Corning). HM cells were cultured in DMEM/F-12 (Life Technologies), supplemented with 0.5% essential amino acids (Life Technologies), 1% N2 supplement (Life Technologies), 2% L-glutamine (Life Technologies), GM-CSF (100 ng/mL, Peprotech, Rocky Hill, NJ), and IL-34 (50 ng/mL, Peprotech). HO cells were initially cultured in a propagation media and replaced by differentiation media 72 hours prior to spheroid formation. Propagation media was made of DMEM/F12 supplemented with HEPES, 2 mM L-glutamine (Life Technologies), 1X non-Essential amino acids (Life Technologies), StemPro neural supplement (Invitrogen), 10 ng/mL PDGF-AA (Peprotech), 10 ng/mL PDGF-AB (Peprotech), 10 ng/mL NT3 (Peprotech), 100 ng/mL biotin (Sigma Aldrich), and 5 µM/mL cAMP (Sigma Aldrich). Differentiation media was made of 50% DMEM/F12 and 50% neural basal (Life Technologies), and supplemented with 1X non-essential amino acids, 1x B27 (Life Technologies), 2 mM L-glutamine, 100 ng/mL biotin, 5 ng/mL PDGF-AA, 10 ng/ml BDNF (Peprotech), 20 µg/mL ascorbic acid (Sigma Aldrich), 1 µM/ml cAMP, and

71

200 ng/ml T3 (Sigma Aldrich). HN stem cells (Axol Biosciences Ltd., Cambridge, UK) were cultured and expanded on plates coated with SureBond (Axol Biosciences) in neural plating-XF media (Axol Biosciences). After 24 hours, the media was replaced with neural expansion-XF media (Axol Biosciences) with recombinant human 20 ng/mL FGF2 (Axol Biosciences) and 20 ng/mL recombinant human EGF Axol Biosciences). After a sufficient number of cells was achieved, neuronal phenotypic differentiation was ensured by replacing the expansion media with neural differentiation-XF media (Axol Biosciences).

To make the spheroids, initially, 1,100 cells of HA, HN, HO, and HM were aggregated in 96-well hanging drop culture plates (InSphero AG, Schlieren, Switzerland) in the ratio described above with 45% astrocyte media without astrocyte growth supplements, 45% neural maintenance-XF media, 10% heat-inactivated FBS (Thermo Fisher), and 10 ng/μL rat tail collagen I (Corning). After 48 hrs, the neuroglial organoid was subsequently coated with HBMEC and HBVP cells by adding them in the suspension media. These organoids were then cultured in 60% neural maintenance-XF media (Axol Biosciences Ltd., Cambridge, UK), 20% astrocyte media (ScienCell Research Laboratories, Carlsbad, CA) and 20% complete classic media until they matured and then were transferred into a 96-well plate for subsequent use (see *In situ patterning of organoids*).

2.2.3 Extracellular matrix (ECM) hydrogel preparation:

ECM-mimicking HA/gelatin-based hydrogel (HyStem-HP, ESI-BIO, Alameda, CA) was used as the 3D organoid scaffold and was prepared as previously described.[39] Briefly, a thiolated HA component (Glycosil®), a thiolated gelatin component (Gelin-S®), and polyethylene glycol diacrylate crosslinker (PEGDA, Extralink®) were dissolved separately

in sterile water containing 0.05% w/v of the photoinitiator 2-Hydroxy-4′-(2-hydroxyethoxy)-2-methylpropiophenone (Sigma, St. Louis, MO) to make solutions containing 1% w/v. These solutions were then mixed in a 2:2:1 ratio by volume, respectively, for immediate use.

2.2.4 In situ patterning of organoids:

Organ-specific tissue constructs were individually biofabricated in individual predetermined chambers of the microfluidic device prior to sealing them. Either individual cells or spheroids were suspended within a 5 μL volume of the ECM-mimicking HA/gelatin-based hydrogel precursor, which was then introduced manually to the chamber and photocrosslinked by ultraviolet light exposure (BlueWave 200, Dymax, Torrington, CT) for 1 s with an intensity of $1W/cm^2$. The vascular organoids, in particular, were exposed for only 0.25 s at the same intensity. The cell density or quantity of spheroids used to bioengineer the different tissue organoids was selected based on physiological *in vivo* tissue volumes. In the 3-organoid system, the first chamber contained 50 liver spheroids, the second chamber contained 10 cardiac spheroids, and the third chamber contained a lung organoid composed of A549 cells suspension at a density of 36×10^6 cells/mL. In the 6-organoid system, the first two chambers again contained 50 liver spheroids and 10 cardiac spheroids, respectively. The third chamber contained 10 lung spheroids, followed by the fourth chamber, which contained a vascular organoid composed of HUVECs in a suspension of 4×10^6cells/mL. The fifth chamber contained 10 brain spheroids, and finally, the sixth chamber contained four testicular organoids. In all cases, organoids were photopatterned sequentially, with only one construct exposed to UV at a time.

2.2.5 Experimental Setup:

Following organoid biofabrication, the device was immediately sealed with a prefabricated PMMA lid featuring fixed inlet and outlet ports fitted with PTFE tubing (Corning, Inc., Corning, NY). The inlet tubing of each device was connected to a media reservoir through a metal coupler (Instech, Plymouth, PA), and the outlet tubing was connected through a second coupler to a 2-stop PVC 0.51 mm ID tubing (Cole-Parmer, Vernon Hills, IL). The loop was closed with a third coupler between the reservoir inlet and the free side of the PVC tubing. Media recirculation was achieved through the mounting of the 2-stop braces through a micro-peristaltic pump (MP2 Precision, Elemental Scientific, Inc., Omaha, NE) operating at the rate of 4 μL/min (**Figure 2.1c**). The media reservoir was filled with 1.5 mL of common media formulation, which consisted of testis organoid media and EGM media (with supplements, but without FBS) mixed in a 1:1 ratio by volume. All devices were allowed to stabilize and prime the common media for at least two weeks to establish a baseline interaction between organs. For all systems, three conditions were investigated: Control: with liver, without the drug; Condition 1: with liver, with the drug; Condition 2: without liver, with the drug. For the 6-organoid system, one chip was used as a Control and two more chips each for Conditions 1 & 2, respectively. After 14 days of incubation, the liver organoid chamber was removed from Condition 2 devices by connecting the media reservoir coupler directly to the cardiac inlet. Drug for both Condition 1 and 2 was introduced through media replenishment to the corresponding reservoirs. To ensure both high viability of the constructs and consistent drug concentration, the reservoirs were refreshed with clean common media (with or without drug) every two days. All the systems were sacrificed on day 21 and assessed for overall viability and targeted drug impact.

2.2.6 Preparation of drug stock solutions:

All three drugs, capecitabine (a 5-fluorouracil prodrug), Cyclophosphamide (alkylating chemotherapy prodrug), and ifosfamide (nitrogen mustard containing chemotherapy prodrug) were obtained commercially (Sigma Aldrich, St. Louis, MO). A 10 mM stock solution of capecitabine in DMSO, which was then reconstituted in media to reach 20 μM concentration with 0.2% DMSO. A 1 mM stock solution of Cyclophosphamide and ifosfamide was prepared directly in media.

2.2.7 LIVE/DEAD cell viability:

Cell viability was assessed by LIVE/DEAD (L/D) assay. Briefly, the stain solution was made by preparing 2 μM calcein-AM and 2 μM ethidium homodimer-1 (L/D Viability/Cytotoxicity Kit for mammalian cells, Thermo Fisher, Waltham, MA) in a 1:1 mixture of DMEM and PBS. Each multi-organoid system was flushed with clean PBS before introducing the L/D solution into the channels. The system reservoir of each chip was reconditioned with 500 μL of L/D solution and incubated for 1 hr underflow as above to maximize the diffusion of the fluorescent dyes into the organoids. The channels were flushed again with PBS before *in situ* imaging with an Olympus FluoView™ FV1000 confocal microscope. 5 μm z-stacks of each organoid were obtained using 405 nm (green) and 559 nm (red) fluorescence filters. Images from these channels were then overlaid to produce a maximum projection image with calcein-AM (green fluorescence) indicating live cells and ethidium homodimer (red fluorescence) indicating dead cells. Cell viability of individual spheroids or organoids were quantified using Imaris MeasurementPro software (Bitplane, Concord, MA) as described previously[16] by comparing the total

number of cells in the green channel to the combined total number of cells in both the green and red channel.

2.2.8 Statistical Analysis:

Each experimental condition was investigated at least in duplicate except the control condition due to the limited availability of cells. Viability was calculated as the mean ± the standard deviation between replicates. For hydrogel suspension organoids, the whole construct was analyzed. For spheroid organoids, at least three co-incubated spheroids in each construct were analyzed collectively. The significant differences between the means were determined using Student's t-tests with confidence intervals of 95% or p-value<0.05.

2.3 Results and Discussion

2.3.1 Implementation of a high viability 3-organoid platform with drug assessment

Our group has previously reported on a 3-organoid integrated model with liver, cardiac, and lung, in which each of these tissue models were extensively characterized.[29] This previous system consisted of three independent fluidic devices, each containing a single organoid or tissue construct. These organoids were produced with multiple biofabrication methods and were integrated by connecting the devices via PTFE tubing to establish a closed circulatory perfusion system. One of the drawbacks of this device was its bulkiness, requiring substantial fluid and cell volumes and making it difficult to deploy for high-throughput screening. It also featured a non-physiological media-to-cell ratio (i.e., larger media volume compared to cell volume than the blood-to-tissue volume in humans), which

76

may have pharmacological implications. Finally, the use of PDMS as a fabrication material creates potential obstacles in terms of adsorption of signaling molecules and even drugs.

One of the goals of this study was to develop a low-cost microfluidic device that is both easy to fabricate and faithfully reproduces the complex interactions of drugs within the human body. As a first step, we fabricated the multi-organoid chip by rapid prototyping of adhesive films that were subsequently layered between glass and PMMA substrates to form an enclosed microfluidic device. In our system, we estimate that the surface area of each chamber is composed of ~42.5% PMMA, ~42.5% glass, and only ~15% adhesive film. This becomes advantageous for long-term experiments by reducing the effects of evaporation and non-specific adsorption through the surface of the device itself. Furthermore, the use of glass and PMMA thermoplastic provides high mechanical strength and optical transparency in the visible light range,[40, 41] allowing easy access to direct imaging of the organoids. Glass and PMMA are also less hydrophobic than typical materials like PDMS,[42] and therefore reduce the adsorption of hydrophobic molecules to the interior channels, which can be a significant drawback in PDMS-based devices. A current trend in organ-on-a-chip systems is transitioning towards other thermoplastics like cyclo-olefin (co)polymer (COC/COP),[13] polycarbonate,[26] and polysulfone plastics[31, 43] that are generally computer micromachined or commercially fabricated, thus requiring thermal or solvent-based bonding if not clamped using screws. The AFB device fabrication method allows the microfluidic devices to be produced rapidly, allowing device designs to be iterated quickly and optimized and provides intrinsic bonding via the adhesive films.

The system was designed with simple fluid dynamics to achieve uniform velocity. In addition, the hydrogel matrix shielded fluid flow and reduced the fluid shear stress on the

cells within the organoids. This mitigated any detrimental mechanical force effects while also increasing the time of exposure, interaction, and diffusion of the small volume of media to the organoids for maximum impact. Moreover, the AFB device accommodated a total fluid volume of less than 150 μL (~15 μL per individual chamber) to aid in conditioning the media during recirculation. Tissue volume was calculated to be approximately 17.3 μL, based on the average organoid size. From these values, we determined the tissue-to-liquid volume ratio on-chip to be approximately 1:8.7, rivaling the lowest reported ratio used in any multi-organoid microphysiological system.[44, 45]

The individual chambers of the three-tissue chip contained ECM hydrogel matrices that encapsulated multiple tissue spheroids or cells to emulate the liver, heart, and lung tissues, respectively. We approached our 3D tissue modeling by implementing photopolymerization of the HA-based hydrogel precursor in the device (**Figure 2. 1 b**) as it can be challenging to develop a spatially controlled 3D construct that is fabricated directly into a microfluidic system. We previously reported *in situ* biofabrication method of HA and gelatin hydrogels being photocrosslinked by PEGDA and a photoinitiator, yielding rapid gelation kinetics and improved spatial control over construct formation within the device.[16, 32, 46, 47] Compared to traditionally used collagen, alginate, or Matrigel-based hydrogel scaffolds that rely on relatively slow or uncontrolled crosslinking kinetics, this photopolymerizing hydrogel allows both spheroids and cells to be encapsulated in the desired chambers. This method not only improved the efficiency in biofabricating tissue organoids, but also reproduced several aspects of native ECM and provided thoroughly tested hydrogel properties like cytocompatibility, elastic modulus, and porosity.[18, 32, 48-50]

78

The 3-organoid systems were initially connected to reservoirs with 2000 μL of common organoid media recirculated in a closed loop and used to assess the long-term viability of all cells. Each chamber was sequentially and externally interconnected via PTFE tubing to form an integrated system. The flow of the media into the device was initiated through the liver organoid chamber, followed by the cardiac and lung tissue chambers. The ratios of the functional liver and cardiac spheroids immobilized in each chamber were approximately 50 liver spheroids to approximately 10 cardiac spheroids, thus simulating the 5:1 ratio of liver to heart in terms of mass.[51] Both spheroid types have been validated thoroughly for organ-like functionality through a variety of immunological, metabolic, and drug response assays.[29, 48] The third tissue type was the lung construct fabricated by photocrosslinking the hydrogel precursor with suspended A549 cells at a density to provide approximately the same cellular mass as the liver constructs, thereby simulating the nearly 1:1 ratio of liver to the lung in terms of mass.[52]

The platform was set under continuous perfusion of common organoid media that contained a 1:1 ratio of serum-free endothelial cell media and testicular cell media that flowed through the chambers at 4 μL/min flow rate. Note that the media formulation of the common media (1:1 ratio of serum-free endothelial cell media and testicular cell media) was established based on ongoing parallel studies used to optimize cell culture media for augmented 6-tissue systems (described below). The viability of the organoids in the system was analyzed by L/D assay after 21 days. The maximum projection images acquired by confocal microscopy (**Figure 2.2.a-c**) demonstrated high viability of over 80% for all three organoid types (**Figure 2.3**), showing that cell viability could be maintained in an integrated fashion in our system for extended periods.
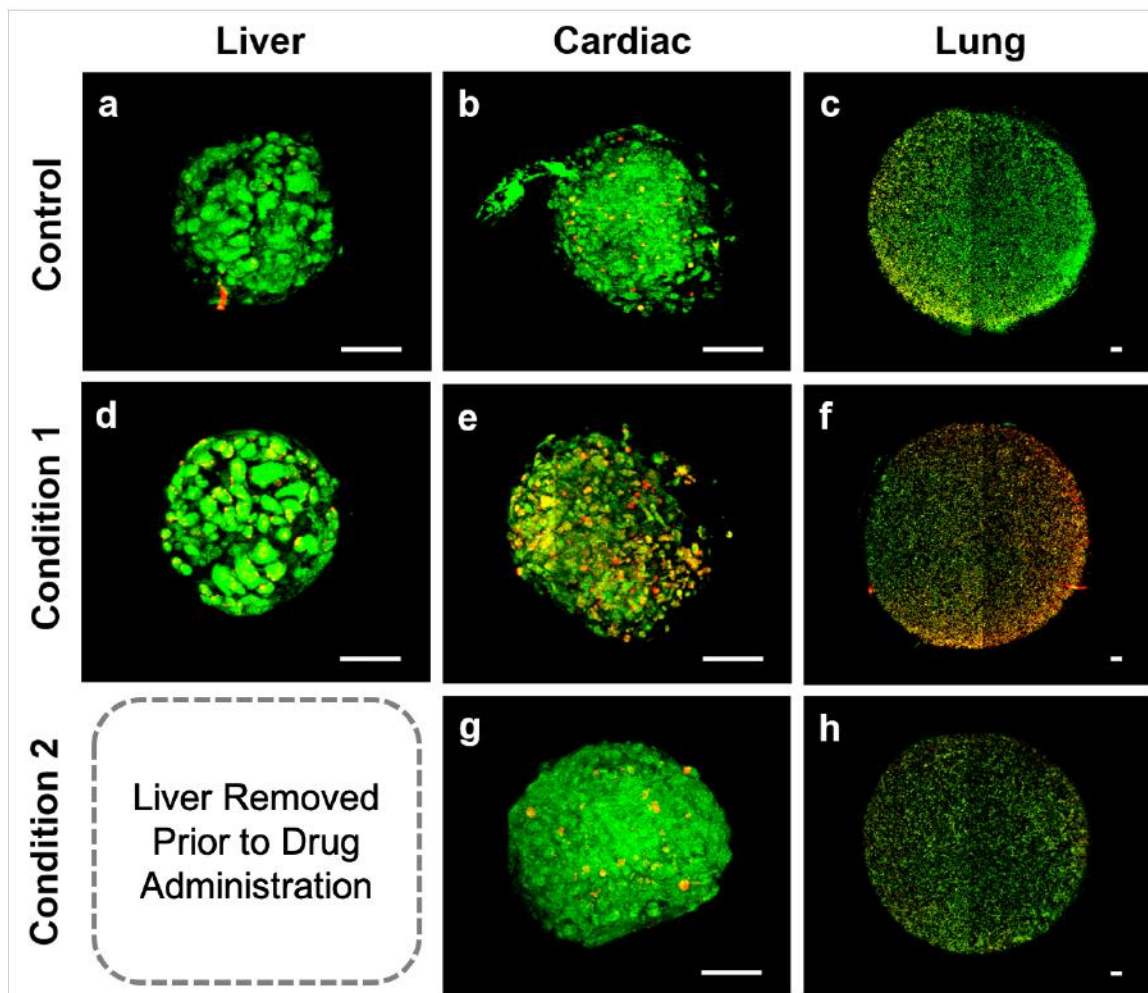
Figure 2.2. Drug toxicity assessment of capecitabine in a 3-organoid system. *L/D imaging of the liver, cardiac, and lung organoids under Control (no drug, a-c), Condition 1 (with capecitabine and liver organoid, d-f), and Condition 2 (with capecitabine and without liver organoid, g-h). In Condition 1, the metabolized drug caused downstream toxicities in cardiac and lung organoids; in Condition 2, no significant toxicity occurred. Green stain: calcein AM-stained viable cells; Red stain: ethidium homodimer 1-stained dead cells. Scale bar represents 100μM.*

Administration of targeted drug compounds can cause a given tissue or organ to secrete cytokines or produce metabolites that have downstream effects on other tissue types. In

one of our previous studies, dependent and independent enzymatic-activation of 5-fluorouracil (5-FU) cardiotoxicity impact was reproduced, where damage to the cardiac organoid was observed exclusively in the presence of a healthy liver organoid.[20] Capecitabine is an oral prodrug that is converted into its active metabolite by a three-step process. The drug is metabolized into 5'-deoxy-S-fluorocytidine (5'-DFCR) by carboxylesterase and then to 5'-deoxy-S-fluorouridine (5'-DFUR) by cytidine deaminase. These two steps take place in the liver, and the enzyme thymidine phosphorylase – which is found in higher levels in liver compared to other tissues – converts it into the active metabolite 5-FU,[53, 54] which is itself commonly used as a chemotherapeutic. Cardiotoxicity has been reported in patients receiving 5-FU treatment, and during the course of such therapies, patients are recommended to monitor for cardiac abnormalities.[55] There have also been reported cases of pulmonary fibrosis developing during 5-FU therapy.[56]

To recapitulate this physiological process, we first allowed the 3-tissue system to be stabilized under the conditioned media for 14 days prior to adding 20 μM drug to the system. This allowed to stabilize the organoids and prime the common media to establish a baseline on all organoids systems. The 3-organoid system was then exposed to capecitabine by infusion into the common media. This concentration was chosen based on previous studies using 5-FU in the context of a different set of liver and tumor organoid models.[57-60] On day 7, after the prodrug was added (day 21 in total), the viability of the individual organoids was assessed by L/D staining and imaged by confocal microscopy. Following capecitabine exposure, we observed a qualitative reduction in cell viability in both the cardiac and the lung organoid (**Figure 2.2.e-f**). Indeed, L/D quantification

revealed a 38.3% decrease in cardiac cell viability and a 37.1% decrease in lung cell viability compared to control conditions (**Figure 2.3**). This cardiac and lung toxicity was consistent with the established capecitabine metabolism pathway [20, 52], suggesting that the prodrug was converted into 5-FU by the liver organoid.

Viability Under Capecitabine Treatment
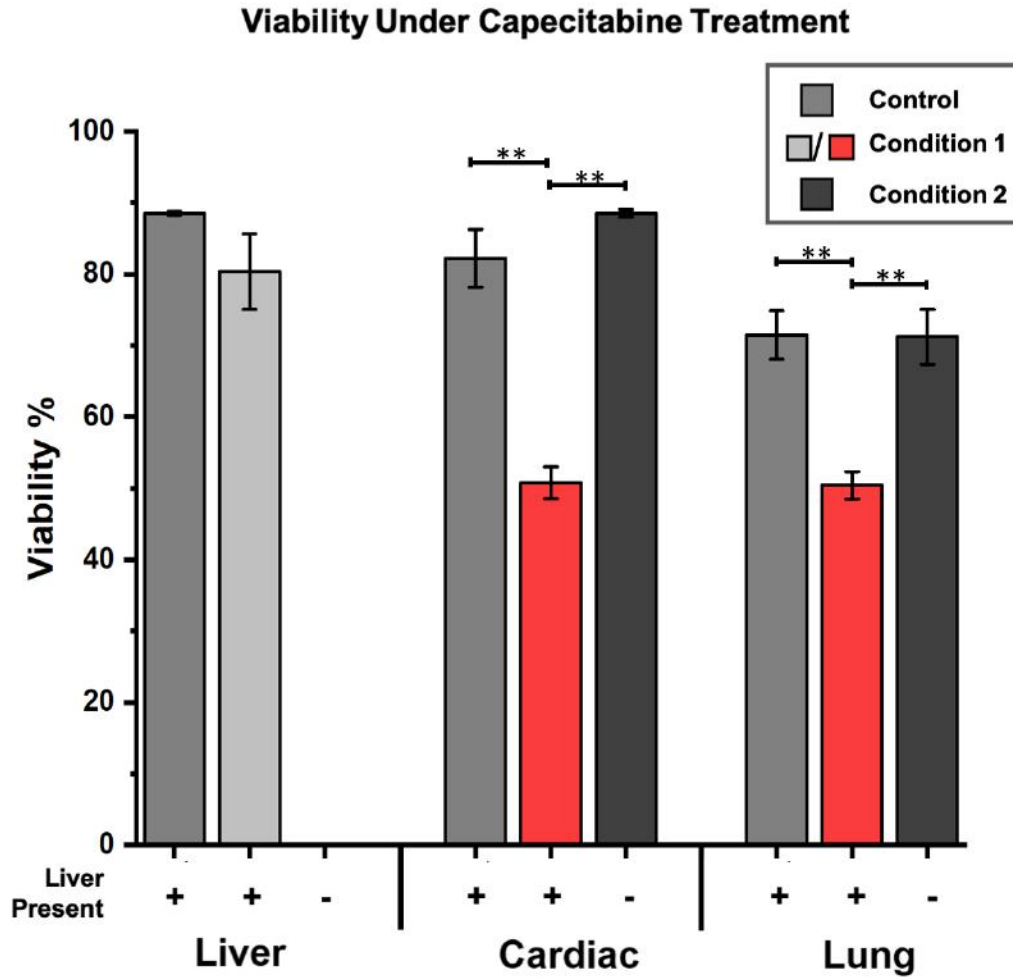
Figure 2.3: Viability quantification under insult by capecitabine in a 3-organoid system.
Quantification of live cell ratios (L/L+D) for liver, cardiac, and lung organoids under
Control (no drug), Condition 1 (a drug with liver organoid), and Condition 2 (drug without

*liver organoid). Reductions in viability are observed for both cardiac and lung organoids under Condition 1 (red). Statistical significance: ** $p < 0.05$.*

To validate that the effects were a result of these integrated tissue interactions, we repeated the experiment but removed the liver organoid from circulation after the 14 days baseline period and before the capecitabine introduction. Without the liver, capecitabine should not be metabolized and converted to the active 5-FU compound, providing a negative control to the study. In this scenario, we hypothesized that there should not be downstream toxicity in the cardiac or lung organoids. We were able to confirm this prediction, finding no significant viability difference in the cardiac or lung organoids compared to control (**Figure 2.2.g-h**), in contrast to observations under the same prodrug conditions with the integrated liver organoid. These data corroborate that the prodrug capecitabine can be metabolized by a liver organoid into the 5-FU *in vitro*, as has been reported.

2.3.2 Implementation of a high viability 6-organoid platform with drug assessment

Following the demonstration of 3-tissue organoid integration, the device was extended to incorporate additional tissue types in a single platform to further enable testing of multi-tissue interactions following drug treatment. To this end, we sought next to integrates six different tissues, including liver, heart, lung, endothelium, brain, and testis. To further miniaturize and improve the media-to-cell ratio, all chambers were internally connected through narrow channels at equidistant positions, except for the liver chamber, which remained connected through external tubing to facilitate rerouting of media flow as in the 3-organoid system above. The revised pattern allowed us to decrease the working volume of media inside the chip itself significantly to less than 200 µL total, an increase of only

33% compared to the 3-organoid device despite doubling the number of organoid chambers. This ultimately improved the tissue-to-liquid volume ratio inside the chip to be 1:4.7. While still significantly different than the physiological 4:1 ratio of tissue:extracellular fluid found in humans[44], this is the most physiological ratio reported to date. This further concentrates the metabolites and cytokines released by each organoid and better conditions the environment, allowing for a more *in vivo*-like integrated system.[26, 51, 61, 62]

The existing three organ system was extended to incorporate even more organoids comprised of primary human cells and iPS-derived cells. Similar to the 3-tissue system, the first three-chamber contained liver spheroids, cardiac spheroids, and A549 3D cell culture construct in a similar quantity as mentioned above. The following chamber contained a vascular construct fabricated as hydrogel encapsulated HUVEC endothelial cells, brain tissue formed by 10 brain organoids, and finally, 4 testis organoids. The organoids are positioned in this order to emulate the *in vivo* blood flow to the organs.[63-65] Note that, like liver and heart above, the brain and testis spheroids have been characterized extensively with immunostaining and molecular assays to show physiological accuracy.[37, 38]

The system stability and robustness were assessed by probing into the long term viability of the organoids in the device under common condition media. The BOC system was fabricated with all six tissue organs and was kept under continuous perfusion of common organoid media for 14 days before assessing for viability using L/D assay. The confocal microscopy images of the organoids with L/D staining (**Figure 2.4**.a-f) demonstrated that most organoids had a viability of over 75% (**Figure 2.5**) except for HUVEC and brain

tissue, which was 52.9±1.7% and 51.3±1.8% respectively as shown in **Figure 2.5**. The lower viability of the HUVEC cell construct compared to other organoids was attributed to the effect of UV light exposure, which was harsh to these cells compared to other organoids. By lowering the exposure time from 2 to 0.25 seconds and providing a few seconds to auto-crosslink, it increased the viability of the HUVEC cells embedded in the hydrogel. The brain spheroid in this system had lower viability as they were not freshly made but instead thawed from a frozen vial and added to the system directly. The brain spheroids were only sustainable for three weeks and had better viability when made prior to setting up the experiment than the frozen and thawed spheroids.

Though the system did not demonstrate the anticipated viability for all the organoids, the system integration was investigated by using a prodrug like cyclophosphamide that causes secondary toxic effects on the cardiac and lung organoids due to the drug metabolites produced in the liver. As the drug had no known direct toxic impact on the HUVEC and brain tissue, the related drug toxicity for these organs were not considered.

Cyclophosphamide is also an anticancer prodrug that is metabolized in the liver into hydroxycyclophosphamide, acrolein, and phosphoramide mustard. Though cyclophosphamide itself is not toxic, the active metabolite induces pulmonary toxicity by peroxidative damage and systemic inflammatory response. This causes an increase in TGF-β and procollagen mRNA and leads to collagen deposition and fibrosis in the lung[66]. There have also been reports of significant cardiac toxicity with higher doses of this drug. This is believed to be caused due to the oxidative stress and endothelial capillary damage that causes toxic metabolites to extravasate[67, 68].
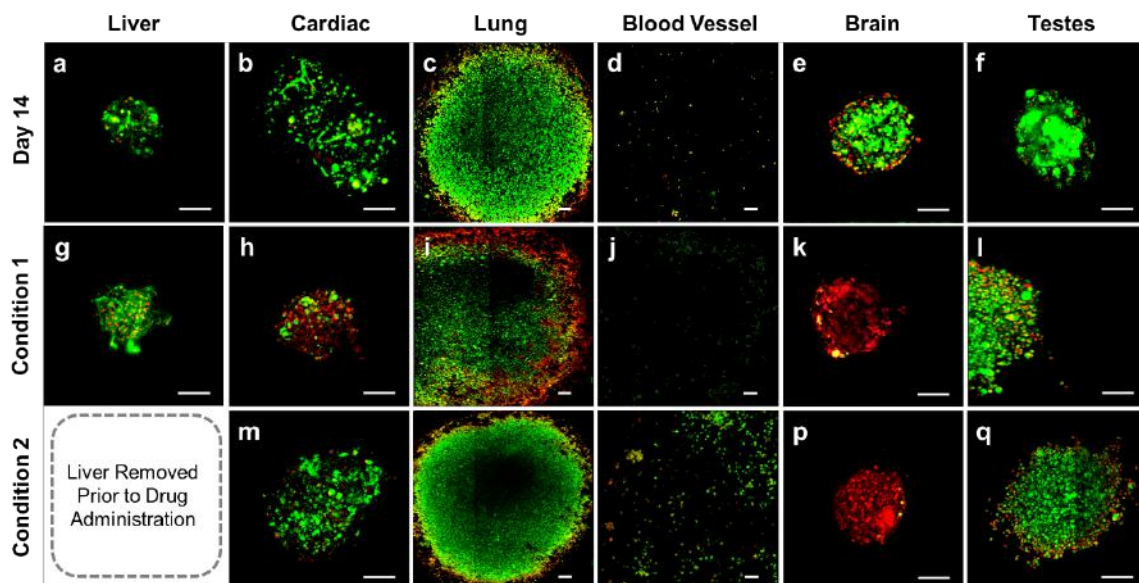
*Figure 2.4. **Drug toxicity assessment of cyclophosphamide in the six-organ system**. Cyclophosphamide is activated by metabolism in Liver organoids that results in downstream toxicities in other organoids. The control L/D assay (a-f) was performed on day 14, before adding the drug to verify the healthy state of the system. In Condition 1 (g-l), the liver module was still present, it can be observed that the metabolized drug causes downstream toxicities in cardiac and lung organoids. Conversely, in Condition 2 (l-q), where the liver was removed as negative control and we could observe no significant toxicity compared to the control. Green stain – calcein AM-stained viable cells; Red stain – ethidium homodimer-stained dead cells. Scale bar represents 100μM.*

Once the integrated organoids were stabilized for 14 days, the system was exposed to anticancer prodrug cyclophosphamide (1mM)[52] as a condition 1 system. On day 21, after 7 days of drug exposure, the viability of the individual organoids was assessed by L/D staining, and it was imaged using confocal microscopy. Following the exposure of cyclophosphamide in the system with the liver, it metabolized to toxic metabolites phosphoramide mustard that induced pulmonary and cardiac toxicity. This was evident by

the increased number of dead cells in the cardiac and lung organoid, as previously reported [52] and shown in **Figure 2.4. h-i** and **Figure 2.5**. The viability of the lung and cardiac tissue decreased to $58.6 \pm 0.02\%$ and $37.9 \pm 8\%$ However, and the brain organoids had very low viability of $27.87 \pm 13.7\%$ compared to the day 14 control of $51.32 \pm 1.8\%$. This is because the brain organoids were not used in the system immediately once the spheroids were formed. The L/D assay performed on day 14 showed that the brain organoid was not highly viable. Hence after a week, the organoids showed even reduced viability by decreasing 45.7%.

For condition 2, a 5-organ system that had cardiac, lung, vascular, brain, and testis without the liver was integrated and baselined for 14 days in common media. This panel is considered to be a negative control, as this drug requires the liver to metabolize and convert it into an active compound that creates toxic side effects. As a result, there is only a non-reactive cyclophosphamide compound present in the system and is expected to produce no downstream toxicity in any of the organoids.

Similar to the 6-organ system, on day 21, the health of the system was evaluated by analyzing the viability of the organoids by L/D staining of live and dead cells in the organoid. The non-reactive cyclophosphamide drug did not cause any downstream toxicity to be cardiac and lung organoid, as observed in condition 1 with liver (**Figure 2.4.m-n** and **Figure 2.5)** and was comparable to day 14 control. In this system, too, the brain organoids were completely dead or expressed very low viability of only $2.34 \pm 0.7\%$ because of similar reasons explained above. It is to be also noted here that the control, unlike the previous experiment, is the chip before adding the drug on day 14. As there were not enough cell

resources to do a control (no drug) out to 21 days, it makes it difficult to draw any firm conclusions.

In this set-up, though the 6-organ system was successful in producing an integrated drug response, it required optimization in organoid formation and maintenance to attain a higher viability system.
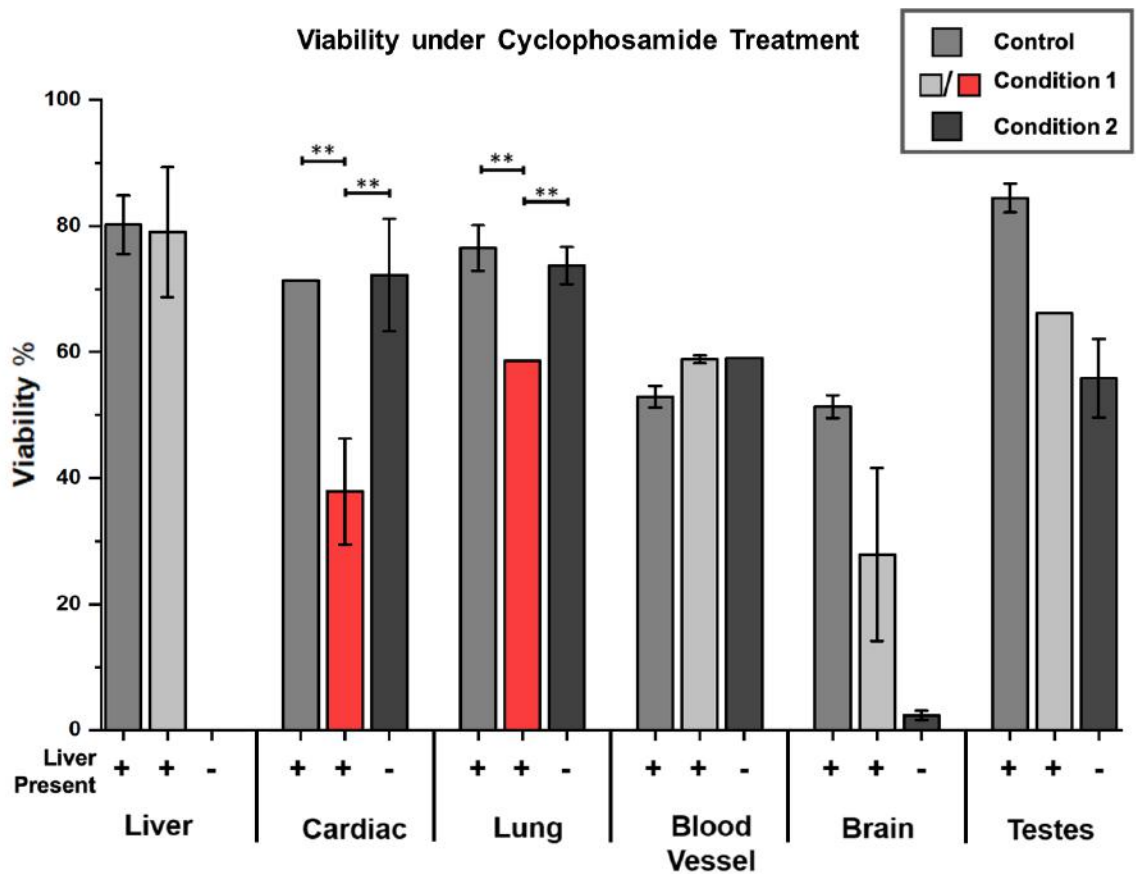
Figure 2.5. **Viability quantification under insult by cyclophosphamide in a 6-organoid system.** *Quantification of live cell ratios (L/L+D) for liver, cardiac, lung, endothelial, brain, and testis organoids under Control (no drug), Condition 1 (a drug with liver organoid), and Condition 2 (drug without liver organoid). A significant reduction in viability is observed for the cardiac and lung organoid under Condition 1 (red). Statistical significance: ** p < 0.05.*

The next step was to overcome the issues from the previous experimental setup and develop a 100% humanized BOC system by fabricating all the six organ tissues with only primary human cells and iPSC derived cells. Hence the lung module fabricated as A549 3D cell culture was replaced by 8 -10 lung spheroids made of primary human cells. To increase the viability of the HUVEC cell construct, the hydrogel precursor was only exposed to a second, and all the spheroids/organoids were made within a week of the experiment initiation. Thus we were able to achieve the maximum viability of all the organoids in the system.

Once the 6-tissue system was assembled, the platform was maintained under continuous perfusion of common organoid media for 21 days before assessing for viability using L/D staining. The maximum projection images of stained organoids were acquired by confocal microscopy (**Figure 2.4.a-f**) and demonstrated >80% viabilit*y* (**Figure 2.5**). Though other multi-tissue platforms have established more extended viability periods, those systems were mostly 2D cell cultures or comprised only of cell lines in 3D.[19, 21, 25] Here, we have demonstrated the viability of multiple human primary cells and iPS cell-based 3D organoids in a common media. ELISA and colorimetric tests conducted on the previous PDMS-based 3-organoid system probed biomarkers like IL-8 and IL-1β and showed that these stress markers only spiked when the platform was subjected to chemical insult.[29] These data, combined with the 3- and 6-organoid systems described herein, suggest that the tissues condition the media through autocrine and paracrine signaling to generate a media that can support the bulk of the system in the same way that blood is capable of supporting the vastly integrated organ system that is the human body.

After establishing a stable baseline for 14 days under common media flow, we again introduced a drug compound: the prodrug ifosfamide, an alkylating antineoplastic agent.[69] Ifosfamide is a structural isomer of cyclophosphamide that has demonstrated efficacy in treating a wide range of tumors.[70-72] To be effective, the prodrug must be biotransformed to an active compound by cytochrome P-450 mixed-function oxidase enzymes that are primarily found in liver hepatocytes.[52, 73, 74] The ring hydroxylation of the drug eventually produces isophosphoramide mustard, which is the primary alkylating compound, along with the toxin acrolein. Hydroxylation also leads to increased alternative pathway metabolism that undergoes chloroethyl side-chain oxidation, resulting in the formation of alkylating metabolites such as chloracetaldehyde, which is known to further contribute to ifosfamide-induced neurotoxicity.[69, 75-77] Indeed, lethal toxicity of ifosfamide toward 3D glial organoids has been reported in another microphysiological system.[77]

To further validate our platform, we aimed to recapitulate this targeted toxicity *in vitro*. Following our 14-day incubation under common media, we introduced ifosfamide to systems either with (Condition 1) or without (Condition 2) the liver organoid in circulation. After 7 days of exposure to 1 mM ifosfamide,[52, 54, 77], we analyzed the viability of the organoids using L/D assays as described above. From the maximum projection images, an apparent reduction in brain organoid viability was observed under Condition 1 (**Figure 2.4k**) even while no such change was observed under Condition 2 (**Figure 2.4p**). Consequently, ifosfamide exhibits significant neurotoxicity in the presence of liver organoids, implying hepatic P-450 metabolic activity and conversion of the drug into the neurotoxin chloracetaldehyde. To quantify cytotoxicity, viability was determined from Z stacks of the L/D signals. **Figure 2.5** shows the viability of all organoids with or without

ifosfamide and/or liver. Indeed, Condition 1 brain organoid viability (48.8%) is substantially less than that of the control system (72.4%), while the Condition 2 viability (72.9%) is not significantly different. No obvious differences were observed in any other organoids relative to their Controls.
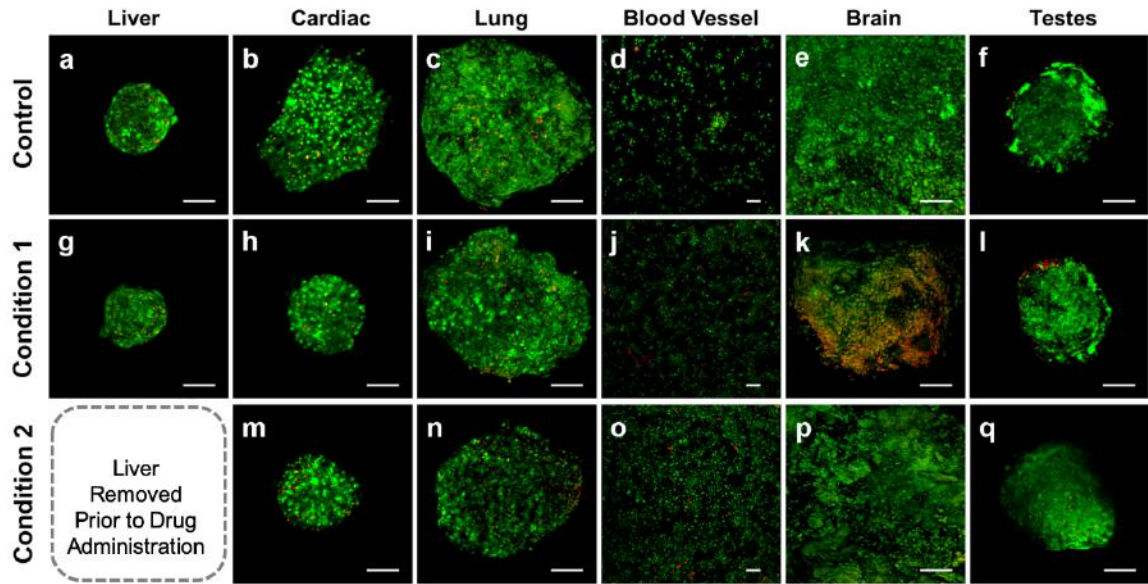
Figure 2. 6. Drug toxicity assessment of ifosfamide in a 6-organoid system. *L/D imaging of the liver, cardiac, lung, endothelial, brain, and testis organoids under Control (no drug, a-c), Condition 1 (with ifosfamide and liver organoid, d-f), and Condition 2 (with ifosfamide and without liver organoid, g-h). In Condition 1, the metabolized drug caused downstream toxicity in the brain organoid; in Condition 2, no significant toxicity occurred. Green stain: calcein AM-stained viable cells; Red stain: ethidium homodimer 1-stained dead cells. Scale bar represents 100μM.*
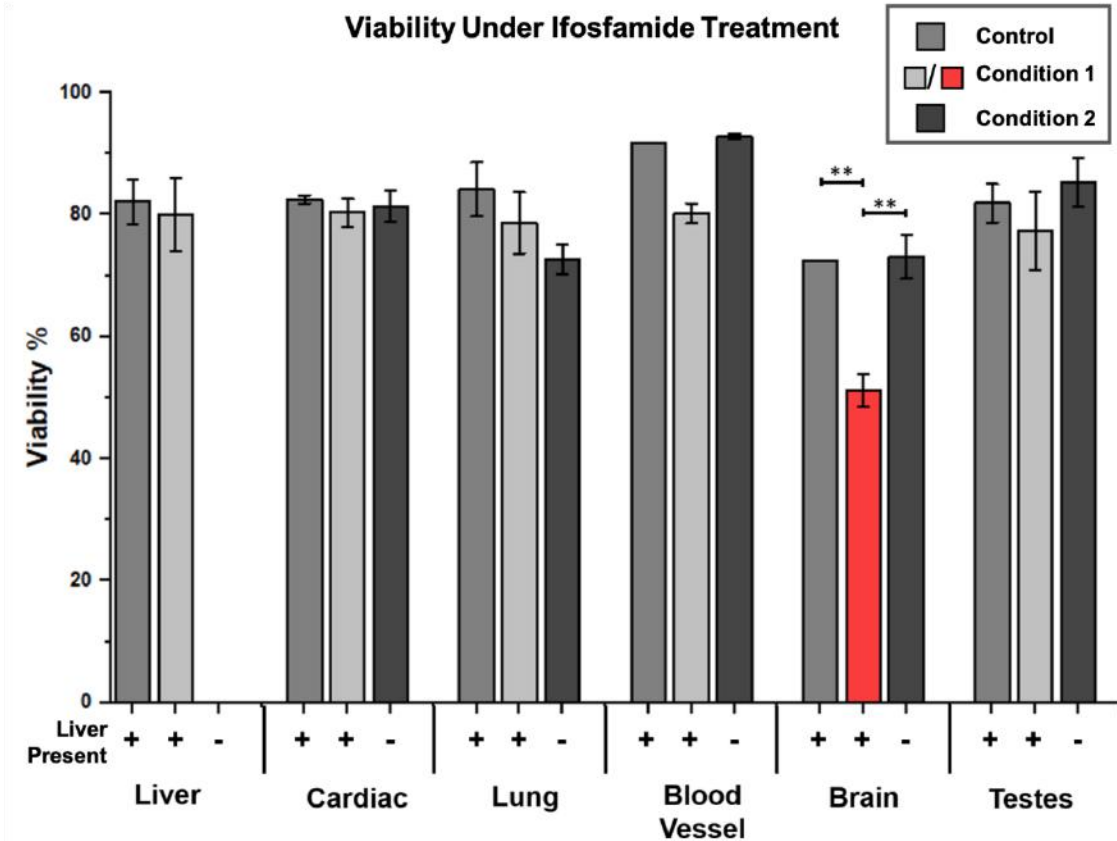
Figure 2.7. Viability quantification under insult by ifosfamide in a 6-organoid system.
*Quantification of live cell ratios (L/L+D) for liver, cardiac, lung, endothelial, brain, and testis organoids under Control (no drug), Condition 1 (a drug with liver organoid), and Condition 2 (drug without liver organoid). A significant reduction in viability is observed for the brain organoid under Condition 1 (red). Statistical significance: ** $p < 0.05$.*

The bioavailability of a drug determines the amount of circulating drug into the body that remains active for an established period of time. In this way, drug efficacy is directly related to bioavailability. The oral bioavailability of ifosfamide has been reported to be between 1.04 and 0.95 for 5.5 hours for patients receiving 1 g/m2 and 2 g/m2 ifosfamide, respectively.[78] Portrayals of bioavailability on-chip have been attempted by dividing the mortality ratio of control to the mortality ratio of a system with disrupted physiology in the

presence of drug,[52] similar to our no-liver condition. We note that more accurate empirical methods of evaluating bioavailability, including mass spectrometry, would increase the quantitative accuracy of our results. However, this approach would be challenging to incorporate with our system given the small fluid volumes used. The mortality ratio method described here, while more speculative in nature, allows an initial consideration of bioavailability in this system. The ratio of mortality in our control system (27.7%) divided by that found in Condition 1 (51.2%) yields an approximate ifosfamide bioavailability of 0.53. However, when the control is divided by the mortality ratio in Condition 2 (27.2%), giving 1.01 for the same time period. These results reinforce the idea that circulating ifosfamide in our system needs liver-associated metabolism to be neurologically toxic; while the Condition 2 systems had the drug in circulation, its efficacy was null as it required enzymatic activity to be damaging to the neural organoid. It should be noted that the cell-staining method using L/D is one of the most common methods for measuring cellular viability and death, but more precise methods for validation of this toxicity could be applied in the future, using assays to measure outcomes such as necrosis or apoptosis through immunostaining, ELISAs, RNA inhibition quantification, and dosage-dependent toxicity. In addition, investigations using metabolomics and proteomics to characterize total system function would be useful to gain a more comprehensive look at these systems, as would genomic assessments to determine whether cells in the system experience genetic drift or phenotypic changes in vitro. However, our approach provides an initial indication of the interactions that occur between organoids on-chip. By replicating well-understood, metabolically-dependent, and targeted toxicity events in our 3- and 6-organoid systems, we have advanced towards a clinically relevant human system.

Lastly, one additional limitation of this platform is the representation of the vascular component. The platform described herein employed encapsulated endothelial cells, not a vascular network. It is possible that given time and additional signals such as growth factor loading, the cells might reorganize into a network, but in this scenario, this did not occur. We acknowledge that this is a limitation of our current system. We included endothelial cells as a representation of vascular biology rather than structure but agree that it could be considered somewhat artificial. Our ultimate goal here was to show examples of integrated drug response where the presence or lack of drug metabolism influences other tissues when drugs are administered. We believe that the inclusion of endothelial cells even without the critical structures they form in vivo served this purpose. That being said, we aim to improve on the structure and function of the vascular component of the platform in ongoing studies.

2.4 Conclusion

The primary goal of this study was to develop a functional and physiologically-relevant multi-tissue organ-on-a-chip system with six integrated tissue types. To this end, we demonstrated the viability of both a 3- and a 6-organoid system, each operating in a common recirculating media for at least 21 days. Once these systems were established, functional drug responses were tested using capecitabine, cyclophosphamide, and ifosfamide, respectively. As hypothesized, the integrated nature of the system was critical: when exposed to these drugs with the liver present, each was metabolized into a product with downstream toxicity in other organoids (cardiac, lung, or brain tissues, depending on the particular drug) while removal of the liver from the system resulted in no significant toxicity response in any tissue type. These results show how a single platform consisting

of combinations of organoids can create a more complex and integrated response where the functionality of one organoid influences the response of others.

In addition, we demonstrate the utility of *in situ* photopatterning tissue constructs inside closed microfluidic devices using a photosensitive ECM-derived hydrogel matrix with a versatility that can be expanded to a variety of applications. For example, the photopatterning technique can be expanded to multi-step spatial patterning of selective zones of particular cells or ECM compositions, creating more complex constructs, an approach we are using in other ongoing research. Furthermore, the chemistry behind the hydrogel components supports the addition of other ECM factors that can deliver a more faithful mimic of native tissue ECM. Along with HA, gelatin, and heparin that are already present, additional ECM components like chemically modified laminin and fibronectin, growth factors, and other cytokines can be included via direct covalent bonding or heparin-modulated binding. The versatility of this biofabrication method is currently being utilized to model healthy and diseased tissues with multi-domain structures thus emulating essential *in vivo* structural and physiological components.

A typical concern with 3D systems in general is whether they perform significantly better than 2D systems. While 2D cell cultures have yielded invaluable data and discoveries, there is a growing body of work demonstrating that in many cases 3D organoids and other models of increased complexity may be a superior technology overall. For example, we have previously reported significant differences in critical aspects like liver functionality [18], accuracy of phenotypes in cancer cell models [60, 79], and drug screening differences [59]. These results are part of a growing body of work demonstrating the advantages of 3D culture compared to 2D. The system can also be extended to develop more complicated

and physiological relevant organs like the lung-on-a-chip system (**Appendix I**). With multi-organoid integration, our system exemplifies a vital capability of *in vitro* drug and toxicology screening and disease modeling. We anticipate that future iterations of this platform and others like it will be important drivers of drug development efforts, allowing for more accurate, human-based drug response data to be collected and ultimately reducing costs and improving the chances of success for novel drug compounds.

Acknowledgments

References

[1] J. Arrowsmith, *Trial watch: phase III and submission failures: 2007-2010.* Nat Rev Drug Discov, 2011. **10**(2): p. 87.

[2] M. Allison, *Clinical setbacks reduce IGF-1 inhibitors to cocktail mixers.* Nat Biotechnol, 2012. **30**(10): p. 906-7.

[3] G.a. Pretorius, *Phase III trial failures: costly, but preventable.* Applied Clinical Trials, 2016. **25**(8).

[4] H.R. Ferdowsian and N. Beck, *Ethical and scientific considerations regarding animal testing and research.* PLoS One, 2011. **6**(9): p. e24059.

[5] K. Duval, H. Grover, L.H. Han, Y. Mou, A.F. Pegoraro, J. Fredberg, and Z. Chen, *Modeling Physiological Events in 2D vs. 3D Cell Culture.* Physiology (Bethesda), 2017. **32**(4): p. 266-277.

[6] D. Huh, G.A. Hamilton, and D.E. Ingber, *From 3D cell culture to organs-on-chips.* Trends Cell Biol, 2011. **21**(12): p. 745-54.

[7] M. Devarasetty, A.R. Mazzocchi, and A. Skardal, *Applications of Bioengineered 3D Tissue and Tumor Organoids in Drug Development and Precision Medicine: Current and Future.* BioDrugs, 2018. **32**(1): p. 53-68.

[8] A. Skardal, T. Shupe, and A. Atala, *Organoid-on-a-chip and body-on-a-chip systems for drug screening and disease modeling.* Drug Discov Today, 2016. **21**(9): p. 1399-1411.

[9] K.H. Benam, S. Dauth, B. Hassell, A. Herland, A. Jain, K.J. Jang, K. Karalis, H.J. Kim, L. MacQueen, R. Mahmoodian, S. Musah, Y.S. Torisawa, A.D. van der Meer, R. Villenave, M. Yadid, K.K. Parker, and D.E. Ingber, *Engineered in vitro disease models.* Annu Rev Pathol, 2015. **10**: p. 195-262.

[10] D. Huh, B.D. Matthews, A. Mammoto, M. Montoya-Zavala, H.Y. Hsin, and D.E. Ingber, *Reconstituting organ-level lung functions on a chip.* Science, 2010. **328**(5986): p. 1662-8.

[11] A. Polini, L. Prodanov, N.S. Bhise, V. Manoharan, M.R. Dokmeci, and A. Khademhosseini, *Organs-on-a-chip: a new tool for drug discovery.* Expert Opin Drug Discov, 2014. **9**(4): p. 335-52.

[12]   N.S. Bhise, J. Ribas, V. Manoharan, Y.S. Zhang, A. Polini, S. Massa, M.R. Dokmeci, and A. Khademhosseini, *Organ-on-a-chip platforms for studying drug delivery systems.* J Control Release, 2014. **190**: p. 82-93.

[13]   J. Theobald, A. Ghanem, P. Wallisch, A.A. Banaeiyan, M.A. Andrade-Navarro, K. Taškova, M. Haltmeier, A. Kurtz, H. Becker, S. Reuter, R. Mrowka, X. Cheng, and S. Wölfl, *Liver-Kidney-on-Chip To Study Toxicity of Drug Metabolites.* ACS Biomaterials Science & Engineering, 2018. **4**(1): p. 78-89.

[14]   Y.S. Zhang, A. Arneri, S. Bersini, S.R. Shin, K. Zhu, Z. Goli-Malekabadi, J. Aleman, C. Colosi, F. Busignani, V. Dell'Erba, C. Bishop, T. Shupe, D. Demarchi, M. Moretti, M. Rasponi, M.R. Dokmeci, A. Atala, and A. Khademhosseini, *Bioprinting 3D microfibrous scaffolds for engineering endothelialized myocardium and heart-on-a-chip.* Biomaterials, 2016. **110**: p. 45-59.

[15]   A. Agarwal, J.A. Goss, A. Cho, M.L. McCain, and K.K. Parker, *Microfluidic heart on a chip for higher throughput pharmacological studies.* Lab Chip, 2013. **13**(18): p. 3599-608.

[16]   A.R. Mazzocchi, S.A.P. Rajan, K.I. Votanopoulos, A.R. Hall, and A. Skardal, *In vitro patient-derived 3D mesothelioma tumor organoids facilitate patient-centric therapeutic screening.* Sci Rep, 2018. **8**(1): p. 2886.

[17]   P. Loskill, S.G. Marcus, A. Mathur, W.M. Reese, and K.E. Healy, *muOrgano: A Lego(R)-Like Plug & Play System for Modular Multi-Organ-Chips.* PLoS One, 2015. **10**(10): p. e0139587.

[18]   A. Skardal, S.V. Murphy, M. Devarasetty, I. Mead, H.W. Kang, Y.J. Seol, Z.Y. S., S.R. Shin, L. Zhao, J. Aleman, A.R. Hall, T. Hartung, A. Khademhosseini, S. Soker, C.E. Bishop, and A. Atala, *Multi-tissue interactions in an integrated three-tissue organ-on-a-chip platform.* Scientific Reports, 2017. **7**: p. 8837.

[19]   C.D. Edington, W.L.K. Chen, E. Geishecker, T. Kassis, L.R. Soenksen, B.M. Bhushan, D. Freake, J. Kirschner, C. Maass, N. Tsamandouras, J. Valdez, C.D. Cook, T. Parent, S. Snyder, J. Yu, E. Suter, M. Shockley, J. Velazquez, J.J. Velazquez, L. Stockdale, J.P. Papps, I. Lee, N. Vann, M. Gamboa, M.E. LaBarge, Z. Zhong, X. Wang, L.A. Boyer, D.A. Lauffenburger, R.L. Carrier, C. Communal, S.R. Tannenbaum, C.L. Stokes, D.J. Hughes, G. Rohatgi, D.L. Trumper, M. Cirit,

[12]   N.S. Bhise, J. Ribas, V. Manoharan, Y.S. Zhang, A. Polini, S. Massa, M.R. Dokmeci, and A. Khademhosseini, *Organ-on-a-chip platforms for studying drug delivery systems.* J Control Release, 2014. **190**: p. 82-93.

[13]   J. Theobald, A. Ghanem, P. Wallisch, A.A. Banaeiyan, M.A. Andrade-Navarro, K. Taškova, M. Haltmeier, A. Kurtz, H. Becker, S. Reuter, R. Mrowka, X. Cheng, and S. Wölfl, *Liver-Kidney-on-Chip To Study Toxicity of Drug Metabolites.* ACS Biomaterials Science & Engineering, 2018. **4**(1): p. 78-89.

[14]   Y.S. Zhang, A. Arneri, S. Bersini, S.R. Shin, K. Zhu, Z. Goli-Malekabadi, J. Aleman, C. Colosi, F. Busignani, V. Dell'Erba, C. Bishop, T. Shupe, D. Demarchi, M. Moretti, M. Rasponi, M.R. Dokmeci, A. Atala, and A. Khademhosseini, *Bioprinting 3D microfibrous scaffolds for engineering endothelialized myocardium and heart-on-a-chip.* Biomaterials, 2016. **110**: p. 45-59.

[15]   A. Agarwal, J.A. Goss, A. Cho, M.L. McCain, and K.K. Parker, *Microfluidic heart on a chip for higher throughput pharmacological studies.* Lab Chip, 2013. **13**(18): p. 3599-608.

[16]   A.R. Mazzocchi, S.A.P. Rajan, K.I. Votanopoulos, A.R. Hall, and A. Skardal, *In vitro patient-derived 3D mesothelioma tumor organoids facilitate patient-centric therapeutic screening.* Sci Rep, 2018. **8**(1): p. 2886.

[17]   P. Loskill, S.G. Marcus, A. Mathur, W.M. Reese, and K.E. Healy, *muOrgano: A Lego(R)-Like Plug & Play System for Modular Multi-Organ-Chips.* PLoS One, 2015. **10**(10): p. e0139587.

[18]   A. Skardal, S.V. Murphy, M. Devarasetty, I. Mead, H.W. Kang, Y.J. Seol, Z.Y. S., S.R. Shin, L. Zhao, J. Aleman, A.R. Hall, T. Hartung, A. Khademhosseini, S. Soker, C.E. Bishop, and A. Atala, *Multi-tissue interactions in an integrated three-tissue organ-on-a-chip platform.* Scientific Reports, 2017. **7**: p. 8837.

[19]   C.D. Edington, W.L.K. Chen, E. Geishecker, T. Kassis, L.R. Soenksen, B.M. Bhushan, D. Freake, J. Kirschner, C. Maass, N. Tsamandouras, J. Valdez, C.D. Cook, T. Parent, S. Snyder, J. Yu, E. Suter, M. Shockley, J. Velazquez, J.J. Velazquez, L. Stockdale, J.P. Papps, I. Lee, N. Vann, M. Gamboa, M.E. LaBarge, Z. Zhong, X. Wang, L.A. Boyer, D.A. Lauffenburger, R.L. Carrier, C. Communal, S.R. Tannenbaum, C.L. Stokes, D.J. Hughes, G. Rohatgi, D.L. Trumper, M. Cirit,

and L.G. Griffith, *Interconnected Microphysiological Systems for Quantitative Biology and Pharmacology Studies.* Sci Rep, 2018. **8**(1): p. 4530.

[20]   Y.S. Zhang, J. Aleman, S.R. Shin, T. Kilic, D. Kim, S.A. Mousavi Shaegh, S. Massa, R. Riahi, S. Chae, N. Hu, H. Avci, W. Zhang, A. Silvestri, A. Sanati Nezhad, A. Manbohi, F. De Ferrari, A. Polini, G. Calzone, N. Shaikh, P. Alerasool, E. Budina, J. Kang, N. Bhise, J. Ribas, A. Pourmand, A. Skardal, T. Shupe, C.E. Bishop, M.R. Dokmeci, A. Atala, and A. Khademhosseini, *Multisensor-integrated organs-on-chips platform for automated and continual in situ monitoring of organoid behaviors.* Proc Natl Acad Sci U S A, 2017. **114**(12): p. E2293-E2302.

[21]   C. Oleaga, C. Bernabini, A.S. Smith, B. Srinivasan, M. Jackson, W. McLamb, V. Platt, R. Bridges, Y. Cai, N. Santhanam, B. Berry, S. Najjar, N. Akanda, X. Guo, C. Martin, G. Ekman, M.B. Esch, J. Langer, G. Ouedraogo, J. Cotovio, L. Breton, M.L. Shuler, and J.J. Hickman, *Multi-Organ toxicity demonstration in a functional human in vitro system composed of four organs.* Sci Rep, 2016. **6**: p. 20030.

[22]   M.L. Shuler, *Organ-, body- and disease-on-a-chip systems.* Lab Chip, 2017. **17**(14): p. 2345-2346.

[23]   J.P. Wikswo, E.L. Curtis, Z.E. Eagleton, B.C. Evans, A. Kole, L.H. Hofmeister, and W.J. Matloff, *Scaling and systems biology for integrating multiple organs-on-a-chip.* Lab Chip, 2013. **13**(18): p. 3496-511.

[24]   M.B.E. Michael L. Shuler *Body-on-a chip: Using microfluidic systems to predict human responses to drugs.* Pure and Applied Chemistry, 2010. **82**(8): p. 1635–1645.

[25]   C. Oleaga, A. Riu, S. Rothemund, A. Lavado, C.W. McAleer, C.J. Long, K. Persaud, N.S. Narasimhan, M. Tran, J. Roles, C.A. Carmona-Moran, T. Sasserath, D.H. Elbrecht, L. Kumanchik, L.R. Bridges, C. Martin, M.T. Schnepper, G. Ekman, M. Jackson, Y.I. Wang, R. Note, J. Langer, S. Teissier, and J.J. Hickman, *Investigation of the effect of hepatic metabolism on off-target cardiotoxicity in a multi-organ human-on-a-chip system.* Biomaterials, 2018. **182**: p. 176-190.

[26]   P.G. Miller and M.L. Shuler, *Design and demonstration of a pumpless 14 compartment microphysiological system.* Biotechnol Bioeng, 2016. **113**(10): p. 2213-27.

[27]   A.G. Jannick Theobald, Patrick Wallisch, Amin A. Banaeiyan, Miguel A. Andrade-Navarro, Katerina Taškova, Manuela Haltmeier, Andreas Kurtz, Holger Becker, Stefanie Reuter, Ralf Mrowka, Xinlai Cheng, and Stefan Wölfl, *Liver-Kidney-on-Chip To Study Toxicity of Drug Metabolites.* ACS Biomaterials Science & Engineering, 2018. **4**(1): p. 78-89.

[28]   O. Frey, P.M. Misun, D.A. Fluri, J.G. Hengstler, and A. Hierlemann, *Reconfigurable microfluidic hanging drop network for multi-tissue interaction and analysis.* Nat Commun, 2014. **5**: p. 4250.

[29]   A. Skardal, S.V. Murphy, M. Devarasetty, I. Mead, H.W. Kang, Y.J. Seol, Y. Shrike Zhang, S.R. Shin, L. Zhao, J. Aleman, A.R. Hall, T.D. Shupe, A. Kleensang, M.R. Dokmeci, S. Jin Lee, J.D. Jackson, J.J. Yoo, T. Hartung, A. Khademhosseini, S. Soker, C.E. Bishop, and A. Atala, *Multi-tissue interactions in an integrated three-tissue organ-on-a-chip platform.* Sci Rep, 2017. **7**(1): p. 8837.

[30]   J.H. Sung, Y.I. Wang, N. Narasimhan Sriram, M. Jackson, C. Long, J.J. Hickman, and M.L. Shuler, *Recent Advances in Body-on-a-Chip Systems.* Anal Chem, 2019. **91**(1): p. 330-351.

[31]   W.L.K. Chen, C. Edington, E. Suter, J. Yu, J.J. Velazquez, J.G. Velazquez, M. Shockley, E.M. Large, R. Venkataramanan, D.J. Hughes, C.L. Stokes, D.L. Trumper, R.L. Carrier, M. Cirit, L.G. Griffith, and D.A. Lauffenburger, *Integrated gut/liver microphysiological systems elucidates inflammatory inter-tissue crosstalk.* Biotechnol Bioeng, 2017. **114**(11): p. 2648-2659.

[32]   J. Aleman and A. Skardal, *A multi-site metastasis-on-a-chip microphysiological system for assessing metastatic preference of cancer cells.* Biotechnol Bioeng, 2018.

[33]   P.M. van Midwoud, A. Janse, M.T. Merema, G.M. Groothuis, and E. Verpoorte, *Comparison of biocompatibility and adsorption properties of different plastics for advanced microfluidic cell and tissue culture models.* Anal Chem, 2012. **84**(9): p. 3938-44.

[34]   N.P. Zarandi, G. Galdon, S. Kogan, A. Atala, and H. Sadri-Ardekani, *Cryostorage of immature and mature human testis tissue to preserve spermatogonial stem cells*

(SSCs): a systematic review of current experiences toward clinical applications. Stem Cells Cloning, 2018. **11**: p. 23-38.

[35] H. Sadri-Ardekani, M.A. Akhondi, F. van der Veen, S. Repping, and A.M. van Pelt, *In vitro propagation of human prepubertal spermatogonial stem cells.* JAMA, 2011. **305**(23): p. 2416-8.

[36] H. Sadri-Ardekani, S.C. Mizrak, S.K. van Daalen, C.M. Korver, H.L. Roepers-Gajadien, M. Koruji, S. Hovingh, T.M. de Reijke, J.J. de la Rosette, F. van der Veen, D.G. de Rooij, S. Repping, and A.M. van Pelt, *Propagation of human spermatogonial stem cells in vitro.* JAMA, 2009. **302**(19): p. 2127-34.

[37] S.S. Pendergraft, H. Sadri-Ardekani, A. Atala, and C.E. Bishop, *Three-dimensional testicular organoid: a novel tool for the study of human spermatogenesis and gonadotoxicity in vitro.* Biol Reprod, 2017. **96**(3): p. 720-732.

[38] G. Nzou, R.T. Wicks, E.E. Wicks, S.A. Seale, C.H. Sane, A. Chen, S.V. Murphy, J.D. Jackson, and A.J. Atala, *Human Cortex Spheroid with a Functional Blood Brain Barrier for High-Throughput Neurotoxicity Screening and Disease Modeling.* Sci Rep, 2018. **8**(1): p. 7413.

[39] A. Skardal, L. Smith, S. Bharadwaj, A. Atala, S. Soker, and Y. Zhang, *Tissue specific synthetic ECM hydrogels for 3-D in vitro maintenance of hepatocyte function.* Biomaterials, 2012. **33**(18): p. 4565-75.

[40] H. Becker and U. Heim, *Hot embossing as a method for the fabrication of polymer high aspect ratio structures.* Sensors and Actuators A: Physical, 2000. **83**(1): p. 130-135.

[41] C.-W. Tsao, D.L.J.M. DeVoe, and Nanofluidics, *Bonding of thermoplastic polymer microfluidics.* 2009. **6**(1): p. 1-16.

[42] K.S. Yun and E. Yoon, *Fabrication of complex multilevel microchannels in PDMS by using three-dimensional photoresist masters.* Lab Chip, 2008. **8**(2): p. 245-50.

[43] N. Tsamandouras, W.L.K. Chen, C.D. Edington, C.L. Stokes, L.G. Griffith, and M. Cirit, *Integrated Gut and Liver Microphysiological Systems for Quantitative In Vitro Pharmacokinetic Studies.* AAPS J, 2017. **19**(5): p. 1499-1512.

[44] E.M. Materne, I. Maschmeyer, A.K. Lorenz, R. Horland, K.M. Schimek, M. Busek, F. Sonntag, R. Lauster, and U. Marx, *The multi-organ chip--a microfluidic platform for long-term multi-tissue coculture.* J Vis Exp, 2015(98): p. e52526.

[45] E.M. Materne, A.G. Tonevitsky, and U. Marx, *Chip-based liver equivalents for toxicity testing--organotypicalness versus cost-efficient high throughput.* Lab Chip, 2013. **13**(18): p. 3481-95.

[46] A. Skardal, M. Devarasetty, S. Soker, and A.R. Hall, *In situ patterned micro 3D liver constructs for parallel toxicology testing in a fluidic device.* Biofabrication, 2015. **7**(3): p. 031001.

[47] J. Aleman, S.K. George, S. Herberg, M. Devarasetty, C.D. Porada, A. Skardal, and G. Almeida-Porada, *Deconstructed Microfluidic Bone Marrow On-A-Chip to Study Normal and Malignant Hemopoietic Cell-Niche Interactions.* Small, 2019. **15**(43): p. e1902971.

[48] S.D. Forsythe, M. Devarasetty, T.D. Shupe, C.E. Bishop, A. Atala, S. Soker, and A. Skardal, *Environmental toxin screening using human-derived 3D bioengineered liver and cardiac organoids.* Frontiers in Public Health, 2018. ***In press.***

[49] A. Skardal, S.V. Murphy, K. Crowell, D. Mack, A. Atala, and S. Soker, *A tunable hydrogel system for long-term release of cell-secreted cytokines and bioprinted in situ wound cell delivery.* J Biomed Mater Res B Appl Biomater, 2016.

[50] A. Skardal, J. Zhang, and G.D. Prestwich, *Bioprinting vessel-like constructs using hyaluronan hydrogels crosslinked with tetrahedral polyethylene glycol tetracrylates.* Biomaterials, 2010. **31**(24): p. 6173-81.

[51] T. Takebe, B. Zhang, and M. Radisic, *Synergistic Engineering: Organoids Meet Organs-on-a-Chip.* Cell Stem Cell, 2017. **21**(3): p. 297-300.

[52] H. Kimura, T. Ikeda, H. Nakayama, Y. Sakai, and T. Fujii, *An on-chip small intestine-liver model for pharmacokinetic studies.* J Lab Autom, 2015. **20**(3): p. 265-73.

[53] C.M. Walko and C. Lindley, *Capecitabine: a review.* Clin Ther, 2005. **27**(1): p. 23-44.

[54] C.G. Yang, Y.F. Wu, Z.R. Xu, and J.H. Wang, *A radial microfluidic concentration gradient generator with high-density channels for cell apoptosis assay.* Lab Chip, 2011. **11**(19): p. 3305-12.

[55] J.D. Sara, J. Kaur, R. Khodadadi, M. Rehman, R. Lobo, S. Chakrabarti, J. Herrmann, A. Lerman, and A. Grothey, *5-fluorouracil and cardiotoxicity: a review.* Ther Adv Med Oncol, 2018. **10**: p. 1758835918780140.

[56] A.K. Chan, B.A. Choo, and J. Glaholm, *Pulmonary toxicity with oxaliplatin and capecitabine/5-Fluorouracil chemotherapy: a case report and review of the literature.* Onkologie, 2011. **34**(8-9): p. 443-6.

[57] M. Devarasetty, A. Skardal, K. Cowdrick, F. Marini, and S. Soker, *Bioengineered Submucosal Organoids for In Vitro Modeling of Colorectal Cancer.* Tissue Eng Part A, 2017. **23**(19-20): p. 1026-1041.

[58] M. Devarasetty, E. Wang, S. Soker, and A. Skardal, *Mesenchymal stem cells support growth and organization of host-liver colorectal-tumor organoids and possibly resistance to chemotherapy.* Biofabrication, 2017. **9**(2): p. 021002.

[59] S. Forsythe, N. Mehta, M. Devarasetty, H. Sivakumar, W. Gmeiner, S. Soker, K. Votanopoulos, and A. Skardal, *Development of a Colorectal Cancer 3D Micro-tumor Construct Platform From Cell Lines and Patient Tumor Biospecimens for Standard-of-Care and Experimental Drug Screening.* Ann Biomed Eng, 2019.

[60] A. Skardal, M. Devarasetty, C. Rodman, A. Atala, and S. Soker, *Liver-Tumor Hybrid Organoids for Modeling Tumor Growth and Drug Response In Vitro.* Ann Biomed Eng, 2015. **43**(10): p. 2361-73.

[61] J.H. Sung, M.B. Esch, J.M. Prot, C.J. Long, A. Smith, J.J. Hickman, and M.L. Shuler, *Microfabricated mammalian organ systems and their integration into models of whole animals and humans.* Lab Chip, 2013. **13**(7): p. 1201-12.

[62] I. Wagner, E.M. Materne, S. Brincker, U. Sussbier, C. Fradrich, M. Busek, F. Sonntag, D.A. Sakharov, E.V. Trushkin, A.G. Tonevitsky, R. Lauster, and U. Marx, *A dynamic multi-organ-chip for long-term cultivation and substance testing proven by 3D human liver and skin tissue co-culture.* Lab Chip, 2013. **13**(18): p. 3538-47.

[63] S.N. Bhatia and D.E. Ingber, *Microfluidic organs-on-chips.* Nat Biotechnol, 2014. **32**(8): p. 760-72.

[64]   J.H. Sung, B. Srinivasan, M.B. Esch, W.T. McLamb, C. Bernabini, M.L. Shuler, and J.J. Hickman, *Using physiologically-based pharmacokinetic-guided "body-on-a-chip" systems to predict mammalian response to drug and chemical exposure.* Exp Biol Med (Maywood), 2014. **239**(9): p. 1225-39.

[65]   S.H. Lee and J.H. Sung, *Microtechnology-Based Multi-Organ Models.* Bioengineering (Basel), 2017. **4**(2).

[66]   K.Y. Yoneda and C.E. Cross, *The Pulmonary Toxicity of Anticancer Agents*, in *Comprehensive Toxicology*. 2010. p. 477-510.

[67]   S. Dhesi, M.P. Chu, G. Blevins, I. Paterson, L. Larratt, G.Y. Oudit, and D.H. Kim, *Cyclophosphamide-Induced Cardiomyopathy: A Case Report, Review, and Recommendations for Management.* J Investig Med High Impact Case Rep, 2013. **1**(1): p. 2324709613480346.

[68]   M.A. Goldberg, J.H. Antin, E.C. Guinan, and J.M. Rappeport, *Cyclophosphamide cardiotoxicity: an analysis of dosing as a risk factor.* Blood, 1986. **68**(5): p. 1114-8.

[69]   K.L. Dechant, R.N. Brogden, T. Pilkington, and D. Faulds, *Ifosfamide/mesna. A review of its antineoplastic activity, pharmacokinetic properties and therapeutic efficacy in cancer.* Drugs, 1991. **42**(3): p. 428-67.

[70]   M. Zalupski and L.H. Baker, *Ifosfamide.* J Natl Cancer Inst, 1988. **80**(8): p. 556-66.

[71]   M. Furlanut and L. Franceschi, *Pharmacology of ifosfamide.* Oncology, 2003. **65 Suppl 2**: p. 2-6.

[72]   R.B. Weiss, *Ifosfamide vs cyclophosphamide in cancer therapy.* Oncology (Williston Park), 1991. **5**(5): p. 67-76; discussion 76-82, 84-6.

[73]   L. Choucha-Snouber, C. Aninat, L. Grsicom, G. Madalinski, C. Brochot, P.E. Poleni, F. Razan, C.G. Guillouzo, C. Legallais, A. Corlu, and E. Leclerc, *Investigation of ifosfamide nephrotoxicity induced in a liver-kidney co-culture biochip.* Biotechnol Bioeng, 2013. **110**(2): p. 597-608.

[74]   R. Polimanti, S. Piacentini, D. Manfellotto, and M. Fuciarelli, *Human genetic variation of CYP450 superfamily: analysis of functional diversity in worldwide populations.* Pharmacogenomics, 2012. **13**(16): p. 1951-60.

[75] P. Nicolao and B. Giometto, *Neurological toxicity of ifosfamide.* Oncology, 2003. **65 Suppl 2**: p. 11-6.

[76] M.H. Cohen, P.J. Creaven, F. Tejada, H.H. Hansen, F. Muggia, A. Mittelman, and O.S. Selawry, *Phase I clinical trial of isophosphamide (NSC-109724).* Cancer Chemother Rep, 1975. **59**(4): p. 751-5.

[77] L. Ma, J. Barker, C. Zhou, W. Li, J. Zhang, B. Lin, G. Foltz, J. Kublbeck, and P. Honkakoski, *Towards personalized medicine with a three-dimensional micro-scale perfusion-based two-chamber tissue model system.* Biomaterials, 2012. **33**(17): p. 4353-61.

[78] T. Wagner and P. Drings, *Pharmacokinetics and bioavailability of oral ifosfamide.* Arzneimittelforschung, 1986. **36**(5): p. 878-80.

[79] A. Skardal, M. Devarasetty, S. Forsythe, A. Atala, S. Soker, A reductionist metastasis-on-a-chip platform for in vitro tumor progression modeling and drug screening, Biotechnol Bioeng 113(9) (2016) 2020-32.

CHAPTER 3

Developing an in vitro model of patient-derived 3D tumor organoids and integrate with microfluidics to facilitate patient-centric therapeutic screening

Though cancer research has been carried on for over a century, there is no complete cure for the disease. This is attributed to the unique nature of cancer, where the individual tumor is not comparable with others, despite having a similar origin or tumor type. But in traditional treatment planning, a particular cancer type is treated in a similar fashion. This 'one-size-fits-all' approach does not produce uniform therapy outcomes for all patients. This variability in treatment response is associated with the heterogeneity of the tumor microenvironment. Precision medicine is one step in the right direction, where the treatment strategies are based on the targeted drug for the specific mutation. But this mutation doesn't necessarily mean that the tumor will be sensitive to the targeted drug. Hence the ideal solution is to develop personalized tumor models from patients' own tumor cells and use it as a drug testing platform to identify the optimal treatment candidate.

In this chapter, an *in vitro* patient-derived tumor organoids were developed and validated for drug response and mechanism of apoptosis. The established tumor organoid was then integrated with the adhesive film-based microfluidic platform by *in situ* photopatterning the tumor organoid directly on to the chip. In Chapter 2, we developed the AFB microfluidic architecture that was validated for 3D cell culture viability by sustaining multiple primary healthy cells for long term and drug testing capabilities. This microfluidic platform was utilized to develop a disease model like cancer here and test drugs in a dynamic environment to produce *in vivo* like drug response comparable to the patient itself. This system can be extended to incorporate immune-cancer cell interaction, design

complex multi-layered tumor microenvironment, or model metastatic microenvironment to realize the capabilities of the microfluidic platform fully. Also, the tumor organoid can be integrated with the body-on-a-chip system developed in Chapter 2 to simulate the organ interaction for testing pharmacodynamics of the chemotherapeutic drugs. In conclusion, we have developed a personalized disease model of cancer in the AFB microfluidic system that can be expanded to replicate the complexity of the cancer microenvironment.

Note:

The contents of this chapter have been published as a peer-reviewed article.

Peer-reviewed Publication:

'In vitro, patient-derived 3D mesothelioma tumor organoids facilitate patient-centric therapeutic', Andrea R. Mazzocchi, **Shiny A. Rajan,** *Konstantinos I. Votanopoulos, Adam R. Hall, Aleksander Skardal. Scientific Reports (2018).*

Abstract:

Variability in patient response to anti-cancer drugs is currently addressed by relating genetic mutations to chemotherapy through precision medicine. However, the practical benefits of precision medicine to therapy design are less clear. Even after the identification of mutations, oncologists are often left with several drug options, and for some patients, there is no definitive treatment solution. There is a need for model systems to help predict personalized responses to chemotherapeutics. We have microengineered an *in vitro* 3D tumor organoids directly from fresh tumor biopsies to provide patient-specific models with which treatment optimization can be performed before initiation of therapy. We demonstrate the initial implementation of this platform using tumor biospecimens surgically removed from eight head and neck squamous cell carcinoma (HNSCC) patients and two mesothelioma patients. First, we show using HNSCC patient-derived organoids (PDO) our ability to biofabricated an *in vitro* system that is superior and consistent to commonly used sponge gel-supported histoculture or sponge assay method for chemosensitivity correlations in patients. Second, we validate the β-Lapachone-mediated cytotoxicity on the PDO by co-administrating dicoumarol (an NQO1 inhibitor), as NQO1 expression is correlated with β-lap sensitivity. We also verified the maximum inhibition effect by dicoumarol on β-lap by testing it on the HNSCC cell line (SCC-61 and rSCC-61) based tumor organoid. Third, we integrate the established disease model with microfluidics by *in situ* photopatterning of 3D tumor constructs and demonstrate our ability to maintain viability within a tumor-on-a-chip microfluidic device. Finally, we validated the results of on-chip chemotherapy screening with those observed in subjects themselves. This patient-

derived tumor organoid strategy is adaptable to a wide variety of cancers and may provide

a framework with which to improve efforts in precision medicine oncology.

3.1 Introduction

Resistance to anti-cancer drugs is one of the most critical challenges in clinical oncology. The roots of resistance are most often ascribed to tumor heterogeneity, genetic mutation, oncogenic amplification, and changes in protein expression that influence the uptake, metabolism, and removal of drugs from the cell. As a result, resistance can arise dynamically during treatment and has been observed with every major anti-cancer agent. Chemotherapy decisions traditionally have been made based on the statistical success rate of a drug for clinical patient populations, but not on how that drug affects the tumor of a specific patient. Precision or personalized medicine (PM) has emerged as a response to these challenges. Here, a tumor biopsy is profiled genetically to identify mutations that may indicate drugable targets [1-3]. Subsequently, if FDA-approved drugs or ongoing clinical trials are identified that address one of these targets, the therapy for that patient can be adjusted accordingly (**Figure 3.1**, red arrows). However, the non-monolithic nature of tumors and the sheer complexity of the various factors that can be at play individually or in unison in the patient have made such data-driven prognostication both daunting and varying ineffectiveness. In practice, the benefits of precision medicine are still ambiguous[4]. Even after the identification of targeted mutations, oncologists are left with several drug options and with no way to predict if a particular treatment will be more beneficial to the patient than another. As such, even in cases where "actionable" mutations are identified, modification of a predetermined fixed treatment strategy is rare, given the unknown impact of that mutation on tumor biology and the equally unknown effect of chemotherapy options on a specific cellular phenotype.
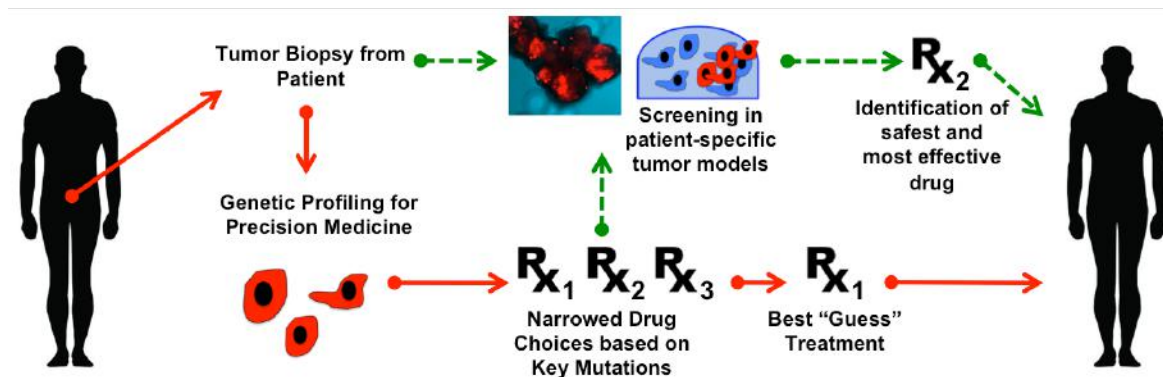
Figure 3.1. Patient-derived models for personalized precision medicine. The concept of using engineered 3D in vitro models to better inform precision medicine treatment regimens on a patient-by-patient basis. Red arrows: The current state of the art precision medicine pipeline, in which treatments are identified for patients based on their tumor genetic profiles. In practice, even after the identification of key mutations, oncologists are often left with several potential drug options, resulting in the best guess of the optimal treatment. Green arrows: Implementation of organoids created with patient cells can supplement genetic screens of biopsied tumor cells, ultimately predicting the optimal therapies for patients.

As a potential improvement (**Figure 3.1**, green arrows), the same biospecimen could also be employed for screening of multiple candidate drug agents to determine effectiveness *in vitro* by developing a patient-specific tumor model. Consequently, there is a tremendous need for accurate model systems to help predict response to anti-cancer drugs in individual patients [5, 6]. However, tumor models have been limited by an inability to accurately replicate both progression and signaling mechanisms of cancer in a controlled environment. Animal models allow limited manipulation and study of these mechanisms but are not necessarily predictive of results in humans[7]. Meanwhile, traditional *in vitro*

2D cell culture fails to recapitulate the 3D microenvironment of *in vivo* tissues[8]; in these planar systems, drug diffusion kinetics vary dramatically, and cell-cell/cell-matrix interactions are inaccurate. Moreover, drug doses found to be effective in 2D cultures are frequently ineffective when applied to patients[9, 10]. 3D cell culture has been shown to better reproduce *in vivo* effects, and as a result, are more accurate systems for *in vitro* cancer modeling. For example, we recently demonstrated that metastatic colorectal cancer (CRC) cells appear epithelial in conventional 2D tissue culture dishes, but take on the expected mesenchymal and metastatic phenotype when transitioned into a 3D liver organoid environment[11]. Specifically, patient-derived tumor culture assays have the potential to mimic *in vivo* like drug sensitivity as their microenvironment and the heterogeneity are maintained. For example, considering all the established preclinical models in Head and neck squamous cell carcinom[12], it was demonstrated that the sponge gel-supported histoculture or sponge assay had the most successful culture rates and best clinical correlations for histoculture drug response assay (HDRA)[13] . Sponge assay was initially developed in an effort to accurately represent the patient's tumor[14] as the technique preserves the native 3D histological architecture by using tumor fragments itself. This assay allows to co-culture of the heterogeneous mixture of all cells, tumor and stromal cells, resulting in a clinically relevant and comparable in vitro model for chemosensitivity correlation of 90% approximately[13]. But the drug response result of this assay have often had wide variability and has no standardization of the samples except by weight normalization. Hence it is important to develop an organoid model that can be more controlled and standardized to capture accurate drug response.

Additionally, integration of bioengineering[15, 16] with microfluidics has further resulted in organ-on-a-chip technologies for accurate and addressable testing of compact 3D organoids in parallel. These platforms can combine a variety of essential parameters that permit better mimicry of *in vivo* conditions, including 3D architecture, cell-cell/cell-matrix interactions, circulation, and integration of multiple tissues within one platform, and have been used for drug testing[17], toxicology[18], high throughput screens, and disease modeling[19]. However, to date, because primary tumor cells have been challenging to maintain *in vitro*, such technologies have not been widely applied to patient cells, where the resulting analyses could be used to supplement genetic screens or ultimately allow robust prediction of optimal therapies.

Here, we present a report of drug screening with 3D organoids incorporating patient-derived tumor cells. For this, we utilize a 3D extracellular matrix-inspired hydrogel system [20-25] that supports a biofabrication procedure that can be integrated with a microfluidic delivery system. This general approach has been applied previously to yield a broad collection of organoids that model the structure and function of *in vivo* tissues and serve as hosts for tumor constructs[11, 18, 21, 26-29]. First, using cells derived from HNSCC tumors from 8 patients, we demonstrate the formation of 3D tumor organoids of high cellular viability and then perform a series of drug exposures, including β-Lapachone. The drug response results of the patient-derived organoid were then compared to the results from sponge histoculture assay performed on the same patient tumor. The drug response of β-lap-mediated cytotoxicity was validated by co-administrating dicoumarol, a specific inhibitor of NQO1, as there has been a known correlation between NQO1 and cell apoptosis by β-lap in various cancers [30-33]. Also, the maximum inhibition effect of dicoumarol on β-lap

sensitivity was verified on the HNSCC cell line (SCC-61 and rSCC-61) based tumor organoid and compared with the drug response of the PDO. Finally, after validating and establishing a physiologically relevant personalized tumor model, we integrated the microfluidic system to *in situ* fabricate organoids of mesothelioma tumor biospecimens from two patients and demonstrated the organoid viability and ability to recapitulate patient drug response to chemotherapy. These results demonstrate the efficacy of integrated, personalized tumor organoids for chemotherapy drug screening and suggest the potential of the system to help optimize treatments for cancer patients.

3.2 Materials and Methods

3.2.1 Tumor biospecimen procurement and cell processing

As described, human patient tumor biospecimens (both head and neck tumor and mesothelioma) were acquired for the study and handled according to a Wake Forest Baptist Medical Center Institutional Review Board-approved protocol. Under this protocol, subjects give informed consent for resected tumor tissue removed during surgery to be employed in the study.

Head and Neck Tumor Processing:

HNSCC tumor biospecimens were either processed within three hours of removal or stored for longer in RPMI 1640 media (Sigma Aldrich) and processed later. The tumor biopsy was dissociated by following the protocol of a commercial tumor dissociation kit (MACS, Miltenyi Biotec, Germany). In brief, a combination of enzymatic degradation and mechanical dissociation was used to generate single-cell suspension from the primary

tumor tissue. First, Reagents (Enzyme H, R, and A) from the kit were prepared and mixed as per the manufacturers' protocol for severe tumor type as HNSCC is considered a robust tumor based on its histological composition. Then, the fragmented pieces of tumor that were cut to approximately 2- 4 mm, was added to the enzyme mix in gentle MASC C Tube. This was attached to the MACS Dissociator, and the appropriate program for severe tumor type was chosen and run. After termination of the program, the sample was incubated for 30 minutes at 37 °C under continuous rotation. This process was repeated for two more runs with an appropriate program and the cell suspension was strained through a cell strainer to remove any non-dissociated large tumor pieces. The extracted cell suspension was then centrifuged at 300 x g for 7 minutes before aspirating the supernatant and resuspending in fresh Dulbecco's Modified Eagle Medium: Nutrient Mixture F-12 (DMEM/F-12, ThermoFisher Scientific, Waltham, MA) media or RPMI 1640 medium (Sigma). Any dead cell, debris or erythrocyte present in the cell suspension was removed using a Dead Cell Removal Kit (MACS, Miltenyi Biotec, Germany), Debris Removal solution (MACS, Miltenyi Biotec, Germany) or blood cell lysis solution (10X, MACS, Miltenyi Biotec, Germany) respectively. The final cell pellet was counted for the number of viable cells and processed immediately for use.

Mesothelioma Tumor Processing:

The mesothelioma tumor biospecimens were delivered within one hour of removal to the lab for cell processing. Once received, the sample was washed in phosphate-buffered saline (PBS) with 2% penicillin-streptomycin for three 5 min cycles and then washed in Dulbecco's Modified Eagle's Medium (DMEM) with 2% penicillin-streptomycin (P/S) for two 5 minute cycles. The tumor was minced and placed into a conical containing DMEM

with 10% collagenase/hyaluronidase (10X Collagenase/Hyaluronidase in DMEM, STEMCELL Technologies, Seattle, WA) and 2% penicillin-streptomycin for 18 hours on a shaker plate in 37°C. The digested tumor was then filtered through a 100 μm cell filter and centrifuged to create a pellet. Plasma and non-cell material were removed, and the pellet was re-suspended in 1 mL BD PharmLyse (BD PharmLyse, San Diego, CA) and 9 mL deionized water for 5 minutes. The mixture was diluted to 50 mL with deionized water and centrifuged, lysis buffer with lysed cells was aspirated, and the cell pellet was counted for use.

3.2.2 Cell culture

Radiation-sensitive head and neck squamous cell cancer cell line (SCC-61) and radiation resistance head and neck squamous cell cancer cell line (rSCC-61)[34] were provided to us by Dr. Cristina Furdui, department of Molecular Medicine, Wake Forest School of Medicine. Both the cell lines were cultured independently in DMEM/F12 medium that was supplemented with 10% fetal bovine serum (FBS, Atlanta Biologicals, Flowery Branch, GA), and 1% (v/v) penicillin-streptomycin (P/S) solution. Cultures were maintained in an incubator at 37°C with 5% CO2. Cells were passaged twice a week upon reaching 70–80% confluency using trypsin (0.05%, Difco Laboratories, Detroit, MI). Cells were collected using the same trypsinization approach prior to their incorporation into organoids.

3.2.3 Sponge Assay

The sponge assay protocol was adapted from a previously published methodology [35]. The HNSCC tumor biopsy was minced into approximately equal-sized pieces of 1 mm^3 in size and was individually weighed for normalizing the data by weight. The minced tumor pieces were the placed on a 1 cm^3 piece of hydrated collagen-gel matrices (Health Design Industries, Rochester, NY) in a 24 well plate within 6 hours of removal from the patient and RPMI 1640 media with 10% FBS, and 1% P/S in solution was added to wells. After 24 hours of incubation with the control media at 37°C and 5% CO2, the tissue specimens were exposed to the drug spiked media that were administered by dissolving in the culture media.

3.2.4 Extracellular matrix (ECM) hydrogel preparation and basic organoid formation

The ECM-mimicking HA/gelatin-based hydrogel (HyStem-HP, ESI-BIO, Alameda, CA) was prepared as previously described [18, 21, 36]. Briefly, a thiolated HA component (Glycosil) and a thiolated gelatin component (Gelin-S) were dissolved in sterile water containing 0.05% w/v of the photoinitiator 2-Hydroxy-4′-(2-hydroxyethoxy)-2-methylpropiophenone (Sigma, St. Louis, MO) to make a 1% w/v solution. The polyethylene glycol diacrylate (PEGDA) crosslinker (Extralink, ESI-BIO) was dissolved in the photoinitiator solution to make a 2% w/v solution. Glycosil, Gelin-S, and Extralink were then mixed in a 2:2:1 ratio by volume, respectively. For tumor construct formation,

the resulting solution was mixed thoroughly by vortexing and then used to resuspend cells (20 million cells/mL).

3.2.5 Tumor organoid biofabrication

Patient-Derived Tumor organoid (PDO):

The PDOs were biofabricated in a flat-bottom 48-well plate (Cole Parmer, Vernon Hills, IL) coated with a thin layer of polydimethylsiloxane (PDMS; SYLGARD™ 184 Silicone Elastomer, Dow Corning). The dissociated cells were suspended in hydrogel precursor with Glycosil, Gelin-S, and Extralink at a density of 2×10^7 cells/mL. 10 µL of the cell suspension was pipetted into each well to form a consistent dome-shaped droplet, so each PDO had approximately 200,000 cells, as shown in **Figure 3.2**. This was subsequently photocrosslinked by exposing the organoid to ultraviolet light exposure (365 nm, 18 W cm$^-$2) for 1 sec. The UV exposure initiates rapid thiol-ene crosslinking and encapsulates the tumor cells in the hydrogel scaffold. The organoids were maintained in DMEM/F-12 – 10 media for stabilization for 3 days and the drug was added on day 3 by dissolving the media.

Cell line-based Tumor organoid (CTO):

The effect of the drug β-Lapachone seen in the presence of dicoumarol and the impact of its concentration in the PDOs was validated on the cell line-based organoid. For this purpose, SCC-61 and rSCC-61 –based CTOs were created and exposed to a range of concentrations of both β-lap and DIC. First, SCC-61 and rSCC-61 cells were trypsinized in the method mentioned above and centrifuged at 1500 rpm for 5 minutes. Then the

resulting pellet was counted for the number of viable cells and used for organoid formation. Similar to the PDOs, the cell pellet was resuspended in hydrogel precursor at a density of 2×10^7 cells/mL and pipetted into a PDMS-coated 48 well plate. Once UV photocrosslinked, 500 µL of DMEM/F-12 – 10 media was added to each well with organoid.
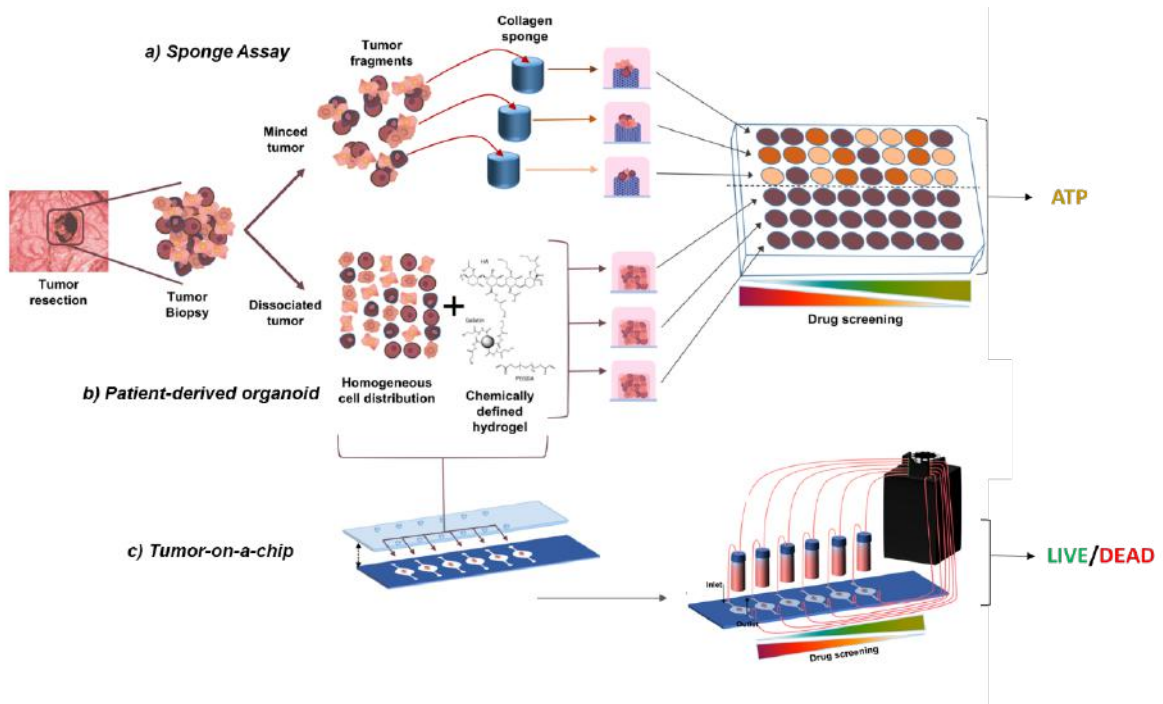
Figure 3.2. Experimental methodology flow chart for patient-derived tumor models. *The tumor resected from the patient is divided for sponge assay and PDOs. For the sponge assay, the tumor is minced to multiple fragments of approximately 1mm³ size and placed on a collagen sponge. This is placed into a 24 well plate with drug spiked media. The second half of the tumor is dissociated, and the heterogeneous mixture of tumor cells are isolated and made into PDO's by crosslinking the hydrogel precursor with suspended tumor cells. These organoids are made in either a PDMS-coated 48-well plate or in a microfluidic platform. After 1-3 days of control media, the drug is added to the organoids.*

3.2.6 Adhesive film microfluidic device fabrication

The microfluidic device fabrication approach (**Figure 3.3 a**) is based on methods reported elsewhere[37]. Independently-addressable channels leading to and from individual sample chambers were produced in an adhesive film (cat. # 9495MPF, 3M, St. Paul, MN) using a cutting plotter (CE6000-40, Graphtec, Tokyo, Japan) and the bottom surface of the resulting patterned layer was attached to a clean glass microscope slide. On the top surface was adhered to a polystyrene slide (cat. # 260225, Ted Pella, Redding, CA) featuring holes produced by drill press to act as inlets and outlets for fluid delivery to the channels. Following device assembly, PTFE tubing was connected to each port and secured using a UV cure polyester resin (Solarez, Vista, CA).
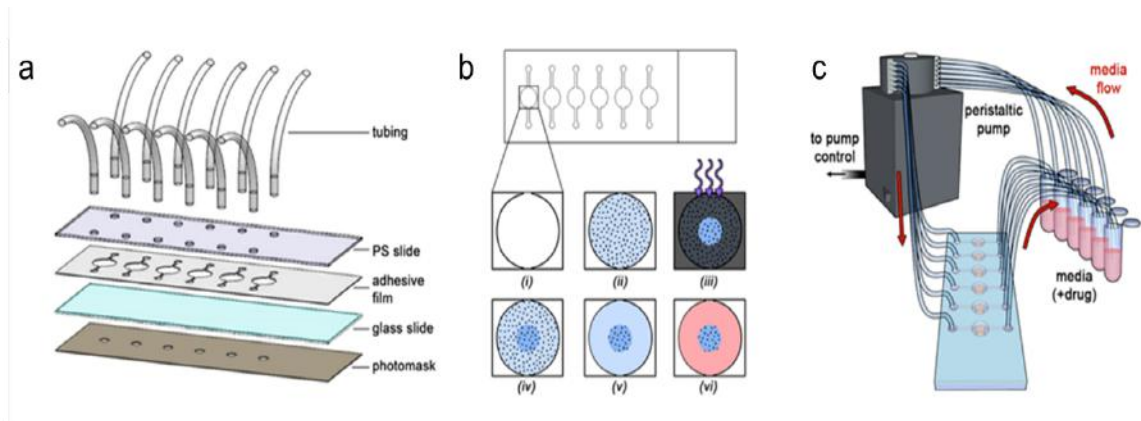
Figure 3.3. PDO in a Tumor-on-a-chip system. a) Schematic assembly of a microfluidic device (see text). The patterned adhesive film both attaches surrounding layers together and forms the channels and chambers in which organoids are formed. b) In situ organoid patterning technique: a microfluidic chamber (i) is filled with a mixture (blue) containing hydrogel precursors, photoinitiator, and patient-derived tumor cells (ii) and then illuminated with UV light through a photomask (gray) (iii). The exposed precursor is crosslinked into a hydrogel (dark blue), detaining cells within the region (iv), and non-

crosslinked gel is flushed from the chamber with clean PBS from the chamber (v). Finally, PBS is replaced with DMEM (red) (vi) for incubation. c) The total measurement set-up, featuring a low-volume, closed-loop fluidic circuit for each organoid facilitated by a computer-controlled peristaltic pump.

3.2.7 Tumor-on-a-chip biofabrication

Tumor constructs were biofabricated (**Figure 3.3b**) in the microfluidic devices using a photopatterning technique similar to our previous work [18]. Here, a photomask featuring 1-3 mm apertures was produced in an aluminum foil/adhesive film bilayer with the same cutting plotter technique used for channel definition and adhered directly to the bottom surface of the microfluidic device. The mixture of hydrogel precursor solutions and tumor cells derived from the mesothelioma biospecimen was prepared at a density of 20 million cells/mL and then introduced to each of the device channels via the inlet ports, and organoid constructs were defined by ultraviolet light exposure (365 nm, 18 W cm^{-2}) for 3 s through the attached photomask. This exposure initiated a rapid thiol-ene stepwise crosslinking reaction that encapsulated cells in a 3D column defined by the photomask aperture. Finally, an unexposed precursor/cell mixture was flushed from the device with clean PBS, leaving discrete 3D patient-derived mesothelioma constructs. Each channel of the device, featuring one cell construct, was connected to a separate reservoir of DMEM. The media was flowed through the device (**Figure 3.3 c**) from the reservoir by silastic tubing connected to MP2 Precision micro-peristaltic pump (Elemental Scientific, Inc., Omaha, NE). The flow was maintained at a rate of 4 μL/min.

3.2.8 ATP Assay

An ATP assay (CellTiter- Glo® 3D cell viability assay, Promega, Madison, WI) was performed to determine the viability of the organoids in control and drug-exposed conditions for the PDOs and sponge assay only. For this assay, an opaque 96 well plate (white, Corning) was prepared with individual organoid and 100µL of culture media in each well, including triplicates for media background. 100 µL of CellTiter-Glo® reagent is added to each well of the prepared plate and incubated at room temperature for 25 minutes. Then the output luminescence is recorded using Molecular Devices SpectrumMax M5 (Molecular Devices) tunable plate reader system.

3.2.9 LIVE/DEAD cell viability determination

LIVE/DEAD assay was used to access viability mainly in the tumor-on-a-chip system, with the exception of initial viability assessment in PDO's along with ATP assay. In the PDO system, before exposing the organoids to drugs, the live and dead cells in the organoids were stained for assessing the viability. For this, 200 µL of LIVE/DEAD solution containing $2\,\mu$M calcein-AM and $2\,\mu$M ethidium homodimer-1 (LIVE/DEAD Viability/Cytotoxicity Kit for mammalian cells, ThermoFisher, Waltham, MA) in mixture of PBS and DMEM (1:1) was added to each well of the organoid replacing the spent media and incubated for 1 hour. The media was aspirated, and the organoid was washed with clean PBS before imaging using Leica TCS LSI macro confocal microscope. A 200-µm z-stacks were obtained for each construct using filters appropriate for both red and green fluorescence (594 nm and 488 nm, respectively) and then overlaid.

For the Tumor-on-a-chip system, the circulating media was first flushed from the device channels with clean PBS, and then a 1 mL mixture of PBS and DMEM (1:1) containing 2 μM calcein-AM and 2 μM ethidium homodimer-1 (LIVE/DEAD Viability/Cytotoxicity Kit for mammalian cells, ThermoFisher, Waltham, MA) was introduced. Constructs were incubated for 1 hour, after which the channels were again flushed with clean PBS. *In situ* imaging was performed using an Olympus FluoView™ FV1000 confocal microscope. For the latter, 5 μm z-stacks were obtained for each construct using filters appropriate for red and green fluorescence, respectively, and then overlaid. Image quantification was performed using Imaris MeasurementPro software (Bitplane, Concord, MA), through which images in each color channel were analyzed for cell size, shape, and fluorescence intensity and cell locations were marked through segmentation (**APPENDIX II A2. 1 and A2. 2**). For consistency, a 450 μm x 900 μm area of each image was considered. Cell viability was calculated through quantification of the total number of identified cells in the green channel (LIVE) compared to the total number in the red channel (DEAD).

3.2.10 Drug studies

The *in vitro* drug studies on the patient tumor was performed on the sponge assay, PDOs, and tumor-on-a-chip.

For the sponge assay, the drug was added after 24 hours of incubation in control media. The stock solution of the drugs was directly dissolved into the media to achieve the desired concentration and replaced the spent media. The tumor fragments were incubated for another three days before assessing for drug response using ATP assay. Except, β-

Lapachone (β-Lap) and Olaparib (AZD2461, Sigma) were only incubated for 2 and 4 hours, respectively, and the drug spiked media was replaced with DMEM cell culture media.

For the PDOs and CTOs, the system was stabilized for 3 days with DMEM media before adding the drug. Similar to the sponge assay, 500μL of drug spiked media was added to the organoids after aspirating the spent media and incubated for another 3 days before assessing the effects of drugs.

Both the patient-derived systems were subjected to treatment with β-Lapachone (2.5μM, 5 μM, 10 μM, 20 μM, and 100 μM), Cisplatin (0.5 μM, 5 μM, 50 μM, 500 μM, Sigma), β-Lap + Dicoumorol (50 μM), Erlotinib (1 μM, 2.5 μM, 10 μM, 100 μM, Sigma), 5-Fluorouracil (10 μM, 100 μM, 1mM, Sigma), Olaparib (15 μM, Sigma), β-Lap + Olaparib(15 μM), and radiation (2Gy). For the chemo drugs, a stock solution was initially prepared in DMSO and then diluted in DMEM cell culture media to obtain desired concentrations. Except for dicoumarol, a 5mM stock solution was prepared in sterile DI water, and NaOH was added to the stock solution to allow concentrated dicoumarol to dissolve . To irradiate the tumor organoid, the culture dish was placed inside a 444 TBq 12,000 Ci self-shielded 137Cesium (Cs) irradiator. Each organoid achieved a homogenous dose at the rate of 392 rad/min for a required exposure time that was calculated to deliver the desired dose.

For the CTO system, the organoids were exposed to a combination of β-Lapachone (2.5μM, 5 μM, 10 μM, 20 μM, 35 μM, 50 μM, 75 μM, and 100 μM) and Dicoumorol (25 μM, 50 μM, 75 μM, 100 μM, 200 μM). Both β-Lap and DIC were added to the organoid at the same time.

After 3 days of drug exposure, both the sponge assay and PDO's were assessed for viability by using ATP assay that measures the amount of ATP present in each organoid, which is directly proportional to the number of live cells in the culture.

For the tumor-on-a-chip organoid, the following drugs were employed in drug studies: cisplatin (Sigma), carboplatin (Sigma), and pemetrexed (Sigma). Cisplatin/pemetrexed and carboplatin/pemetrexed cocktails were reconstituted in DMEM cell culture media with a matched platinum agent and pemetrexed concentrations at 0.1 μM and 10 μM or 0.2 μM and 20 μM for administration to organoids.

3.2.11 Histological and immunohistochemistry (IHC) staining

5 μm thick organoid sections were created from paraffin-embedded constructs, and then deparaffinized for staining. IHC was used to visualize biomarkers cytokeratin 5/6 (CK5/6), calretinin, and thrombomodulin. Blocking was performed by incubation under Dako Protein Block for 15 minutes. Primary antibodies CK5/6 (Abcam, ab17133, raised in mouse) and calretinin (Abcam, ab702, raised in rabbit) or CK5/6 and thrombomodulin (Abcam, ab109189, raised in rabbit) were applied to the sections on the slides at a 1:200 dilution in Dako Antibody Diluent and incubated at room temperature for 1 hour. Next, secondary Alexa Fluor 488 or Alexa Fluor 594 antibodies with appropriate species reactivity were applied to all samples at 1:200 in Dako Antibody Diluent and left at room temperature for 1 hour (anti-mouse Alexa Fluor 488 and anti-rabbit Alexa Fluor 594, Life Technologies, Carlsbad, CA, A-11070). Sections were then incubated with Dapi for 5 minutes prior to coverslipping. For Annexin V and Ki67 staining (Abcam, Cambridge,

MA, ab14196, and ab16667, respectively) in subsequent biomarker-driven experiments, an identical protocol was employed. Fluorescence images were taken using a Leica DM400B Compound Microscope and overlaid for analysis.

3.2.12 Statistical Analysis

Data were expressed for each experimental group as mean ± SD, and statistical significance determined using statistical analysis methods (Origin, OriginLab Corp., USA, or GraphPad Prism, Graphpad Software Inc., USA). An *n=3* or higher was employed for all studies. Histological, immunohistochemical, or fluorescent images presented in figures are representative of their respective experimental groups. One-way ANOVA was employed for multiple comparisons. Student's t-tests were performed to compare the means of a normally distributed interval dependent variable for two independent groups. Confidence intervals of 95% or better were considered significant.

3.3 Results

3.3.1 Biospecimen processing, organoid production, and assessment of patient-specific HNSCC tumor organoids.

For the study with PDOs, tumor tissues were obtained from eight patients during their surgical treatment. For these specimens, known information about the tumor type, patients' treatment histories, and drugs administered to PDOs are listed in **Table 3.1.**

|	Tumor type	Drugs administered to PDO
Patient #1		β-Lapachone (2.5μM, 10μM, 100μM), Erlotinib (2.5μM, 10μM, 100μM), Cisplatin (0.5μM, 5μM, 50μM), 5FU (10μM, 100μM, 1mM).
Patient #2	G2 moderately differentiated	β-Lapachone (2.5μM, 10μM, 100μM), B-Lapachone (2.5μM, 10μM, 100μM) + Pembrolizumab (100nM), Pembrolizumab (100 nM); Dimedone (500μM, 1mM, 10mM) + Pembrolizumab (100nM), Cisplatin (0.5μM, 5μM, 50μM).
Patient #3	Larynx SCC G3 poorly differentiated	β-Lapachone (2.5μM, 5μM, 10μM, 100μM), Olaparib (15μM), β-Lapachone (5 μM)+ Olaparib (15μM), Erlotinib (2.5μM, 10μM, 100μM), Cisplatin (5μM, 50μM, 500μM), Radiation (1 Gy, 2Gy, 4 Gy), Radiation (1 Gy, 2Gy, 4 Gy) + B-Lapachone (2.5μM, 5μM)
Patient #4	Mandible SCC	β-Lapachone (50μM), B-Lapachone (50μM) + Dicoumorol (50μM), β-Lapachone (50μM) + IR 2Gy, IR 2Gy
Patient #5	T1-2 squamous cell carcinoma of the right tongue base.-N1;	β-Lapachone (2.5μM, 5μM, 10μM, 50μM, 100μM), β-Lapachone (10μM, 50μM, 100μM) + Dicoumorol (50μM), Cisplatin (5μM, 50μM, 100μM, 500μM), Radiation (2 Gy, 6 Gy, 10 Gy), Radiation (2Gy) + β-Lapachone (50μM), Radiation (2Gy) + Cisplatin(50uM)

Patient #6		β -Lapachone (2.5µM, 10µM, 50µM, 100µM), β -Lapachone (2.5µM, 10µM, 50µM, 100µM) + Dicoumorol (50µM), Cisplatin (50µM), Radiation (2 Gy), B-Lapachone (50µM) + Radiation (2Gy), Cisplatin (50µM) + Radiation (2Gy).
Patient #7	Neck	β -Lapachone (50µM), β -Lapachone (50µM) + dicoumarol (50µM)
Patient #8	Tongue	β -Lapachone (10µM, 50µM), B-Lapachone (10µM, 50µM) + dicoumarol (50µM), Cisplatin (5µM, 50µM, 500µM), Radiation (2 Gy)

Table 3.1. Patient tumor characteristics and treatment history along with the administered drug to respective PDOs.

The resected tumor biospecimen was delivered fresh for processing within an hour of resection. Approximately half of the retrieved tumor was used for sponge assay and the other half was processed for making PDOs. For the sponge assay, the minced tissue was carefully weighed and placed on a sponge gel immediately. For the remaining tissue, tumor cells were isolated by dissociating the extracellular matrix of the specimen and kept on ice for use within 1 hr. The isolated cell pellet was mixed with the photopolymerizable hydrogel precursor and pipetted into the PDMS-coated well plate to form dome-shaped HNSCC organoids to which media was added directly.

As-produced tumor organoids were assessed for viability after 3 days using LIVE/DEAD staining (**Figure 3.4.a**) before adding drug. Organoid viability was determined to be over 80% from the maximum projection image by finding the ratio of live cells (green-stained) to the total number of cells (green- and red-stained). Histology was performed on patient #3 to verify that the organoids contain actual tumor cells and not only stromal cells. All

histology slides were double-stained to visualize the co-localization of EGFR and EGFR-P. Previously it has been reported that HNSCC overexpresses EGFR[38-40], especially for poorly-differentiated tumors (like that of patient #3), for which almost all cells have been shown to express EGFR compared to moderately or well-differentiated tumor[41]. Both EGFR and ECFR-p are overexpressed in the cells retrieved from patient #3 (**Figure 3.4.b-6**), confirming the abundance of tumor cells in the specimen. Additionally, we found the EGFR-p IHC stain, which shows the activated EGF receptor, to be highly co-localized with the EGFR[38]. Similarly, Ki-67 protein was stained separately, whose function is related to cell proliferation. It has been reported that Ki67 expression correlates positively to the degree of cell differentiation [42]. This is evident from **Figure 3.4.g,** which shows the expression of Ki67 protein in most cells of the poorly differentiated patient #3 tumor.
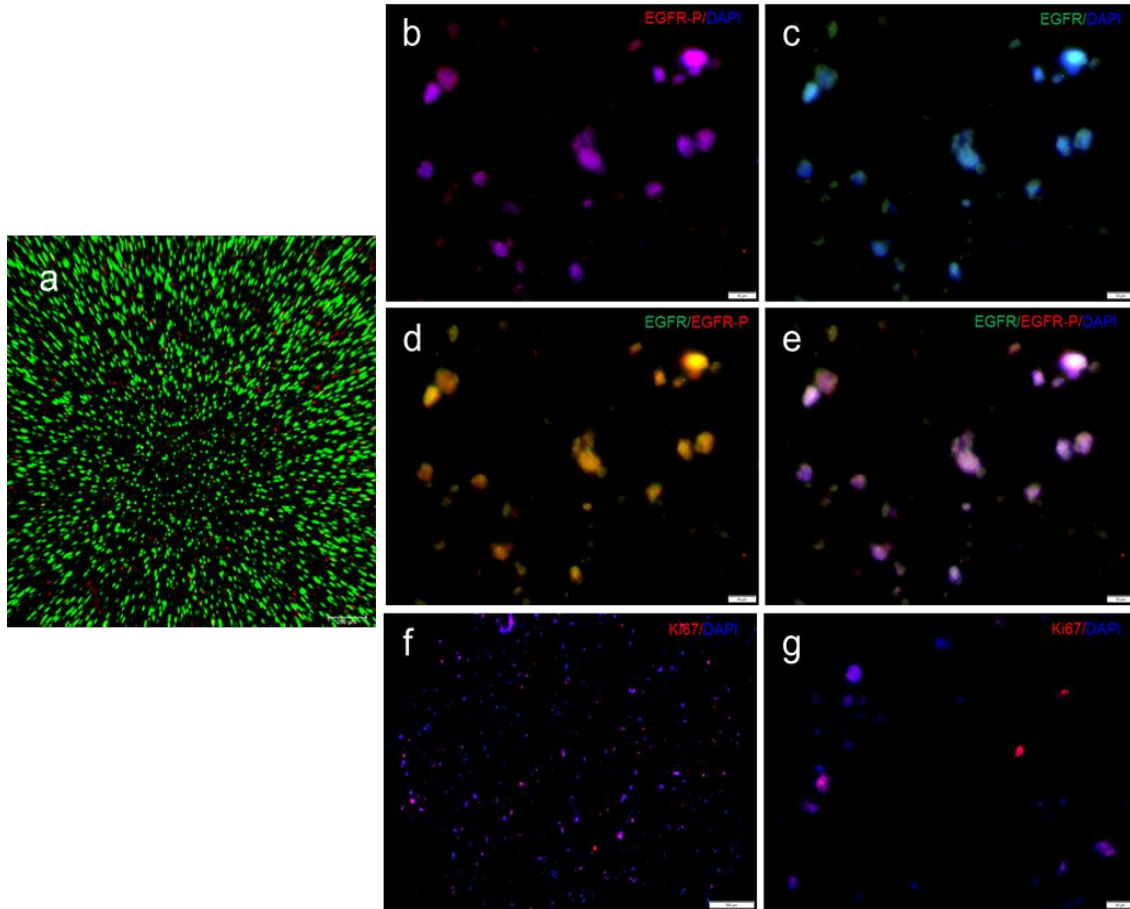
Figure 3.4 HNSCC Patient tumor construct histological assessment. *Histological assessment of patient-derived HNSCC organoids from patient #3 after three days of incubation in DMEM/F12-10. a) LIVE/DEAD staining of organoids on day 3. Green represents live cells by Calcein AM staining. Red represents dead cells by ethidium homodimer staining. b-e) EGFR double-stained with EGFR-P along with DAPI-stained nuclei organoid sections and f, g) Ki67 double stained with DAPI-stained nuclei organoid sections. g) Representative images of 'f' (10x) at increased resolution (60x) showing the ki67 expression in the red channel, respectively. Scale bars for panels' b- e, g are 100 μm; panel f is 10 μm.*

3.3.2 Comparison of cancer treatment responses between sponge assay and PDOs.

The HNSCC biospecimens received were used to make both the traditional sponge assay and organoids and were exposed to similar drugs and concentration for a period of 3 days. The drug sensitivities of the organoid and tumor fragment were assessed by quantifying the terminal ATP activity as determined by the luminescence readout of an ATP assay. For the sponge assay, it has been shown that the weight of the tumor and the cell metabolic assay are directly proportional[43]. Therefore, for comparison purposes, results between different tumor fragments were normalized by the weight of the specimen. The PDOs that were produce were all identical and standardized, and so were directly comparable. The two patient samples considered for comparison between the two systems were patients #3 and #4.

For the sponge assay (**Figure 3.5.a)**, each condition for patient #3 had n=12 for each condition, as previous data showed significant variations within each sample. For this tumor sample, the ATP results showed the expected response to β-Lap, with a dose-dependent sensitivity. The tumor seemed to be responsive to the drug olaparib also, but no significant difference was observed when the drug was added along with βLap in comparison to olaparib alone. Though the results from the sponge assay are consistent, the variability between the samples was still too large to draw any decisive conclusion from the data. For patient #4, the sponge assay had a sample size of $n = 9$ and was exposed to β-Lap, both alone and in combination with the β-Lap inhibitor dicoumarol. As expected, the tumor exposed to both dicoumarol and β-Lap showed less sensitivity compared to β-Lap alone. Similarly, the combination treatment of radiation with β-Lap showed better response compared to the radiation-only treatment option.

For the PDO system (**Figure 3.5.b**), each patient specimen was probed under multiple conditions, each with a sample size of *n=3*. In patient #3 PDOs, the drug sensitivity to β-Lap agreed with previous patient data and qualitatively with the sponge assay data, but critically, yielded far less variability in the results. The tumor was also found to be sensitive to cisplatin in a dose-dependent manner, similar to β-Lap, and was insensitive to the drug erlotinib and olaparib alone. Combining olaparib with β-Lap induced cytotoxic effects, but not beyond the effect of the same dose of β-Lap alone. Meanwhile, patient #4 data showed comparable results to the sponge data, though again with significantly less variability. Similar to the previous assay, the ATP luminesce showed that the tumor was sensitive to β-Lap and when used with dicoumarol, there was a significant increase in the viability of the cells. This suggested that tumor sensitivity was only due to β-Lap-mediated cytotoxicity. These tumor organoids were not responsive to radiation (2 Gy). Radiation combined with β-Lap yielded a significant decrease in viability, but again, not more than the same concentration of β-Lap alone. From the comparison of all patient data between the two assays, it could be concluded that PDOs produce more consistent and reliable data without significant variations between samples in the same condition.
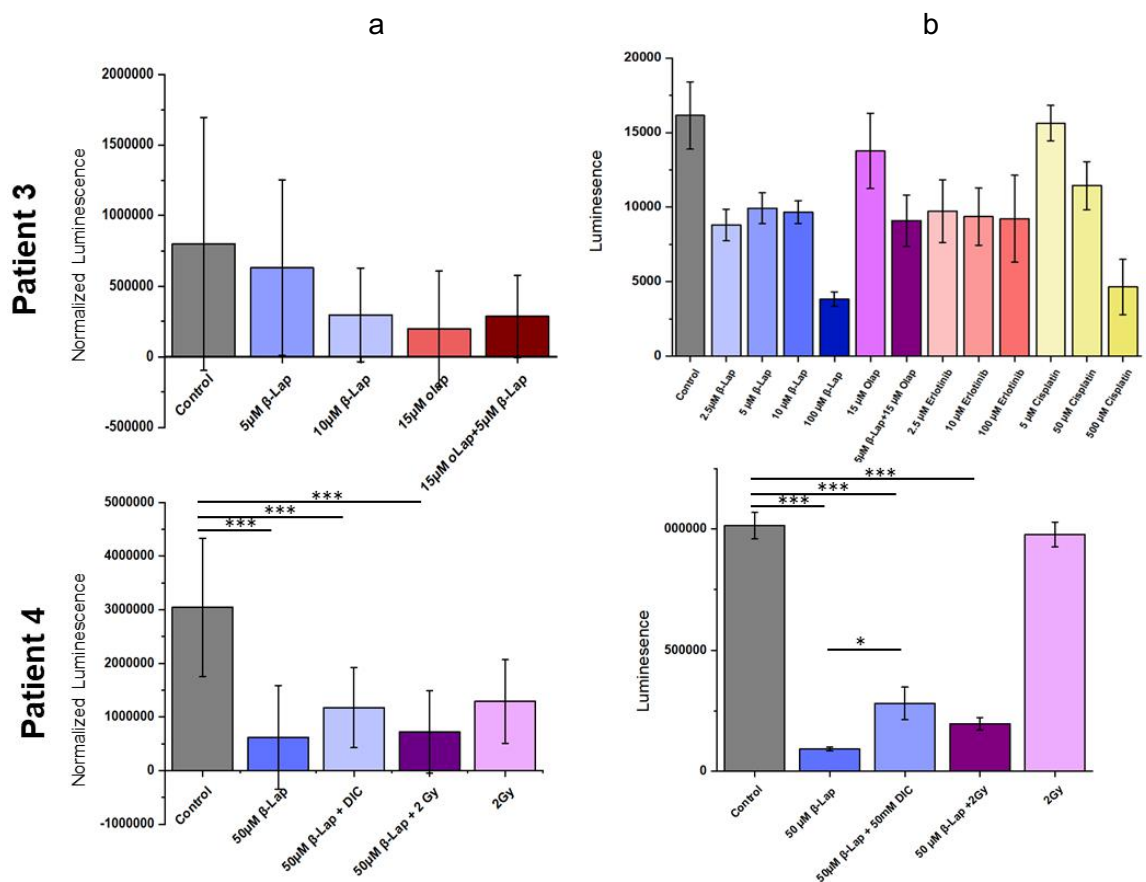
Figure 3.5 In vitro drug response comparison of head and neck tumor between sponge assay and Patient-derived Organoid*. Drug-induced cytotoxicity was evaluated under diverse conditions for patients #3 and #4 using both sponge assay (a) and PDO (b) by quantifying the viability of tumor fragment/PDO determined by the luminescence reading of a 3D ATP assay.*

The initial outcome from the results of PDOs was our ability to successfully develop personalized tumor organoids, bioengineered using a patients' own tumor cells. These organoids could be maintained in 3D culture at high viability (about 80%) for extended periods, which was verified using LIVE/DEAD assay in the as-produced tumor organoids. Next, we demonstrated the capability of administering both chemotherapeutic drugs and radiation therapy to the organoids. As radiation is one of the most common treatment

options for HNSCC patients, it was critical to show the feasibility in our system to radiate the organoids *in vitro*. We were also able to capture the dose-dependent drug response of these organoids, especially for drugs cisplatin and β-Lap, and recapitulate the effectiveness of combination cancer therapy, as seen with patients #3 (given olaparib and β-Lap) and #4 (given radiation and β-Lap). When comparing the drug sensitivity between patients (**Figure 3.6),** which shows a heterogeneous drug response of 8 patients to cisplatin, β-Lapachone, and radiation that was comparable to how each patient has different drug sensitivity to the same drug. This validates that the PDO system was able to capture this heterogeneity of the tumor between patients. The organoids captured not only the patient heterogeneity but the tumor heterogeneity, as demonstrated by the correlation between patient #4 data from the sponge assay and PDOs. The sponge assay gained its popularity as an *in vitro* tumor model as it was able to preserve heterogeneity and native tissue architecture through the variations in the results were frustrating. Producing comparable results proved that PDOs comprised a physiologically-relevant tumor model. Most importantly, based on the ATP results from the PDOs and the sponge assay, it was evident that the PDOs were relatively more consistent and better optimized to produce results for drug response. The PDOs were able to produce data within each condition with only minor variability, whereas the sponge assay had large variabilities that skewed the output data. From these results, it is clear that we have developed an *in vitro* tumor model that recapitulates *in vivo* like drug response, which can be used as a personalized model to improve patient outcomes.
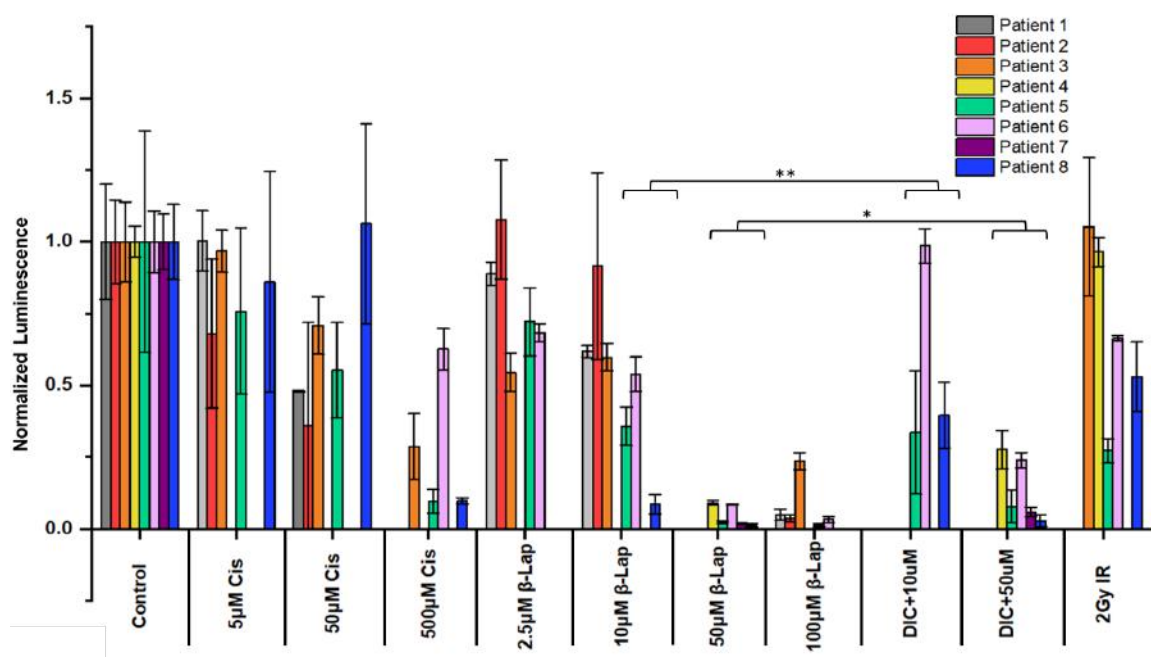
Figure 3.6. Normalized and consolidated ATP assay viability data of 8 head and neck

cancer patients. *The ATP assays luminescence readout is normalized to the control and*
grouped based on the cancer treatment drug or radiation. The system shows the dose-
dependency and variability of drug response between the 8 patients in our study. Here, β-
Lapachone is considerably the most effective drug across all patients. Also, there is a
bright tread of dose-dependent drug sensitivity between different concentrations of the
drug. Note that not all conditions were tested across patients; zero luminescence indicates
no data rather than 100% response. Drug abbreviations: Cisplatin (Cis); β-Lapachone (β-
Lap); Dicoumorol (DIC); Irradiation (IR).

Figure 3.6 shows the consolidated data of the most commonly used therapeutic options for
all patients like radiation therapy and chemotherapeutic drugs like cisplatin and β–
Lapachone. Across all samples, we were able to see a strong dose-dependent response
consistently. But the degree of drug sensitivity was variable from patient to patient. In

general, the patient better responded to a higher concentration of cisplatin and β–Lapachone.

3.3.3 Validation of β-Lapachone-mediated cytotoxicity on the PDOs

The most common treatment plan for HNSCC is radiation therapy alone or combination therapy with targeted chemotherapeutic agents. One critical issue is that the tumor gains resistance to these standard care treatments, rendering them ineffective. Mechanisms of therapy resistance include dysfunction of the redox metabolism that occurs in multiple stages of tumor progression by suppressing the reactive oxygen species (ROS) and upregulating DNA damage response [44]. Therefore, developing a targeted strategy that bypasses the resistance mechanism and exploits the redox alteration could serve as an integral component to improving clinical outcomes. One such target is the combination of NAD (P) H: quinine oxidoreductase 1 (NQO1) overexpression [45, 46] coupled with the reduced levels of catalase [46, 47] present in HNSCC [44]. β-Lapachone is an NQO1 bioactivatable drug[48] that metabolizes to undergo a futile redox cycle and produces two molecules of superoxide, causing an imbalance in the intercellular ROS that can induce cell death[49]. Because the primary function of catalase is to dismutate the superoxide H_2O_2 into H_2O and O_2, its low level can be saturated quickly by the H_2O_2 produced by NQO1 overexpression, causing significant damage to the cells. In contrast, the higher levels of catalase in healthy tissue will be able to protect it from the same damage [50].

Though the NQO1-dependent metabolism of β-Lap has been studied extensively [33, 51-53], here we validate this mechanism of β-Lap-mediated cytotoxicity on a 3D PDO. As seen in **Figure 3.6,** the consolidated drug sensitivity of all patients indicated that the tumors

responded best to higher concentrations of β-Lap. To verify that the cytotoxicity caused in these conditions was mainly due to the action of superoxide produced by β-Lap metabolism by NQO1, the NQO1 inhibitor dicoumarol was added to counteract the effect.
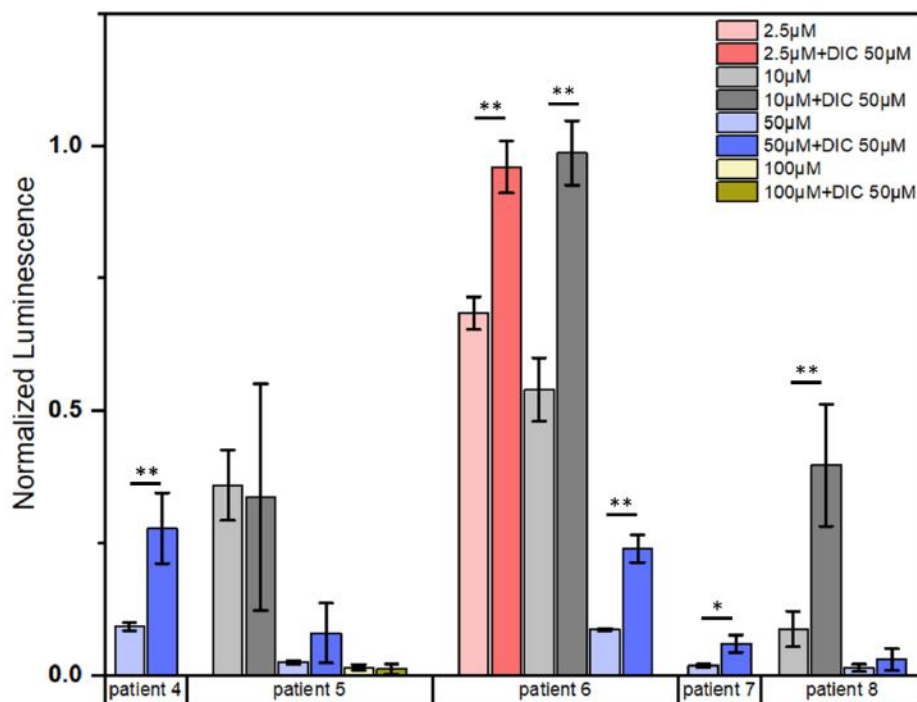
Figure 3.7 Inhibition effect by dicoumarol on β-lap cytotoxicity. *From the results of the ATP assay, it was demonstrated that the viability of the PDOs increases when 50μM dicoumarol, an NQO1 inhibitor, was added.*

Figure 3.7 is a subset of **Figure 3.6**, where we have plotted the PDO sensitivity to β-Lap and β-Lap with dicoumarol (DIC) data alone. Most of the patients have a significant increase in the viability of the tumor except for patient #5. This decrease in drug sensitivity is caused by the inhibition effect of dicoumarol that prevents the production of ROS. On the other hand, for patient#5, adding dicoumarol has no significant effect on drug sensitivity in any concentration (10μM, 50μM, 100μM) of β-Lap. This shows that the drug

might not be inducing cytotoxicity through NQO1 metabolism itself but might be causing β-Lap induced apoptosis through other possible alternative pathways[54]. Some of the reported alternative routes for causing β-Lap-induced apoptosis are involvement of caspase protease CPP32[54], activation of cysteine protease[55], mitochondrial electron transport chain (METC) complex I induced ROS formation[56],and activation of poly (ADP-ribose) polymerase (PARP1)[57].

Next, we validated the inhibition effect of dicoumarol on β-Lap, especially for higher concentrations of the drug. As it was observed in **Figure 3.7,** for β-Lap concentration over 50μM, the inhibition effect of dicoumarol did not protect all or most cells as seen in a lower concentration of drug in patient #6. Here, for the β-Lap concentration of 2.5 μM and 10 μM, the improved viability by dicoumarol is not significantly different compared to 50 μM. So we treated tumor organoids made of two cell lines – rSCC-61 and SCC-61 – with different concentrations of β-Lap (2.5 μM, 10 μM, 20 μM, 35 μM, and 50 μM) and dicoumarol (25 μM, 50 μM, 100 μM, and 200 μM,).

From **Figure 3.8,** it could be observed that for β-Lap concentrations above 50 μM for rSCC-61 and above 20 μM for SCC-61, the dicoumarol inhibition effect becomes obsolete and cannot adequately protect the cells from β-Lap-induced cytotoxicity. Even increasing the amount of dicoumarol concentration did not significantly impact the cytotoxic effect caused by β-Lap as in lower concentration. This could be due to alternative pathways that may be available to higher concentrations of β-Lap for producing ROS that is not inhibited efficiently by dicoumarol. We also observed that, at lower concentrations, rSCC-61 is more sensitive to the drug than SCC-61. This can be explained by the two-fold higher NQO1 mRNA known to be present in the former cells[58]. But at higher concentrations, the SCC-

61 cells appear to become more sensitive than the rSCC-61 as determined by ATP luminescence. However, this particular observation may be misleading. It has been reported that rSCC-61 cells have 1.56 times increased conversion of $NADP^+$ to $NADPH$[59]. Because these molecules are critical to ATP synthesis in the cell, rSCC-61 cells may have a higher baseline ATP level, possibly skewing results. Hence, additional experimentation may be necessary to verify the suggested mechanism.

From this validation experiment, there are two main conclusions to be drawn. First, we were able to verify with the PDOs that the (dose-dependent) cytotoxicity of the organoids under the influence β-Lap insult was caused primarily by the metabolism of the drug by NQO1 to produce superoxide. This was the first time that this effect has been studied on an HNSCC patient-derived specimen. Second, an experiment to determine the maximum inhibition effect of the dicoumarol on the organoid derived from radiation-sensitive SCC-61 cells and radiation-resistant rSCC-61 cells demonstrated that at high β-Lap concentrations, inhibition of dicoumarol becomes ineffective. The results and conclusions from the PDOs were correlated with published 2D studies, as mentioned above.
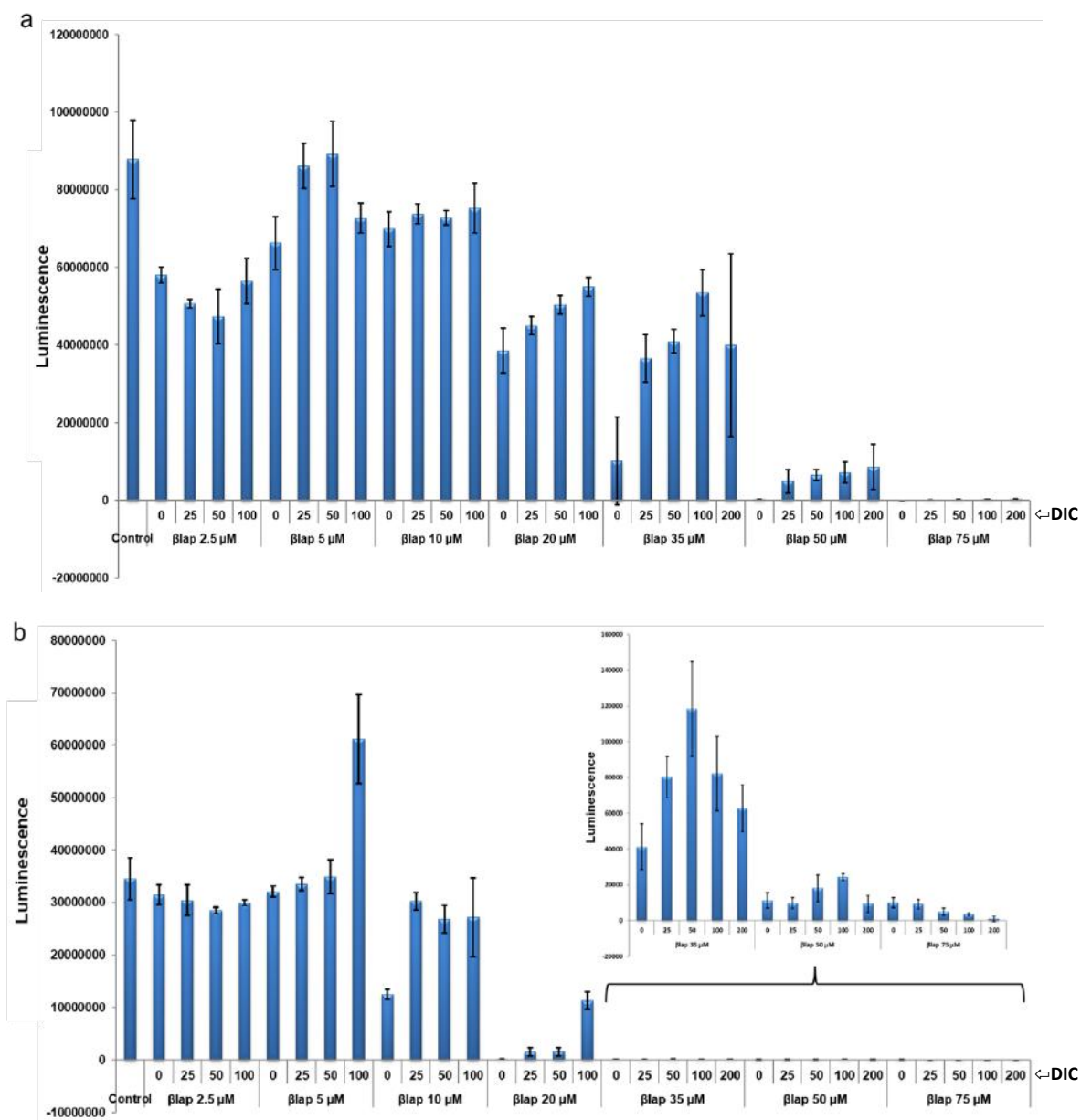
Figure 3.8. *Inhibition effect of Dicoumorol (DIC) on β-Lap induced toxicity tested on radiation insensitive rSCC-61(a) and radiation-sensitive SCC-61 (b) cells in 3D tumor organoids.*

3.3.4 Biospecimen processing, organoid production, and assessment of patient-specific mesothelioma tumor organoids in an AFB microfluidic chip.

Tumor tissues for the experiment were obtained from two subjects during the course of standard treatment. Subject 1 was a 50-year-old male who was diagnosed with epithelioid malignant peritoneal mesothelioma. Precision medicine analysis of the tumor revealed two genomic alterations (BAP1 splice site 1729+1G>A and PBRM1 N258fs*6) for which no targeted drugs or clinical trials were available. Due to the excessive volume of disease, the subject was referred for neoadjuvant systemic chemotherapy. Treatment was conducted with 6 cycles of cisplatin-gemcitabine followed by a single cycle of carboplatin-gemcitabine due to concerns of cisplatin-associated ototoxicity. Excellent clinical response to cisplatin-based chemotherapy was observed, with almost complete resolution of malignant ascites on a repeat 3-month re-staging CT. Subsequently, a cytoreductive surgery (CRS) with cisplatin-based heated intraperitoneal chemotherapy (HIPEC) was performed. During CRS, a segment of the tumor was resected, placed on ice, and transferred fresh to the lab for tumor organoid development. Importantly, the subject remains without radiologic evidence of disease 6 months after the operation without adjuvant treatment.

Subject 2 was a 38-year-old female who was also diagnosed with epithelioid peritoneal mesothelioma. She was treated with 4 cycles of cisplatin and pemetrexed with mixed response followed by 2 CRS without HIPEC. During CRS, a segment of the omental tumor was resected and treated as described for the previous tumor biospecimen. Final pathology indicated that, rather than epithelioid peritoneal mesothelioma, the tumor was actually well-differentiated papillary-cystic mesothelioma. Precision medicine analysis of the

tumor revealed no targetable genomic alterations. The patient remains without radiologic evidence of disease 6 months after her operation without adjuvant treatment.

The tumor biospecimens were kept on ice following retrieval and delivered to the lab for cell processing within one hour. Following dissociation of the extracellular matrix, isolated tumor cells were mixed with a photopolymerizable hyaluronic acid (HA) and gelatin hydrogel precursor and introduced inside an adhesive film-based microfluidic device with multiple, independent sets of channels (**Figure 3.2.a**). A tumor construct was biofabricated in each circular chamber of the device by patterning through an integrated photomask (**Figure 3.2.b**), similar to our previous work [18]. Following the flushing of unexposed precursor/cell mixture from the device, discrete 3D patient-derived mesothelioma constructs remained in each channel, after which media was continuously flowed from independent reservoirs by tubing connected to a micro-peristaltic pump (**Figure 3.2.c**).

Tumor organoids from both subjects were assessed by histological methods to verify the viability and presence of biomarkers associated with mesothelioma. Imaging of tumor constructs with LIVE/DEAD stain after 7 days (**Figure 3.9.a&d**) indicated that viable (green-stained) cells far outweighed dead (red-stained) cells within the construct. Double-stained sections were obtained to highlight colocalization of CK5/6, high molecular weight keratin, with both calretinin, a calcium-binding protein closely linked to mesothelioma (**Figure 3.9.b&e**), and with thrombomodulin (also called CD141), a well-established marker for mesothelioma[60-63] (**Figure 3.9c&f**). Observation of substantial overlap with non-selective nuclear stain DAPI confirmed that these constructs retained the mesothelioma phenotype.
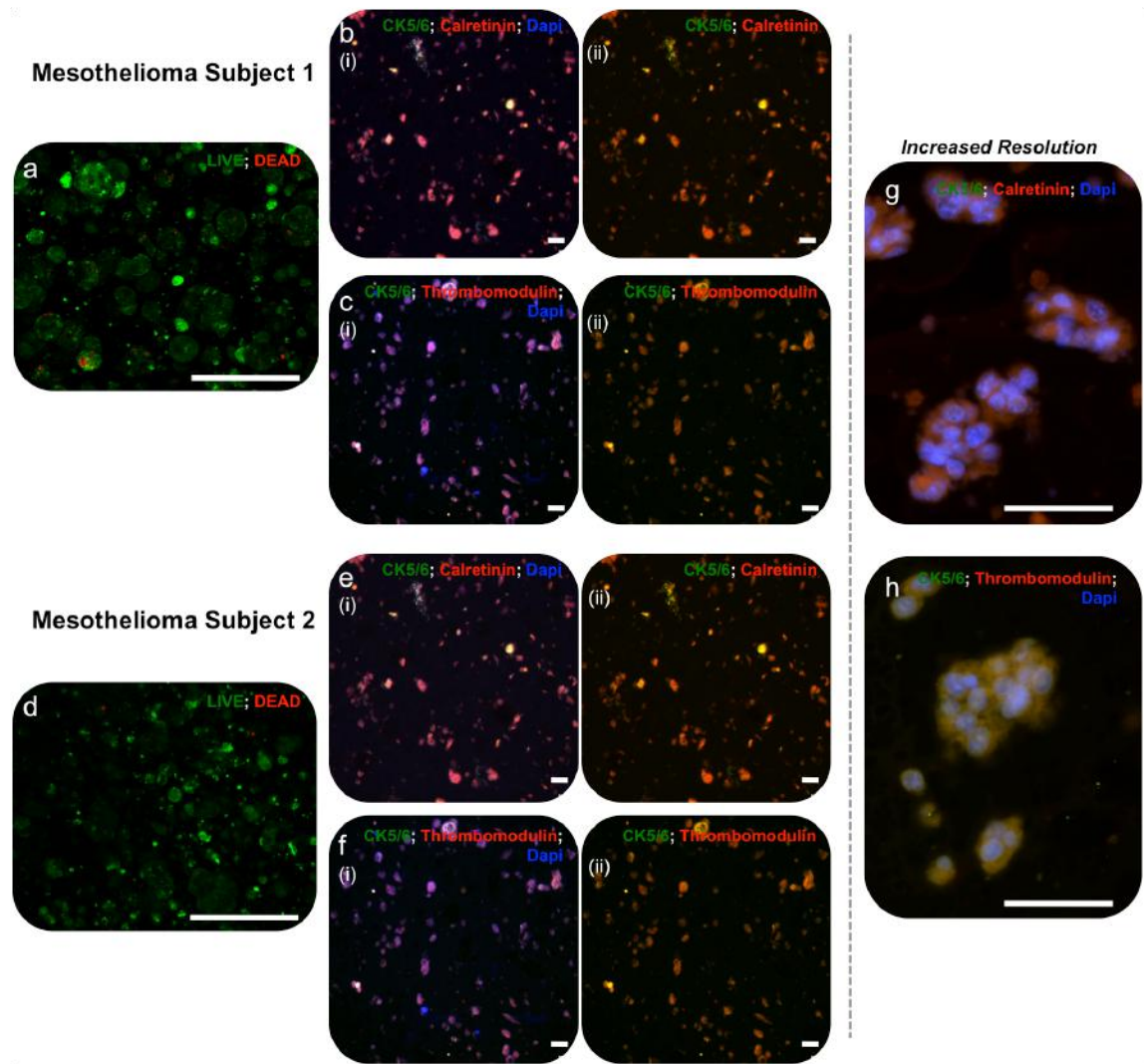
Figure 3.9. Mesothelioma patient tumor constructs histological assessment. *Histological*

assessment of patient-derived mesothelioma organoids from both subjects after seven days

of incubation in DMEM. a, d) LIVE/DEAD-stained organoids. Green – calcein AM-stained

viable cells; Red – ethidium homodimer-stained dead cells. b, e) Cytokeratin 5/6 and

calretinin double-stained organoid sections and c, f) cytokeratin 5/6 and thrombomodulin

double-stained organoid sections. Scale bars for panels' a-f are 20 μm. For both, panel (i)

shows the double stain with DAPI-stained nuclei, and panel (ii) shows the double stain

with the DAPI channel removed, thereby highlighting the colocalization of biomarkers

(orange). g-h) Representative images (in this case subject 2 organoids) at increased resolution showing the yellow-red overlapping expression of the green channel (ck5/6) and the red channel (calretinin or thrombomodulin). Scale bars for panels' g-h are 10 μm.

3.3.5 *In vitro* chemotherapeutic drug screens correlate with subject drug response.
For both subjects, a series of constructs were initially kept under DMEM circulation for viability assessment. At the first time point (day 7 for subject 1 and day 1 for subject 2, due to relative growth kinetics of each population), viability analysis was performed on one construct from each subject (**Fig. 3a&c, top left**). We observed that the vast majority of cells were alive in each sample (93.3% and 84.5%, respectively), confirming that our device architecture could support patient-derived cells. On the same day, circulation to the remaining tumor constructs was either changed to one of two different doses of chemotherapeutic mixtures carboplatin/pemetrexed or cisplatin/pemetrexed or maintained with no drug as a control. Following an extended exposure, LIVE/DEAD analysis was performed on all organoids. Under control conditions, tumor constructs from both subjects were observed to maintain high viability: subject 1 organoids showed a statistically insignificant decrease to 87% live cells after a total of 14 days in the system (**Fig. 3a, top right**), while subject 2 organoids showed 83.1% live cells after a total of 7 days in the system (**Fig. 3c, top right**). These results demonstrated an ability to maintain tumor organoid viability *in vitro*. However, organoids exposed to drug mixtures showed differential reductions in the live-cell ratio (**Fig. 3a&c, bottom**). For subject 1 organoids treated with carboplatin/pemetrexed (0.1 μM/0.1 μM or 10 μM/10 μM), we found viabilities reduced to 52.1% for a circulating concentration of 0.1 μM and to 39.8% for 10

µM. While the high dose was two orders of magnitude greater concentration than the low dose, the observed change in viability indicated a potentially moderate effect of the drug. In contrast, organoids treated with cisplatin/pemetrexed (0.1 µM/0.1 µM or 10 µM/10 µM) yielded decreases in viability to 39.0% for 0.1 µM concentration and to 11.8% for 10 µM. These represented significant declines relative both to each other ($p<0.05$) and to control measurements ($p<0.05$ and $p<0.01$, respectively). Consequently, cisplatin/pemetrexed was considerably more effective than carboplatin/pemetrexed in our *in vitro* system. Interestingly, subject 2 organoids displayed a differing drug response, thereby illustrating patient-to-patient tumor heterogeneity. Specifically, subject 2 organoids did not respond significantly to cisplatin/pemetrexed (0.2 µM/0.2 µM or 20 µM/20 µM) in a dose-dependent manner, with viabilities reduced to 62.2% for a circulating concentration of 0.1 µM and to 62.5% for 10 µM. Conversely, subject 2 organoids responded to carboplatin/pemetrexed (0.2 µM/0.2 µM or 20 µM/20 µM), which yielded decreases in viability to 54.5% for 0.1 µM concentration and to 43.7% for 10 µM, similar to patient 1.

These results have two central outcomes. First, they demonstrate that cells derived from patient tumor biopsies can be sustained in a bioengineered organoid system long-term for extensive study and, importantly, that they maintain their mesothelioma phenotype. To our knowledge, this is the first report of this capability. Second, they show that *in vitro* drug screening of such organoids is feasible, yielding drug-dependent reductions in cellular viability. This represents a potential asset to therapy design, as drug efficacy could, in principle, be established in a patient-specific manner prior to the administration of treatment. For example, in these measurements, our results with subject 1 organoids would suggest cisplatin/pemetrexed as a superior treatment option to carboplatin/pemetrexed. The

nature of personalized medicine prevents a systematic comparison of the effectiveness of the two agents in the patient. Crucially, subject 1 was treated with cisplatin/pemetrexed with excellent response. Conversely, subject 2 had no significant response to cisplatin therapy. This is also observed in our organoid platform experiments and suggests that patient-specific drug effectiveness may be recapitulated accurately in our system. Additionally, our approach supports inter-patient heterogeneity of drug response. For example, in subject 2 organoid drug screens, we observed a more effective drug response to carboplatin/pemetrexed therapy, rather than cisplatin/pemetrexed therapy. This result demonstrates that drug responses measured *in vitro* are not a function of the system, which was identical for subjects 1 and 2, but rather dependent on individual susceptibilities. Notably, it is often the case clinically that drug responses can vary wildly despite patients having similar tumor types or grades, thus illustrating the need for improved personalized medicine approaches.
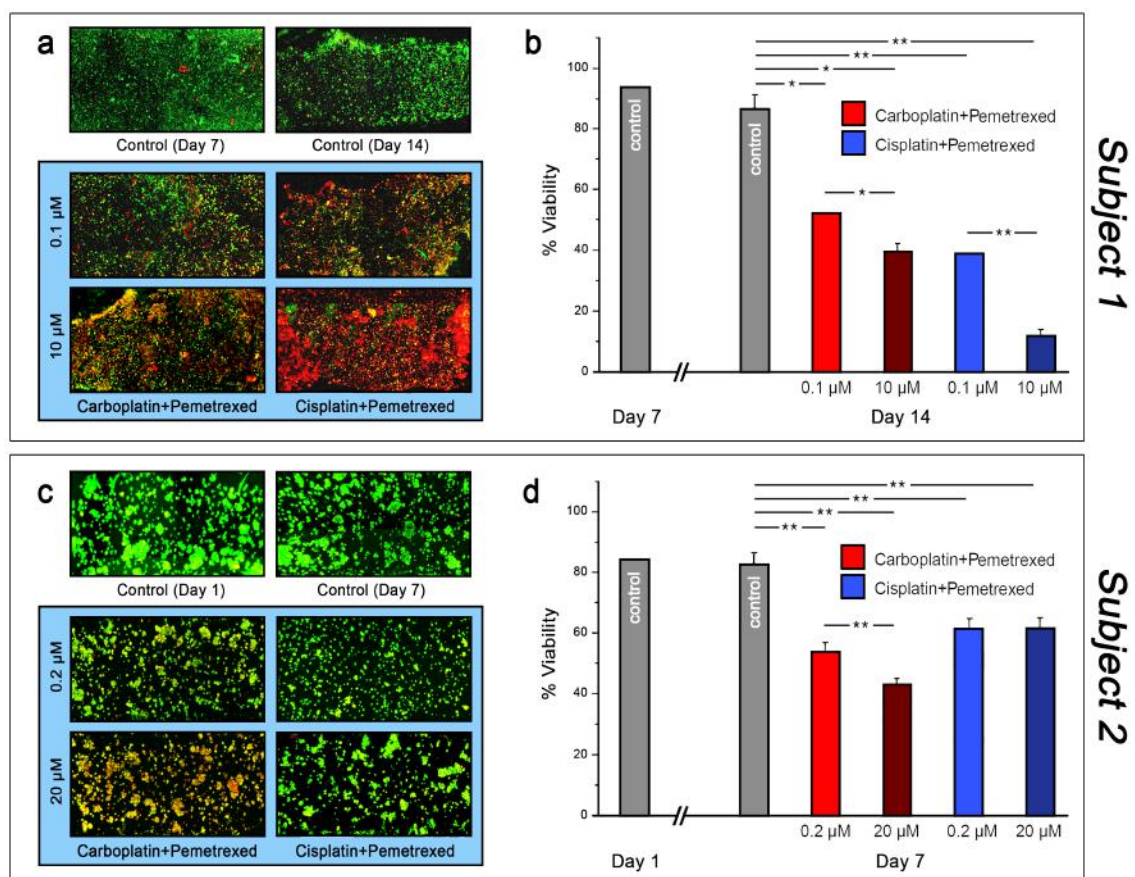
Figure 3.10. In vitro chemotherapy assessment in organoids derived from mesothelioma patients. *Maximum projection confocal images of LIVE/DEAD-stained tumor constructs for subject 1 (a) and subject 2 (c) under conditions indicated. Green: Calcein AM-stained viable cells; Red: Ethidium homodimer-stained dead cells. Analyses of drug-treated constructs collected on day 14 (a) and day 7 (c). Viability (% live cell count) measurements derived from images for all conditions for subject 1 (b) and subject 2 (d). Significance: * p<0.05, ** p<0.01.*

3.4 Discussion and Conclusion

Precision oncology, whereby tumor DNA is sequenced to identify actionable gene mutations, is poised to become a standard clinical practice for therapeutic decision making of cancer treatment [64-66]. Currently, however, only 11% of precision medicine tested patients will follow a precision medicine guided treatment [67] because any expected correlation between genetic alteration and a potential drug cannot be verified prior to initiation of treatment. Moreover, the biological behavior of cancer varies tremendously based on histologic type, grade, and volume of disease. Therefore, novel technologies capable of extending the diagnostic utility of tissue specimens are critically needed for robust assessment of genetic alterations and validation of these alterations as actionable targets.

As a research tool, sponge-gel-supported 3D histoculture and patient-derived xenografts (PDX) have been used to study patient tumor progression and drug treatment response. The critical challenge with the sponge assay, though it very well correlates with the *in vivo* drug sensitivity, is its high variability between samples. These differences caused by the variation in the size of the tumor requires data normalization to make comparisons between different tumor fragments feasible. Also, this technique has a very low culture success rate, making it less desirable for clinical applications [68]. On the other hand, a challenge of animal PDX models is that they must be hosted by immunodeficient mice and can thus become infiltrated with cells from the mouse, perturbing their natural states. Patient cells also adapt to their new environment and exhibit genetic drift, adding variability. However, the most fundamental limitation to the widespread adoption of PDX technology is that only the most aggressive tumor biospecimens prosper in immunodeficient mice. This reduced

take rate limits the application of PDX technology to predictive diagnostics for the majority of cancer patients. A major open question for *in vitro* platforms like the ones described here has been whether the low take rate observed in sponge assay and PDX (and equally in conventional 2D cell culture) could be overcome. Crucially, this can be achieved easily in our platform, where we can obtain high cell viability in organoids up to 14 days (**Fig. 3.9.a**). Moreover, in accompanying studies using identical techniques to produce organoids from additional mesothelioma biospecimens and other GI tumor biospecimens (data not shown), we have observed a take rate above 80%. Beyond high viability, we have also confirmed maintenance of the key HNSCC (overexpressed EGFR, cathepsin B &D) and mesothelioma biomarkers (CK5/6, calretinin, and thrombomodulin) in patient-derived organoids (**Figure 3.4 and 3.9**), showing that our approach supports a degree of the accurate tumor phenotype. These results are the first of their kind and suggest that the use of 3D organoid technology incorporating ECM-mimicking microenvironments may be deployable as accurate tumor models for more patients than PDX. Further studies of platform robustness, reproducibility, and take rate efficiency are currently underway.

As our first step, we demonstrated our ability to biofabricate highly viable patient-derived tumor organoids modeling HNSCC. These organoids were made from the primary tumor cells derived from the patient without any passaging, thus maintaining the genetic makeup and heterogeneity of the tumor. Also, we fabricated our organoids using HA-based hydrogel as a scaffold that has similar physically and chemically properties as native ECM. These two aspects of the organoid make its better representative model of the disease and accurately capturing the *in vivo* conditions. We then used this personalized tumor model to establish an *in vitro* drug testing platform that can accurately predict the drug response of

the patient. Hence these PDOs were used to test a range of drugs commonly used for HNSCC treatment along with radiation therapy. It is to be noted that there have not been many previous HNSCC models that tested radiation therapy effects along with chemotherapy. We were able to observe both dose-dependent and tumor dependent drug responses between each patient in our organoid verifying our ability to capture the *in vivo* heterogeneity of the tumor. The superiority of the organoid developed was evident from the comparison of data with the most commonly used 3D sponge assay model. The sponge assays' substantial variability between sample drug response leads to inconclusive results, whereas PDOs were able to produce very consistent data. Using the PDOs, we also demonstrated our ability to validate the functioning of the experimental drug β-Lap by using an NQO1 inhibitor, dicoumarol. This suggests that the system can also be expended to conduct drug discovery and preclinical testing.

Using our patient-specific tumor-on-a-chip technology, we demonstrated the feasibility of *in vivo* like tumor organoid drug response that was validated against the patient's own drug sensitivity results. With mesothelioma biospecimens from 2 different subjects with mesothelioma, we employed the organoid platform to screen two standard chemotherapy regimens used clinically for mesothelioma. Specifically, we tested responses to the combination of cisplatin and pemetrexed versus carboplatin and pemetrexed (**Figure 3.10**). Exposure to each drug for 7 days through infusion into circulating media via the microfluidic system yielded a distinctly higher efficacy for cisplatin/pemetrexed as compared to carboplatin/pemetrexed at the same concentrations in organoids derived from subject 1. On its own, this result validates the utility of the platform for performing drug screening studies in general. But importantly, the result is also consistent with clinical

outcomes; the patient donor responded dramatically to cisplatin-based chemotherapy, presenting almost complete resolution of voluminous ascites on CT imaging performed at the conclusion of cisplatin-based chemotherapy. This kind of significant correlation between patient and *in vitro* model is crucial to validate a methodology for clinical adoption. Additionally, we demonstrated an aspect of patient-to-patient tumor heterogeneity. Specifically, while subject 1 organoids responded best to cisplatin/pemetrexed, subject 2 organoids responded more effectively to carboplatin/pemetrexed. This is a significant result, as differential responses to the same therapies are often observed in the clinic. Moreover, subject 2 organoids did not respond significantly to cisplatin-based therapy, matching what was observed *in vivo*. While we consider only two subjects in this foundational study, these striking similarities to subject responses speak to the potential of our platform technology to provide relevant information for clinical practice. Continuing work will further validate this concept as additional patient samples are employed.

A key feature of our platform is the integration of PDOs with the AFB microfluidic delivery system. Though PDOs were able to capture the complexity of *in vivo* tumor microenvironment, it is essential also to recapitulate the fluid dynamics in the system to enhance the culture viability for the long term while maintaining the biological and mechanical properties of the organoid. In these foundational studies, we have employed this platform to act as a delivery system to supply nutrients and remove waste from each chamber to better mimic the microenvironment of tumor cell growth[69]. It also supported moderate parallelization of the system, but the overall approach could be easily expanded to study a broader range of drugs, drug combinations, and exposure doses. The form factor

of such devices also enables direct cellular imaging, which, in addition to viability assessment, could be exploited for tracking the kinetics of tumor progression, migration, and intravasation into circulation. Additionally, the platform opens a route to evolve the tumor-on-a-chip device to a multi-organoid metastasis-on-a-chip device, thereby allowing the analysis of tumor progression all the way to distant metastatic sites. We have demonstrated such a system using cell lines [36], and are currently working to incorporate patient-specific biospecimens.

While personalized tumor organoid technology is in its infancy, it holds incredible clinical potential. Once validated through correlation of additional patient-derived organoid drug responses with clinical outcomes, wide adoption of such systems may be able to significantly improve outcomes of cancer patients and reduce unnecessary health care costs through quick matching with the best available effective drugs at the single patient level.

References

[1]   N.H. Tran, L.L. Cavalcante, S.J. Lubner, D.L. Mulkerin, N.K. LoConte, L. Clipson, K.A. Matkowskyj, and D.A. Deming, *Precision medicine in colorectal cancer: the molecular profile alters treatment strategies.* Ther Adv Med Oncol, 2015. **7**(5): p. 252-62.

[2]   G. Miles, J. Rae, S.S. Ramalingam, and J. Pfeifer, *Genetic Testing and Tissue Banking for Personalized Oncology: Analytical and Institutional Factors.* Semin Oncol, 2015. **42**(5): p. 713-723.

[3]   H. Bando and N. Takebe, *Recent innovations in the USA National Cancer Institute-sponsored investigator initiated Phase I and II anticancer drug development.* Jpn J Clin Oncol, 2015.

[4]   D.F. Hayes and A.F. Schott, *Personalized Medicine: Genomics Trials in Oncology.* Trans Am Clin Climatol Assoc, 2015. **126**: p. 133-43.

[5]   M.A. Cantrell and C.J. Kuo, *Organoid modeling for cancer precision medicine.* Genome Med, 2015. **7**(1): p. 32.

[6]   D. Gao, I. Vela, A. Sboner, P.J. Iaquinta, W.R. Karthaus, A. Gopalan, C. Dowling, J.N. Wanjala, E.A. Undvall, V.K. Arora, J. Wongvipat, M. Kossai, S. Ramazanoglu, L.P. Barboza, W. Di, Z. Cao, Q.F. Zhang, I. Sirota, L. Ran, T.Y. MacDonald, H. Beltran, J.M. Mosquera, K.A. Touijer, P.T. Scardino, V.P. Laudone, K.R. Curtis, D.E. Rathkopf, M.J. Morris, D.C. Danila, S.F. Slovin, S.B. Solomon, J.A. Eastham, P. Chi, B. Carver, M.A. Rubin, H.I. Scher, H. Clevers, C.L. Sawyers, and Y. Chen, *Organoid cultures derived from patients with advanced prostate cancer.* Cell, 2014. **159**(1): p. 176-87.

[7]   S. Bhattacharya, Q. Zhang, P.L. Carmichael, K. Boekelheide, and M.E. Andersen, *Toxicity testing in the 21 century: defining new risk assessment approaches based on perturbation of intracellular toxicity pathways.* PLoS One, 2011. **6**(6): p. e20887.

[8]   L.A. Kunz-Schughart, J.P. Freyer, F. Hofstaedter, and R. Ebner, *The use of 3-D cultures for high-throughput screening: the multicellular spheroid model.* J Biomol Screen, 2004. **9**(4): p. 273-85.

[9]   W.J. Ho, E.A. Pham, J.W. Kim, C.W. Ng, J.H. Kim, D.T. Kamei, and B.M. Wu, *Incorporation of multicellular spheroids into 3-D polymeric scaffolds provides an improved tumor model for screening anticancer drugs.* Cancer Sci, 2010. **101**(12): p. 2637-43.

[10]   M. Drewitz, M. Helbling, N. Fried, M. Bieri, W. Moritz, J. Lichtenberg, and J.M. Kelm, *Towards automated production and drug sensitivity testing using scaffold-free spherical tumor microtissues.* Biotechnol J, 2011. **6**(12): p. 1488-96.

[11]   A. Skardal, M. Devarasetty, C. Rodman, A. Atala, and S. Soker, *Liver-Tumor Hybrid Organoids for Modeling Tumor Growth and Drug Response In Vitro.* Ann Biomed Eng, 2015. **43**(10): p. 2361-73.

[12]   B. Mery, C. Rancoule, J.B. Guy, S. Espenel, A.S. Wozny, P. Battiston-Montagne, D. Ardail, M. Beuve, G. Alphonse, C. Rodriguez-Lafrasse, and N. Magne, *Preclinical models in HNSCC: A comprehensive review.* Oral Oncol, 2017. **65**: p. 51-56.

[13]   A.J. Dohmen, J.E. Swartz, M.W. Van Den Brekel, S.M. Willems, R. Spijker, J. Neefjes, and C.L. Zuur, *Feasibility of Primary Tumor Culture Models and Preclinical Prediction Assays for Head and Neck Cancer: A Narrative Review.* Cancers (Basel), 2015. **7**(3): p. 1716-42.

[14]   J. Leighton, *A sponge matrix method for tissue culture; formation of organized aggregates of cells in vitro.* J Natl Cancer Inst, 1951. **12**(3): p. 545-61.

[15]   D. Huh, G.A. Hamilton, and D.E. Ingber, *From 3D cell culture to organs-on-chips.* Trends in Cell Biology, 2011. **21**(12): p. 745-754.

[16]   A.M. Ghaemmaghami, M.J. Hancock, H. Harrington, H. Kaji, and A. Khademhosseini, *Biomimetic tissues on a chip for drug discovery.* Drug Discov Today, 2011.

[17]   A. Polini, L. Prodanov, N.S. Bhise, V. Manoharan, M.R. Dokmeci, and A. Khademhosseini, *Organs-on-a-chip: a new tool for drug discovery.* Expert Opin Drug Discov, 2014. **9**(4): p. 335-52.

[18]   A. Skardal, M. Devarasetty, S. Soker, and A.R. Hall, *In situ patterned micro 3D liver constructs for parallel toxicology testing in a fluidic device.* Biofabrication, 2015. **7**(3): p. 031001.

[19]   K.H. Benam, S. Dauth, B. Hassell, A. Herland, A. Jain, K.J. Jang, K. Karalis, H.J. Kim, L. MacQueen, R. Mahmoodian, S. Musah, Y.S. Torisawa, A.D. van der Meer, R. Villenave, M. Yadid, K.K. Parker, and D.E. Ingber, *Engineered in vitro disease models.* Annu Rev Pathol, 2015. **10**: p. 195-262.

[20]   A. Skardal, S.V. Murphy, K. Crowell, D. Mack, A. Atala, and S. Soker, *A tunable hydrogel system for long-term release of cell-secreted cytokines and bioprinted in situ wound cell delivery.* J Biomed Mater Res B Appl Biomater, 2016.

[21]   A. Skardal, L. Smith, S. Bharadwaj, A. Atala, S. Soker, and Y. Zhang, *Tissue specific synthetic ECM hydrogels for 3-D in vitro maintenance of hepatocyte function.* Biomaterials, 2012. **33**(18): p. 4565-75.

[22]   G.D. Prestwich, *Simplifying the extracellular matrix for 3-D cell culture and tissue engineering: a pragmatic approach.* J Cell Biochem, 2007. **101**(6): p. 1370-83.

[23]   G.D. Prestwich, *Evaluating drug efficacy and toxicology in three dimensions: using synthetic extracellular matrices in drug discovery.* Acc Chem Res, 2008. **41**(1): p. 139-48.

[24]   G.D. Prestwich, Y. Liu, B. Yu, X.Z. Shu, and A. Scott, *3-D culture in synthetic extracellular matrices: new tissue models for drug toxicology and cancer drug discovery.* Adv Enzyme Regul, 2007. **47**: p. 196-207.

[25]   M.A. Serban and G.D. Prestwich, *Modular extracellular matrices: solutions for the puzzle.* Methods, 2008. **45**(1): p. 93-8.

[26]   A. Skardal, M. Devarasetty, S. Forsythe, A. Atala, and S. Soker, *A reductionist metastasis-on-a-chip platform for in vitro tumor progression modeling and drug screening.* Biotechnol Bioeng, 2016.

[27]   A. Skardal, M. Devarasetty, H.W. Kang, I. Mead, C. Bishop, T. Shupe, S.J. Lee, J. Jackson, J. Yoo, S. Soker, and A. Atala, *A hydrogel bioink toolkit for mimicking native tissue biochemical and mechanical properties in bioprinted tissue constructs.* Acta Biomater, 2015. **25**: p. 24-34.

[28]   A. Skardal, M. Devarasetty, H.W. Kang, Y.J. Seol, S.D. Forsythe, C. Bishop, T. Shupe, S. Soker, and A. Atala, *Bioprinting Cellularized Constructs Using a Tissue-specific Hydrogel Bioink.* J Vis Exp, 2016(110).

[29] A. Skardal, S.F. Sarker, A. Crabbe, C.A. Nickerson, and G.D. Prestwich, *The generation of 3-D tissue models based on hyaluronan hydrogel-coated microcarriers within a rotating wall vessel bioreactor.* Biomaterials, 2010. **31**(32): p. 8426-35.

[30] E.J. Park, K.j. Min, T.J. Lee, Y.H. Yoo, Y.S. Kim, and T.K. Kwon, *β-Lapachone induces programmed necrosis through the RIP1-PARP-AIF-dependent pathway in human hepatocellular carcinoma SK-Hep1 cells.* Cell Death & Disease, 2014. **5**(5): p. e1230-e1230.

[31] J.J. Pink, S.M. Planchon, C. Tagliarino, M.E. Varnes, D. Siegel, and D.A. Boothman, *NAD(P)H:Quinone oxidoreductase activity is the principal determinant of beta-lapachone cytotoxicity.* J Biol Chem, 2000. **275**(8): p. 5416-24.

[32] M. Ough, A. Lewis, E.A. Bey, J. Gao, J.M. Ritchie, W. Bornmann, D.A. Boothman, L.W. Oberley, and J.J. Cullen, *Efficacy of beta-lapachone in pancreatic cancer treatment: exploiting the novel, therapeutic target NQO1.* Cancer Biol Ther, 2005. **4**(1): p. 95-102.

[33] E.J. Park, K.S. Choi, and T.K. Kwon, *beta-Lapachone-induced reactive oxygen species (ROS) generation mediates autophagic cell death in glioma U87 MG cells.* Chem Biol Interact, 2011. **189**(1-2): p. 37-44.

[34] N. Bansal, J. Mims, J.G. Kuremsky, A.L. Olex, W. Zhao, L. Yin, R. Wani, J. Qian, B. Center, G.S. Marrs, M. Porosnicu, J.S. Fetrow, A.W. Tsang, and C.M. Furdui, *Broad phenotypic changes associated with gain of radiation resistance in head and neck squamous cell cancer.* Antioxid Redox Signal, 2014. **21**(2): p. 221-36.

[35] K.T. Robbins, K.M. Connors, A.M. Storniolo, C. Hanchett, and R.M. Hoffman, *Sponge-gel-supported histoculture drug-response assay for head and neck cancer. Correlations with clinical response to cisplatin.* Arch Otolaryngol Head Neck Surg, 1994. **120**(3): p. 288-92.

[36] A. Skardal, M. Devarasetty, S. Forsythe, A. Atala, and S. Soker, *A reductionist metastasis-on-a-chip platform for in vitro tumor progression modeling and drug screening.* Biotechnol Bioeng, 2016. **113**(9): p. 2020-32.

[37] G.A. Cooksey and J. Atencia, *Pneumatic valves in folded 2D and 3D fluidic devices made from plastic films and tapes.* Lab Chip, 2014. **14**(10): p. 1665-8.

[38]   Y. Hiraishi, T. Wada, K. Nakatani, K. Negoro, and S. Fujita, *Immunohistochemical expression of EGFR and p-EGFR in oral squamous cell carcinomas.* Pathol Oncol Res, 2006. **12**(2): p. 87-91.

[39]   A.C. Ford and J.R. Grandis, *Targeting epidermal growth factor receptor in head and neck cancer.* Head Neck, 2003. **25**(1): p. 67-73.

[40]   J. Rubin Grandis, M.F. Melhem, W.E. Gooding, R. Day, V.A. Holst, M.M. Wagener, S.D. Drenning, and D.J. Tweardy, *Levels of TGF-alpha and EGFR protein in head and neck squamous cell carcinoma and patient survival.* J Natl Cancer Inst, 1998. **90**(11): p. 824-32.

[41]   M.E. Christensen, *The EGF receptor system in head and neck carcinomas and normal tissues. Immunohistochemical and quantitative studies.* Dan Med Bull, 1998. **45**(2): p. 121-34.

[42]   R.G. Bonhin, G.M. Carvalho, A.C. Guimaraes, C.T. Chone, A.N. Crespo, A.M. Altemani, and E.M. Amstalden, *Histologic correlation of expression of Ki-67 in squamous cell carcinoma of the glottis according to the degree of cell differentiation.* Braz J Otorhinolaryngol, 2014. **80**(4): p. 290-5.

[43]   T. Furukawa, T. Kubota, M. Watanabe, T. Takahara, H. Yamaguchi, T. Takeuchi, S. Kase, S. Kodaira, K. Ishibiki, M. Kitajima, and et al., *High in vitro-in vivo correlation of drug response using sponge-gel-supported three-dimensional histoculture and the MTT end point.* Int J Cancer, 1992. **51**(3): p. 489-98.

[44]   X. Chen, J. Mims, X. Huang, N. Singh, E. Motea, S.M. Planchon, M. Beg, A.W. Tsang, M. Porosnicu, M.L. Kemp, D.A. Boothman, and C.M. Furdui, *Modulators of Redox Metabolism in Head and Neck Cancer.* Antioxid Redox Signal, 2018. **29**(16): p. 1660-1690.

[45]   D.A. Boothman, S. Greer, and A.B. Pardee, *Potentiation of halogenated pyrimidine radiosensitizers in human carcinoma cells by beta-lapachone (3,4-dihydro-2,2-dimethyl-2H-naphtho[1,2-b]pyran- 5,6-dione), a novel DNA repair inhibitor.* Cancer Res, 1987. **47**(20): p. 5361-6.

[46]   L.S. Li, S. Reddy, Z.H. Lin, S. Liu, H. Park, S.G. Chun, W.G. Bornmann, J. Thibodeaux, J. Yan, G. Chakrabarti, X.J. Xie, B.D. Sumer, D.A. Boothman, and

J.S. Yordy, *NQO1-Mediated Tumor-Selective Lethality and Radiosensitization for Head and Neck Cancer.* Mol Cancer Ther, 2016. **15**(7): p. 1757-67.

[47] G. Chakrabarti, D.E. Gerber, and D.A. Boothman, *Expanding antitumor therapeutic windows by targeting cancer-specific nicotinamide adenine dinucleotide phosphate-biogenesis pathways.* Clin Pharmacol, 2015. **7**: p. 57-68.

[48] K.E. Reinicke, E.A. Bey, M.S. Bentle, J.J. Pink, S.T. Ingalls, C.L. Hoppel, R.I. Misico, G.M. Arzac, G. Burton, W.G. Bornmann, D. Sutton, J. Gao, and D.A. Boothman, *Development of beta-lapachone prodrugs for therapy against human cancer cells with elevated NAD(P)H:quinone oxidoreductase 1 levels.* Clin Cancer Res, 2005. **11**(8): p. 3055-64.

[49] R. Docampo, F.S. Cruz, A. Boveris, R.P. Muniz, and D.M. Esquivel, *beta-Lapachone enhancement of lipid peroxidation and superoxide anion and hydrogen peroxide formation by sarcoma 180 ascites tumor cells.* Biochem Pharmacol, 1979. **28**(6): p. 723-8.

[50] L. Cao, L.S. Li, C. Spruell, L. Xiao, G. Chakrabarti, E.A. Bey, K.E. Reinicke, M.C. Srougi, Z. Moore, Y. Dong, P. Vo, W. Kabbani, C.R. Yang, X. Wang, F. Fattah, J.C. Morales, E.A. Motea, W.G. Bornmann, J.S. Yordy, and D.A. Boothman, *Tumor-selective, futile redox cycle-induced bystander effects elicited by NQO1 bioactivatable radiosensitizing drugs in triple-negative breast cancers.* Antioxid Redox Signal, 2014. **21**(2): p. 237-50.

[51] K.E. Reinicke, *Development of -Lapachone Prodrugs for Therapy Against Human Cancer Cells with Elevated NAD(P)H:Quinone Oxidoreductase 1 Levels.* Clinical Cancer Research, 2005. **11**(8): p. 3055-3064.

[52] S.M. Planchon, J.J. Pink, C. Tagliarino, W.G. Bornmann, M.E. Varnes, and D.A. Boothman, *beta-Lapachone-induced apoptosis in human prostate cancer cells: involvement of NQO1/xip3.* Exp Cell Res, 2001. **267**(1): p. 95-106.

[53] J.Z. Li, Y. Ke, H.P. Misra, M.A. Trush, Y.R. Li, H. Zhu, and Z. Jia, *Mechanistic studies of cancer cell mitochondria- and NQO1-mediated redox activation of beta-lapachone, a potentially novel anticancer agent.* Toxicology and Applied Pharmacology, 2014. **281**(3): p. 285-293.

[54] J. Kumi-Diaka, S. Saddler-Shawnette, A. Aller, and J. Brown, *Potential mechanism of phytochemical-induced apoptosis in human prostate adenocarcinoma cells: Therapeutic synergy in genistein and beta-lapachone combination treatment.* Cancer Cell Int, 2004. **4**(1): p. 5.

[55] J.J. Pink, S. Wuerzberger-Davis, C. Tagliarino, S.M. Planchon, X. Yang, C.J. Froelich, and D.A. Boothman, *Activation of a cysteine protease in MCF-7 and T47D breast cancer cells during beta-lapachone-mediated apoptosis.* Exp Cell Res, 2000. **255**(2): p. 144-55.

[56] J.Z. Li, Y. Ke, H.P. Misra, M.A. Trush, Y.R. Li, H. Zhu, and Z. Jia, *Mechanistic studies of cancer cell mitochondria- and NQO1-mediated redox activation of beta-lapachone, a potentially novel anticancer agent.* Toxicol Appl Pharmacol, 2014. **281**(3): p. 285-93.

[57] X. Sun, Y. Li, W. Li, B. Zhang, A.J. Wang, J. Sun, K. Mikule, Z. Jiang, and C.J. Li, *Selective induction of necrotic cell death in cancer cells by beta-lapachone through activation of DNA damage response pathway.* Cell Cycle, 2006. **5**(17): p. 2029-35.

[58] J.E. Lewis, F. Costantini, J. Mims, X. Chen, C.M. Furdui, D.A. Boothman, and M.L. Kemp, *Genome-Scale Modeling of NADPH-Driven β-Lapachone Sensitization in Head and Neck Squamous Cell Carcinoma.* Antioxidants & Redox Signaling, 2018. **29**(10): p. 937-952.

[59] J. Mims, N. Bansal, M.S. Bharadwaj, X. Chen, A.J. Molina, A.W. Tsang, and C.M. Furdui, *Energy metabolism in a matched model of radiation resistance for head and neck squamous cell cancer.* Radiat Res, 2015. **183**(3): p. 291-304.

[60] Y. Takeshima, V.J. Amatya, K. Kushitani, and K. Inai, *A useful antibody panel for differential diagnosis between peritoneal mesothelioma and ovarian serous carcinoma in Japanese cases.* Am J Clin Pathol, 2008. **130**(5): p. 771-9.

[61] C. Doglioni, A.P. Dei Tos, L. Laurino, P. Iuzzolino, C. Chiarelli, M.R. Celio, and G. Viale, *Calretinin: a novel immunocytochemical marker for mesothelioma.* Am J Surg Pathol, 1996. **20**(9): p. 1037-46.

[62]   M.P. Leers, M.M. Aarts, and P.H. Theunissen, *E-cadherin and calretinin: a useful combination of immunochemical markers for differentiation between mesothelioma and metastatic adenocarcinoma.* Histopathology, 1998. **32**(3): p. 209-16.

[63]   C.L. Collins, N.G. Ordonez, R. Schaefer, C.D. Cook, S.S. Xie, J. Granger, P.L. Hsu, L. Fink, and S.M. Hsu, *Thrombomodulin expression in malignant pleural mesothelioma and pulmonary adenocarcinoma.* Am J Pathol, 1992. **141**(4): p. 827-33.

[64]   J. Glade Bender, A. Verma, and J.D. Schiffman, *Translating genomic discoveries to the clinic in pediatric oncology.* Curr Opin Pediatr, 2015. **27**(1): p. 34-43.

[65]   F. Andre, E. Mardis, M. Salm, J.C. Soria, L.L. Siu, and C. Swanton, *Prioritizing targets for precision cancer medicine.* Ann Oncol, 2014. **25**(12): p. 2295-303.

[66]   S. Roychowdhury and A.M. Chinnaiyan, *Translating genomics for precision cancer medicine.* Annu Rev Genomics Hum Genet, 2014. **15**: p. 395-415.

[67]   D.P. Sohal, B.I. Rini, A.A. Khorana, R. Dreicer, J. Abraham, G.W. Procop, Y. Saunthararajah, N.A. Pennell, J.P. Stevenson, R. Pelley, B. Estfan, D. Shepard, P. Funchain, P. Elson, D.J. Adelstein, and B.J. Bolwell, *Prospective Clinical Study of Precision Oncology in Solid Tumors.* J Natl Cancer Inst, 2015. **108**(3).

[68]   Y.C. Lim, S.Y. Oh, Y.Y. Cha, S.H. Kim, X. Jin, and H. Kim, *Cancer stem cell traits in squamospheres derived from primary head and neck squamous cell carcinomas.* Oral Oncol, 2011. **47**(2): p. 83-91.

[69]   M. Kapalczynska, T. Kolenda, W. Przybyla, M. Zajaczkowska, A. Teresiak, V. Filas, M. Ibbs, R. Blizniak, L. Luczewski, and K. Lamperska, *2D and 3D cell cultures - a comparison of different types of cancer cell cultures.* Arch Med Sci, 2018. **14**(4): p. 910-919.

CHAPTER 4

Multi-domain photo-patterned 3D tumor constructs in a micro-physiological system for analysis, quantification, and isolation of infiltrating cells

Metastasis is a multi-step process in tumor progression were highly aggressive cancer cells migrate from their primary tumor location through a complex microenvironment to invade into a distant tissue and colonize to form a secondary tumor. Understanding the mechanisms of this process has been a significant challenge and hence, developing anti-metastatic treatment strategies has been difficult. This ineffectiveness in treating metastases has led to the development of multiple cancer invasion assays in both 2D and 3D to understand metastasis better and eventually aid in evaluations of anti-metastatic drugs. Though migration assays based on 2D cell culture have provided some information on cancer cell motility, they do not capture the *in vivo* complexity of the metastatic process. Hence, 3D models are better suited to study migration under a more realistic microenvironment and extracellular matrix (ECM) architecture. However, such models have significant challenges, including difficulties in direct imaging to track cell movement, inadequate control of microenvironment characteristics, and limited throughput. To date, animal studies are considered a golden standard for the preclinical model. The model does provide a highly complex environment, but it becomes challenging to do most analysis and quantification as direct visualizing is challenging. Moreover, manipulating the pharmacology and mechanobiology is not very easy to achieve. These challenges can be overcome by integrating microfluidics with an *in situ* 3D invasion assay as it provides a highly controllable environment for mechanical interactions. These systems are highly reproducible and support directed migration with a concentration gradient.

In this chapter, we discuss a multi-domain photopatterned cancer model in an adhesive-film based (AFB) microfluidic device to study the initial step of metastases: cell migration. The 3D *in vitro* cancer model developed in chapter 2 is adapted by integrating *in situ*, multi-step photopatterning in a microfluidic device to realize a parallelizable invasion assay. We have already demonstrated that the tumor model mimics the *in vivo* environment and drug response. Hence, integrating the invasion assay with this model provides relevant information on tumor cell migration. The system also allows cell-tracking via confocal imaging for quantification and analysis of the infiltrating cells. First, we show the influence of interstitial flow on directed cell migration. Then we probe the effect of ECM stiffness on migration using a colorectal tumor construct composed of HCT116 cells. Next, we investigate the effects on the migration ability of HCT116 cells of two chemotherapeutic drugs: the anti-proliferative 5-Fluorouracil and the anti-migratory Marimastat. Finally, we demonstrate selective isolation of infiltrating cells by employing a cleavable hydrogel. In total, our results build on the past tumor-on-a-chip systems to advance the study of cancer cell migration.

Note:

The contents of this chapter have been submitted as a peer-reviewed article.

Peer-reviewed Publication:

'Multi-domain photopatterned 3D tumor constructs in a micro-physiological system for analysis, quantification, and isolation of infiltrating cells', **Shiny A. P. Rajan,** *Aleksander Skardal, and Adam R. Hall. Advanced Biosystems 2020. (In press)*

Abstract:

Cancer cell motility plays a central role in metastasis and tumor invasion, but it can be challenging to study accurately *in vitro*. Here, we describe a simple approach to address this challenge through the novel use of monolithic, photopatterned 3D tumor constructs formed *in situ* in a microfluidic device. Through the step-wise fabrication of adjoining hydrogel regions with and without incorporated cells, we produced multidomain structures with defined boundaries. By imaging cells over time, we were able to study cellular activity with arbitrary control over medium conditions, including drug concentration and flow rate. Using this approach, we first studied the influence of mechanical properties like the interstitial flow and ECM stiffness on highly malignant human colon carcinoma cells (HCT116) for 7 days by comparing the invasion dynamics of these cells into the hydrogel. Then we analyzed the invasion dynamics and viability between HCT116 tumor construct in traditional media to those exposed to two independent chemotherapeutic drugs: the anti-proliferative 5-fluorouracil and the anti-migratory Marimastat. We measured dose-dependent cytotoxicity and observed significant differences in cellular dynamics (i.e., distance traveled, velocity, and the number of migrated cells) that correlated with the mechanism of each drug. Then, we established that the platform also enables the selective isolation of infiltrated cells through the photopatterning and subsequent dissolution of a cleavable hydrogel domain. As a demonstration, we show the preferential collection of highly migratory cells (HCT116) over a comparable cell line with low malignancy and migratory potential (Caco-2).

4.1 Introduction

Metastasis are thought to be responsible for more than 90% of cancer-related deaths[1]. It is generally agreed that the process of metastasis involves multiple steps[2], including the movement of tumor cells into adjacent tissues, migration through the endothelium into blood vessels or lymphatics (intravasation), passage via circulation, and extravasation to and proliferation in distant tissue. However, the factors that contribute to this complex cascade of events are poorly understood; thus, there is a need for improved model systems to investigate them. Even the initial stage of metastasis, in which cancer cells infiltrate locally into adjacent tissue, is difficult to study *in vitro* because available technologies represent the *in vivo* environment poorly and have characteristics that may be practically or experimentally restrictive. For example, established techniques[3] like the classical transwell migration assay[4] and scratch assay[5] have proven to be valuable for probing chemotaxis and wound healing potential, respectively, however, they feature two-dimensional (2D) cell cultures that do not reflect the three-dimensional (3D) nature of tissues in which cancer cells reside and require large amounts of cells. Additionally, many conventional assays typically do not allow for the real-time assessment of cell viability; a capacity that is especially critical for studying the effects of therapeutic agents that may target metastasis.

Microfluidic systems can be used to offset several of the limitations encountered with conventional assays by requiring a low number of cells and enabling direct cell imaging and can also facilitate dynamic fluid delivery. However, most microfluidic-based approaches that have been reported to date probe single-cell[6] motility, often through artificial channels, or else involve 2D culture[7, 8] motility. As a result, their relationship to

physiological systems is uncertain. A limited number of strategies have been developed to integrate 3D cell cultures into the platform, including invasion from spheroids into surrounding gels[9]. However, most such efforts have employed either laminar flow profiles or physical barriers[10-15] to produce adjoining domains, thus restricting construct geometry, limiting parallelization and rapid fluid exchange, and increasing overall device complexity.

Here, we describe a simple and versatile approach for the *in situ* formation of 3D constructs in a pre-formed microfluidic architecture (**Figure 4.1.a**) that can be used for concurrent cell migration and viability assessment under media exposure (**Figure 4.1.b**). We utilize a serial *in situ* photopatterning technique (**Figure 4.1.c**) to define multi-domain constructs composed of both cell-laden and cell-free regions. The entire construct is composed of a single, monolithic hyaluronic acid (HA)/gelatin hydrogel, but features a defined boundary between regions (**Figure 4.1.c, right**) for quantitative analysis of cell infiltration. As a demonstration, we integrated highly invasive HCT-116 human colon carcinoma cells that express mCherry fluorescent protein into our constructs to enable direct imaging of cells over time. We first showed that the interstitial flow-induced bias of cell movement could be mitigated through intermittent delivery of fresh buffer to the construct to maintain high viability and yield purely cell-driven motility. We then probed the effects of ECM stiffness on the migration of cells and demonstrated that the increasing matrix stiffness influences cell migration positively and promotes proliferation. Then we investigated the effects of two chemotherapeutic drugs: the thymidylate synthase inhibitor 5-fluorouracil (5FU) and the matrix metalloproteinases (MMP) inhibitor Marimastat. We demonstrated that the total number of cells infiltrating into the adjacent regions of the construct was reduced with increasing 5FU concentration, even while both the distance traveled by and the mean

velocity of infiltrating cells were not significantly affected. In contrast, we found that increasing Marimastat exposure significantly reduced the total number of infiltrating cells, their distance migrated, and their mean velocity. Furthermore, we demonstrated our ability to biofabricate a cell-free region of the construct with a cleavable hydrogel, enabling the domain to be chemically dissolved to isolate and recover the infiltrating cells. Our results illustrate the efficacy of our platform in delivering quantitative cell migration and viability data with dynamic control of buffer and drug conditions using a simple and rapid system.

4.2 Experimental Methods

4.2.1 Microfluidic device fabrication:

Microfluidic devices were produced using a low-cost, rapid-prototyping approach pioneered by Cooksey et al. [16] based on patterned adhesive films. **Figure 4.1.a** shows a diagram of the overall device fabrication strategy. Six discrete channels were formed in an adhesive film (140 μm thickness, part number 3M9495MPF, Strouse, Westminster, MD) using a computer-controlled razor plotter (CE6000-40, Graphtec, Irvine, CA) and layered on a clean glass microscope slide (VWR, Radnor, PA). Next, a polymethylmethacrylate (PMMA, McMaster-Carr, Elmhurst, IL) sheet cut to the same slide dimensions was furnished with inlet/outlet openings using a laser etcher (Full Spectrum Laser H-series, Las Vegas, NV) and subsequently layered on the patterned film to facilitate access to the enclosed channels. Even pressure was applied to ensure proper sealing of the device. The completed structure was further layered with four layers of patterned adhesive films and laser-etched PMMA to form an on-device bubble trap based on the design of Zheng et al.

[17], to aid in preventing bubble formation or deposition in the channel that could interfere with performance. The functioning of the bubble trap component is described in more detail in **APPENDIX III – A3. 1**. Finally, polytetrafluoroethylene (PTFE) tubing was inserted into each port in the PMMA slide for fluid delivery and was secured using a UV-cure polyester resin (Solarez, Vista, CA). Each channel in the device was connected to an independent reservoir by Silastic tubing (Corning, Inc., Corning, NY) through a micro-peristaltic pump (MP2 Precision, Elemental Scientific, Inc., Omaha, NE) to facilitate flow through all channels simultaneously (**Figure 4.1.b**). Cell culture constructs were maintained under intermittent flow (4 µL/min for 10 min, followed by 120 min with no flow), as controlled by an in-house-designed LabView program (National Instruments, Austin, TX) for the duration of the experiments unless otherwise noted. The purpose of the intermittent flow was to introduce a fresh supply of nutrients and oxygen at regular intervals as well as remove any high local concentration of waste products. Because the system was closed, secreted signaling molecules were recirculated.

4.2.2 Culturing of cells:

A human colon carcinoma cell line (HCT-116) engineered to express mCherry[18] was used in all experiments representing colorectal cancer. For co-culture experiments, human epithelial colorectal adenocarcinoma cells (Caco-2) cells were also used. Both cell types were cultured independently in 15 cm round cell culture dishes using 15 mL of Dulbecco's Modified Eagle's Medium (DMEM-10) supplemented with 10% (v/v) fetal bovine serum, 1% (v/v) L-glutamine, and 1% (v/v) penicillin-streptomycin solution. Both cultures were

maintained in an incubator at 37°C with 5% CO_2. Cells were passaged twice a week upon reaching 70–80% confluency using trypsin (0.05%, Difco Laboratories, Detroit, MI). Cells were collected using the same trypsinization approach prior to their incorporation into microfluidic devices.

4.2.3 Cell labeling using Qtracker®:

Caco-2, SCC-61 and rSCC-61 cells with no intrinsic fluorophore expression were tracked using Qtracker® 525 (ThermoFisher, Waltham, MA) according to the manufacturer's instructions; this delivered green-fluorescent Qdot® 525 nanocrystals into the cytoplasm of live cells. Briefly, a 20 nM labeling solution was prepared by mixing 2 μL each of Qtracker® Components A and B in DMEM-10 media. The cell suspension (~1.8×10^7 cells/mL) was added to the labeling solution and incubated at 37°C for 60–90 minutes. The cells were mixed thoroughly in the labeling solution by pipetting every 15 mins during the incubation to improve cell labeling efficiency. The cells were then washed twice with DMEM-10, and the labeling was confirmed through fluorescence imaging of a small aliquot. The labeled cells were then centrifuged to form a pellet for use in experiments.

4.2.4 Hydrogel preparation:

The HA/gelatin hydrogel (HyStem-HP, ESI-BIO, Alameda, CA) was prepared as previously described previously [19-21]. Briefly, sterile water was mixed with 0.05% (w/v) 2-hydroxy-4′-(2-hydroxyethoxy)-2-methylpropiophenone photoinitiator (Sigma Aldrich,

St. Louis, MO) and then used to produce solutions of thiol-modified hyaluronan (Heparasil®), thiol-modified gelatin (Gelin-S®), and thiol-reactive polyethylene glycol diacrylate (PEGDA) crosslinker (Extralink®) at concentrations of 1% w/v each. The Heparasil®, Gelin-S®, and Extralink® solutions were then mixed at a ratio of 2:2:1 (v/v), respectively, to form the HA hydrogel precursor. For experiments requiring downstream dissolving of the hydrogel, the PEGDA crosslinker was replaced with disulfide-containing polyethylene glycol diacrylate (PEGSSDA®) crosslinker. The remaining components were prepared, as described above. Similarly, for generating stiffer hydrogel, the acrylate-functionalized 4-arm PEG crosslinker (10 kDa MW, Creative PEGworks, Winston-Salem, NC) was used instead of Extralink®) at a concentration of 4% and 8% w/v. To accelerate cell migration in co-culture, 200 ng/mL of human stromal cell-derived factor 1-alpha (SDF-1α or CXCL12, Peprotech, Inc., Rocky Hill, NJ) were added to the PEGSSDA® mixture.

4.2.5 In situ biofabrication of 3D cell culture constructs:

Hydrogel constructs were produced in a pre-formed microfluidic device using *in situ* photopatterning [22]. To achieve this, photomasks were prepared from an aluminum foil/adhesive film bilayer using a razor plotter and attached directly to the bottom surface of the glass slide (see **Figure 4.1.a**). The photomasks featured rectangular slots with dimensions 3.0x0.5 mm at the center of each microfluidic chamber. Unless otherwise noted, slots were oriented parallel to the direction of flow. The HA hydrogel precursor mixed with HCT-116 cells at a concentration of 3.6×10^7 cells/mL was introduced to all the channels in the device (**Figure 4.1.c, *i-ii***) through the inlet ports using a syringe or a pipette,

and was subsequently exposed through the photomask (**Figure 4.1.c, *iii*)** to initiate rapid thiol-ene crosslinking with to UV light using a handheld source (BlueWave® 75, Dymax, Torrington, CT; 365 nm wavelength, 18 W/cm2) held ~ 12 cm from the device surface for 3 seconds. to initiate rapid thiol-ene crosslinking. Given the distance from the UV source, we estimate a total dose delivered to the cells of <0.2 W/cm2. Note that this exposure level has not been found to induce any significant perturbation to cell behavior. The uncrosslinked precursor was then flushed away using fresh phosphate-buffered saline (PBS, **Figure 1.c, *iv***), leaving discrete 3D constructs of hydrogel-encapsulated cells spanning from the bottom surface of the channel to the top surface as defined by the photomask. For co-culturing HCT-116 and Caco-2 cells, the HA precursor was mixed with both cell types, each at a concentration of 1.8×10^7 cells/mL to maintain the same total cell density as above. Next, the photomask was replaced with another that featured identical slots rotated by 90º. The same HA hydrogel precursor *without* cells was then added to the device channels (**Figure 4.1.c, *v***) and exposed to UV light as above (**Figure 4.1. c, *vi***) to yield cross-shaped hydrogel constructs with cell-free regions in two arms (**Figure 4.1.c, *vii***). Precursor containing PEGSSDA® (with or without SDF-1α) was used in experiments requiring select regions to be dissolved. Clean PBS was again used for flushing any uncrosslinked precursor before the introduction of culture media (DMEM-10, **Figure 4.1.c, *viii***). Experiments where the mechanical properties of the hydrogel were manipulated, 4-arm PEG crosslinker was used instead that generated stiffer hydrogels with increasing concentration of the PEG crosslinker.
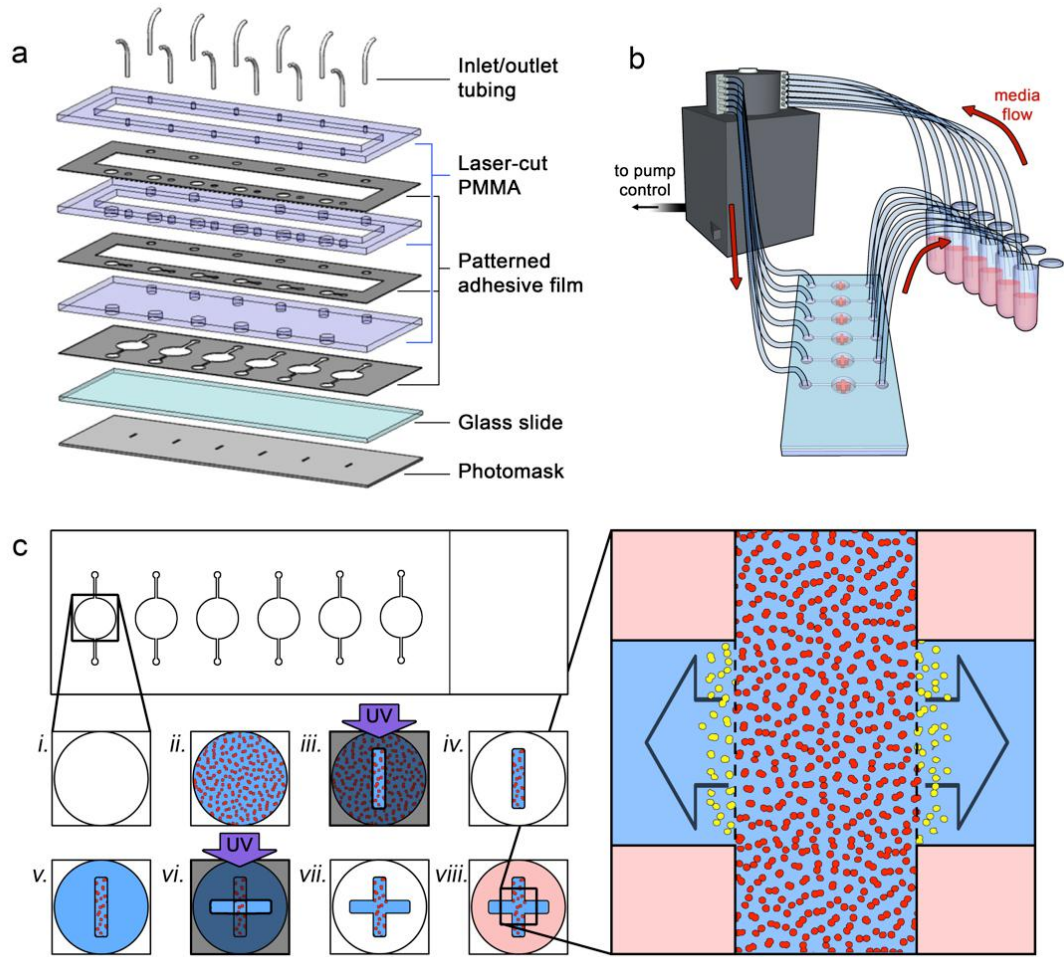
Figure 4.1. Device and construct fabrication *(a) Exploded view of the components used to form the microfluidic system. See the Experimental section for details. (b) Process workflow for in situ biofabrication of monolithic, multi-region 3D cell culture constructs. A microfluidic chamber (i) is filled with cells (red) in a photopolymerizable HA hydrogel precursor (ii). UV light exposure through a slot photomask is used to cross-link the precursor (iii) and the channel is flushed with a clean buffer to leave a cell-laden oblong cuboid (iv). New photopolymerizable HA hydrogel precursor (no cells) is then added to the same chamber (v) and an additional UV exposure is performed through a second slot photomask, perpendicular to the first (vi), adding contiguous cell-free regions to the*

construct that remain after flushing with clean buffer (vii). The media is added to the final construct (viii) to support embedded cells. Right: expanded view of the construct; the inter-region border (dashed lines) defined by the constructed geometry can be used to quantify the distance and speed of invading cells (yellow) moving into the cell-free regions. (c) Schematic view of the experimental setup, showing flow from independent media reservoirs controlled via a peristaltic pump.

4.2.6 Hydrogel characterization:

The shear elastic moduli of the hydrogels, which is proportional to gel stiffness as previously described[19, 20, 23, 24], were determined by rheology. Briefly, the HA hydrogels were prepared as mentioned above with three different formulations containing linear PEG (Extralink®) and 4-arm PEG dissolved at concentrations of 1%, 4%, and 8% w/v respectively, were pipetted into a custom mold of 9 mm diameter and thickness 3 mm and crosslinked for 5 seconds. An HR-2 Discovery Rheometer (TA Instruments, Newcastle, DE) was used to perform testing on each condition using n=3 samples, each with steel, 8 mm parallel plate geometry in ambient conditions. Each sample was placed on the rheometer stage directly below the parallel geometry and was lowered until contact was established between the hydrogel and parallel plate. The plate was further lowered until the axial force of the instrument was equal to 0.4 N. Once this axial force was achieved, the shear elastic modulus G_o was measured using a shear strain sweep test ranging from 0.1 to 10% strain at an oscillation frequency of 1 Hz.

4.2.7 Drug study

Both the drugs, 5-Fluorouracil and Marimastat, were purchased from Sigma Aldrich (St. Louis, MO). For Marimastat, an anti-migratory drug, a stock solution of 50mM was initially prepared in DMSO and then diluted in DMEM cell culture media to obtain desired concentrations. Whereas for 5-FU, an anti-proliferative drug, was prepared by dissolving it directly in the media.

4.2.8 Cancer cell motility assessment:

Direct imaging of constructs was performed using an Olympus FluoView™ FV1000 confocal microscope. For all time points except day 10, an image of the complete construct was formed by stitching together multiple z-stacks (5 µm steps) collected using a 559 nm laser excitation wavelength (mCherry; red) and performing a maximum intensity projection into a single 2D image. On day 10, a comparable image was acquired by combining the red and green channel (λ=405 nm) signals following LIVE/DEAD (L/D) staining of the sample (see below). Note that HCT-116 mCherry fluorescence intensity decreased by 90-95% by day 10 due to photobleaching and other effects so that it was not a significant perturbation to the combined L/D signal. Microscope sensitivity was sufficient to resolve mCherry fluorescence easily at all other time points despite reduction in signal intensity. For all data sets, infiltration distances were quantified using the Imaris MeasurementPro software (Bitplane, Concord, MA) by determining the position of each cell (see **APPENDIX III- A3. 3 - 4**) relative to the border defined by the adjacent arms of the cross-shaped structure (see the dashed line in **Figure 4.1.c, right,** as an example).

4.2.9 Live/Dead cell viability determination:

L/D solution comprised 2 µM calcein-AM and 2 µM ethidium homodimer-1 (LIVE/DEAD Viability/Cytotoxicity Kit for mammalian cells, ThermoFisher, Waltham, MA) in 1 mL of DMEM-10 and PBS mixed in a 1:1 ratio. After flushing each channel with clean PBS, the L/D solution was introduced and incubated for 1 hour. Channels were flushed again with clean PBS prior to imaging. Cell viability for each construct was determined by calculating the ratio of the number of cells in the 405 nm (green) channel (LIVE) to the total number of cells in both the green (LIVE) and the 559 nm (red) channels (DEAD) using Imaris MeasurementPro software (Bitplane, Concord, MA).

4.2.10 Selective recovery of migrated cells:

The cell-free PEGSSDA® regions were dissolved to release migrated cells by cleaving the disulfide bonds with N-Acetyl-L-Cysteine (NAC; Sigma-Aldrich, St. Louis, MO) using a modified version of the manufacturer's protocol (ESI-BIO, Alameda, CA) as previously described[25, 26]. To aid with visualization, fluorescent dye (Alexa Fluor 488 maleimide) was mixed with the PEGSSDA® hydrogel precursor to covalently bond with the thiols in the hydrogel network. For the co-culture experiments, the chemokine SDF-1α was added directly to the PEGSSDA® precursor that was used for the cell-free domain to promote directed cell migration. The heparin component of the hydrogel provides a role similar to heparan sulfate proteoglycans in ECM[27], forming an ionic bond with the SDF-1α and facilitating the slow and localized release of the chemokine. This method promoted the cells to specifically migrate into the cell-free domain in contrast to mixing the

chemoattractant into the media, which would promote non-directional migration. After 7-10 days of cell migration in the construct (as indicated in the text), the channels were flushed with clean DMEM-10 to wash away any cells that were present outside of the construct. Next, 50 mM NAC was prepared in DMEM-10 and the pH adjusted to 7.4. Then 30 μL of the NAC solution was added to each channel using a pipette or syringe and the device was incubated for 2 hours at 37 °C in 5% CO_2. After incubation, the fluid in each channel was slowly removed using a syringe and introduced into the individual wells of a 96 well plate, and 100 μL of clean DMEM-10 media was added to each well containing any retrieved cells. Each construct in the microfluidic device was imaged after the experiment to confirm that the cell-free domain was dissolved entirely and that the cell-laden region remained intact. The well plate was incubated at 37 °C with 5% CO_2 for 4 hours to promote cell adhesion. To remove residual dissolved hydrogel, the media was aspirated from the well plate and each well was rinsed with PBS before fresh DMEM-10 was added to the migrated cells recovered from the cell construct. The wells were imaged in fluorescence using an Olympus IX83 Inverted Microscope. It was essential to image prior to 12 hours to avoid any cell proliferation effects on the isolated cells.

4.2.11 Statistical analysis:

For each experimental condition, identical constructs were prepared in triplicate to enable statistical analyses. Student's t-tests were used to determine differences between means with $p < 0.05$ considered statistically significant. The two-sample Kolmogorov-Smirnov (K-

S) test was used for non-parametric comparison of distributions. Confidence intervals of 95% or better were considered to be significant.

4.3 Results and Discussion

4.3.1 Interstitial flow

Interstitial hypertension is a hallmark of tumors and is thought to be an essential driver of metastasis by promoting increased cell movement out of the primary tumor and into the surrounding tissue[28]. This role has been studied previously using microfluidic systems [12] through which interstitial flow, or the movement of fluid through the extracellular matrix (ECM), was shown to have a substantial effect on cell migration through a combination of factors that includes shear forces. Our system is particularly well-suited to assess these directional effects since the geometry of each construct enables an analysis of cell motility in two opposing directions simultaneously (see **Figure 4.1.c, right**). As an initial test, we prepared constructs with HCT-116 cell-laden regions that were oriented perpendicularly to the microfluidic channel such that cell migration into the two cell-free regions necessitated movement with and against the direction of flow, respectively. We then allowed the device to incubate under the constant flow of DMEM (4 µL/min) for 10 days. Confocal micrographs of the constructs revealed an asymmetrical infiltration pattern (**Figure 4.2.a**) with analyses of migration distance distributions (**Figure 4.2.b**) showing that the mean distance traveled in the direction of flow was 44.3 µm and only 25.1 µm in the direction opposite to the flow. A comparison of the distributions using a two-sample K-S test confirmed their statistical dissimilarity. Note that while we did not measure the generated

pressure or shear stress directly, these values were likely very low. For example, in our past work with a variety of cell types,[17–20] we utilized higher flow rates (~10 uL/min) in comparable microfluidic devices and observed no significant effects.

Given that the goals of this study also required probing the intrinsic, unbiased cell motility, we sought to establish conditions under which the effects of interstitial flow were mitigated while maintaining sufficient buffer exchange for high cell viability. To accomplish this, we made two changes to the system. First, we reoriented the constructs such that the cell-laden regions were parallel to the direction of flow so that fluid movement would neither oppose nor promote motion into the cell-free regions. Second, we reduced the overall exposure of the constructs to shear forces by incorporating intermittent flow, through which the same 4 µL/min flow rate of DMEM was applied for only 10 minutes, followed by a 120-minute flow interruption. Under these alternative conditions, we found that cell viability after 10 days remained high (mean, 77%) and also observed that cells moved equivalently into both the cell-free regions of our constructs (**Figure 4.2.c**). The mean infiltration distance distributions (**Figure 4.2.d**) on each of the two sides of the construct were 48.8 and 54.5 µm, respectively, with a two-sample KS test showing no statistical difference between populations. Consequently, we used the system under these conditions for all subsequent investigations and considered motility into both cell-free regions jointly.
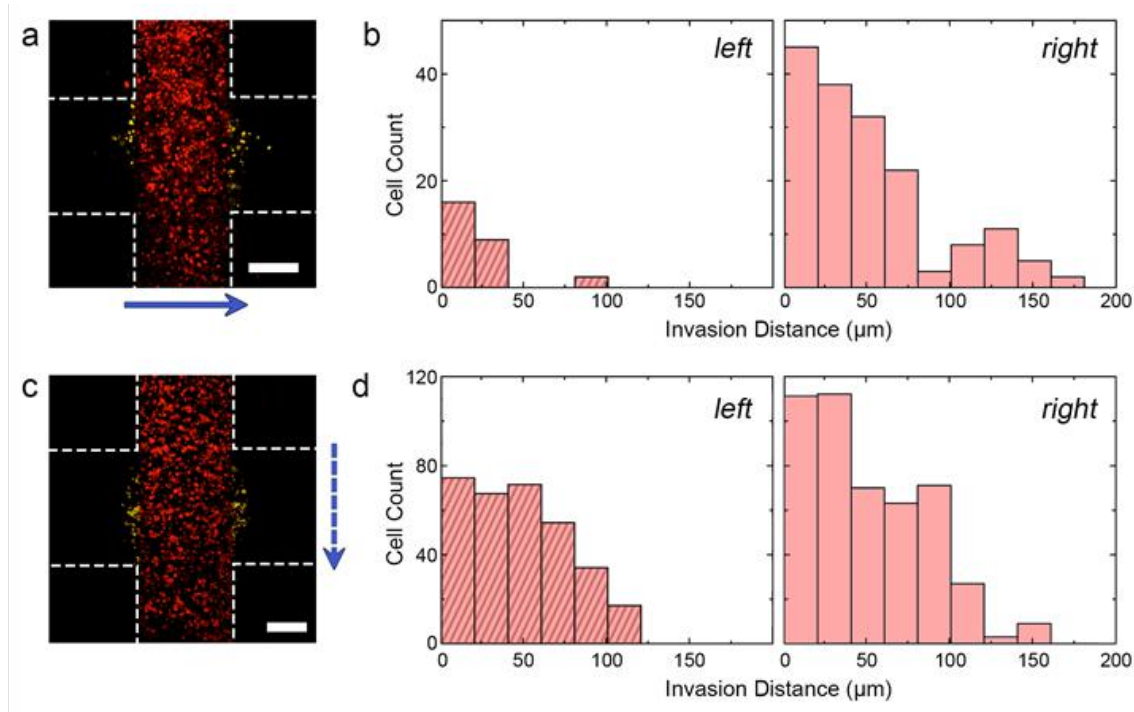
Figure 4 2. Interstitial flow effects (a) Maximum projection confocal micrograph of HCT-116 cells after 10 days of continuous flow (4 µL/min). The blue arrow indicates the direction of flow. Construct borders are roughly indicated by white dashed lines (inter-region border not indicated for clarity) and positions of invading cells (i.e., cells entering the cell-free region) are shaded yellow. (b) Histograms of distances traveled into the left and right cell-free regions of (a), relative to the respective inter-region borders. (c) Maximum projection confocal micrograph of HCT-116 cells after 10 days of intermittent flow (4 µL/min for 10 min, no flow for 120 min). The blue arrow shows the direction of flow, and other indicators match those found in (a). (d) Histograms of distances traveled into the left and right cell-free regions of (c), relative to the respective inter-region borders. Scale bars are 300 µm. See also APPENDIX III – 3A. 2.
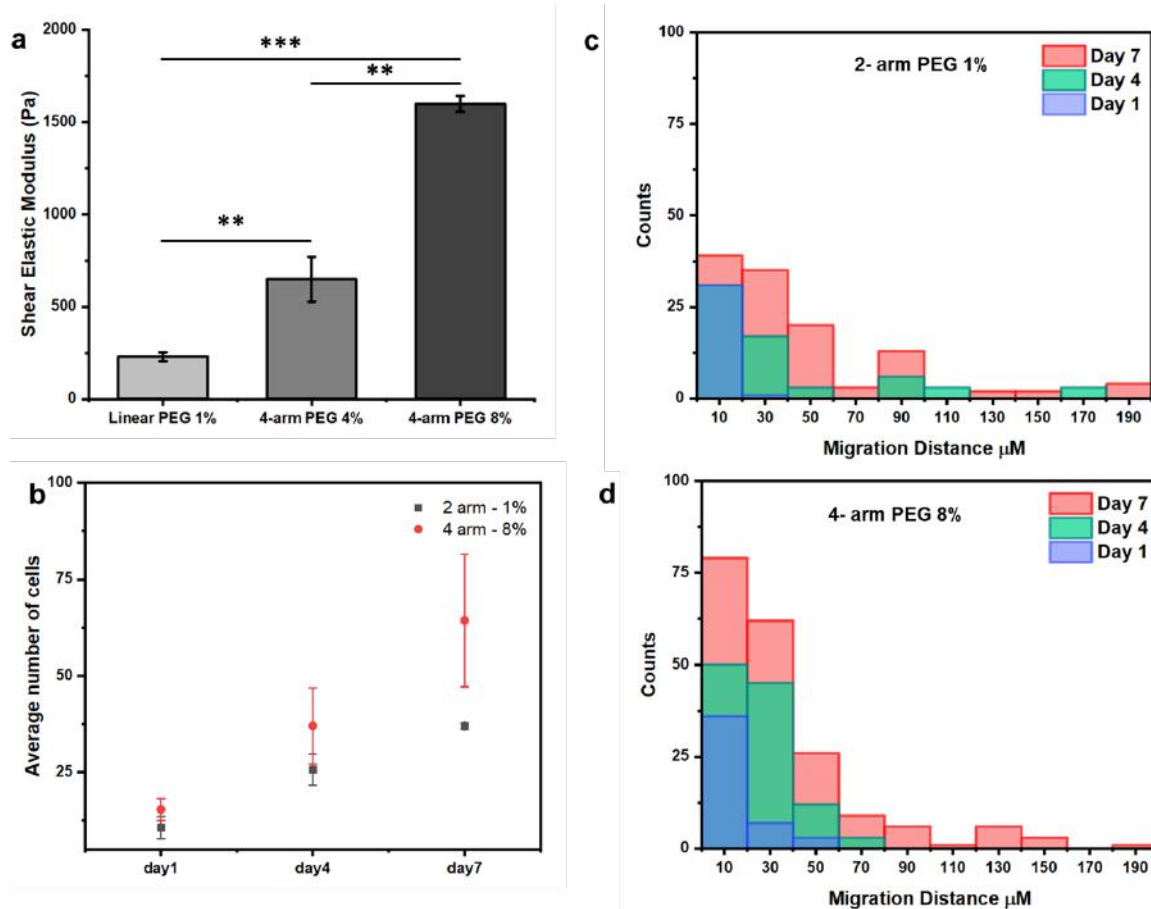
4.3.2 Effect of hydrogel matrix stiffness on tumor cell migration

Migration is an integrated process involving both the cell and the matrix substrate. Consequently, there is a strong correlation between the mechanical elasticity or stiffness of the ECM and the rate of migration and proliferation[20, 29-35]. During cancer progression, the stiffness of the tumor and the stroma increases due to excessive ECM deposition and crosslinking that helps to maintain and influence tumor invasiveness[31, 36, 37]. It has been well established in 2D *in vitro* studies that cell motility is influenced by manipulating substrate stiffness. But, cells migrate and invade in 3D space via a mechanism that is significantly different from those found in a 2D substrate. Indeed, cells embedded in a 3D matrix migrate through a multi-step process that requires extensive matrix degradation and remodeling to overcome steric barriers. As a result, studying migration in 3D becomes more relevant to compare to *in vivo* mechanisms. It has been demonstrated previously that cells from different cancer types tend to exhibit a metastatic phenotype better in an optimal stiffness range that can vary between tumors.[29, 38] Also, increasing matrix stiffness has been shown to enhance the expression of cancer stem cell markers, thus leading to chemotherapeutic drug resistance[39]. Hence, it becomes crucial to biofabricate a tumor environment that has physiological relevant mechanical properties like matrix stiffness to understand better and model tumor migration.

Therefore, to investigate the effect of stiffness dependent tumor migration using the developed microfluidic-based migration assay, we manipulated the hydrogel stiffness chemically by altering crosslinking concentration. The stiffness of the hydrogel varied when different geometry of the acrylate PEG crosslinker was replaced in the hydrogel precursor that altered the effective crosslinker density [20, 24]. The stiffness was measured

as a function of shear elastic modulus G' by rheometer (**Figure 4.3.a**). When the linear PEG crosslinker (Extralink®) was used in the hydrogel matrix at 1% w/v concentration, the G' value was 228.8 ± 23.9, which falls under the softer matrix stiffness. When the linear arm was replaced by 4-arm PEG crosslinker at 4% w/v concentration, the shear modulus G' increased to 647.8 ± 120.8. To further increase the stiffness, the concentration of the 4-arm PEG crosslinker was increased to 8%, measuring a G' value of 1595.8 ± 42.8, which is approximately a seven-fold increase in stiffness. This shows that by increasing the concentration of the crosslinker or by changing the crosslinker geometry, we can significantly vary the stiffness of the matrix. The linear arm PEG and 4-arm PEG crosslinker at a concentration of 1% and 8% respectively were used for the experiment. HCT 116 cells and linear arm PEG crosslinker to form soft tumor matrix with Heparail® and Gelin-s® component of the hydrogel. Then the cell-free zone is fabricated with either linear PEG (condition 1) or 4-arm PEG (condition 2) crosslinker to create a soft or stiffer matrix, respectively. This was connected in a closed-loop circuit with intermittent flow through the peristaltic pump for 7 days. The migration distance of HCT116 cells was tracked by imaging on days 1, 4 and 7 and it was observed that the cell migration was effectively more in the stiffer gel compared to the softer matrix. On day 7, there were 64.3 ± 17.1 number cells that migrated in condition 2, which was 95% more than condition1 (**Figure 4.3.b**). From the histogram plot in **figure 4.3.c-d,** it can be observed that the number of cells migrated is significantly higher in condition 2 which is a stiffer matrix compared to the less stiff matrix in condition 1. These results confirm that the stiffness levels of the matrix are capable of inducing cell migration and invasiveness that might cause downstream metastasis of the tumor.

Figure 4. 3. Effect of hydrogel matrix stiffness on metastatic migration of HCT116 cells in 3D *(a) Measurement of shear elastic modulus by rheometer by using PEG-based crosslinkers of varying geometry and concentration that allows manipulating the stiffness of the hydrogel. b) The average number of cells migrated into the matrix of two different stiffness. Time evolution of histograms for HCT-116 invasion distances (total count across all constructs) in c) 2-arm, and d) 4-arm 8% concentration of PEG crosslinker. Plots show data for day 1 (blue), 4 (green), and 7 (red), and 10 (red).*

It is crucial to study and understand these physical and mechanical parameters that influence cell migration and drug sensitivity, especially when we model patient-derived tumors. To better mimic the *in vivo* like physiological responses, most of these critical

mechanical cues much be integrated with the system. Moving forward, to isolate the effects of matrix stiffness influencing migration, we only employ linear arm PEG (Extralink®/ PEGSSDA) for our experiments involving migration assay.

4.3.3 Influence of the chemotherapeutics agents 5FU on HCT-116 infiltration

5FU is an antimetabolite fluoropyrimidine analog that inhibits nucleotide synthase[40] and causes apoptosis in cells with high metabolic activity. Owing to this mechanism, it is an effective antiproliferative drug that is employed widely in the treatment of solid tumors, including as the principal chemotherapeutic agent used for the systematic treatment of colorectal cancer. We first used our system to study the effects of 5FU on the migration and viability of HCT-116 cells.

Fabricating four identical sets of cross-shaped migration constructs (three constructs per set), each individual structure was placed into intermittent circulation with DMEM spiked with 5FU at one of four concentrations: 0 (control), 1, 10, or 100 mM. Using maximum projection confocal images acquired across a 10-day incubation period, the number of migrating cells and their dynamics were then determined. Using infiltration histograms (**Figure 4.4.a**), we observed that the migration of HCT-116 cells under control conditions evolved predictably, with more cells moving across more considerable distances throughout the experiment. Under 5FU insult, however, the number of cells crossing the boundary into the cell-free region was markedly reduced compared to the control; this reduction did not appear to be drug concentration-dependent. The mean infiltration distances of cells progressed non-monotonically with time under all conditions, showing a

quasi-asymptotic relationship (**Figure 4.5.a**). We interpreted this shape to be the result of new cells crossing the boundary and thus reducing the mean. By considering the total number of infiltrating cells under all conditions, we found that their counts increased linearly with time (**Figure 4.5.c**). We could, therefore, determine the infiltration rate for each condition (**Figure 4.5.e** and quantitively confirmed that exposure to 5FU reduced the number of migrating cells in a dose-independent manner. Critically, we found that infiltration dynamics were not sensitive to 5FU, with no significant differences observed between the mean distances traveled with versus without 5FU.

As a final metric, we also analyzed HCT-116 viability in response to 5-FU exposure. Because of the long (10 days) duration of our incubation, decomposition of early-dying cells following apoptosis could significantly influence cell quantification, resulting in an overestimation of the total viability at the conclusion of the experiment. This possibility is supported by the reduction in total cell count (LIVE plus DEAD) observed as a function of 5FU (**Figure 4.6.b**) despite the use of a uniform initial cell density. To account for this, we calculated L/D ratios by comparing live cell count under each condition to the total average number of cells in control (0 mM 5FU) constructs on the same day (**Figure 4.6.c**). Under this alternative scaling, we observed a substantial decrease in relative cell viability, reaching as low as $37 \pm 5.0\%$ under 100 mM 5FU. Note that a similar but less severe decrease was also observed in direct (non-relative) viability quantification (**APPENDIX III – A3. 5**).
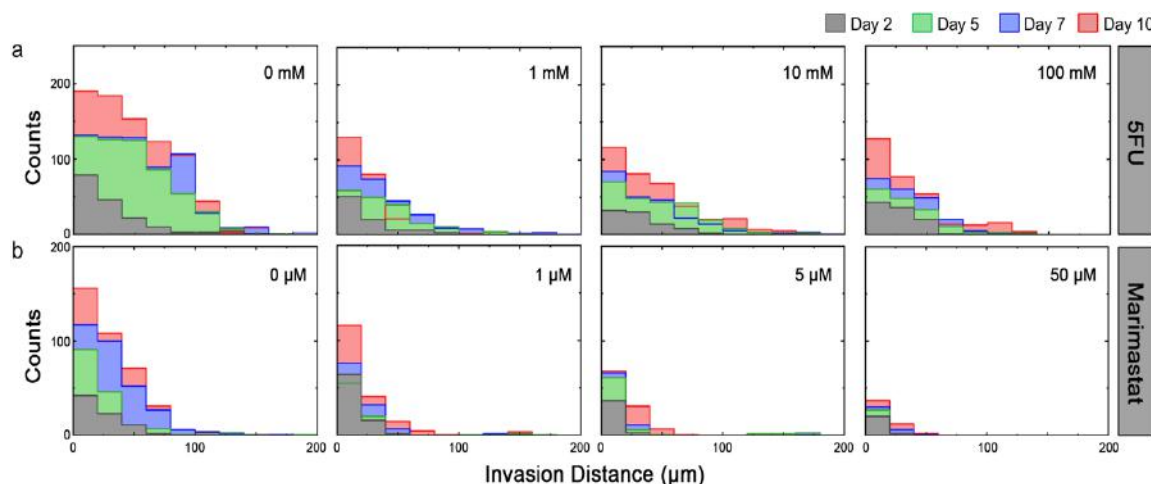
Figure 4. 4. Effects of drugs on in vitro HCT-116 invasion. Time evolution of histograms for HCT-116 invasion distances (total count across all constructs) under conditions a) 0, 1, 10, and 100 mM 5FU and b) 0, 1, 5, and 50 μM Marimastat. Plots show data for day 2 (grey), 5 (green), 7 (blue), and 10 (red).

Taken together, our results were indicative of the anti-proliferative mechanism of 5-FU: the drug kills cells efficiently, but resistant phenotypes [41, 42] retain the same migratory activity as observed under control conditions. Because cellular motility pathways are not known to be directly impacted by 5FU, it is perhaps unsurprising that surviving cells retain native motility. However, decoupling viability from infiltration adds a valuable perspective; for example, previous studies using conventional transwell migration and scratch assays concluded that 5FU produces an apparent decrease in HCT-116 invasiveness[43, 44]. However, without accompanying viability data to account for cell death, it is unclear that the observed decrease in the number of migrated cells is a result of direct drug activity or simply a reduction in the total number of viable cells owing to the increasing 5FU exposure. Our results demonstrate that active proliferation and high metabolism (i.e., the cellular states that are prone to 5FU sensitivity) do not necessarily

184

predict invasiveness. This suggests that the effectiveness of 5FU that drives its clinical use in colorectal cancer may only prevent metastasis [45] insomuch as it kills cells that could otherwise metastasize; this concept is also supported by previous work [46].
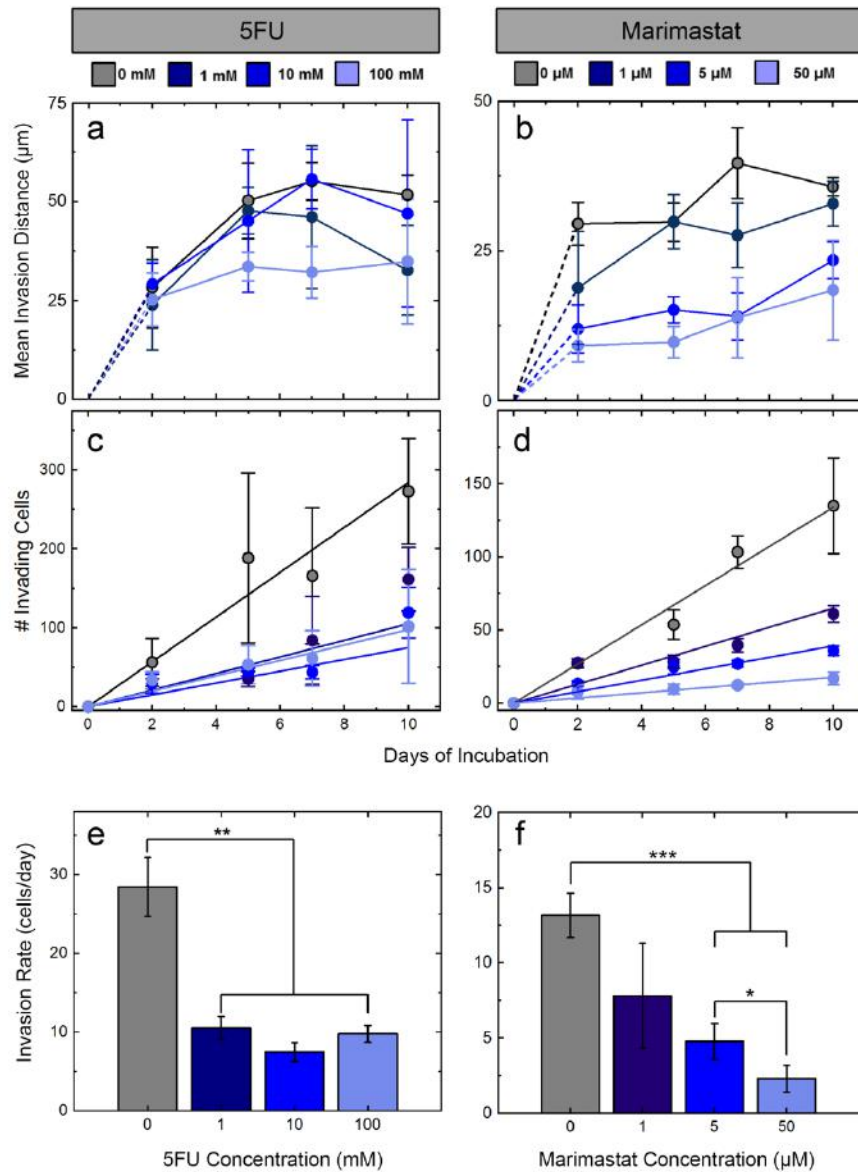
Figure 4.5. HCT-116 invasion quantification for all conditions and all time points. *Colors represent different concentrations of 5FU (left) and Marimastat (right) (indicated at the top). Mean invasion distances (a and b) and the number of cells crossing into the*

cell-free region (c and d) for increasing drug concentrations. Rates of invasion for all concentrations of 5FU (e) and Marimastat (f). Drug insult reduces invasion rate for each, but a concentration dependence is observed only for the anti-migratory Marimastat. Significance: * p<0.05, ** p<0.01, *** p<0.001
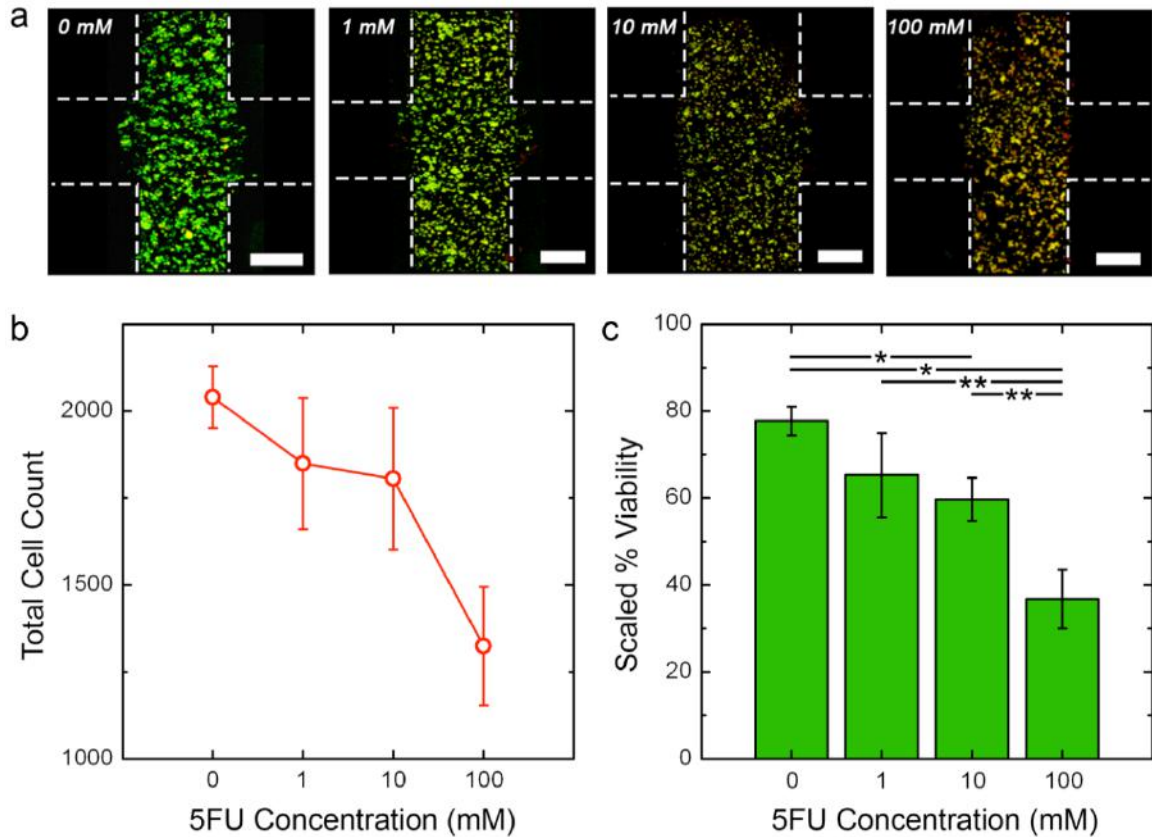
***Figure 4.6. HCT-116 viability under 5FU insult** (a) Maximum projection LIVE/DEAD (L/D) confocal micrographs of HCT-116 cells after 10 days of the intermittent flow of the indicated 5FU concentration. Green cells are live and red cells are dead. Construct borders are roughly indicated by white dashed lines (inter-region border not indicated for clarity), and scale bars are 300 μm. (b) Viability (L/D ratio) on day 10 as a function of 5FU concentration, determined directly from L/D image analyses. (c) Total cell count (live*

plus dead) on day ten, indicating the net loss of cells as a function of 5FU concentration. (d) Viability on day 10 calculated as the ratio of live cells under a given condition to the total number of cells in control (0 mM) construct. This value better accounts for the undercounting of dead cells induced by decomposition during the long-term measurement. Significance: * p<0.01, ** p<0.05

4.3.4 Influence of the chemotherapeutics agents Marimastat on HCT-116 infiltration

As a counter-test to the 5-FU measurements, we next investigated an alternate chemotherapeutic drug known to operate through a different mechanism. Marimastat is a synthetic anti-migratory drug that inhibits a broad spectrum of MMPs, which are secreted by cancer cells to degrade type IV collagens present in the surrounding ECM, thereby promoting migration and ultimately metastasis[47]. Denatured collagen is a significant component of the HA hydrogel scaffold surrounding our cells, suggesting a pathway for Marimastat may significantly impact cell migration in our system. Consequently, we followed the precedent of the 5-FU measurements and fabricated four sets of cross-shaped migration constructs to determine the effect of Marimastat on HCT-116 cell migration and viability. The four drug concentrations used were 0 (control), 1, 5, and 50 μM, and constructs were probed for the same 10 day incubation period as described above.

Like 5FU, infiltration histograms (see **Figure 4.4.b**) demonstrated that Marimastat insult reduced the total number of HCT-116 cells migrating into the cell-free region. However, in contrast to prior results, we also observed a strong dose-dependence on this quality. Indeed, direct quantification of the infiltrating cell counts for all conditions (**Figure 4.5.d**)

showed linear increases with time, similar to 5FU above, but their rises were strongly impacted by drug concentration. As a result, significant decreases in infiltration rates (i.e., slopes of cell count data) were found with increasing Marimastat exposure (**Figure 4.5.f**). Mean infiltration distances were again found to follow a quasi-asymptotic trend, with distances traveled increasing quickly at early time points but then moderating later. However, under Marimastat exposure, we observed a considerable dose-dependent reduction in the distances traveled by the cells (**Figure 4.5.b**). Additionally, we also showed that the overall cell viability (relative to control, as described above) on day 10 was reduced to $47 \pm 2.74\%$ at the highest concentration (50 μM) of Marimastat (**Figure 4.7.c**). Because the total cell count across drug concentrations was considerably more stable than those treated with 5FU (**Figure 4.7.b**), the non-scaled viability accounting for the decomposed dead cells yielded a comparable value of $54 \pm 1.5\%$ (**APPENDIX III A3. 6**). These results again corresponded with mechanism: as an anti-migratory drug, Marimastat caused fewer cells to infiltrate the cell-free regions of the constructs, and those that did had decreased migratory capacity.

Previous studies[48-50] have shown that Marimastat is an anti-metastatic agent that is not effective in inhibiting the proliferation of tumor cells[51, 52]. It is not a cytotoxic agent, as the pharmacokinetics of the drugs specifically chelate the active site of the MMP and only potently inhibits cell invasion by preventing ECM degradation. It was clear from our experimental results that Marimastat was able to significantly inhibit migration in a dose-dependent manner, as seen in preclinical studies[49, 53]. Furthermore, the poorer cytotoxicity of the drug was evident in our study, as even the scaled viability of the highest concentration used ($47 \pm 2.74\%$) was higher than that for 5FU ($37 \pm 5.01\%$). Although

Marimastat was shown to be a promising chemotherapeutic agent in cell lines and animal models, it has shown no efficacy in clinical trials and requires anti-proliferation drugs in combination to increase selective cancer cell cytotoxicity[54]. Nevertheless, it serves as an effective mechanistic tool for *in vitro* studies such as those presented here.
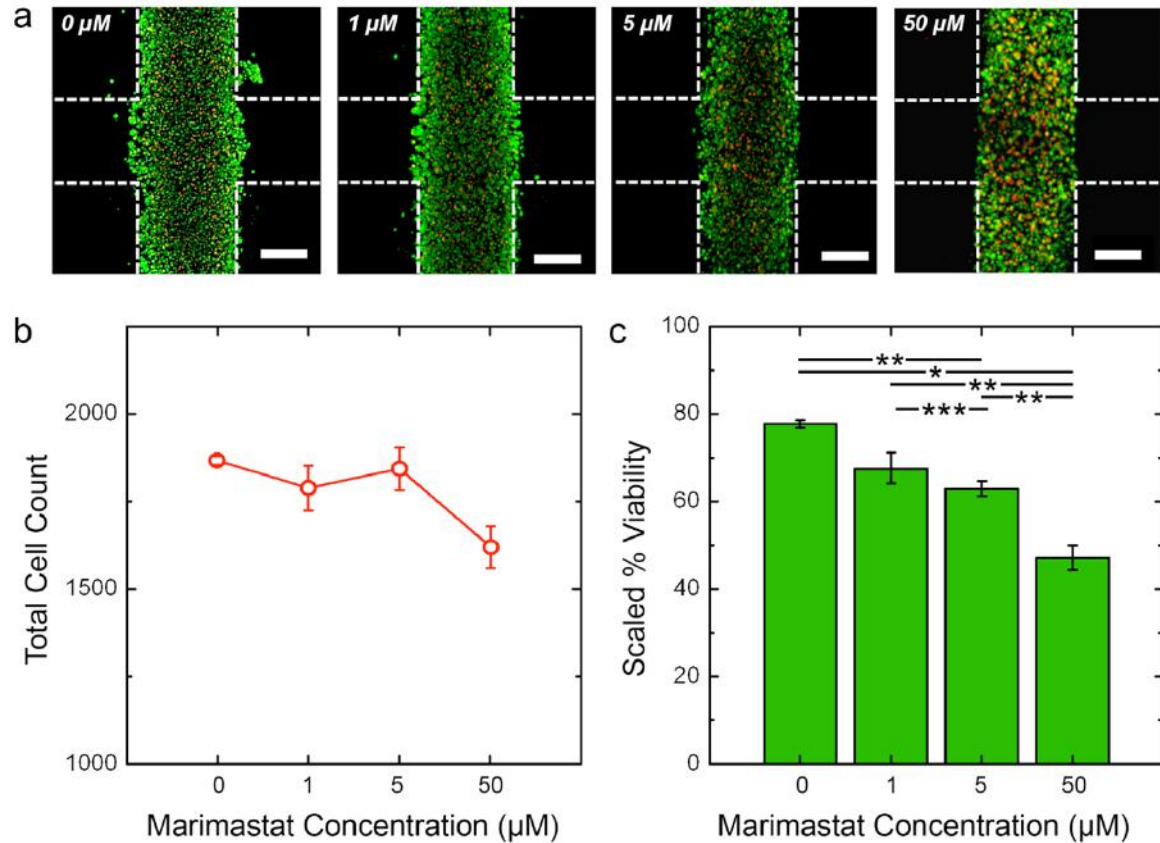
Figure 4. 7. HCT-116 viability following Marimastat insult *(a) Maximum projection LIVE/DEAD (L/D) confocal micrographs of HCT-116 cells after 10 days of the intermittent flow of the indicated 5FU concentration. Green cells are alive and red cells are dead. Construct borders are roughly indicated by white dashed lines (inter-region border not indicated for clarity), and scale bars are 300 μm. (b) Viability (L/D ratio) on day 10 as a function of 5FU concentration, determined directly from L/D image analyses. (c) Total cell*

count (live plus dead) on day ten, indicating the net loss of cells as a function of 5FU concentration. (d) Viability on day 10 calculated as the ratio of live cells under a given condition to the total number of cells in control (0 mM) construct. This value better accounts for the undercounting of dead cells induced by decomposition during the long-term measurement. Significance: * p<0.001, ** p<0.01, *** p<0.05.

4.3.5. Selective hydrogel dissolution to isolate migrated cells

An advantage of the conventional transwell assay is the ability to retrieve migrated cells for subsequent analyses. The cells from the top chamber pass through the porous membrane of the transwell insert to a lower chamber[55, 56] where they can be collected, enabling the examination of the phenotypes that promote invasion. Typically, infiltrating cells are fixed and stained using cytological dyes for quantification using a fluorescent reader; the non-migrated cells in the top chamber are removed prior to staining, commonly with a cotton swab. This is considered tedious and inconsistent; moreover, information about non-migrated cells is lost[3].

To address this limitation, we employed a strategy of dissolving the hydrogel only in the cell-free region, thus releasing infiltrated cells selectively for downstream analysis. This was achieved by using PEGSSDA® crosslinkers in the hydrogel precursor, through which disulfide bonds could be formed between thiol-modified hyaluronan and thiol-modified gelatin to form a hydrogel with properties that are comparable to the gel used above[26]. However, the disulfide bonds enabled cleaving through chemical reduction to rapidly dissociate regions formed with this gel in a convenient, non-enzymatic way[26].

Consequently, by using PEGSSDA® to form the cell-free regions of our cross-shaped migration construct, the reducing agent NAC could subsequently be used to release infiltrated cells selectively into the microfluidic channel for retrieval **(Figure 4. 8)**.
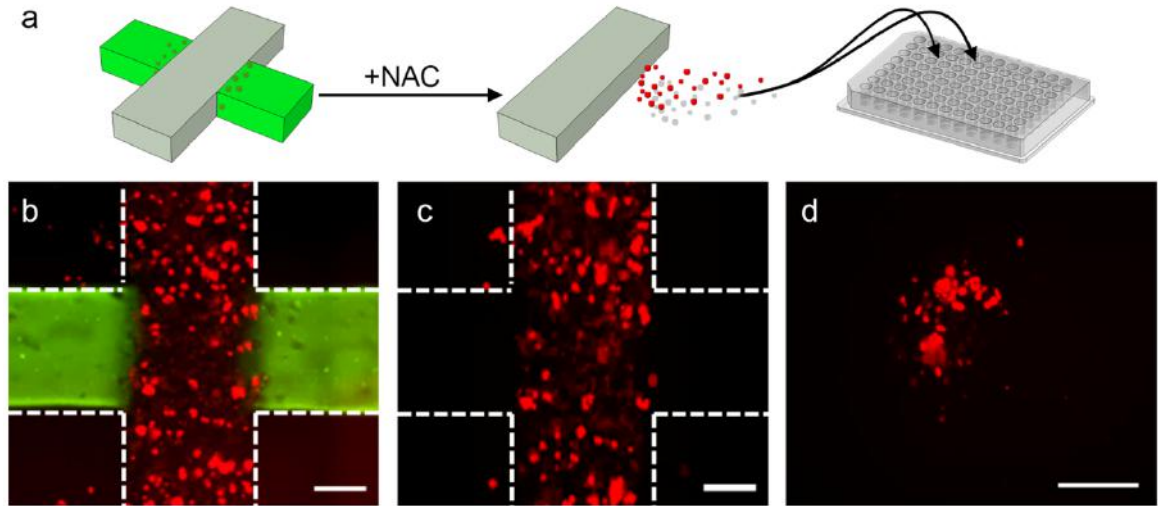
*Figure 4. 8. Dissolving of PEGSSDA based hydrogel. (a) Schematic representation of the selective recovery of infiltrated cells (red) from a cross structure (left). Non-infiltrating cells in the grey region are not shown for clarity. N-Acetyl-L-Cysteine (NAC) is used to dissolve the gel in the cell-free domain (green), releasing only invaded cells into circulation (center) where they can then be recovered and loaded onto a 96-well plate (right) for analysis. Overlaid 2D images of the multidomain construct on day 10 before (b) and after (c) dissolving the gel with NAC. The vertical cell-laden domain encapsulates mCherry cells (red) and the horizontal domain is stained with Alexa fluor 488 for structure visualization. Construct borders are roughly indicated by white dashed lines and scale bars are 300 μm. Following NAC (c), the green fluorescent region (hydrogel with PEGSSDA crosslinker) is selectively removed along with any infiltrated cells it contained.*

(d) 2D image of cells recovered from the construct in a 96-well plate and incubated for 4 hours. Scale bar is 300 μm.

As an initial experiment, we incorporated mCherry HCT 116 cells into the PEGDA/ PEGSSDA® cross structures. After a 10-day incubation period as described above, constructs were imaged to ensure the presence of both the cell-laden and cell-free domains and to confirm cell movement **(Figure 4.8.a)**. We then introduced media containing 50 mM NAC to the device and incubated. Subsequent imaging after treatment **(Figure 4.8.b)** showed selective dissolution of the cell-free regions only, leaving the cell-laden zone intact and releasing infiltrated cells into the surrounding fluid. Indeed, by recovering the media after dissolution and transferring it into a cell culture plate, we observed cell growth **(Figure 4.8.c)** that confirmed the liberation of infiltrated cells.

For heterogeneous cell mixtures, selective retrieval could enable the identification and differentiation of invasive and non-invasive phenotypes. To demonstrate this concept, we implemented a co-culture approach in which the cell-laden region was populated with both the highly invasive HCT-116 cells[57] and minimally-invasive Caco-2 cells[58]. After a 7-day incubation, the PEGSSDA® matrix with infiltrated cells was again dissociated using NAC, and the media was collected and imaged. Based on these analyses, we found that the invasive HCT-116 cells accounted for $92.4 \pm 2.1\%$ of retrieved cells compared to 7.6 ± 2.1 % for minimally-invasive Caco-2 cells **(Figure 4. 9. c)**. This result demonstrates that highly-invasive phenotypes can be isolated selectively from cell mixtures, and shows the utility of the assay in investigating patient-derived samples.
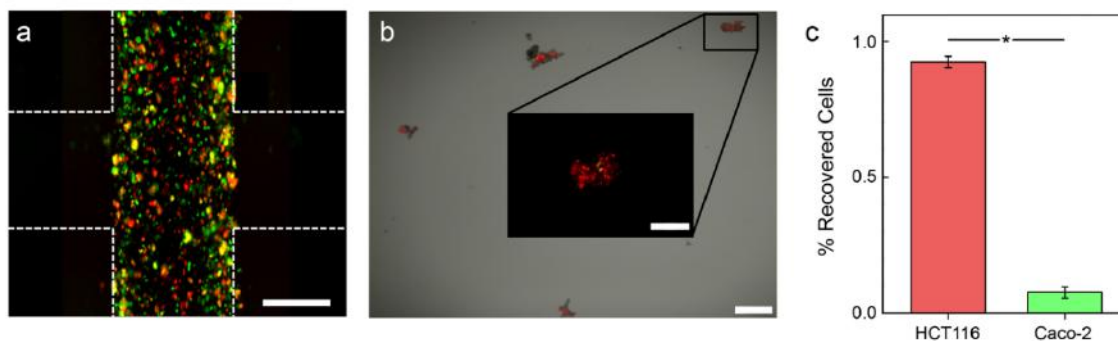
*Figure 4. 9. Isolating migrated cells in Co-culture of mCherry HCT116 and Caco-2 (a) Overlaid 2D image of the multi-domain construct with horizontal cell-laden domain encapsulating mCherry HCT116 cells and Qtracker® 525-labeled Caco-2 cells on day 10 before dissolving the gel. Construct borders are roughly indicated by white dashed lines, and the scale bar is 300 μm. (b) 2D image of cells recovered from the construct, loaded on a 96-well plate, and incubated for 4 hours. Scale bar is 300 μm. Inset shows red and green signals for a zoom of a typical region. (c) Percentage of all recovered cells analyzed in the red (HCT116) and green (Caco-2), showing the invasive phenotype is dominant in the infiltrated population. Significance: * p<0.005.*

4.4 Conclusion

In this study, we have presented a simple and powerful new assay for the direct co-assessment of cellular migration and viability. Using serial photopatterning, we biofabricated monolithic 3D hydrogel constructs featuring localized cell-laden and cell-free regions with well-defined borders inside a pre-formed microfluidic device. The approach enabled straightforward, parallel control over buffer conditions and supported the

direct imaging and assessment of cell invasion over extended timeframes and of viability via conventional double-stain fluorescence assays.

As a demonstration, we used the platform to probe highly invasive human colon carcinoma cells (HCT- 116) over 10 days, showing that the extrinsic effects of shear can be negated. We also showed our ability to manipulate the mechanical properties of the matrix by varying stiffness of the hydrogel, which influences the invasiveness of the tumor. Here we have only established the role of stiffness on migration. But cell invasion is also influenced by other microstructural ECM properties like pore size and fiber morphology, which alters when manipulating the matrix stiffness chemically, as done above. This microfluidic-based assay gives that platform to explore these variabilities' influence of cell migration. We then exploited the parallel nature of our microfluidic device to perform a drug study by investigating the concentration-dependent effects of two chemotherapeutic agents in common use: 5FU, a thymidylate synthase inhibitor, and Marimastat, an MMP inhibitor. We showed that increasing chronic exposure to 5FU decreased cell viability and, consequently, the number of invading cells but did not significantly impact the invasive activity of surviving cells. In contrast, we found that Marimastat reduced both the number and extent of infiltration. Our observations are in line with the anti-proliferative and anti-migratory mechanisms of the drugs, respectively, and highlight that 5FU alone prevents migration only by decreasing the probability of metastatic invasion by reducing the total cell population. Cells capable of escaping 5FU cytotoxicity through low metabolism, cell cycle arrest, or another means of chemoresistance can retain an invasive phenotype.

In addition, we showed an ability to retrieve invading cells selectively via the targeted dissociation of the hydrogel. By incorporating PEGSSDA® as the matrix for the cell-free

194

regions, infiltrated cells could be released and collected for downstream analysis. We demonstrated this concept by isolating invasive HCT-116 cells relative to the minimally-invasive cell line Caco-2.

Our overall assay is well-positioned to expand toward further applications and address additional aspects of tumor cell invasion. For example, an identical biofabrication approach could be used to incorporate a broad range of other cell types, including both cell lines and patient-derived cells[59]. To support this, the hydrogel can be engineered to match the properties of arbitrary tissue types[19, 24, 60], and can be supplemented with additional factors to better represent physiological ECM[19, 25, 61]. In addition, the flexibility of photopatterning supports the ability to produce more complex constructs, potentially featuring multiple, discrete regions containing different cell types to investigate the effects of cell-cell interactions. The adaptability of the microfluidic architecture itself allows for integration with more complex subsystems for complementary processing. It also supports the rapid temporal control of conditions, potentially allowing clinical treatment schedules to be reproduced in vitro. Finally, selective retrieval of infiltrated cells will allow the assessment of mutations or biomarkers associated with the invasive phenotype and enable independent drug studies on that subpopulation alone. Taken together, our simple system is a powerful addition to the tumor-on-a-chip[62] toolbox.

References

[1]   C.L. Chaffer and R.A. Weinberg, *A perspective on cancer cell metastasis.* Science, 2011. **331**(6024): p. 1559-64.

[2]   F. van Zijl, G. Krupitza, and W. Mikulits, *Initial steps of metastasis: cell invasion and endothelial transmigration.* Mutat Res, 2011. **728**(1-2): p. 23-34.

[3]   N. Kramer, A. Walzl, C. Unger, M. Rosner, G. Krupitza, M. Hengstschlager, and H. Dolznig, *In vitro cell migration and invasion assays.* Mutat Res, 2013. **752**(1): p. 10-24.

[4]   S. Boyden, *The chemotactic effect of mixtures of antibody and antigen on polymorphonuclear leucocytes.* J Exp Med, 1962. **115**: p. 453-66.

[5]   G.J. Todaro, G.K. Lazar, and H. Green, *The initiation of cell division in a contact-inhibited mammalian cell line.* J Cell Physiol, 1965. **66**(3): p. 325-33.

[6]   Y.C. Chen, S.G. Allen, P.N. Ingram, R. Buckanovich, S.D. Merajver, and E. Yoon, *Single-cell Migration Chip for Chemotaxis-based Microfluidic Selection of Heterogeneous Cell Populations.* Sci Rep, 2015. **5**: p. 9980.

[7]   F.Q. Nie, M. Yamada, J. Kobayashi, M. Yamato, A. Kikuchi, and T. Okano, *On-chip cell migration assay using microfluidic channels.* Biomaterials, 2007. **28**(27): p. 4017-22.

[8]   C. Wu, S.B. Asokan, M.E. Berginski, E.M. Haynes, N.E. Sharpless, J.D. Griffith, S.M. Gomez, and J.E. Bear, *Arp2/3 is critical for lamellipodia and response to extracellular matrix cues but is dispensable for chemotaxis.* Cell, 2012. **148**(5): p. 973-87.

[9]   K.T. Chan, S.B. Asokan, S.J. King, T. Bo, E.S. Dubose, W. Liu, M.E. Berginski, J.M. Simon, I.J. Davis, S.M. Gomez, N.E. Sharpless, and J.E. Bear, *LKB1 loss in melanoma disrupts directional migration toward extracellular matrix cues.* J Cell Biol, 2014. **207**(2): p. 299-315.

[10]   S. Chung, R. Sudo, P.J. Mack, C.R. Wan, V. Vickerman, and R.D. Kamm, *Cell migration into scaffolds under co-culture conditions in a microfluidic platform.* Lab Chip, 2009. **9**(2): p. 269-75.

[11]   G.S. Jeong, G.H. Kwon, A.R. Kang, B.Y. Jung, Y. Park, S. Chung, and S.H. Lee, *Microfluidic assay of endothelial cell migration in 3D interpenetrating polymer semi-network HA-Collagen hydrogel.* Biomed Microdevices, 2011. **13**(4): p. 717-23.

[12]   W.J. Polacheck, J.L. Charest, and R.D. Kamm, *Interstitial flow influences direction of tumor cell migration through competing mechanisms.* Proc Natl Acad Sci U S A, 2011. **108**(27): p. 11115-20.

[13]   L. Businaro, A. De Ninno, G. Schiavoni, V. Lucarini, G. Ciasca, A. Gerardino, F. Belardelli, L. Gabriele, and F. Mattei, *Cross talk between cancer and immune cells: exploring complex dynamics in a microfluidic environment.* Lab Chip, 2013. **13**(2): p. 229-39.

[14]   S. Mi, Z. Du, Y. Xu, Z. Wu, X. Qian, M. Zhang, and W. Sun, *Microfluidic co-culture system for cancer migratory analysis and anti-metastatic drugs screening.* Sci Rep, 2016. **6**: p. 35544.

[15]   L. Blaha, C. Zhang, M. Cabodi, and J.Y. Wong, *A microfluidic platform for modeling metastatic cancer cell matrix invasion.* Biofabrication, 2017. **9**(4): p. 045001.

[16]   G.A. Cooksey and J. Atencia, *Pneumatic valves in folded 2D and 3D fluidic devices made from plastic films and tapes.* Lab Chip, 2014. **14**(10): p. 1665-8.

[17]   W. Zheng, Z. Wang, W. Zhang, and X. Jiang, *A simple PDMS-based microfluidic channel design that removes bubbles for long-term on-chip culture of mammalian cells.* Lab Chip, 2010. **10**(21): p. 2906-10.

[18]   D. Horst, J. Chen, T. Morikawa, S. Ogino, T. Kirchner, and R.A. Shivdasani, *Differential WNT activity in colorectal cancer confers limited tumorigenic potential and is regulated by MAPK signaling.* Cancer Res, 2012. **72**(6): p. 1547-56.

[19]   A. Skardal, S.V. Murphy, K. Crowell, D. Mack, A. Atala, and S. Soker, *A tunable hydrogel system for long-term release of cell-secreted cytokines and bioprinted in situ wound cell delivery.* J Biomed Mater Res B Appl Biomater, 2017. **105**(7): p. 1986-2000.

[20] A. Skardal, M. Devarasetty, S. Forsythe, A. Atala, and S. Soker, *A reductionist metastasis-on-a-chip platform for in vitro tumor progression modeling and drug screening.* Biotechnol Bioeng, 2016. **113**(9): p. 2020-32.

[21] A. Skardal, S.V. Murphy, M. Devarasetty, I. Mead, H.W. Kang, Y.J. Seol, Y. Shrike Zhang, S.R. Shin, L. Zhao, J. Aleman, A.R. Hall, T.D. Shupe, A. Kleensang, M.R. Dokmeci, S. Jin Lee, J.D. Jackson, J.J. Yoo, T. Hartung, A. Khademhosseini, S. Soker, C.E. Bishop, and A. Atala, *Multi-tissue interactions in an integrated three-tissue organ-on-a-chip platform.* Sci Rep, 2017. **7**(1): p. 8837.

[22] A. Skardal, M. Devarasetty, S. Soker, and A.R. Hall, *In situ patterned micro 3D liver constructs for parallel toxicology testing in a fluidic device.* Biofabrication, 2015. **7**(3): p. 031001.

[23] A. Skardal, J. Zhang, L. McCoard, X. Xu, S. Oottamasathien, and G.D. Prestwich, *Photocrosslinkable hyaluronan-gelatin hydrogels for two-step bioprinting.* Tissue Eng Part A, 2010. **16**(8): p. 2675-85.

[24] A. Skardal, J. Zhang, and G.D. Prestwich, *Bioprinting vessel-like constructs using hyaluronan hydrogels crosslinked with tetrahedral polyethylene glycol tetracrylates.* Biomaterials, 2010. **31**(24): p. 6173-81.

[25] A. Skardal, S.F. Sarker, A. Crabbe, C.A. Nickerson, and G.D. Prestwich, *The generation of 3-D tissue models based on hyaluronan hydrogel-coated microcarriers within a rotating wall vessel bioreactor.* Biomaterials, 2010. **31**(32): p. 8426-35.

[26] J. Zhang, A. Skardal, and G.D. Prestwich, *Engineered extracellular matrices with cleavable crosslinkers for cell expansion and easy cell recovery.* Biomaterials, 2008. **29**(34): p. 4521-31.

[27] A. Amara, O. Lorthioir, A. Valenzuela, A. Magerus, M. Thelen, M. Montes, J.L. Virelizier, M. Delepierre, F. Baleux, H. Lortat-Jacob, and F. Arenzana-Seisdedos, *Stromal cell-derived factor-1alpha associates with heparan sulfates through the first beta-strand of the chemokine.* J Biol Chem, 1999. **274**(34): p. 23916-25.

[28] S.J. Lunt, N. Chaudary, and R.P. Hill, *The tumor microenvironment and metastatic disease.* Clin Exp Metastasis, 2009. **26**(1): p. 19-34.

[29]   X. Tang, T.B. Kuhlenschmidt, J. Zhou, P. Bell, F. Wang, M.S. Kuhlenschmidt, and T.A. Saif, *Mechanical force affects expression of an in vitro metastasis-like phenotype in HCT-8 cells.* Biophys J, 2010. **99**(8): p. 2460-9.

[30]   T.A. Ulrich, E.M. de Juan Pardo, and S. Kumar, *The mechanical rigidity of the extracellular matrix regulates the structure, motility, and proliferation of glioma cells.* Cancer Res, 2009. **69**(10): p. 4167-74.

[31]   M.J. Paszek, N. Zahir, K.R. Johnson, J.N. Lakins, G.I. Rozenberg, A. Gefen, C.A. Reinhart-King, S.S. Margulies, M. Dembo, D. Boettiger, D.A. Hammer, and V.M. Weaver, *Tensional homeostasis and the malignant phenotype.* Cancer Cell, 2005. **8**(3): p. 241-54.

[32]   R.J. Pelham, Jr. and Y. Wang, *Cell locomotion and focal adhesions are regulated by substrate flexibility.* Proc Natl Acad Sci U S A, 1997. **94**(25): p. 13661-5.

[33]   A. Pathak and S. Kumar, *Biophysical regulation of tumor cell invasion: moving beyond matrix stiffness.* Integr Biol (Camb), 2011. **3**(4): p. 267-78.

[34]   A. Pathak and S. Kumar, *Independent regulation of tumor cell migration by matrix stiffness and confinement.* Proc Natl Acad Sci U S A, 2012. **109**(26): p. 10334-9.

[35]   X. Tang, T.B. Kuhlenschmidt, Q. Li, S. Ali, S. Lezmi, H. Chen, M. Pires-Alves, W.W. Laegreid, T.A. Saif, and M.S. Kuhlenschmidt, *A mechanically-induced colon cancer cell population shows increased metastatic potential.* Mol Cancer, 2014. **13**: p. 131.

[36]   A.M. Baker, D. Bird, G. Lang, T.R. Cox, and J.T. Erler, *Lysyl oxidase enzymatic function increases stiffness to drive colorectal cancer progression through FAK.* Oncogene, 2013. **32**(14): p. 1863-8.

[37]   J.I. Lopez, I. Kang, W.K. You, D.M. McDonald, and V.M. Weaver, *In situ force mapping of mammary gland transformation.* Integr Biol (Camb), 2011. **3**(9): p. 910-21.

[38]   E. Mylona, Z. Dailiana, X. Trepat, and M. Lagoudakis, *SUBSTRATE RIGIDITY DICTATES PHENOTYPE, SURVIVAL, AND MECHANICS OF PRIMARY HUMAN OSTEOSARCOMA CELLS.* 2008.

[39]   J. Schrader, T.T. Gordon-Walker, R.L. Aucott, M. van Deemter, A. Quaas, S. Walsh, D. Benten, S.J. Forbes, R.G. Wells, and J.P. Iredale, *Matrix stiffness*

modulates proliferation, chemotherapeutic response, and dormancy in hepatocellular carcinoma cells. Hepatology, 2011. **53**(4): p. 1192-205.

[40] D.B. Longley, D.P. Harkin, and P.G. Johnston, *5-fluorouracil: mechanisms of action and clinical strategies.* Nat Rev Cancer, 2003. **3**(5): p. 330-8.

[41] P.M. De Angelis, D.H. Svendsrud, K.L. Kravik, and T. Stokke, *Cellular response to 5-fluorouracil (5-FU) in 5-FU-resistant colon cancer cell lines during treatment and recovery.* Mol Cancer, 2006. **5**: p. 20.

[42] D. Bose, L.J. Zimmerman, M. Pierobon, E. Petricoin, F. Tozzi, A. Parikh, F. Fan, N. Dallas, L. Xia, P. Gaur, S. Samuel, D.C. Liebler, and L.M. Ellis, *Chemoresistant colorectal cancer cells and cancer stem cells mediate growth and survival of bystander cells.* Br J Cancer, 2011. **105**(11): p. 1759-67.

[43] P. Zhu, N. Zhao, D. Sheng, J. Hou, C. Hao, X. Yang, B. Zhu, S. Zhang, Z. Han, L. Wei, and L. Zhang, *Inhibition of Growth and Metastasis of Colon Cancer by Delivering 5-Fluorouracil-loaded Pluronic P85 Copolymer Micelles.* Sci Rep, 2016. **6**: p. 20896.

[44] K. Seo, S.H. Ki, E.Y. Park, and S.M. Shin, *5-Fluorouracil inhibits cell migration by induction of Sestrin2 in colon cancer cells.* Arch Pharm Res, 2017. **40**(2): p. 231-239.

[45] D. Otsubo, K. Yamashita, M. Fujita, M. Nishi, Y. Kimura, H. Hasegawa, S. Suzuki, and Y. Kakeji, *Early-phase Treatment by Low-dose 5-Fluorouracil or Primary Tumor Resection Inhibits MDSC-mediated Lung Metastasis Formation.* Anticancer Res, 2015. **35**(8): p. 4425-31.

[46] J. Warusavitarne, P. Ramanathan, A. Kaufman, B.G. Robinson, and M. Schnitzler, *5-fluorouracil (5FU) treatment does not influence invasion and metastasis in microsatellite unstable (MSI-H) colorectal cancer.* Int J Colorectal Dis, 2006. **21**(7): p. 625-31.

[47] E.I. Deryugina, G.X. Luo, R.A. Reisfeld, M.A. Bourdon, and A. Strongin, *Tumor cell invasion through matrigel is regulated by activated matrix metalloproteinase-2.* Anticancer Res, 1997. **17**(5A): p. 3201-10.

[48] S.I. Fraley, P.H. Wu, L. He, Y. Feng, R. Krisnamurthy, G.D. Longmore, and D. Wirtz, *Three-dimensional matrix fiber alignment modulates cell migration and*

MT1-MMP utility by spatially and temporally directing protrusions. Sci Rep, 2015. **5**: p. 14580.

[49]   H.S. Rasmussen and P.P. McCann, *Matrix metalloproteinase inhibition as a novel anticancer strategy: a review with special focus on batimastat and marimastat.* Pharmacol Ther, 1997. **75**(1): p. 69-75.

[50]   M. Hidalgo and S.G. Eckhardt, *Development of matrix metalloproteinase inhibitors in cancer therapy.* J Natl Cancer Inst, 2001. **93**(3): p. 178-93.

[51]   Y. Lv, X. Zhao, L. Zhu, S. Li, Q. Xiao, W. He, and L. Yin, *Targeting intracellular MMPs efficiently inhibits tumor metastasis and angiogenesis.* Theranostics, 2018. **8**(10): p. 2830-2845.

[52]   N.S. Waleh, B.J. Murphy, and N.T. Zaveri, *Increase in tissue inhibitor of metalloproteinase-2 (TIMP-2) levels and inhibition of MMP-2 activity in a metastatic breast cancer cell line by an anti-invasive small molecule SR13179.* Cancer Lett, 2010. **289**(1): p. 111-8.

[53]   M. Kimata, Y. Otani, T. Kubota, N. Igarashi, T. Yokoyama, N. Wada, N. Yoshimizu, M. Fujii, K. Kameyama, Y. Okada, K. Kumai, and M. Kitajima, *Matrix metalloproteinase inhibitor, marimastat, decreases peritoneal spread of gastric carcinoma in nude mice.* Jpn J Cancer Res, 2002. **93**(7): p. 834-41.

[54]   P.D. Brown, *Ongoing trials with matrix metalloproteinase inhibitors.* Expert Opin Investig Drugs, 2000. **9**(9): p. 2167-77.

[55]   A. Albini, Y. Iwamoto, H.K. Kleinman, G.R. Martin, S.A. Aaronson, J.M. Kozlowski, and R.N. McEwan, *A rapid in vitro assay for quantitating the invasive potential of tumor cells.* Cancer Res, 1987. **47**(12): p. 3239-45.

[56]   A. Albini and R. Benelli, *The chemoinvasion assay: a method to assess tumor and endothelial cell invasion and its modulation.* Nat Protoc, 2007. **2**(3): p. 504-11.

[57]   M. Ogawa, H. Jing, D.D. Kitts, S. Nakai, and S. Nakamura, *In vitro anti-cancer activities in Caco-2 and HCT-116 cells of recombinant cystatin C prepared by a Pichia expression system.* J Med Food, 2003. **6**(4): p. 317-22.

[58]   N.J. de Both, M. Vermey, W.N. Dinjens, and F.T. Bosman, *A comparative evaluation of various invasion assays testing colon carcinoma cell lines.* Br J Cancer, 1999. **81**(6): p. 934-41.

[59]   A.R. Mazzocchi, S.A.P. Rajan, K.I. Votanopoulos, A.R. Hall, and A. Skardal, *In vitro patient-derived 3D mesothelioma tumor organoids facilitate patient-centric therapeutic screening.* Sci Rep, 2018. **8**(1): p. 2886.

[60]   A. Skardal, M. Devarasetty, H.W. Kang, I. Mead, C. Bishop, T. Shupe, S.J. Lee, J. Jackson, J. Yoo, S. Soker, and A. Atala, *A hydrogel bioink toolkit for mimicking native tissue biochemical and mechanical properties in bioprinted tissue constructs.* Acta Biomater, 2015. **25**: p. 24-34.

[61]   A. Skardal, M. Devarasetty, H.W. Kang, Y.J. Seol, S.D. Forsythe, C. Bishop, T. Shupe, S. Soker, and A. Atala, *Bioprinting Cellularized Constructs Using a Tissue-specific Hydrogel Bioink.* J Vis Exp, 2016(110): p. e53606.

[62]   H.F. Tsai, A. Trubelja, A.Q. Shen, and G. Bao, *Tumour-on-a-chip: microfluidic models of tumour morphology, growth and microenvironment.* J R Soc Interface, 2017. **14**(131).

CHAPTER 5

Development of a patient-specific 3D invasion model to improve therapy outcomes of cancer patients

It is well known that cancer-related mortality is mainly caused by metastasis of solid cancer rather than the primary tumor itself. Yet, most current therapies are highly concentrated on anti-proliferative drugs that cause cytotoxicity or cytostatic of the tumor cells. While these may cause the tumor size to reduce or inhibit further growth, they do not interrupt the metastasis process. This can lead to ineffective treatments, wherein patients in remission for years can develop a secondary tumor that drastically reduces their survival expectancy. On the other hand, the anti-migratory drug helps to inhibit cell migration and invasion but with less cell death. Hence, it has become essential to develop adjuvant or neoadjuvant therapies, which produce cytotoxic and anti-metastatic effects on tumors. Neoadjuvant therapies must be tailored to the makeup of a patient's own tumor to be most effective. But in the current state of precision medicine, genomic analyses only suggest appropriate drugs that target specific driver mutations in a large pool that does not explicitly target invasive phenotype it effectively becomes challenging to isolate these invasive markers selectively from a heterogeneous mixture of tumor cells. To bridge this gap, we have integrated the patient tumor model elaborated in Chapter 3 on an AFB microfluidic platform with the migration assay detailed in Chapter 4. This integration provides an opportunity to both tests the effect of an anti-migratory drug in 3D on a patient-derived tumor organoid and isolates the most invasive phenotype selectively from the total tumor cell population for downstream analyses. Our system can also quantify the effects of different anti-proliferative and anti-migratory drugs (as demonstrated in Chapter 4 on HCT116 cell line)

on inhibiting invasion of patient tumor cells from helping optimize therapy choices. Overall, this approach could significantly improve cancer patient outcomes.

Abstract:

There has been much progress made in cancer research on developing novel anti-cancer treatments and advanced preclinical model, yet, the disease has not been cured. This is mainly because (i) most cancer-related deaths are caused by metastasis and cancer invasion, but conventional therapies are focused mainly on anti-proliferation treatment rather than on the anti-metastatic or adjuvant approaches, and (ii) the heterogeneity of tumors perturbs the drug sensitivity between patients. Though the current 3D *in vitro* model can recapitulate the physiological relevance, the patient-to-patient variation cannot be recreated with cell lines. These two shortcomings can be overcome by developing a personalized *in vitro* platform that can assess tumor progression and drug sensitivity of both anti-proliferative and anti-migratory drugs. Here, we have developed a patient-specific tumor invasion/migration assay in a microfluidic platform that can be used both for phenotypic drug screening *and* isolation of invasive cells. First, we revisited a patient-derived mesothelioma tumor construct and demonstrated through quantification of the invaded cellular dynamics (i.e., distance traveled, and the number of migrated cells) that the common chemotherapeutic agents' cisplatin and carboplatin do not inhibit cell migration. Then we fabricate a multi-domain tumor construct in an adhesive film-based microfluidic device using patient-derived glioblastoma cells and study invasion dynamics in normal media after 10 days. We confirmed the invasive and metastatic phenotype of the invaded cells by on-chip staining for MMP-2 and N-cadherin markers. These results showcase the potential of our platform as a predictive tool for patient-specific response to therapies for multiple cancer types.

5.1 Introduction

Cancer has remained a significant health challenge despite decades of intense research and technological advancement[1]. There are various reasons that contribute to this challenge, like poor prognosis and ineffective preclinical models. But the most crucial cause is the intratumor heterogeneity between patients that leads to differential drug sensitivity and treatment failure[2]. To accurately predict the treatment outcome of each patient and choose the appropriate therapy, we need advanced patient-specific models that recapitulate patients' *in vivo* tumor physiologies and genetic diversity. This type of personalized approach could be used to identify the right treatment based on a given tumor's genetic expression and alterations.

There has been a considerable effort in developing tumor type-specific and patient-specific 3D tumor organoids[3-8] in which conditions have been optimized variously to maintain tumor cell culture viability, differentiation status, histoarchitecture, genetic heterogeneity and alterations, and tumor microenvironment as in the patient tumor. Most of the drug screening studies conducted on these organoids have targeted only the cytotoxic or cytostatic effect caused by the drug, but none of these models have probed the metastatic outcomes of these tumor models. This is critical because 90% of cancer-related mortality is caused by metastasis of the primary tumor[9].

All tumors except leukemia have the tendency to invade and metastasize. Even if the tumor is surgically removed or shrunk using chemotherapy or radiation, the disseminated cells from the tumor may lead to a secondary tumor later. So, it is critical that treatment strategies involve both cancer proliferation and migration. Most drug development is targeted towards anti-proliferation, especially because tumor shrinkage is considered as the

response criterion for regulatory approval of a drug[10]. However, this underestimates the effect of cancer invasion.

The traditional treatment options for metastasis are similar to the anti-proliferation strategies in the sense that they are assumed to control tumor invasion, similar to primary tumor growth effectively. But the metastatic/invasive tumor cells have specific traits and mechanisms that distinguish them from the other tumor cells in the primary tumor. Gaining invasive phenotype is considered as one of the most important features that separate malignant from benign tumors[11]. Even in preclinical models, anti-migratory drugs are mostly tested on irrelevant metastatic models to try to understand the influence of a drug on cancer cell invasion. This creates a need to develop a more pathophysiologically-relevant and predictive tumor model that will help us understand both the cytotoxic and anti-migratory effects of chemotherapeutic drugs.

To address this demand, we have developed a novel 3D tumor invasion-on-a-chip model that facilitates patient-specific cells and helps to study the influence of chemotherapeutic drugs on both tumor cell proliferation and cell migration, in addition to potentially enabling the isolation of infiltrated cells. In this chapter, we first revisit a patient-derived mesothelioma specimen described in Chapter 3 to probe the effect of chemotherapy on its invasion. We quantify both cellular dynamics (i.e., distance traveled and the number of migrated cells) and cytotoxicity under the chemotherapeutic agents' cisplatin and carboplatin. Then, we apply the multi-domain microfluidic migration assay to patient-specific glioblastoma multiforme (GBM) using low passage patient-derived cancer cells. The resulting model is maintained under normal culture conditions for 10 days to study the invasion dynamics of the tumor cells. To confirm the invasive and metastatic phenotype of

the invaded cells, we performed an on-chip staining protocol for the migratory markers MMP-2 and N-cadherin. Our results suggest the value of the platform for more comprehensive predictive modeling of viability and migration (related to metastatic potential) for patient-specific tumors of various types.

5.2 Experimental methods

5.2.1 Adhesive film-based (AFB) Microfluidic device fabrication

The fabrication of the AFB microfluidic device is detailed in Chapter 4. Briefly, a patterned adhesive film was sandwiched between a glass slide and a PMMA slide, the latter of which is laser-cut to house inlet and outlet ports. Each channel was individually connected in a closed-loop to a reservoir through a micro-peristaltic pump (MP2 Precision, Elemental Scientific, Inc.). The constructs were maintained at intermittent flow (4 µL/min for 10 min, followed by 120 min with no flow) for 10 days.

5.2.2 Tumor biospecimen procurement and cell processing

Mesothelioma tumor processing:

The tumor processing of mesothelioma biospecimens is detailed in Chapter 3. Briefly, the minced tumor is digested using collagenase/hyaluronidase (STEMCELL Technologies) and filtered through a 100 µm cell filter to remove any undigested tumor pieces and centrifuged to form a pellet. The pellet was removed of any lysed cells and blood cells

present using a lysis buffer and counted for the number of viable cells. the cell pellet was used immediately for the experiment.

GBM tumor processing:

Tumors were acquired following IRB-approved guidelines on the day of resection and processed within 24 hours. First, the tumors were washed in Dulbecco's phosphate-buffered saline (PBS) solution with 5 µg/mL Gentamicin (G1272, Sigma) 5 µg/mL Amphotericin B (A2942, Sigma) and 10 µL/mL Penicillin/Streptomycin for five minutes. Tumors were manually fragmented into pieces measuring less than 1 mm, removing any fat or necrotic tissue. Tissue was placed into a 15 mL conical containing DMEM low glucose with no supplements, 3.3 mg/ mL Hyaluronidase (Sigma), and 22,000 NPA units/ mL BP Protease (003-1000, VitaCyte), with the total volume enough to cover the dissected tumor. The conical tube was then placed onto a mixing rack and kept at 37ºC until the tumor was dissociated, with a maximum time of two hours allowed. An equal volume of cold DMEM-10 was added to the tumor dissociation mixture to quench enzymatic activity and contents of the tube were transferred to a sterile 50 mL conical tube. The dissociated tumor mixture was filtered using a filtration kit with 100 µM pore size (SCNY00100, Millipore) to remove undigested pieces and centrifuged. BD Pharm Lyse™ (555899, BD Biosciences) was then added to the cell pellet to perform a red blood cell lyse according to company protocol. Dead cell sorting was performed on the remaining cells (130-090-101, Miltenyi Biotec). The remaining cells were counted and ready for use in experiments.

5.2.3 Culturing of GBM cells

The isolated GBM cells were expanded in a low passage on a poly-L-lysine (PLL, 10mg/mL, Sigma) coated 15 cm round cell culture dish using 15 mL of Astrocyte media (Sciencell) supplemented with 2% FBS, 1% astrocyte growth supplement and 1% penicillin/streptomycin solution. To coat the plate, 15 μL of PLL solution is dissolved in 10 mL of sterile water and added to the culture plate, which was then incubated overnight at 37°C. Prior to seeding, the plate was washed with sterile DI water. Once the cells reached 70% confluency or required density, they were harvested using 0.05% trypsin (Difco Laboratories) and immediately used for the experiment or frozen to maintain low passage.

5.2.4 Cell labeling using Hoechst 33342

To image cells in the GBM tumor construct, Hoechst 33342 (ThermoFisher scientific) solution was diluted at a concentration of 1:1000 in media and added to the reservoir of each channel. The tumor construct was kept under constant flow (4 μL/min) with the labeling solution to ensure complete diffusion into the hydrogel construct. Prior to imaging, the organoids were washed 2X with PBS, which was then replaced with astrocyte media.

5.2.5 Hydrogel preparation

The hydrogel precursor was prepared, as explained in Chapters 3 and 4. Briefly, The HA/gelatin hydrogel (HyStem-HP, ESI-BIO, Alameda, CA) was prepared by mixing thiol-modified hyaluronan (Heparasil®), thiol-modified gelatin (Gelin-S®), and thiol-reactive

polyethylene glycol diacrylate (PEGDA) crosslinker (Extralink®) dissolved in Irgacure photoinitiator(1% concentration each) at a ratio of 2:2:1 (v/v), respectively.

5.2.6 In situ biofabrication of patient-derived 3D tumor constructs

The detailed methodology of the *in situ* tumor construct is described in Chapter 4. Here we replace the cell line with patient-derived tumor cells as in Chapter 3. Briefly, the hydrogel constructs were photopatterned *in situ* through photomasks featuring rectangular slits positioned at the center of each microfluidic chamber. Mesothelioma constructs contained cells at a concentration of 3.6×10^7 cells/mL, and GBM constructs contained cells at a concentration of 2.4×10^7 cells/mL. The uncrosslinked precursor was then flushed away using fresh PBS, leaving discrete 3D constructs of hydrogel-encapsulated cells. The cell-free regions were fabricated by photopatterning the hydrogel without cells using a photomask that featured identical slots rotated by 90º. Clean PBS was again used for flushing any uncrosslinked precursor before the introduction of culture media.

5.2.7 Drug study

Cisplatin (Sigma), carboplatin (Sigma), and pemetrexed (Sigma) were employed in the mesothelioma study. Cisplatin/pemetrexed and carboplatin/pemetrexed cocktails were reconstituted in DMEM cell culture media with the matched platinum agent and pemetrexed concentrations at 0.2 µM and 20 µM for administration to organoids.

5.2.8 Cancer cell motility assessment

Direct imaging of constructs was performed using an Olympus FluoView™ FV1200 confocal microscope. For all time points, an image of the complete construct was formed by stitching together multiple z-stacks (5 µm steps) and performing a maximum intensity projection into a single 2D image. For mesothelioma, the image combined the red and green channel signals following LIVE/DEAD (L/D) staining of the sample as described previously. For GBM, images of Hoechst stained cells were collected using a 405 nm laser excitation wavelength. For all data sets, infiltration distances were quantified using the Imaris MeasurementPro software (Bitplane, Concord, MA) by determining the position of each cell relative to the border defined by the adjacent arms of the cross-shaped structure.

5.2.9 Histological and immunohistochemistry (IHC) staining

The IHC staining for GBM tumor organoids was done directly on -hip to visualized MMP-e and N-Cadherin marker. All of the staining steps were done at room temperature under continuous flow (8 µL/min) to achieve maximum diffusion into the organoids. First, the cells in the tumor construct were fixed using 4% paraformaldehyde (PFA) overnight. The tissue was then permeabilized using 0.2% Triton-X100 for 20 minutes. After washing for 15 minutes with 1X TBS, antigen retrieval was performed using R-Universal epitope recovery buffer (Electron Microscope Science, Hatfield, PA) for 40 minutes. Then the constructs were washed for 30 minutes with 1X TBS and blocked using DAKO protein block for 30 minutes. The constructs were incubated for 2 hours with primary antibodies MMP-2 (Abcam, raised in rabbit) and N-Cadherin (Abcam, raised in mouse) at a 1:200

dilution in Dako Antibody Diluent. Next, secondary Alexa Fluor 488 or Alexa Fluor 594 antibodies with appropriate species reactivity were applied to all samples at 1:100 in Dako Antibody Diluent and left at room temperature for 1 hour (anti-rabbit Alexa Fluor 488 and anti-mouse Alexa Fluor 594, Life Technologies, Carlsbad, CA, A-11070). Because the cells were already stained with Hoechst 33342 before IHC, the construct was not stained with DAPI. Fluorescence images were taken using the Olympus FluoView™ FV1200 confocal microscope (10x magnification) and Olympus IX83 (40X magnification) and overlaid for analysis.

5.2.10 Statistical analysis

An *n=3* or higher was employed for all studies. Histological, immunohistochemical, or fluorescent images presented in figures are representative of their respective experimental groups. Student's t-tests were performed to compare the means of a normally distributed interval dependent variable for two independent groups. Confidence intervals of 95% or better were considered significant.

5.3 Results and discussion

5.3.1 Influence of chemotherapeutic agent on infiltrating cells in a patient-derived mesothelioma tumor organoid

One of the primary reasons for developing personalized tumor models is that it provides the ability to screen multiple drugs *in vitro* to accurately predict the *in vivo* drug response

of the patient. Most of the patient-derived organoids focus only on the cytotoxic effect of the drug. But it is also critical to understand and monitor the effect of drugs on the invasiveness of the tumor. Hence the tumor construct developed with mesothelioma tumor cells (Chapter 3; patient #2) was analyzed for invasion dynamics on day 10 under control and drug conditions (cisplatin – 0.2, 20 mM; carboplatin – 0.2, 20 mM).

Cisplatin and carboplatin are platinum-based chemotherapeutic drugs that bind to purine residues resulting in anti-proliferation activity and DNA damage that leads to apoptotic cell death [12]. From viability data (**Figure 3.10 c-d**), it can be observed that the carboplatin is effective in causing cytotoxicity though it is less potent than cisplatin. For cisplatin, the tumor exhibits some resistance as even with increasing the drug concentration 100-fold, no significant effect on the cytotoxicity is observed. On the contrary, when comparing the number of invaded cells, there is no significant difference in cell invasion (**Figure 5.1.a**). There is a comparable reduction in the number of invading cells in drug-exposed constructs, but with no concentration dependence (**Figure 5.1.b**). This is because the anti-proliferative drug mechanism does not directly impact the migratory activity but only causes damages in the proliferation or growth pathways that lead to cell apoptosis. This result can be compared to the invasion dynamics of HCT116 cells under anti-proliferative drug 5FU (Chapter 4). It was found that the invasion dynamics did not change even with increasing cytotoxic effect caused by increasing concentration of the drug.

From the above results, it is evident that anti-proliferative drugs alone do not adequately control cell invasion. This highlights the importance of combinational therapies that target both proliferation and migration. To choose a better therapy option, the migrated cells can be isolated and RNAseq performed to better understand the differential gene expression

landscape between the whole tumor and migrated cells with developed drug resistance. Then, anti-migratory therapy could potentially be designed based on identified drivers in the invaded cells.
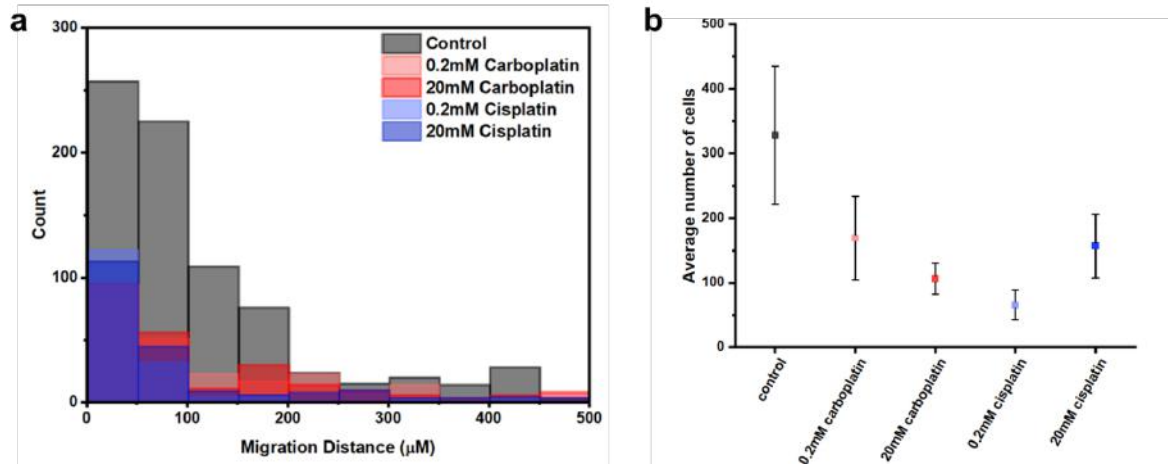
Figure 5.1 *Mesothelioma Patient tumor construct invasion dynamics and drug sensitivity. a) Histograms for mesothelioma patient#2 invasion distances (total count across all constructs) under conditions indicated on day 7.b) the number of cells crossing into the cell-free region under indicated conditions.*

5.3.2 Infiltrated GBM cells display markers of invasive and mesenchymal phenotype

GBM is one of the most aggressive cancers and has a high recurrence rate even after surgically removal of the tumor[13-15]. The heterogeneous and invasive characteristics of the tumor itself make GBM challenging to treat. In the current precision medicine approach, genetic profiling of the tumor does not necessarily yield specific aggressive cell types from the heterogeneous pool of cells. This may fail to identify the phenotypes that

predetermine aggressive or migratory behavior. As with many forms of cancer, the mortality of GBM patients is caused mainly by the infiltration of the tumor cells into nearby tissue or metastasis to a secondary location. This invasive nature emphasizes the importance of determining the alterations in the migratory phenotype to improve the clinical outcome of the patients. It has been shown that the migration phenotype of the brain cancer cells helps to predict the patient outcome[16]. We anticipate that developing a platform to model GBM cell migration in 3D and enable selective examination of the phenotypes of the migrating subpopulation would aid immensely in developing effective treatment plans.

Here we used the developed migration assay (Chapter 4) to study the invasive behavior of the patient GBM in 3D. The GBM patient sample used in the study was isolated cells that were expanded by passaging once prior to use. The patient sample was set up in control media without any drug and incubated for 10 days. At the end of day 10, the cells were fixed and stained for MMP-2 and N-cadherin.

Matrix metalloproteinases (MMPs) are zinc-dependent endopeptidases that degrade collagen in the ECM to facilitate cell movement leading to cell migration and metastasis[17]. Mainly MMP-2 is known to be involved in the tumor progression of GBM by influencing cell proliferation and migration[18-20]. It has been shown that the MMP2 is highly expressed in gliomas and is associated with a high degree of invasion[19, 21]. Their role in tumor malignancy by assisting in tumor invasion[22-24] makes it an ideal biomarker to identify invasive phenotype. Similarly, N-cadherin is a predominant cadherin present in neural tissue and is associated with GBM aggression. It has been shown that the increased level

of N-Cadherin is present in the malignant tumor and also plays a role in cell proliferation[25-27].

From **Figure 5.2,** it is evident that most of the cells are MMP-2 positive, but the migrated cells had colocalization of both MMP-2 and N-cadherin. N-cadherin is a mesenchymal marker that shows increased cytoplasmic expression. The percentage of tumor cells stained with MMP-2 in the tumor construct was only 32.18 ±14.2% compared to the 77±6.8% in the invaded cells. Similarly, for the N-Cadherin marker, 46.8±7.6% of cells stained positive compared to 76±1.4% in the invaded cells. These two markers show the motile and invasive properties that are typical to mesenchymal cells. This mesenchymal transition is vital in the process of cancer progression, invasion, and metastasis[28-30]. Thus we have demonstrated that the cancer cells that infiltrate into the cell-free regions express invasive or mesenchymal phenotype. Genetic profiling these cells might provide crucial information on the alterations that can be targeted during chemotherapy.
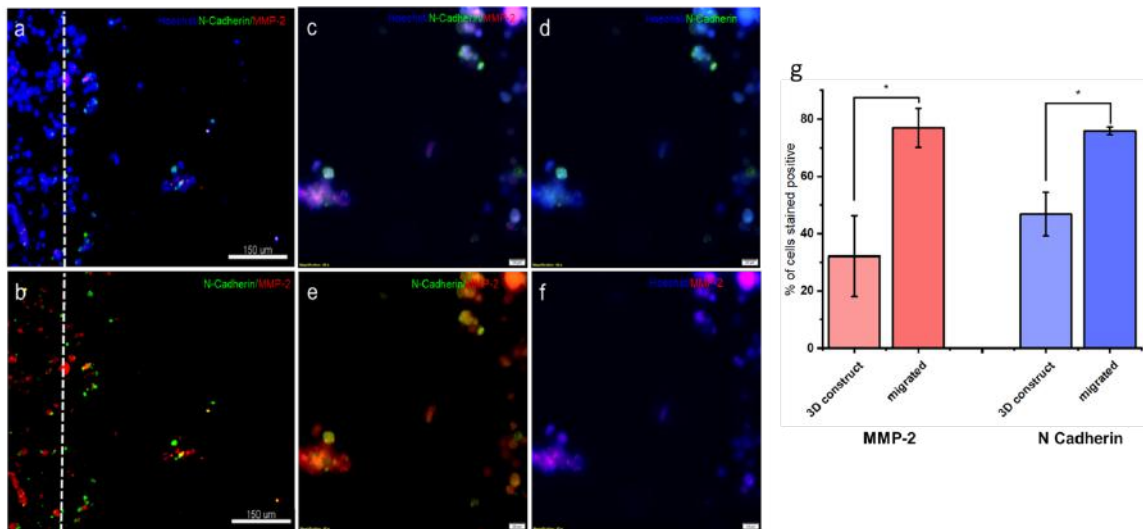
Figure 5.2 *GBM Patient tumor construct histological assessment. Histological assessment of patient-derived GBM tumor constructs for migration assay after ten days of*

incubation in Astrocyte media. a) MMP-2 double-stained with N-cadherin along with Hoechst 33342 organoid stained on-chip and b) shows the double stain with Hoechst 33342 channel removed, thereby highlighting colocalization of biomarkers. c and e) show the representative images of a and b (10x) at increased resolution (40x) showing the MMP-2 and N-cadherin expression in the green and red channels, respectively. d) MMP-2 and Hoechst and f) N-cadherin and Hoechst stained tumor cells indicating a metastatic and mesenchymal proliferative phenotype of migrated cells. g) the percentage of cells stained positive for the biomarker in the entire construct vs. the migrated cells. Scale bars for panels' a - b is 150 μm; panel c-f is 20 μm. Panels' a and b were taken in an upright microscope, and c-f were taken in an inverted microscope causing the image to be inverted.

5.4 Conclusion

3D tumor models have substantially advanced our knowledge and understanding of both disease progression and drug development. The organoids model accurately the *in vivo* tumor heterogeneity and complex histological architecture better than any 2D or animal model. By preserving the genomic and transcriptomic characteristics of the primary tumor[3], we are able to reproduce *in vivo* like drug response on these organoids[31]. By biofabrication, patient-specific organoids that produce consistent drug response as the patient provide a powerful tool to optimize the treatment plan for the individual patient to achieve the best treatment outcome.

Here we have developed a patient-derived invasion assay that can be used for performing drug screening studies that target both migration and proliferation. It is vital to prevent

metastasis from the early stages as treating them in advanced stages becomes complex and reduces the chance of survival. The developed platform has the potential to not only quantify the invasion dynamic under the influence of drugs but also isolate the most invasive cells that can be used for genetic profiling on a personalized basis similar to the precision medicine efforts for whole tumor genetic sequencing. By profiling the driver mutation for proliferation and invasion, a new adjunct therapy plan might increase the drug sensitivity and reduce drug resistance developed in tumor even in initial stages of treatment.

These organoids still lack the essential immune cells and other critical stromal cell factors that restrict the testing of immunotherapy drugs and/or stromal targeted agents on tumor organoids. But these can be overcome by redesigning the functioning of the current microfluidic device and manipulating the matrix scaffold to better mimic *in vivo* conditions. By this personalized approach, we have built a platform that can both advance the understanding of drug influence on metastasis and provide physicians with better, too, to help determine the best treatment option.

REFERENCE

[1]   R.L. Siegel, K.D. Miller, and A. Jemal, *Cancer Statistics, 2017.* CA Cancer J Clin, 2017. **67**(1): p. 7-30.

[2]   R. Weiskirchen, *Intratumor heterogeneity, variability and plasticity: questioning the current concepts in classification and treatment of hepatocellular carcinoma.* Hepatobiliary Surg Nutr, 2016. **5**(2): p. 183-7.

[3]   G. Vlachogiannis, S. Hedayat, A. Vatsiou, Y. Jamin, J. Fernandez-Mateos, K. Khan, A. Lampis, K. Eason, I. Huntingford, R. Burke, M. Rata, D.M. Koh, N. Tunariu, D. Collins, S. Hulkki-Wilson, C. Ragulan, I. Spiteri, S.Y. Moorcraft, I. Chau, S. Rao, D. Watkins, N. Fotiadis, M. Bali, M. Darvish-Damavandi, H. Lote, Z. Eltahir, E.C. Smyth, R. Begum, P.A. Clarke, J.C. Hahne, M. Dowsett, J. de Bono, P. Workman, A. Sadanandam, M. Fassan, O.J. Sansom, S. Eccles, N. Starling, C. Braconi, A. Sottoriva, S.P. Robinson, D. Cunningham, and N. Valeri, *Patient-derived organoids model treatment response of metastatic gastrointestinal cancers.* Science, 2018. **359**(6378): p. 920-926.

[4]   S.S. Taneja, *Re: Organoid cultures derived from patients with advanced prostate cancer.* J Urol, 2015. **193**(4): p. 1442-3.

[5]   S.N. Ooft, F. Weeber, K.K. Dijkstra, C.M. McLean, S. Kaing, E. van Werkhoven, L. Schipper, L. Hoes, D.J. Vis, J. van de Haar, W. Prevoo, P. Snaebjornsson, D. van der Velden, M. Klein, M. Chalabi, H. Boot, M. van Leerdam, H.J. Bloemendal, L.V. Beerepoot, L. Wessels, E. Cuppen, H. Clevers, and E.E. Voest, *Patient-derived organoids can predict response to chemotherapy in metastatic colorectal cancer patients.* Sci Transl Med, 2019. **11**(513).

[6]   Y.S. DeRose, K.M. Gligorich, G. Wang, A. Georgelas, P. Bowman, S.J. Courdy, A.L. Welm, and B.E. Welm, *Patient-derived models of human breast cancer: protocols for in vitro and in vivo applications in tumor biology and translational medicine.* Curr Protoc Pharmacol, 2013. **Chapter 14**: p. Unit14 23.

[7]   C.G. Hubert, M. Rivera, L.C. Spangler, Q. Wu, S.C. Mack, B.C. Prager, M. Couce, R.E. McLendon, A.E. Sloan, and J.N. Rich, *A Three-Dimensional Organoid Culture System Derived from Human Glioblastomas Recapitulates the Hypoxic*

Gradients and Cancer Stem Cell Heterogeneity of Tumors Found In Vivo. Cancer Res, 2016. **76**(8): p. 2465-77.

[8]   L. Huang, A. Holtzinger, I. Jagan, M. BeGora, I. Lohse, N. Ngai, C. Nostro, R. Wang, L.B. Muthuswamy, H.C. Crawford, C. Arrowsmith, S.E. Kalloger, D.J. Renouf, A.A. Connor, S. Cleary, D.F. Schaeffer, M. Roehrl, M.S. Tsao, S. Gallinger, G. Keller, and S.K. Muthuswamy, *Ductal pancreatic cancer modeling and drug screening using human pluripotent stem cell- and patient-derived tumor organoids.* Nat Med, 2015. **21**(11): p. 1364-71.

[9]   J. Sleeman and P.S. Steeg, *Cancer metastasis as a therapeutic target.* Eur J Cancer, 2010. **46**(7): p. 1177-80.

[10]   M. Fernandes, D. Rosel, and J. Brabek, *Translation in solid cancer: are size-based response criteria an anachronism?* Clin Transl Oncol, 2015. **17**(1): p. 1-10.

[11]   Y. Lazebnik, *What are the hallmarks of cancer?* Nature Reviews Cancer, 2010. **10**(4): p. 232-233.

[12]   S. Dasari and P.B. Tchounwou, *Cisplatin in cancer therapy: molecular mechanisms of action.* Eur J Pharmacol, 2014. **740**: p. 364-78.

[13]   G. Filippini, C. Falcone, A. Boiardi, G. Broggi, M.G. Bruzzone, D. Caldiroli, R. Farina, M. Farinotti, L. Fariselli, G. Finocchiaro, S. Giombini, B. Pollo, M. Savoiardo, C.L. Solero, and M.G. Valsecchi, *Prognostic factors for survival in 676 consecutive patients with newly diagnosed primary glioblastoma.* Neuro-Oncology, 2008. **10**(1): p. 79-87.

[14]   M.J. McGirt, K.L. Chaichana, M. Gathinji, F.J. Attenello, K. Than, A. Olivi, J.D. Weingart, H. Brem, and A.R. Quinones-Hinojosa, *Independent association of extent of resection with survival in patients with malignant brain astrocytoma.* J Neurosurg, 2009. **110**(1): p. 156-62.

[15]   K.L. Chaichana, P. Zadnik, J.D. Weingart, A. Olivi, G.L. Gallia, J. Blakeley, M. Lim, H. Brem, and A. Quinones-Hinojosa, *Multiple resections for patients with glioblastoma: prolonging survival.* J Neurosurg, 2013. **118**(4): p. 812-20.

[16]   C.L. Smith, O. Kilic, P. Schiapparelli, H. Guerrero-Cazares, D.H. Kim, N.I. Sedora-Roman, S. Gupta, T. O'Donnell, K.L. Chaichana, F.J. Rodriguez, S. Abbadi, J.

Park, A. Quinones-Hinojosa, and A. Levchenko, *Migration Phenotype of Brain-Cancer Cells Predicts Patient Outcomes.* Cell Rep, 2016. **15**(12): p. 2616-24.

[17]   S.O. Yoon, S.J. Park, C.H. Yun, and A.S. Chung, *Roles of matrix metalloproteinases in tumor metastasis and angiogenesis.* J Biochem Mol Biol, 2003. **36**(1): p. 128-37.

[18]   L.M. Coussens and Z. Werb, *Matrix metalloproteinases and the development of cancer.* Chem Biol, 1996. **3**(11): p. 895-904.

[19]   R.E. Sawaya, M. Yamamoto, Z.L. Gokaslan, S.W. Wang, S. Mohanam, G.N. Fuller, I.E. McCutcheon, W.G. Stetler-Stevenson, G.L. Nicolson, and J.S. Rao, *Expression and localization of 72 kDa type IV collagenase (MMP-2) in human malignant gliomas in vivo.* Clin Exp Metastasis, 1996. **14**(1): p. 35-42.

[20]   P. Guo, Y. Imanishi, F.C. Cackowski, M.J. Jarzynka, H.Q. Tao, R. Nishikawa, T. Hirose, B. Hu, and S.Y. Cheng, *Up-regulation of angiopoietin-2, matrix metalloprotease-2, membrane type 1 metalloprotease, and laminin 5 gamma 2 correlates with the invasiveness of human glioma.* Am J Pathol, 2005. **166**(3): p. 877-90.

[21]   P.A. Forsyth, H. Wong, T.D. Laing, N.B. Rewcastle, D.G. Morris, H. Muzik, K.J. Leco, R.N. Johnston, P.M. Brasher, G. Sutherland, and D.R. Edwards, *Gelatinase-A (MMP-2), gelatinase-B (MMP-9) and membrane type matrix metalloproteinase-1 (MT1-MMP) are involved in different aspects of the pathophysiology of malignant gliomas.* Br J Cancer, 1999. **79**(11-12): p. 1828-35.

[22]   C.F. Yu, F.H. Chen, M.H. Lu, J.H. Hong, and C.S. Chiang, *Dual roles of tumour cells-derived matrix metalloproteinase 2 on brain tumour growth and invasion.* Br J Cancer, 2017. **117**(12): p. 1828-1836.

[23]   J. Gong, S. Zhu, Y. Zhang, and J. Wang, *Interplay of VEGFa and MMP2 regulates invasion of glioblastoma.* Tumour Biol, 2014. **35**(12): p. 11879-85.

[24]   C. Munaut, A. Noël, O. Hougrand, J.-M. Foidart, J. Boniver, and M. Deprez, *Vascular endothelial growth factor expression correlates with matrix metalloproteinases MT1-MMP, MMP-2 and MMP-9 in human glioblastomas.* International Journal of Cancer, 2003. **106**(6): p. 848-855.

[25]   K. Asano, O. Kubo, Y. Tajika, K. Takakura, and S. Suzuki, *Expression of cadherin and CSF dissemination in malignant astrocytic tumors.* Neurosurg Rev, 2000. **23**(1): p. 39-44.

[26]   N. Shinoura, N.E. Paradies, R.E. Warnick, H. Chen, J.J. Larson, J.J. Tew, M. Simon, R.A. Lynch, Y. Kanai, S. Hirohashi, and et al., *Expression of N-cadherin and alpha-catenin in astrocytomas and glioblastomas.* Br J Cancer, 1995. **72**(3): p. 627-33.

[27]   S. Utsuki, Y. Sato, H. Oka, B. Tsuchiya, S. Suzuki, and K. Fujii, *Relationship between the expression of E-, N-cadherins and beta-catenin and tumor grade in astrocytomas.* J Neurooncol, 2002. **57**(3): p. 187-92.

[28]   M. de Vincentiis, A. De Virgilio, F. Bussu, R. Gallus, A. Gallo, G. Bastanza, C. Parrilla, A. Greco, J. Galli, R. Turchetta, G. Almadori, G. Pagliuca, V. Valentini, and G. Paludetti, *Oncologic results of the surgical salvage of recurrent laryngeal squamous cell carcinoma in a multicentric retrospective series: Emerging role of supracricoid partial laryngectomy.* Head & Neck, 2015. **37**(1): p. 84-91.

[29]   J.P. Thiery and J.P. Sleeman, *Complex networks orchestrate epithelial–mesenchymal transitions.* Nature Reviews Molecular Cell Biology, 2006. **7**(2): p. 131-142.

[30]   J. Yang and R.A. Weinberg, *Epithelial-Mesenchymal Transition: At the Crossroads of Development and Tumor Metastasis.* Developmental Cell, 2008. **14**(6): p. 818-829.

[31]   A.R. Mazzocchi, S.A.P. Rajan, K.I. Votanopoulos, A.R. Hall, and A. Skardal, *In vitro patient-derived 3D mesothelioma tumor organoids facilitate patient-centric therapeutic screening.* Sci Rep, 2018. **8**(1): p. 2886.

CHAPTER 6

Conclusion and future directions

6.1 Discussion & Conclusion

Drug discovery and drug development is a costly and lengthy process with a very high failure rate. More than 70% of the drugs that proved effective and safe in the preclinical models failed in Phase I clinical trial due to safety issues. Of the drugs that cleared Phase I trial, more than 50% of the drugs failed in Phase II and Phase III clinical trials[1]. All of the sunk cost invested in these failed trials reflects on the high price of one successful FDA approved drug. By reducing the failure rates in the drug development pipeline, we can ultimately reduce the drug price. Therefore, by analyzing the process, it is clear that the most promising area that could reduce the failure rate is the preclinical model testing. By developing superior models that are more relevant and accurate for drug testing, we can not only improve the drug development process but also better understand the disease mechanism and organ-specific drug interactions.

3D cell culture models overcome the shortcoming of the existing preclinical model. This new cell culture paradigm has gain rapid popularity, as they are more physiologically relevant and better represent the cellular microenvironment. However, the static 3D models fail to capture the dynamic nature of the *in vivo* microenvironment. They essentially lack multicellular and structural complexity, vasculature, precise control of biochemical gradients, and mechanical cues. Integrating microfluidic platform with 3D cell culture techniques, we can bridge the gap of unmet needs in existing 3D models. Microfluidic system allows spatiotemporal control of fluid in a micro-sized channel and induces

biomechanical stresses as observed *in vivo*[2]. This platform can be used as a simple fluid delivery system to the 3D culture and can build sophisticated biomimetic organ-level models, and further interconnect into a highly complex body-on-a-chip-system.

In this dissertation, our overall goal was to build a low-cost, rapid prototyping microfluidic platform and integrate it with advanced 3D cell culture techniques to build complex assays and microphysiological systems. Though PDMS is the most commonly used material to fabricate cell culture-based microfluidic devices, we adopted an adhesive-film based microfluidic fabrication technique. As the AFB microfluidics has not been previously exploited for 3D cell culture applications, here, we aim to develop sophisticated 3D models using this platform.

Our initial goal was to develop a low-cost microfluidic device and challenge the biocompatibility, robustness, and stability of the system for 3D cell culture application. To achieve this goal, in **Chapter 2**, we first designed a simple multi-organoid chip by rapid prototyping technique and integrated a series of healthy organ tissue that included up to 20 primary cells. The resulting system mimics basic circulatory and physiological aspects of the complex human body in a miniaturized format using three or six discrete tissues composed of primary and iPS-derived cells. The system design incorporates simple fluid dynamics to achieve uniform velocity in each chamber, encapsulating a tissue organoid with minimal fluid shear stress on the cells. Then we biofabricated each tissue organoids by encapsulating tissue-specific spheroids or cells in a photopolymerizable hydrogel. For testing the biocompatibility and stability of the platform, we kept the integrated system under continuous perfusion of common organoid media for an extended period. Through

viability analysis at the end of 21 days, we demonstrated a high viability of over 80% on all organoids in the AFB integrated microfluidic system.

Having established a robust fluidic platform that supports even the sensitive primary cells, we validated the multi-organ integrated drug response of three prodrugs: capecitabine, cyclophosphamide, and ifosfamide. All three drugs require the liver tissue to convert the inactive drug into an active metabolite. The metabolized drug is known to cause some downstream drug-induced toxicity in clinical settings, specifically in cardiac, lung, and brain tissue, depending on the drug. Then we exposed the baselined system to the drug for seven days and assessed the organoid viability. As expected, we observed toxicity in the specific organoids that were comparable to clinical outcomes. To confirm if the toxicities were drug-induced, we set up a negative control system without the liver tissue. Here, as the liver was not present to convert the inactive drug into an active metabolite, there was no significant toxicity observed in any organoid in contrast to the system with the liver. These results highlight the importance of using an integrated system for drug testing and safety studies.

Once we demonstrated our ability to sustain healthy primary cells in our platform, we then explored the possibility of developing a physiologically accurate disease model, specifically cancer. To achieve this, in **Chapter 3**, we first developed a 3D patient-derived tumor organoid (PDO) modeling the head and neck squamous cell carcinoma (HNSCC) using cells from patient tumor biospecimen. This model was fabricated by photo-polymerizing HA-based hydrogel with suspended patient-derived tumor cells in a PDMS coated 48-well plate. The simplicity of the set up allows optimizing the tumor organoid before being integrated with the microfluidic platform. Once we biofabricated the PDOs,

they were maintained in culture for seven days and viability analysis showed high viability of 80%. We also confirmed the presence of cancer cells along with stromal cells in the organoid through IHC staining for EGFR, EGFR-p and Ki67. We then used this personalized tumor model for *in vitro* drug testing of traditional chemotherapeutic drugs and radiation. The observed drug response in the PDO was compared with the commonly used sponge assay performed on the same patient tumor biospecimen. The results of sponge assays were sometimes inconclusive due to the significant variability of response in each sample. On the other hand, the PDOs yielded consistent results with negligible variations with every sample, proving the superiority to the model. PDOs also captured the dose-dependent drug response and the heterogeneity in drug response between patients. We also exposed both of these systems to an experimental drug called β-Lapachone. Higher concentrations of this drug proved to be the most effective in both PDO and sponge assay. Therefore, we validated the system by confirming the mechanism of apoptosis of cancer cells exposed to β-Lap. β-Lap is an NQO1 bioactivatable drug that metabolizes to produces superoxide, causing an imbalance in the intercellular ROS that can induce cell death. To counteract the effect of β-Lap-induced toxicity, we used dicoumarol, an NQO1 inhibitor, and observed that most PDOs have a significant increase in the viability. Thus, we were able to show that the decrease in drug sensitivity caused was due to the inhibition effect of dicoumarol that prevents the production of ROS. The results and conclusions from the PDOs were correlated with published 2D studies.

We then adapted the optimized tumor model - PDO system, and integrated with the AFB platform to develop patient-specific tumor-on-a-chip technology. To demonstrate the successful integration and feasibility, we modeled mesothelioma cancer by *in situ* photo

polymerizing of the hydrogel in the platform. Similar to HNSCC, we confirmed the presence of tumor cells in the organoid using mesothelioma specific IHC like CK5/6, calretinin, and thrombomodulin. The 3D culture was sustained for 7 days in continuous flow and was found to be highly viable. This result shows that personalized tumor-on-a-chip was stable and robust. Then we exposed the tumor organoid to two commonly used platin drugs: cisplatin and carboplatin in combination with pemetrexed. The outcome from the chip was comparable to the clinical outcome of the corresponding patient. The result of this experiment showed the heterogeneity in drug sensitivity within and between patients. The integration of PDOs with an AFB microfluidic delivery system was able to capture some of the complexity of the *in vivo* tumor microenvironment and fluid movement to promote long-term culture viability for a while maintaining the biological and mechanical properties of the organoid.

With the established personalized tumor-on-a-chip system, we wanted to probe into the disease state and model the migration or invasion of cancer cells that ultimately leads to metastasis. Therefore, in **Chapter 4**, we started to investigate one of the most critical mechanisms in cancer: metastasis. As a first step, we designed a migration assay that would faithfully capture the complexity of invasion in tumor microenvironment. We developed a simple yet powerful new assay for the direct co-assessment of cellular viability and migration of cancer cells, specifically colon cancer, using human colon cancer cell line HCT116. We used serial photopatterning to biofabricate monolithic 3D hydrogel constructs that featured localized multi-domain cell-laden and cell-free regions with well-defined borders inside a pre-formed microfluidic device. The approach enabled straightforward, parallel control over buffer conditions and supported the direct imaging

and assessment of cell invasion over extended timeframes and of viability via conventional double-stain fluorescence assays. We used this platform to probe into the microenvironment and confirm the influence of two of the important ECM biomechanical forces: interstitial flow and stiffness. Both of these features are known to directly influence cancer cellular behavior and push the cells towards increased metastatic phenotype. These effects were studied using highly invasive human colon carcinoma cells (HCT- 116) over 10 days. The results agreed with the literature, showing that the extrinsic effects of shear stress and increased stiffness of the matrix clearly increased the total number of cell migrating. To study the migration mechanism without the influence of these biomechanical forces, we negated the force by using intermittent flow and low stiffness gel. We then exploited the parallel nature of our microfluidic device to perform a drug study by investigating the concentration-dependent effects of two chemotherapeutic agents in common use: 5FU, a thymidylate synthase inhibitor, and Marimastat, an MMP inhibitor. We showed that increasing chronic exposure to 5FU decreased cell viability and, consequently, the number of invading cells but did not significantly impact the invasive activity of surviving cells. In contrast, we found that Marimastat reduced both the number and extent of infiltration. Our observations are in line with the anti-proliferative and anti-migratory mechanisms of the drugs, respectively, and highlight that 5FU alone prevents migration only by decreasing the probability of metastatic invasion by reducing the total cell population. Cells capable of escaping 5FU cytotoxicity through low metabolism, cell cycle arrest, or another means of chemoresistance can retain an invasive phenotype.

In addition, we showed an ability to retrieve invading cells selectively via the targeted dissociation of the hydrogel. By incorporating PEGSSDA as the matrix for the cell-free

regions, infiltrated cells could be released and collected for downstream analysis. We demonstrated this concept by isolating invasive HCT-116 cells relative to the minimally-invasive cell line Caco-2.

Finally, in **Chapter 5**, we combined the model patient-specific tumor PDO with the migration assay to perform drug-screening studies that targeted both migration and proliferation. First, we revisited the second mesothelioma patient and analyzed for invasion dynamics on day 10 under control and platin drug conditions. Most of the patient-derived organoids focus only on the cytotoxic effect of the drug. However, it is also critical to understand and monitor the effect of drugs on the invasiveness of the tumor. The platin drugs are a known anti-proliferative drug, and their invasion dynamics showed a significant reduction in the total number of cells that invaded but we did not observe any dose dependency. This outcome was comparable to the invasion dynamics of HCT116 under the influence of 5FU and it highlighted the importance of combinational therapies that target both proliferation and migration.

Next, we used the personalized invasion model to probe into the phenotypes of the migrating subpopulation, as it would aid immensely in developing effective treatment plans. To achieve this, we modeled invasion assay for GBM, a highly malignant tumor. Once we fabricated the multi-domain GBM model using patient tumor cells, we maintained the set up in control media without any drug and incubated for 10 days. At the end of day 10, we fixed the cells on-chip and stained for MMP-2 and N-cadherin, ideal biomarker to identify invasive phenotype. The results showed that there was a significantly higher percentage of these markers in the invading cells compared to the cells in the cell-laden construct. These two markers show the motile and invasive properties that are typical to

mesenchymal cells. This mesenchymal transition is essential in the process of cancer progression, invasion and metastasis. Using sequencing techniques, we can identify the mutation driver of the invasive cells that could help in strategizing treatment plans.

Overall, in the dissertation, we were able to develop a rapid prototyping microfluidic platform that, when integrated with 3D cell culture, we can develop versatile and sophisticated models for drug testing. As we discussed at the beginning of the section, it is essential that we design preclinical models that demonstrate *in vivo* like drug sensitivity. Especially in cancer, where there is even patient-to-patient heterogeneity, it becomes crucial that we develop personalized models for drug screening.

6.2 Future direction

Each aspect of this project represents an initial exploration of integrating the AFB microfluidic platform in various 3D cell culture applications. Hence, there are improvements that can be made to broaden the scope of the platform while advancing the modeling accuracy of the system. Below, we discuss some of the challenges to be addressed and improvements that could be made to the existing platform.

In Chapter 2, we developed a multi-organ integrated system that employed spheroids or 3D cell constructs to represent organs. Though the liver, cardiac, brain, and testis are well characterized for their functionality, representations of lung and blood vessels are not optimally functional. For example, a critical aspect of the lung is the air-liquid interface established between the alveoli and blood vessels. To better model a lung system with physiological relevance, the air-liquid interface must be integrated with the body-on-a-chip

system. This can expand the system to enable the administration of the drug through as aerosolized particles. Also, such integration will facilitate the study of airborne particles on human organs *in vitro* with high relevance. Likewise, to model orally administered drug, it will be essential to add a gut model with dual-layer interface representing gut epithelium and endothelium.

Another area of improvement would be to reduce the dead volume of media to improve the plasma: tissue ratio. High liquid volume compared to tissue volume dilutes the dynamic metabolite as well as paracrine and autocrine signals considerably. By reducing the ratio, we can achieve a more physiologically-relevant system. In our platform, one of the reasons to have a high dead volume in the reservoir was to collect media for conducting ELISA. Current assays have not fully caught up with the scales of microscale system and are built primarily to accommodate macroscale experiments; for example, *each* ELISA measurement could require at least 200 µL of media, equivalent to the total chip volume of the 6-organ system. The development of an on-chip ELISA or an ELISA kit that requires smaller amounts of the sample would drastically reduce this dead volume issue.

Here, we have modeled the system to have a uniform velocity in all the organ chambers. But in reality, fluid velocity and pharmacokinetics change between organs. It should also be possible to model this variation in the system by redesigning each organ chambers and channels to match physiologically-relevant values.

In Chapter 3, we developed a patient-derived organoid for drug screening purposes. We used the same hydrogel formulation to model HNSCC, mesothelioma, and GBM tumors. Notably, these tumor types originate in different organs and therefore have differences in the ECM components and also mechanical properties. Hence, by manipulating the ECM

232

components and changing the stiffness of the matrix to emulate that of native tissues, we can better represent the tumor microenvironment.

One crucial factor to be added to our system is the tumor immune microenvironment and other key stromal cell factors that restrict the testing of immunotherapy drugs and/or stromal targeted agents on tumor organoids. In the tumor microenvironment, tumor-infiltrating immune cells play a significant role in modeling the immune cell response and understanding the mechanism of checkpoint blockade. The matrix mechanical properties can be easily manipulated in the system (as briefly explored in Chapter 4) by changing the crosslinker chemistry and/or concentration. Similar to irradiating PDOs in a 48-well plate, we have to integrate radiation therapy on to the chip. The amount of radiation dose should be optimized prior to testing on the organoids itself.

In Chapter 4, we developed an assay to study the invasion dynamics of a colon cancer cell line under the influence of chemotherapeutic drugs. Then we integrated patient-derived cells into the same assay in Chapter 5 to study their invasion dynamics. A logical next step here will be to employ the selective decomposition of target hydrogel regions to isolate the infiltrated tumor cells from patient-derived specimens, as we demonstrated for a cell line in Chapter 4. These isolated cells can be expanded and subsequently probed with RNAseq to identify drivers of metastasis that can potentially be used as a target for therapy. The platform can also be used to study combination therapies that include mixtures of drugs. In addition, we anticipate that the system can ultimately integrate with multiple organoids as in Chapter 2 to study metastasis to other organs as well as off-target therapeutic drug toxicity. As above, future tumor constructs can also be designed to have the similar

physical properties of the tumor and the surrounding matrix to accurately model invasion or can incorporate differential stiffness's to explore mechanotaxis.

Overall we have developed a microfluidic platform that has great potential to employ sophisticated models of 3D cell culture and supports several analyses.

REFERENCE

[1]   J. Arrowsmith and P. Miller, *Phase II and Phase III attrition rates 2011–2012.* Nature Reviews Drug Discovery, 2013. **12**(8): p. 569-569.

[2]   V. van Duinen, S.J. Trietsch, J. Joore, P. Vulto, and T. Hankemeier, *Microfluidic 3D cell culture: from tools to tissue models.* Current Opinion in Biotechnology, 2015. **35**: p. 118-126.

APPENDIX I – Chapter 2

Purpose:

The purpose of this procedure is to describe the steps involved in building a Lung-on-a-Chip with the air-liquid interface and facilitates the delivery of chlorine gas/aerosolized particles into the system.

Scope:

The scope of this procedure applies to staff and students of Hall lab and Sean lab to follow while building the Lung-on-a-chip.

Points to remember:

1) Wear PPE (Personal Protective Equipment) while entering the cell culture room or while doing any lab work.

    a. Cell culture, bench work – Lab coat, gloves, and closed-toe shoes.

    b. Work w/ UV light source - Lab coat, gloves, closed-toe shoes and UV protective eyeglass.

Material Required:

- Microfluidic Device (Lung-on-a-chip; adapter device)

    1) Clean microscopic slide – (25x75x1 mm) – VWR microscope slide

    2) PMMA – McMaster Carr - #8560K239 - Clear Cast Acrylic Sheet (12" x12"x1/8")

    3) 3M double-sided tape – 3M9495MPF, Strouse, Westminster, MD

    4) PDMS – Dow corning Sylgard 184 Silicone Elastomer kit

5) Porous membrane – Millipore 8 um

6) Tweezers

7) Tubing – Cole Parmer – Microbore PTFE Tubing (0.032"ID x 0.056"OD)

- Tygon Tubing (0.030"ID x 0.090"OD)

- Cell Types and Media

1) NHLF (Normal human lung fibroblast) - DMEM 10

2) A 549 (Adenocarcinoma human alveolar basal epithelial cell) - DMEM 10

3) NHBE (Normal human bronchial epithelial cells) – ALI (Air-Liquid interface) complete media / BEGM (Bronchial epithelial growth media)

4) Immune cells - HL-60 (Neutrophil); Jurkat (T-Lymphocyte) and THP-1 (monocyte) cells – alpha MEM

- Hydrogel – Hystem Kit

1) Heparasil/Glycosil

2) Gelin –S

3) Extra-Link

4) 0.5% Photo Initiator – (PI, Irgacure in H2O, pH 7.4)

5) Lung ECM – (220 mg of decellularized lung ECM dissolved in 10mL of PI)

- Airflow Setup

1) Air compressor - Precision Medical PM15 EasyAir Compressor

2) Humidifier (with tubings and fittings)

- Phosphate Buffer Saline – 10mL

- HyClone - Trypsin 0.05%

- Gibco - Trypan blue stain (0.4%)

- UV Lamp - BlueWave® 75, Dymax - 365 nm wavelength, 18 W/cm2.

- Laser cutter - H-series, Full Spectrum Laser.

- Razor plotter - CE6000-40, Graphtec.

- 3M rubber adhesive DST

- 3M liner – 4997 YGI white

Procedure:

I. Device Fabrication:

Laser Cutting PMMA

1) Turn on the laser cutter by pushing down and turning the round red button on the top of the machine clockwise.

 Notes:

- Ensure the water level in the bucket with the motor that flows water through the laser tube is high enough to immerse the motor completely.

- The Ethernet cable between the laser cutter and the computer must be connected prior to turning on the laser cutter to acquire IP address to establish a connection between the software and the machine.

2) Open the lid to the laser cutter and place the PMMA sheet inside. The material should be centered and must be placed on top of the provided honeycomb metal screen platform.

3) Calibrate the distance of the laser lens to focus on the material. Unscrew the laser head and adjust the height by placing the calibration metal cylinder between the PMMA sheet and Laser head. Tighten the screw of the laser head, so it rests parallel on top of the cylinder. DO NOT screw it too tight as it can skew the laser and interfere in the proper cutting of the material.

4) Open both Inkscape and Retina programs installed on the computer.

5) Open the desired LOC pattern previously saved in .tiff format in Inkscape and trace bitmap of the pattern.

6) Send the pattern to print to Retina Engrave software by selecting the Full Spectrum Engineering option.

7) Prior to start cutting, turn ON the air compressor and the motor to run water through the laser tube.

   Note:

   - Without turning on the motor, the laser won't cut the material.

8) Using the laser cutting protocol document laser cut the lung-on-a-chip PMMA design component.

   Notes:

   - Filename: loc_pmma

   - For creating the outline image in the bitmap, use Image → Trace Bitmap → Brightness cut-off → 0.5 parameters → OK

- Always run a job perimeter to ensure the pattern is within the scope of cutting.

- Laser cutter settings

  o Speed - 40

  o Power - 60

  o Passes - 2

9) Once the material is cut, open the laser cutter lid and remove the cut-out components. Save remaining PMMA for future use.

Laser/Razor Cutting Double-sided tape

10) Cut two equal lengths of double-sided tape (DST). Place one tape adhesive (T1) side up on the counter. On the other, peel off the adhesive tape and save the liner (L1).

Note:

- Try not to touch the adhesive side of tape directly as it leaves fingerprint marks

- Wear gloves when handling the tape.

11) Line up the tape liner (L1) to the adhesive side of the tape (T1). While slowly laying the liner onto the adhesive tape, use a rectangular cut PMMA/glass slide to push out any bubbles formed. Once both the tape and liner are attached, remove any remaining bubbles with the cut PMMA. As the DST has one lined and one exposed side, this step lets to line both sides, so the tape is clean, and no dust particles stick to the exposed side throughout the process.

Note:

- If using the Razor plotter, the liner from the double-sided tape can be replaced with commercial liner in the lab. This avoids the wastage of tape to get the liner to cover

the adhesive exposed side. But this liner cannot be used in the laser cutter as it burns through it.

Patterning DST using Laser cutter:

12) Place the DST inside the laser cutter and tape the edges of the tape down using lab tape. This holds the tape in place during the cutting process.

13) Spray the tape with ethanol and swipe with Kim wipes® to evenly spread the ethanol.

   Note:

   - This step lets the tape layer to cool and not burn during the laser cutting process. Also, ethanol maintains sterility of the tape.

14) Recalibrate the laser head using the metal cylinder calibrator.

15) Upload the double-sided tape design to the software. Move the laser head to the upper left corner, ensuring the perimeter of the cut remains within the tape and within the laser movement limits without hitting the edges of the machine.

16) Using the laser cutting protocol document, laser cut the lung-on-a-chip DST design component.

   Notes:

   - Filename: loc_dst

   - For creating the outline image in the bitmap, use Image → Trace Bitmap → Edge detection → 0.3 parameters → OK

   - Always run a job perimeter to ensure the pattern is within the scope of cutting.

   - Laser cutter settings

     o Speed – 78

- o   Power – 6

- o   Passes - 1

17) Once the laser is adjusted, press the green play arrow to begin cutting.

18) After one pass, respray the tape with ethanol slightly.

Note:

Ensure that the tape does not move when being sprayed with ethanol. If the tape moves, then the laser will not cut in the same place and the tape cannot be used.

19) Pass over the tape using the same settings a second time.

20) Make sure that the tape is cut all the way through before removing it from the platform.

21) Open the lid to the laser cutter and remove laser-cut tapes. Turn off the computer, laser cutter, and fan once all device components are complete.

Patterning DST using Razor plotter:

Note:

- DST is recommended to be cut using Razor plotter to avoid burnt remains in the edges and get more precision in dimensions.

22) Place the DST on the carrier sheet and make sure to tape the edges of the DST to avoid moving of the tape during the cutting process.

23) Turn on the plotter and feed the carrier sheet to the Razor plotter. It is essential to ensure the top of the carrier sheet is parallel to the lock knobs of the plotter.

24) Open the Graphtec software and open the Lung-on-a-chip DST design component file.

25) Using the Graphtec Razor cutting protocol, cut the Lung-on-a-chip DST design component.

Note:

- Always make sure that you press the Origin button on the top-right corner of the plotter once the origin point is determined

- Settings

  o Acceleration - 1

  o Force - 31

  o Passes - 1

26) Once done cutting, remove it from the carrier sheet.

Note:

- It is better to leave the negative cut patterns on the tape as particles can attach to the edge of the positive cut pattern.

Building the device:

27) In a sterile environment, preferably inside a cell culture hood, pull out a glass slide (L1; See **figure 1**). Clean the slide with ethanol and make sure it is dry before starting to assemble.

28) Peel off the bottom side liner of the double-sided tape L2.

29) Align the patterned tape L2 to the top of the glass slide. Line up the top of the tape with the glass slide with the inlet on the top right side of the chip. Once the tape is positioned correctly, slowly lay it down on the glass slide.

30) Push any bubbles out of the chip with your thumb while the chip is on a flat surface.

Note:

Holding the chip and attempting to push out air bubbles may break the glass slide.

31) Peel off the top layer of tape using tweezers, so only the DST layer is on the slide. Align the PMMA (L3) with the inlets and outlets on the tape already on the glass slide.

32) Once the PMMA is aligned with the tape, press the PMMA firmly down onto the chip.

33) Place the chip on a flat surface and use a blunt end on a pen to push out any air bubbles that formed in between the PMMA and tape. Ensure there are no air bubbles near the channels or inlet/ outlet of the chip to achieve proper sealing.

34) Peel off the bottom liner of the next layer of tape L4, align it on the PMMA, and remove any bubbles.

35) Cut the membrane to the desired size using scissors and minimizing contact so that it remains sterile. The cut membrane should cover the central circle of the chip as well as the inlet channel. The membrane should not cover the inlet or outlet.

36) Peel off the top layer of the tape L4 and place the membrane on top of the channel and center of the chip. Lightly press down around the edges of the membrane without touching the center of the membrane or near the channel

37) Peel off the back of L5 tape and place it over the membrane. By design layers, L4, L5, and L6 are cut as one piece of DST with perforated lines to aid in the easy alignment of layers.

38) Align layer L6 DST with the aid of the engineered perforated lines.

39) Keep the device sterile inside a cell culture dish to avoid contamination and settling of particles on the membrane.

   Note:

   - The top PMMA and DST layer (L7 – L9) are stacked only after fabricating the hydrogel layer on the membrane (step 67).
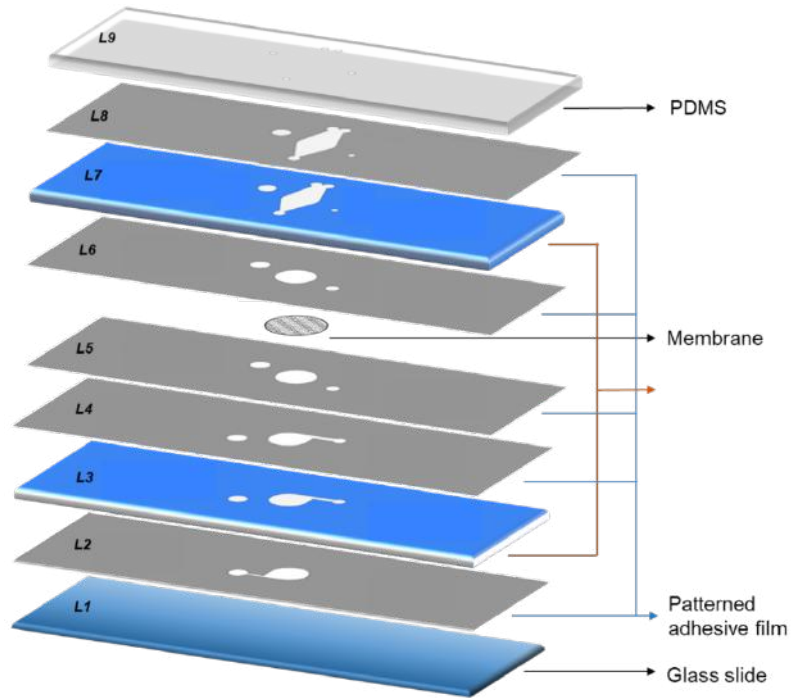
A 1. 1 Lung-on-a-chip device fabrication. The exploded schematic view of Lung-on-a-chip showing the multi-layer architecture.

II. Cell Culture

Epithelial cell culture

40) Prior to seeding cells, coat T-75 cell culture flask with 0.04 mg/ml Type I Bovine Collagen and leave it overnight in the hood with airflow.

41) Next day seed primary irradiated fibroblasts at 10×10^3 cells/cm^2 into pre-coated flasks with complete fibroblast growth medium (alpha-MEM + 10% FBS + 1% L-glutamine) 0r DMEM-10 (Hugh glucose DMEM + 10% FBS +1% L-glutamine +1% Penicillin/Streptomycin).

42) After incubating overnight, wash with DPBS and seed primary epithelial cells at a density of 5 x 10^3 cells/cm^2 in the BEGM + 5 µM Y -27632 (ROCK inhibitor) medium.

43) Examine the cell culture plate under the light microscope with 10X magnification for confluency.

44) Place 0.05% Trypsin (serine protease) and appropriate cell culture media (DMEM-10/ ALI-complete/ BEGM-10) in the bead bath to warm up to 37℃.

   Note:

   - If placed in a water bath, wrap the lids with parafilm to prevent possible contamination.

45) Turn off the UV light and turn on the fan and light in the hood. Spray the hood with 70% EtOH and wipe to remove the residual ethanol. Wipe down two 10 ml Pipettes and a 5 ml pipettes with EtOH and place them in the hood. Wipe down the reagents that were heating with EtOH and place them in the hood.

46) Attach a borosilicate glass pipette to the vacuum line tubing. Open and hold the cell culture dish at an angle, remove media with vacuum pipette and close the lid.

47) Add 10 ml of PBS to the cell culture and remove the PBS with the vacuum pipette in a similar technique. Remember never to have two lids open at once (Including the lid with the cell culture which should always be closed after adding reagents).

48) Add 5 ml of Trypsin to the cells and swirl the plate to ensure the complete coverage of the dish. Wipe with EtOH and place it in an incubator for 5 minutes at 37℃.

Note:

- If trypsinizing epithelial cells with fibroblast feeder cells, remove the trypsin after 30 sec to 1 minute to remove the fibroblast. Then add trypsin again and incubate for 5 minutes

- Before removing the trypsin the first, look under the microscope to make sure the feeder fibroblast cells are detached.

49) Remove the plate from the incubator and view them under a light microscope to ensure the cells are detached from the plate. If they are not in suspension, incubate for one or two more minutes or rigorously shake the plate sideways to detach cells.

50) Add 5 ml of the appropriate media.

51) Transfer the 10 ml cell culture solution into a 15 ml conical centrifuge tube with a 10 ml glass pipette. Make sure to tighten the lid before removing it from the hood.

52) Centrifuge the cell suspension for 5 minutes at 1500 rpm.

53) Use a vacuum pipette to remove the supernatant media leaving the pellet of cells. Add 1 ml of media and resuspend the pellet by moving liquid in and out of the pipette. Do not push the pipette down all the way to avoid bubble formation.

54) For 10X cell density dilution for the ease of cell counting, add 10μL of evenly suspended cell media to 90μL of appropriate media

55) Take the trypan blue dye and place two 10 microliters drop onto a strip of parafilm separately. Take 10 microliters of 10X diluted cells and resuspend with one of the trypan blue droplets on the parafilm. This helps to avoid counting of dead cells as they stain dead cells cytoplasm completely with dark blue.

56) Mix the two solutions thoroughly by pipetting to make a homogenous mixture and load 10 microliters of the cell-trypan solution into a hemocytometer. Repeat the process with another sample of cells and load on the other side of a hemocytometer.

57) Count the cells in all the four quadrants of squares that have 4 by 4 smaller squares within them. Repeat the process for the other side of the hemocytometer.

58) Calculate the number of cells by

$$\frac{\# \ of \ cells * 2}{4} * 10,0000$$

This calculation gives you the number of cells in one 1ml of the sample.

59) If using an automatic cell counter, multiply by 10 as we used 10x dilution.

60) Based on the number of cells required, take the required volume of solution calculated by the formula below to centrifuge and get a cell pellet.

$$Q1V1 = Q2V2$$

Q1 = total number of cells in 1mL counted;

V1 = 1000 µL;

Q2 = Required number of cells for the experiment;

V2 = Unknown volume of cell suspension.

III. Hydrogel Preparation

61) Cover the three components of the hydrogel – Glycosil/Heprasil, Gelin-S and Extralink; with aluminum foil and dissolve these in sterile water containing 0.05% (w/v) of the photoinitiator (PI) to make a 2% w/v solution respectively.

Note:

- Add 500 µL of 0.5% PI to Heprasil/Glycosil and Gelin-S.

- Add 250 µL of 0.5% PI to Extralink.

62) Cover all the components with aluminum foil and secure using tape.

63) Place it on a rotor or rotary shaker in warm room / 37℃ for 40 mins or until the components are completely dissolved and are not viscous, especially Heprasil.

IV. Lung-on-a-Chip

64) Prior to adding the cellular components to the device, plasma treat the membrane of the chip by placing one device at a time in the plasma cleaner.

65) Make sure that the chip is transferred quickly from inside a plate to the plasma machine, so no dust particles settle on the membrane

66) Once the membrane on the devices is plasma treated, leave all chips under the UV light for at least 20 minutes. The hydrogel must be placed on the membrane within 1 hour of plasma treatment.

A. Hydrogel + Fibroblast layer

67) The first layer is the hydrogel and the fibroblast layer (**figure 2c**).

68) After Trypsinizing, the fibroblast cells determine the number of cells. Calculate the number of cells needed by equation

$$\# \ of \ cells = \left(180{,}000 * (\# \ chips + 1)\right) * 2$$

Note:

- If using immune cells in the system, add only --- 150,000 cells.

69) Use M1V1 = M2V2 to determine the volume needed for the correct number of cells. Once this volume is known, divide the total cell suspension into two 1.5 mL centrifuge tubes.

Note:

- One of these tubes will serve as a "back up."

- When pipetting cells, always remember to re-suspend before aliquoting.

70) Centrifuge the two cell suspension aliquots for 5 minutes at 1500 rpm.

71) Use a vacuum pipette to remove the supernatant media leaving the pellet of cells.

72) Each chip requires 15µL of the hydrogel. To determine how much gel to make multiply the number of chips fabricated by 15µL.

Note:

- Add an additional 15µL to avoid miscalculation issues or bubbles.

73) Use ratio 1:1:0.5 parts Gelin, Heprasil, and Extralink for half of the hydrogel. Lung ECM dissolved in 0.5% PI is accounts for the other half.

i.e., of the 15 µL, 7.5 µL is composed of the hydrogel component, and 7.5 µL is lung ECM.

74) Calculate how much of each component is needed for the hydrogel.

Note: 15 µL hydrogel = 3 µL Heprasil +3 µL Gelin + 1.5 µL Extralink + 7.5 µL lung ECM.

75) Turn off the light in the hood when preparing the hydrogel. This alleviates the influence of the ambient light in the gelling process.

76) Add required volume of each component to the cell pellet and re-suspend the gel to ensure it is homogenous. Do not push the pipette all the way down to avoid bubble formation.

77) Pipette 15μL of the hydrogel onto the chip. Place the pipette tip vertical and as close to the membrane as possible without touching.

78) Ensure the hydrogel covers the entire membrane tilting the chip if necessary or using a flat side of the pipette tip to move the hydrogel around.

79) Pipette hydrogel into all chips.

80) Set the UV lamp to 2 seconds. Place the tip directly above hydrogel at 5 cm height approximately and turn on the lamp.

81) Ensure the gel is cross-linked by lightly touching the hydrogel with a pipette tip

82) Continue to cross-link all hydrogels on the chip.

83) Immediately after all hydrogels are successfully crosslinked, layer the PDMS attached to low tack rubber adhesive tape at the bottom with 7mm biopsy punched holes to align on top of the membrane.

84) Add 100 μL of media to the top of the hydrogel.

85) Add media to the bottom of the chip. Place the full tip of the pipette in the outlet of the chip. Tilt the chip up with the front-facing forward to allow media to flow up the chip.

86) When media has reached the central membrane, place the chip flat, and quickly push the media through the chip.

87) If any bubbles are formed underneath the membrane, remove all media using the vacuum pipette and repeat until the media fills the bottom with no bubbles.

88) All chips have media in both the top and bottom channels of the chips on a plate. Fill a
35 mm cell culture dish with PBS and placed in the incubator overnight.

Note:

- PBS creates humidity in the cell culture dish and reduces evaporation at 37°C.
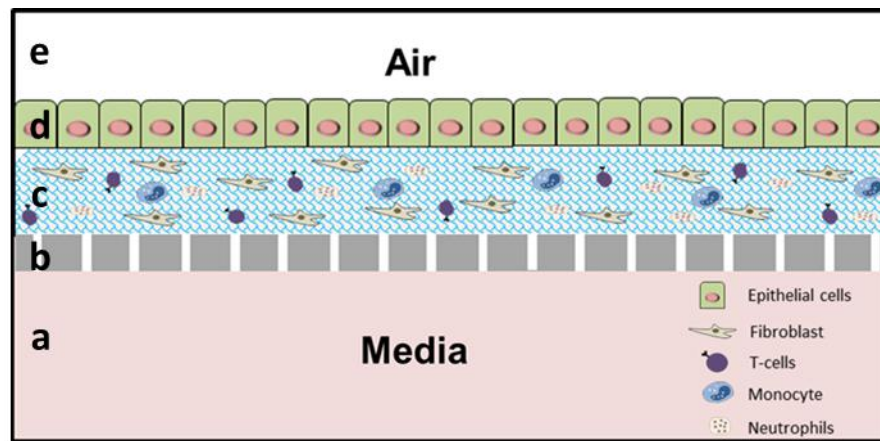
A 1. 2. Schematic of lung organoid layers. a) Culture medium flowing in the bottom
chamber. b) Membrane with 8µM pore size separating the top and bottom chamber. c)
Hyaluronic acid-based hydrogel layer with lung ECM encapsulating fibroblast and immune
cells (neutrophils, monocyte and T-cells). d) A monolayer of epithelial cells. e) Airflow on
the top chamber.

B. Epithelial layer

89) The second layer is the epithelial layer that is biofabricated after a day (**Figure 2d).**

90) After Trypsinizing the epithelial cells or A549 cells and getting a pellet, determine the
number of cells required. Calculate the number of cells needed by equation

$$\# \ of \ cells = \big(250{,}000 * (\# \ chips + 1)\big)$$

91) Use M1V1 = M2V2 to determine the volume needed for the correct number of cells.

92) Take the chips from the incubator and aspirate the media from the top chamber.

93) Add 250,000 cells / 100 µL of media per device.

94) Place the chips back in the cell culture dish and into the incubator.

95) Incubate a minimum of 4 hours to let the cells attach to the hydrogel layer before aspirating the excess cells and changing to ALI complete media.

96) After aspirating the cells, L7 PMMA is attached to the L6 layer.

97) Cut the top PDMS layer using the premade PDMS in a 15mm culture dish (30g: 3g ratio of PDMS kit). Plasma treat the top PDMS L9 and DST layer L8 and attach by layering on a flat surface. Make sure there are no bubbles. Punch holes for inlet and outlet using an appropriate blunt needle.

98) Do not plasma treat the other side of the DST that attached to the PMMA. Now enclose the chip by layering the adhesive side of the DST L8 on top of the chip layer L7.

Notes:

- Remove all the media from the device before attaching the top layer as it might interfere in the proper attachment.

- Plasma bonding works best only when both the surfaces are plasma treated.

99) Incubate and change media twice every day on both the top and bottom chamber until the epithelial cells are 100% confluent.

100)

V. Connecting to flow:

101)   Have the entire component of the flow system EO sterilize.

Materials:

- humidifier chamber consisting of two 500 mL bottles

- Bottle lids with connectors and valves

- Tubings

102) The air compressor is connected to the humidifier through the blue tubing.

103) Through one of the six outlets in the humidifier, each inlet of the top chamber is connected. The outlet of these chips is initially connected to an enclosed container with water. Bubbles formed in the water help to ensure the flow of air through the system as seen in **figure 3**.
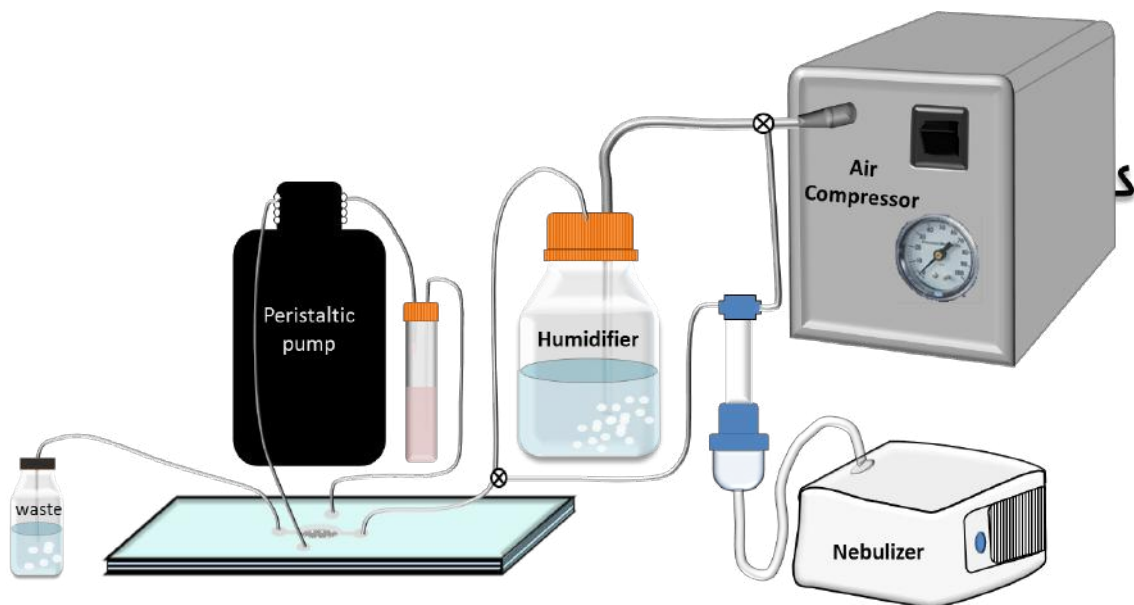
A 1.3. Lung-on-a-chip experimental set-up.

104) Then the chip is connected to individual chip adapter (**figure 4a**) or 3-in-1 inlet adapter chip (**figure 4b**) for mass spectrophotometer flow collection.
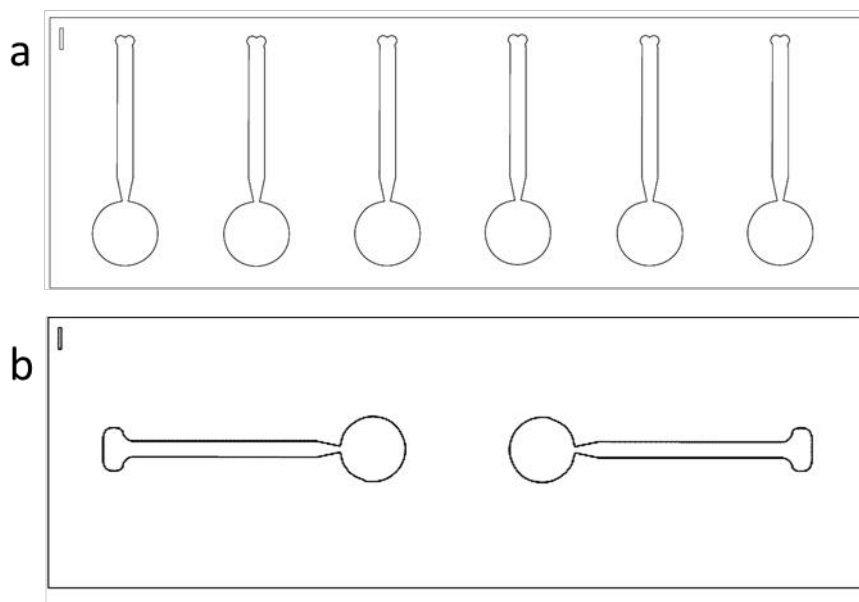
A1. 4. Adapter for the Lung-on-a-Chip. a) A single organoid inlet to outlet format chip accommodating six organoids with or without varying conditions. b) Three inlets to one outlet format chip accommodating six organoids but only two conditions.
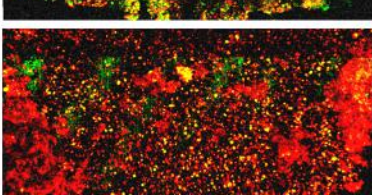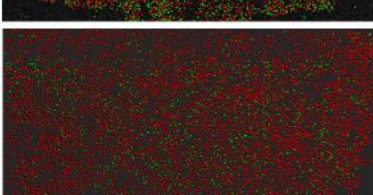
VI. Imaging:
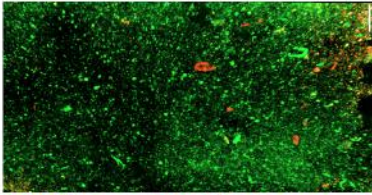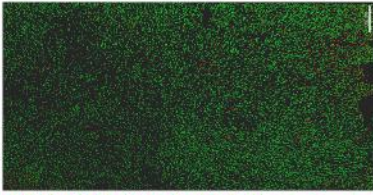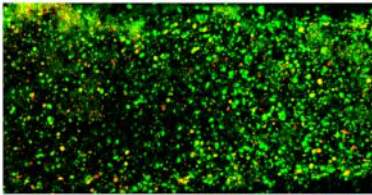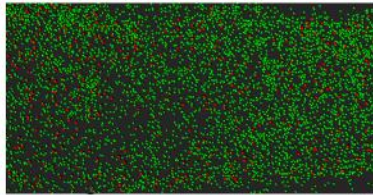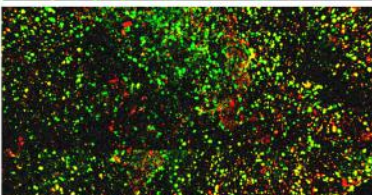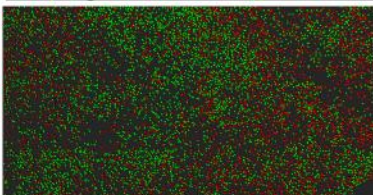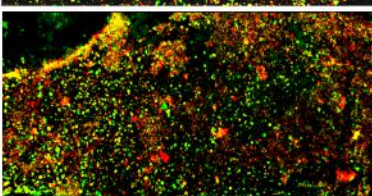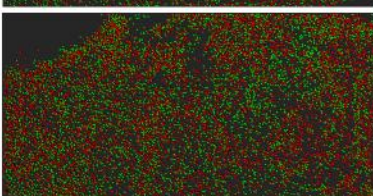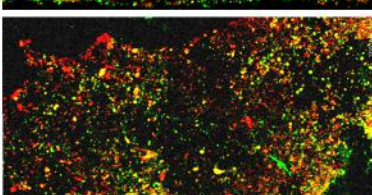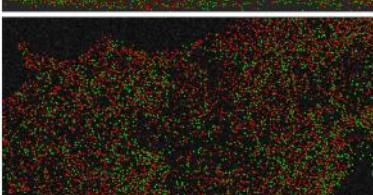
105) The device is imaged in the bright field using any inverted microscope that can accommodate the chip. The images confirm the confluency of the chip as shown in Figures 5a and 5b.

106) At the end of the experiment, the organoids are stained with LIVE/DEAD solution (incubated for 30 min) and imaged using Leica Macro confocal (**figure 5c and 5d**)
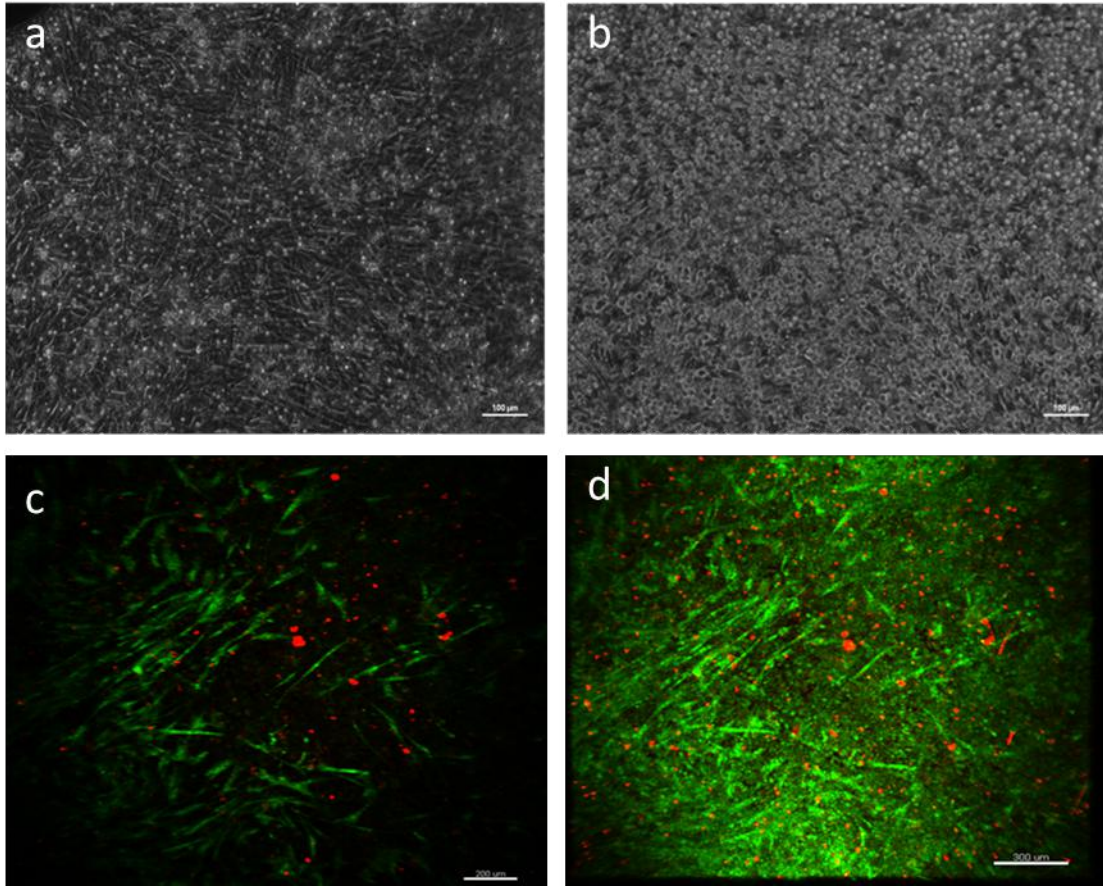
A1. 5. Lung-on-a-chip results. a) Brightfield image of fibroblast monolayer after reaching 100% confluency. b) Brightfield image of A549 monolayer of the cell after 2 days of cell seeding. Live/Dead imaging of c) 2D layer of fibroblast suspended in hydrogel and d) maximum projection image of both fibroblast and monolayer of epithelium on day 7 of organoid exposed to airflow. Green stain – calcein AM-stained viable cells; Red stain – ethidium homodimer-stained dead cells.

A2. 1. Patient 1 organoid LIVE/DEAD segmentation. Same data as in Figure. 3. 10 of the main text, but with segmented images resulting from Imaris analysis software, showing live (green) and dead (red) cell positions**.**
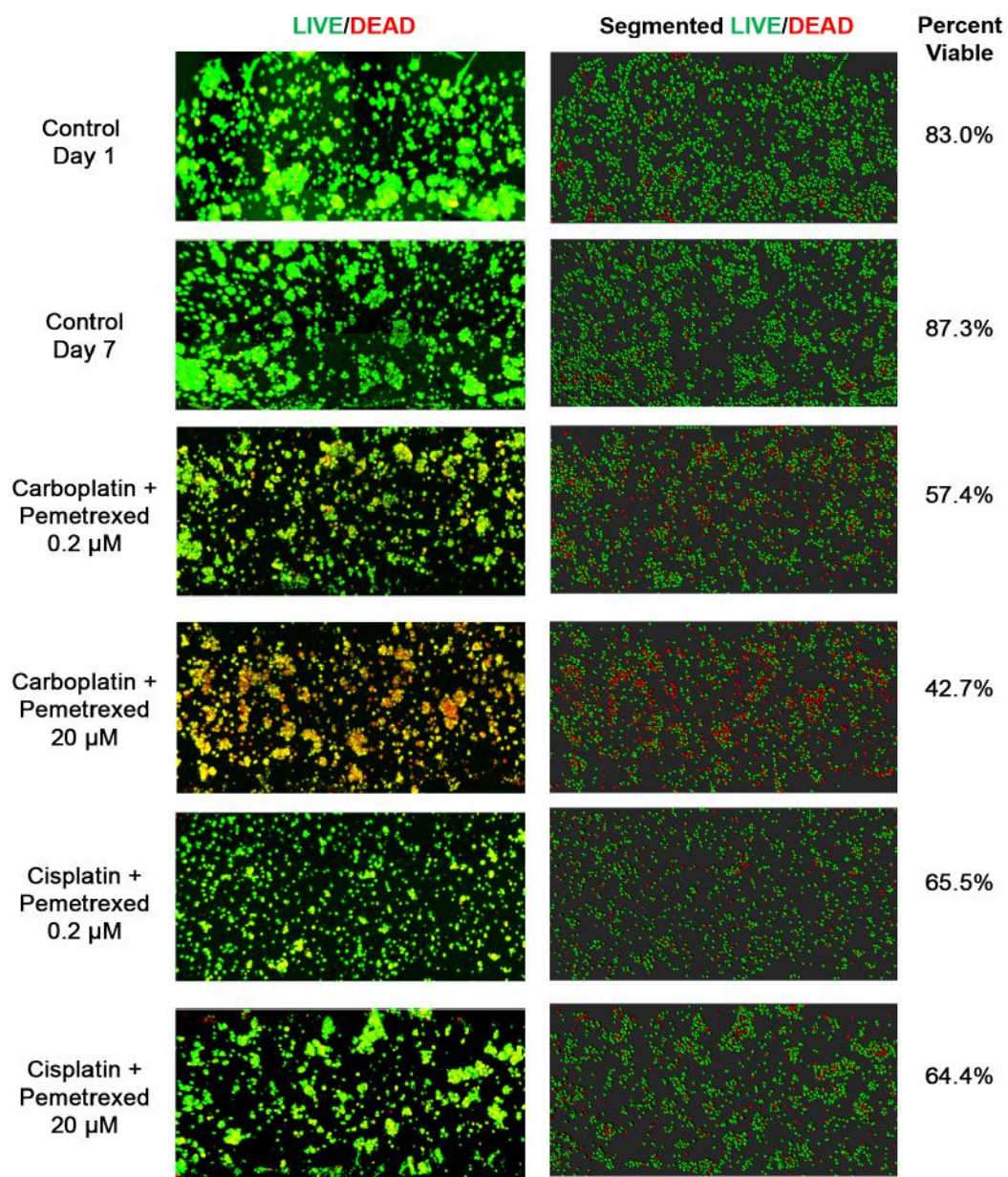
A2. 2. Patient 2 organoid LIVE/DEAD segmentation. Same data as in Figure 3. 10 of the main text, but with segmented images resulting from Imaris analysis software, showing live (green) and dead (red) cell positions.
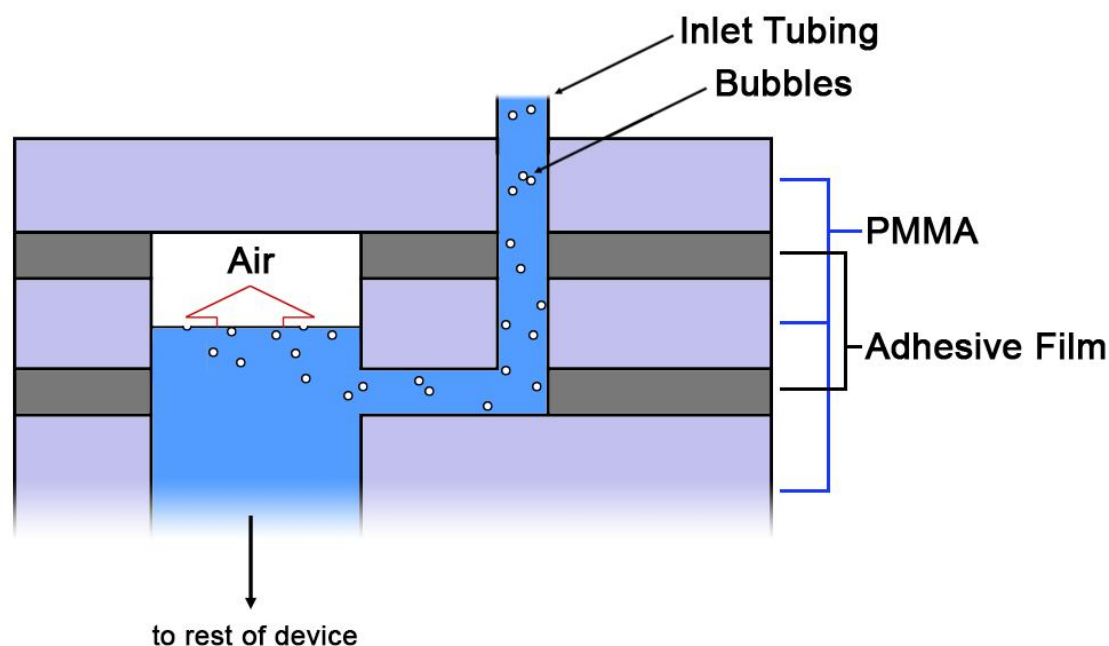
A3. 1. Schematic of bubble trap. Cross-sectional view of the top four layers shown in Figure 1a of the main text, illustrating the functioning of the bubble trap. As bubbles in the fluid pass, they are collected in the air cavity due to buoyancy, removing them from the flowing medium. This structure effectively eliminated small and large bubbles from the system, limited ultimately by the volume of the cavity.
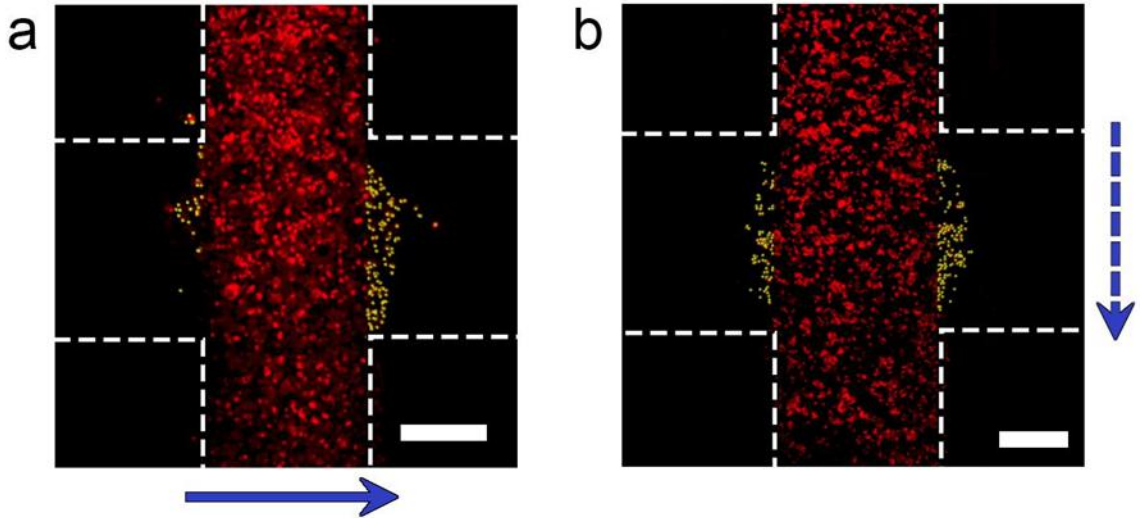
A3. 2. Interstitial flow influence on migrated cells. Processed maximum projection confocal micrographs of HCT-116 cells after 10 days of continuous flow (a, 4 µL/min) and 10 days of intermittent flow (b, 4 µL/min for 10 min, no flow for 120 min). Positions of invading cells are marked digitally with yellow points overlaid on the micrograph. Blue arrow indicates the direction of flow. Construct borders are roughly indicated by white dashed lines (inter-region border not indicated for clarity). Scale bars are 300 µm.
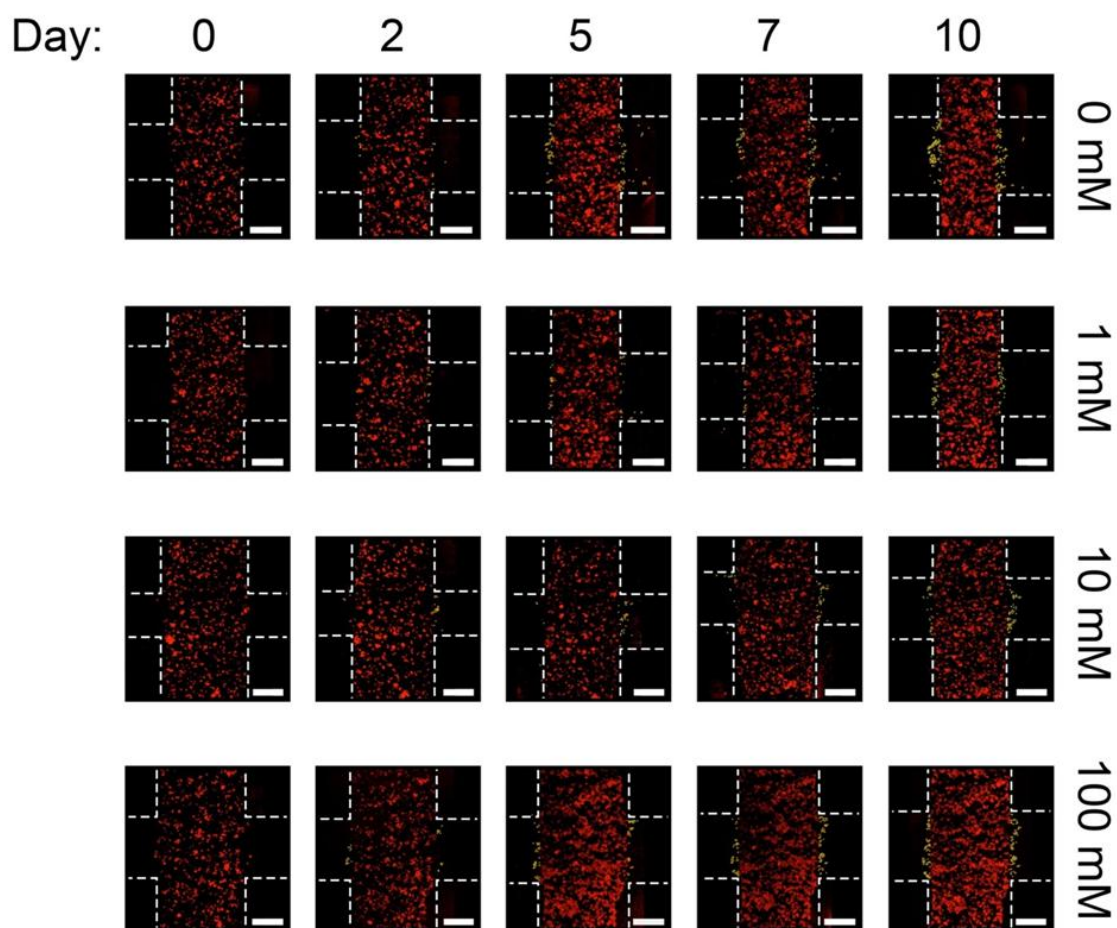
A3. 3. Expanded views of the typical maximum projection confocal micrographs of cell invasion for all 5FU conditions and time points. Images are processed to show positions of invading cells with yellow points overlaid on the micrograph. Construct borders are roughly indicated by white dashed lines (inter-region border not indicated for clarity). All scale bars are 300 μm.
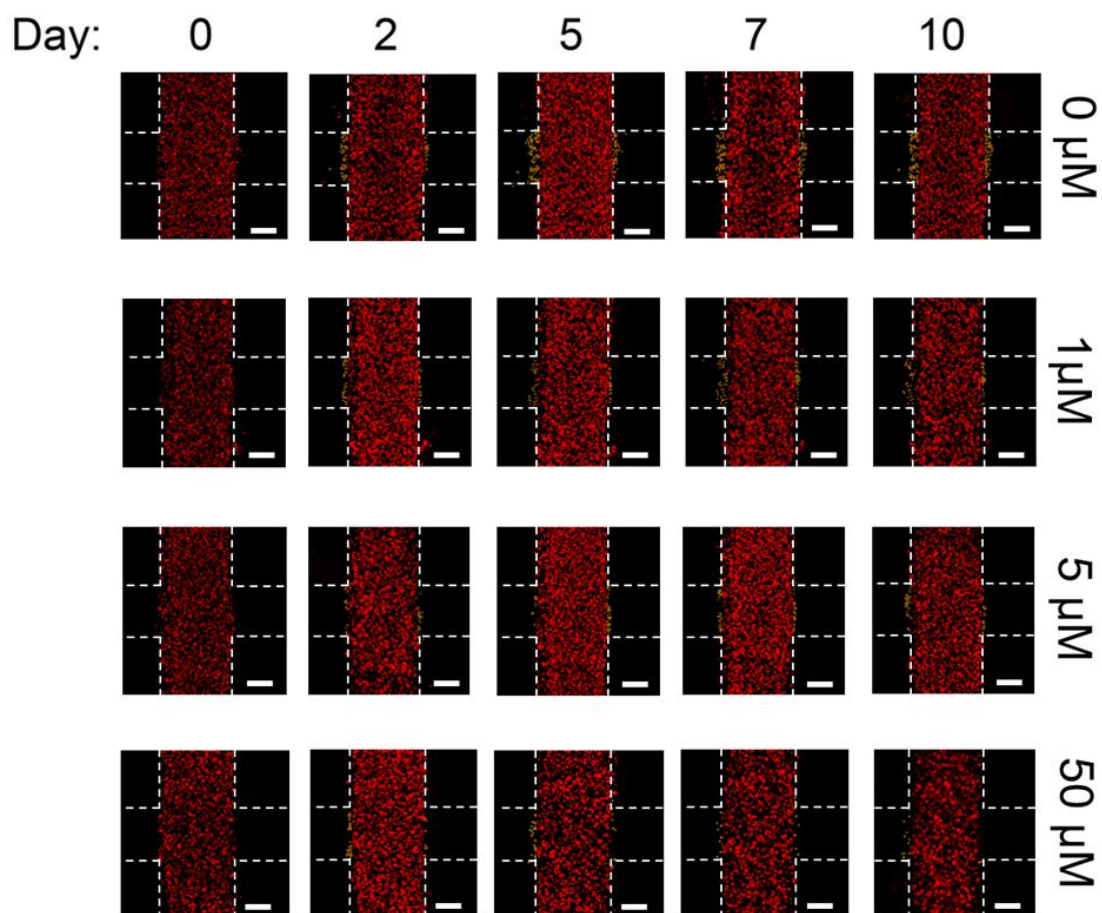
A3. 4. Expanded view of the typical maximum projection confocal micrographs of cell invasion for all Marimastat conditions and time points. Images are processed to show positions of invading cells with yellow points overlaid on the micrograph. Construct borders are roughly indicated by white dashed lines (inter-region border not indicated for clarity). All scale bars are 300 μm.
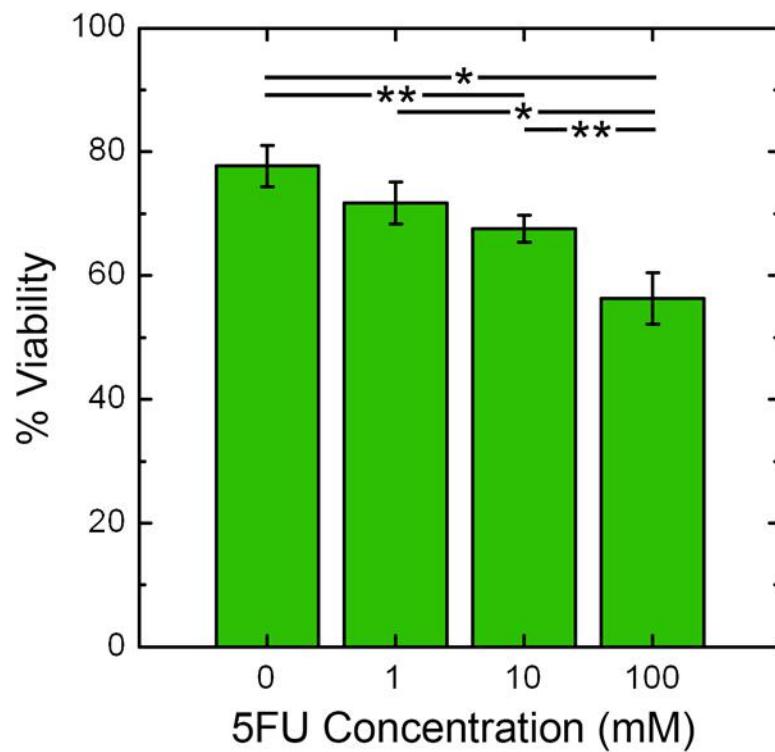
A3. 5. LIVE/DEAD viability of HCT-116 under 5FU insult. Viability on day 10 calculated as the ratio of live cells under a given condition to the total number of live and dead cells in the same construct (i.e., *not* scaled to control construct as in the main text). Significance: * $p<0.01$, ** $p<0.05$.
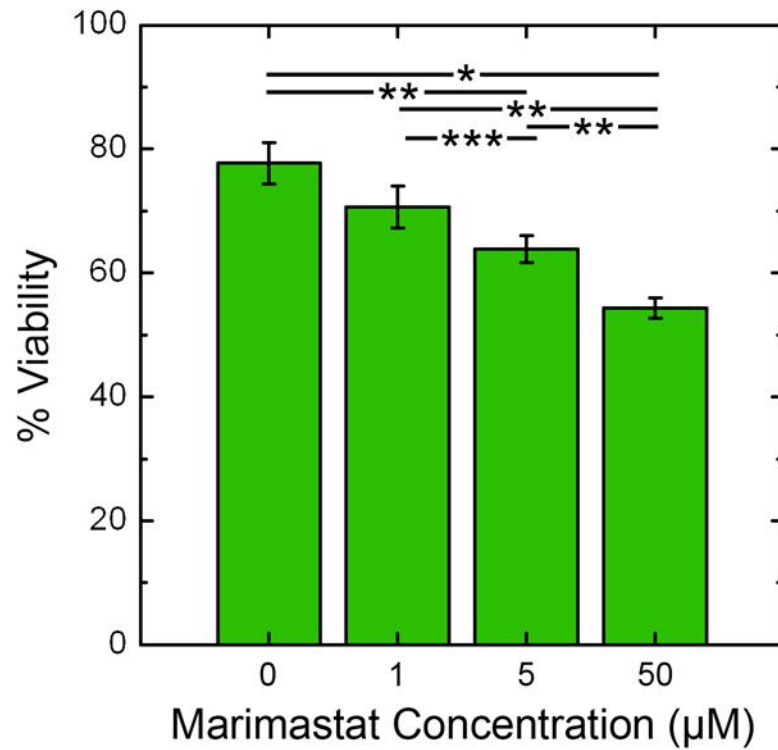
A3. 6. LIVE/DEAD viability of HCT-116 under Marimastat insult. Viability on day 10 calculated as the ratio of live cells under a given condition to the total number of live and dead cells in the same construct (i.e., *not* scaled to control construct as in the main text). Significance: * p<0.001, ** p<0.01, *** p<0.05.

Curriculum Vitae

Shiny Amala Priya Rajan

Cell: (404)579-3086   Email: shinyrajan88@gmail.com

Education and Training

2015-2019   Doctor of Philosophy (Biomedical Engineering, Ph.D./MBA dual degree)

Virginia Tech – Wake Forest School of Biomedical Engineering and Science, Winston-Salem, North Carolina.

Dissertation: Integrating advanced 3D cell culture techniques with rapid-prototyping microfluidics for translational applications. Adam Hall, Ph.D. and Aleksander Skardal, Ph.D., advisors.

2017-2019   Master of Business Administration (Ph.D./MBA dual degree)

Wake Forest University, Winston-Salem, North Carolina.

2011-2013   Master of Science (Biomedical Engineering)

Arizona State University, Tempe, Arizona.

Thesis: Non-invasive method to detect the changes in glucose concentration in whole blood using the photometric technique. Bruce Towe, Ph.D., advisor.

2006-2010   Bachelor of Engineering (Biomedical Engineering)

Anna University, Chennai, India.

Employment

WAKE FOREST INSTITUTE OF REGENERATIVE MEDICINE| WINSTON-SALEM, NC | 2015 – PRESENT

Graduate Researcher

- Investigated various 3D cell culture techniques in an adhesive film-based microfluidic system for translational applications.

- Developed patient-specific tumor model and novel phenotypic 3D assays that can be utilized for devising personalized treatments to enhance the therapeutic outcomes of cancer patients.

- Designed and developed complex integrated 3D multi-organ system on a microfluidic platform for assessing drug toxicity.

- Mastered new techniques in microfabrication, 3D tissue constructs, microscopy, and image analysis.

- Gained extensive experience in scientific communication through publications and presentations all over the United States.

- Work closely with established and emerging expertise in the field, coordinating on complex projects with colleagues to produce new findings and drive innovation.

Team Lead, NIH sponsored Nano Startup Challenge in Cancer: 2016 – 2017

- Responsible for developing award-winning business model and technology roadmap through commercialization.

- Provided exceptional guidance in experimental planning to a five-member team in order to guarantee project success.

- Gained first-hand experience in developing a startup company in a biotechnology field and leadership skills.

WAKE FOREST INNOVATIONS | WINSTON-SALEM, NC | 2017 – 2019

Technology Innovative Associate Fellow

- Collaborated with top-performing professionals on the innovation and commercializing team to review potential technology-related medical devices and cancer treatments for relevant patent filings.

- Coordinated and performed extensive market analytics on platforms such as GlobalData and PatSnap to assess and compare existing patents.

- Engaged with three team inventors including physicians and professors to generate creative developmental plans and advance critical technology for licensing and further investment.

VEROTECH SOLUTIONS | TAMARAC, FL | 2015

Quality Engineer Trainee

- Consulted and supported a number of key projects for medical devices involving injection molding, performing failure mode analysis, risk management, SOP reviews, GAP analysis, Gage R&R studies, test method validation and process parameter control.

- Managed numerous quality engineering projects while providing strategic leadership to the quality team.

ARIZONA STATE UNIVERSITY | TEMPE, AZ | 2012 – 2014

Research Assistant: 2014

- Continually improved the design of an effective glucose sensor, identifying efficient resolutions to complex engineering problems while ensuring the project was completed on time and exceeded expectations.

- Directed a two-member project team while monitoring for maximized productivity and efficiency.

- Designed an innovative sensor to detect glucose changes in diabetics in a non-invasive method and conducted spectrum analysis of blood to detect the optical density changes with respect to the glucose concentration.

Biodesign Institute Biomedical Research Aide: 2013

- Organized and performed complex experiments on the developing technology, including performing high-throughput single live cell metabolic measurement, with a focus on designing verification tests and fixture models.

- Developed and optimized essential procedures and performed data analysis on test results while also creating appropriate SOPs with funding by the NIH.

- Improved the lab efficiency while running processes according to high company and departmental safety standards.

Lab Aide: 2012 – 2013

- Delivered outstanding student support by assisting two disabled students with chemistry and biochemistry lab work, significantly improving their academic grades.

- Created special study plans based on students' short-term and long-term goals while assessing students' current knowledge level, elevating exam scores by two letter grade.

- Provided a supportive and positive environment for all students to allow them to develop the skills, attitudes, and knowledge to meet and exceed all standards.

Grader: 2012

- Accurately graded 60 weekly lab reports for the bio-instrumentation lab along with 60 daily assignments for bio-instrumentation coursework while identifying areas for student improvement.

- Proactively discussed assigned duties with classroom professors in order to coordinate instructional efforts.

GLOBAL HOSPITALS | CHENNAI, INDIA | 2010

Biomedical Intern

- Provided comprehensive assistance in maintaining critical hospital equipment such as imaging systems and assist devices.

- Evaluated various assist devices and analyzed their efficiency for hospital clinical use to assure optimal success.

- Established key procedures for improving the organizational efficiency of the inventory process including maintaining appropriate medical device inventory.

Additional professional Experience

Journal Reviewer

- Lab-on-a-chip (Impact Factor: 6)   2019

Continued Education

- WFIRM – Regenerative Medicine Essentials Course Attendee   2017 - 2019

Professional Memberships

Biomedical Engineering Society - BMES (20015-present).

Tissue Engineering and Regenerative Medicine International Society – TERMIS (2016-2019).

Abbreviated Skills List

Specialization

Drug discovery & high-throughput screening, Organ-on-a-chip technology, Integrated multi- organ systems, Tape microfluidics, Cancer Organoid, Personalized treatment, Disease modeling, Tumor microenvironment, Image processing.

Laboratory Skills

ELISA, Cell / tissue culture, Hydrogel (3D) Histology, IHC staining, Microscopy (confocal, fluroscence), Cell phenotype assays (migration, invasion, etc.), Laser cutter and milling/drilling machine, Microfluidic Fabrication, Rheology, Photolithograph

Software

MATLAB, Solid Works, AutoCAD, Imaris, MetaXpress, Labview, COMSOL, SAS enterprise, OriginPro, MS office.

Honors and Awards

- II place in poster presentation titled "Tumor-on-a-chip microfluidic devices for personalized cancer drug testing" in WFIRM retreat 2018
- II place in Poster presentation titled "Adhesive membrane based body-on-a-chip platform for assessing drug efficiency and toxicity" in TERMIS AM 2017

- Selected as Top 10 talk titled "Tumor-on-a-chip microfluidic devices for personalized cancer drug testing" in TERMIS AM 2017

- Winner of "Innovation Excellence Award" in NIH Nanotechnology Startup Challenge in Cancer.

- Received "Scientist Award" for outstanding contribution to tissue engineering and regenerative medicine at TERMIS-AM 2016

- III place in poster presentation titled "Microfluidic device for motility and biochemical assessment in parallel drug testing" in NCTERMS 2016.

- II Place in Poster presentation titled "Bionic Limbs" at national level symposium held at Rajalakshmi Engineering College.

Publications

1. **Shiny Amala Priya Rajan**, Julio Aleman, MeiMei Wan, Nima P. Zarandi, Goodwell Nzou, Sean Murphy, Colin Bishop, Hooman Sadri-Ardekani, Thomas Shupe, Anthony Atala, Adam Hall, Aleksander Skardal. 'Probing prodrug metabolism and reciprocal toxicity with an integrated and humanized multi-tissue organ-on-a-chip platform. *Acta Biomaterialia 2020* (In press).

2. Aleksander Skardal, Julio Aleman, Steven Forsythe, **Shiny Rajan,** Sean Murphy, Mahesh Devarasetty, Nima Pourhabibi Zarandi, Goodwell Nzou, Robert Wicks, Hooman Sadri-Ardekani, Colin Bishop, Shay Soker, Adam Hall, Thomas Shupe, and Anthony Atala. Body on a chip bio fab Drug compound screening in single and integrated multi-organoid body-on-a-chip systems. *Biofabrication 2020* (In press).

3. **Shiny A. P. Rajan**, Aleksander Skardal, and Adam R. Hall. Multi-domain photopatterned 3D tumor constructs in a micro-physiological system for analysis, quantification, and isolation of infiltrating cells. *Advanced Biosystems 2020* (In press)

4. Erin Maloney, Casey Clark, Hemamylammal Sivakumar, KyungMin Yoo, Julio Aleman, **Shiny A. P. Rajan**, Steven Forsythe, Andrea Mazzocchi, Adrian W. Laxton, Stephen Tatter, Roy Strowd, Konstantinos I. Votanopoulos, Aleksander Skardal. Immersion Bioprinting of Tumor Organoids in Multi-Well Plates for Increasing Chemotherapy Screening Throughput. *Micromachines 2020, 11(2), 208*.

5. Kevin Enck, **Shiny Rajan**, Julio Aleman, Simone Castagno, Emily Long, Fatima Khalil, Adam R. Hall, Emmanuel C. Opara. Design of a Microfluidic Device for Alginate Hydrogel-based Cell Encapsulation. *Annals of Biomedical Engineering* 2020 March, 48(3):1103-1111

6. Andrea R. Mazzocchi*, **Shiny A. P. Rajan***, Konstantinos I. Votanopoulos, Adam R. Hall and Aleksander Skardal. In vitro patient-derived 3D mesothelioma tumor organoids facilitate patient-centric therapeutic screening. *Scientific Reports* (2018).

7. **Shiny A. P. Rajan**, Parker Hambright, Rosemary Burke and A. R. Hall. "Microfluidics in Cell and Tissue Studies" in Tumor Organoids, (Ed. S. Soker, A. Skardal), Springer Press (2016).

8. **Shiny Amala Priya Rajan** and Bruce C. Towe. "Non-invasive method to detect the changes of glucose concentration in whole blood using photometric technique." *2014 36th Annual International Conference of the IEEE Engineering in Medicine and Biology Society* (2014): 4034-4037.

In preparation (titles and author lists are subject to change)

9. **Shiny A. P. Rajan**, Tim Leach, Ryan Szczech, Lucy Vaughn, Sean Murphy and Adam Hall." Biomimetic air-liquid interface lung-on-a-chip for aerosolized toxicity studies"

10. Kirtikar Shukla, **Shiny A. P. Rajan**, Xiaofei Chen, Tom E. Forshaw, Tiffany Walker, Gregory Kucera, Allen W. Tsang, Aleksander Skardal, Adam Hall and Cristina M. Furdui. "Characterization of therapeutic susceptibility in head and neck squamous cell carcinoma (HNSCC) tumors"

Presentations

1. **S Rajan**, A Skardal, AR Hall. Photopatterned multi-domain 3D cell culture constructs in a microfluidic device for quantitative cancer cell motility analysis. Virginia Tech - Wake Forest School of Biomedical Engineering and Sciences Symposium, Blacksburg, VA. May 2019. **(Oral Presentation)**

2. **S Rajan**, A Mazzocchi, K Votanopoulos, A Skardal and AR Hall. Tumor-On-A-Chip Microfluidic Devices for Personalized Cancer Drug Testing. 19th Annual Graduate Student & Postdoc Research Day, Winston-Salem, NC. March 2019. **(Poster Presentation)**

3. **S Rajan,** A Skardal, AR Hall. Photopatterned multidomain 3D cell culture constructs in a microfluidic device for quantitative cancer cell motility analysis. Annual Wake Forest Institute of Regenerative Medicine Retreat 2019, Pinehurst, NC. January 2019. **(Oral Presentation)**

4. **S Rajan,** T Leach, S Murphy, A Skardal, AR Hall. Adhesive film based lung-on-a-chip platform for assessing effects and toxicity of environmental pollutants, chemicals and

drugs. Annual Wake Forest Institute of Regenerative Medicine Retreat 2019, Pinehurst, NC. January 2019. **(Poster Presentation)**

5. **S Rajan**, A Skardal, AR Hall. Photopatterned multidomain 3D cell culture constructs in a microfluidic device for quantitative cancer cell motility analysis. Cellular and Molecular Bioengineering Conference, San Diego, CA. January 2019. **(Poster Presentation)**

6. **S Rajan**, T Leach, S Murphy, A Skardal, AR Hall. Adhesive film based lung-on-a-chip platform for assessing effects and toxicity of environmental pollutants, chemicals and drugs. Cellular and Molecular Bioengineering Conference, San Diego, CA. January 2019. **(Poster Presentation)**

7. **S Rajan**, A Skardal, AR Hall. Tumor-On-A-Chip Microfluidic Devices for Personalized Cancer Drug Testing. Sigma Xi student Research Showcase 2018. **(Online presentation)**

8. **S Rajan**, R Burke, S Murphy, A Skardal, AR Hall. An adhesive film-based lung-on-a-chip system to test environmental pollutants and drugs. STEM Exchange: Research and Career symposium, New York, NY. August 2018. **(Poster Presentation)**

9. **S Rajan**, J Aleman, M Wan, NP Zarandi, G Nzou, U Gandhi, S Murphy, CE Bishop, H Sadri-Ardekani, T Shupe, A Atala A Skardal, AR Hall. Multi-organoid body-on-a-chip platform for assessing drug efficiency and toxicity. STEM Exchange: Research and Career symposium, New York, NY. August 2018. **(Poster Presentation)**

10. **S Rajan**, A Mazzocchi, K Votanopoulos, A Skardal, AR Hall. Tumor-On-A-Chip Microfluidic Devices for Personalized Cancer Drug Testing. Virginia Tech - Wake

Forest School of Biomedical Engineering and Sciences Symposium, Winston-Salem, NC. May 2018. **(Poster Presentation)**

11. **S Rajan**, J Aleman, M Wan, NP Zarandi, G Nzou, U Gandhi, S Murphy, CE Bishop, H Sadri-Ardekani, T Shupe, A Atala A Skardal, AR Hall. Adhesive film based multi-organoid body-on-a-chip platform for assessing drug efficiency and toxicity. Charlotte Biomedical Symposium, Charlotte, NC. May 2018. **(Poster Presentation)**

12. **S Rajan**, A Mazzocchi, K Votanopoulos, A Skardal, AR Hall. Tumor-On-A-Chip Microfluidic Devices for Personalized Cancer Drug Testing. Biomedical Engineering Research symposium, Winston-Salem, NC. March 2018. **(Poster Presentation)**

13. **S Rajan**, A Mazzocchi, K Votanopoulos, A Skardal and AR Hall. Tumor-On-A-Chip Microfluidic Devices for Personalized Cancer Drug Testing. 18th Annual Graduate Student & Postdoc Research Day, Winston-Salem, NC. March 2018. **(Poster Presentation)**

14. **S Rajan**, J Aleman, M Wan, NP Zarandi, G Nzou, U Gandhi, S Murphy, CE Bishop, H Sadri-Ardekani, T Shupe, A Atala A Skardal, AR Hall. Adhesive film based multi-organoid body-on-a-chip platform for assessing drug efficiency and toxicity. Annual Wake Forest Institute of Regenerative Medicine Retreat 2018, Pinehurst, NC. January 2018. **(Oral Presentation)**

15. **S Rajan**, A. R. Hall, and A Skardal Adhesive membrane-based microfluidic device for motility assessment of cancer cells. Tissue Engineering and Regenerative Medicine International Society – Americas. Charlotte, NC. December 2017. **(Poster Presentation)**

16. **S Rajan**, J Aleman, M Wan, NP Zarandi, G Nzou, U Gandhi, S Murphy, CE Bishop, H Sadri-Ardekani, T Shupe, A Atala A Skardal, AR Hall. Adhesive film based multi-organoid body-on-a-chip platform for assessing drug efficiency and toxicity. Tissue Engineering and Regenerative Medicine International Society – Americas. Charlotte, NC. December 2017. **(Poster Presentation)**

17. **S Rajan,** A Mazzocchi, K Votanopoulos, A Skardal and AR Hall. Tumor-On-A-Chip Microfluidic Devices for Personalized Cancer Drug Testing. Tissue Engineering and Regenerative Medicine International Society – Americas. Charlotte, NC. December 2017. **(Oral Presentation)**

18. **S Rajan**, A Mazzocchi, K Votanopoulos, A Skardal and AR Hall. Tumor-On-A-Chip Microfluidic Devices for Personalized Cancer Drug Testing. North Carolina Tissue Engineering and Regenerative Medicine Society. Winston-Salem, NC. November 2017. **(Oral Presentation)**

19. **S Rajan**, A Mazzocchi, K Votanopoulos, A Skardal and AR Hall. Tumor-On-A-Chip Microfluidic Devices for Personalized Cancer Drug Testing. Biomedical Engineering Society Annual Meeting, Phoenix, AZ. October 2017. **(Poster Presentation)**

20. **S Rajan**, A Mazzocchi, K Votanopoulos, A Skardal and AR Hall. Tumor-On-A-Chip Microfluidic Devices for Personalized Cancer Drug Testing. Wake Forest Annual Surgical Day, Winston-Salem, NC. October 2017. **(Poster Presentation)**

21. **S Rajan**, A Skardal, AR Hall. 3D cell culture studies in microfluidic systems for translational applications. 17th Annual Graduate Student & Postdoc Research Day, Winston-Salem, NC. March 2017. **(Poster Presentation)**

22. **S Rajan**, A Skardal, AR Hall. Adhesive film based microfluidic system for 3D cell culture applications. Annual Wake Forest Institute of Regenerative Medicine Retreat 2017, Pinehurst, NC. January 2017. **(Oral Presentation)**

23. **S Rajan**, P Hambright, A Skardal, AR Hall. Microfluidic device for motility and biochemical assessment in parallel drug. Tissue Engineering and Regenerative Medicine International Society – Americas. San Diego, CA. December 2016. **(Poster Presentation)**

24. **S Rajan**, P Hambright, A Skardal, AR Hall. Microfluidic device for motility and biochemical assessment in parallel drug. North Carolina Tissue Engineering and Regenerative Medicine Society. Chapel Hill, NC. November 2016. **(Poster Presentation)**

25. **S Rajan,** P Hambright, A Skardal, AR Hall. Microfluidic device for motility and biochemical assessment in parallel drug. Biofabrication Conference, Winston-Salem, NC. October 2016. **(Oral Presentation)**

26. **S Rajan**, P Hambright, A Skardal, AR Hall. Microfluidic device for motility and biochemical assessment in parallel drug. Biomedical Engineering Society Annual Meeting, Minneapolis, MN. October 2016. **(Poster Presentation)**

27. **S Rajan**, P Hambright, A Skardal, AR Hall. Tumor organoids in an ultra-thin microfluidic system for in situ drug response testing. Virginia Tech - Wake Forest School of Biomedical Engineering and Sciences Symposium, Winston-Salem, NC. May 2016. **(Poster Presentation)**

28. **S Rajan,** P Hambright, A Skardal, AR Hall. Tumor organoids in an ultra-thin microfluidic system for in situ drug response testing. IEEE Winston-Salem Chapter, Winston-Salem, NC. March 2016**. (Oral Presentation)**

29. **S Rajan**, P Hambright, A Skardal, AR Hall. Tumor organoids in an ultra-thin microfluidic system for in situ drug response testing. Annual Wake Forest Institute of Regenerative Medicine Retreat, Pinehurst, NC. January 2016. **(Poster Presentation)**

30. **S Rajan** and BC. Towe. Non-invasive method to detect the changes of glucose concentration in whole blood using photometric technique. 36th Annual International Conference of the IEEE Engineering in Medicine and Biology Society, Chicago, IL. October 2014. **(Oral Presentation)**

<u>Mentoring</u>

Direct mentorship (with supervision of projects) of:

• Parker Hambright, undergraduate senior student; at WFIRM, 2015-2016.

• Rosemary Clare Burke, undergraduate senior student; at WFIRM, 2017.

• Nathan Beatson, undergraduate senior student; at WFIRM, 2017-2018.

• Lucy Vaugh, undergraduate sophomore student; at WFIRM, 2018-2019.

• Samuel Moss, undergraduate senior student; at WFIRM, 2019.

• Nathaniel Hauser, Master's student; at WFIRM, 2019.